The Influence of Quiet Sun Magnetism on Solar Radiative Output

by

Courtney Leigh Peck

B.S., Montana State University, 2012

M.S., University of Colorado, Boulder, 2015

A thesis submitted to the

Faculty of the Graduate School of the

University of Colorado in partial fulfillment

of the requirements for the degree of

Doctor of Philosophy

Department of Physics

2018

This thesis entitled:
The Influence of Quiet Sun Magnetism on Solar Radiative Output
written by Courtney Leigh Peck
has been approved for the Department of Physics

_____

Prof. Mark Rast

_____

Tobin Munsat

_____

Han Uitenbroek

Date _____

The final copy of this thesis has been examined by the signatories, and we find that both the content and the form meet acceptable presentation standards of scholarly work in the above mentioned discipline.

Peck, Courtney Leigh (Ph.D., Physics)

The Influence of Quiet Sun Magnetism on Solar Radiative Output

Thesis directed by Prof. Mark Rast

Spectral solar irradiance (SSI), the radiant energy flux per wavelength of the Sun received at Earth, is an important driver of chemical reactions in the Earth's atmosphere. Accurate measurements of SSI are therefore necessary as an input for global climate models. SSI models and observations, however, disagree on the sign and magnitude of the variations. In this thesis, we analyze the contributions of the currently unresolved low magnetic flux 'quiet sun' to SSI variations. Using measurements of the full solar disk, we demonstrate that the sign of the low magnetic flux contribution to SSI variations depends on the defined reference pixels used to normalize a time series of observations. As these reference pixels typically represent the quiet sun, we conclude that full-disk measurements can not provide insight into the low magnetic field contributions to SSI variations.

Using high-resolution radiative magnetohydrodynamic models, we examine the contribution of the quiet sun to SSI variations. We compare the radiative output of two quiet sun simulations with differing imposed magnetic field morphologies, and find that the differences in radiative output result from the formation of magnetic structures of various sizes. The magnetic structures modify the surrounding convective energy flux based on their size, resulting in size dependent radiative output. We find that this morphology dependent difference in spectral irradiance can contribute substantially to the inferred SSI trends.

Connecting these results with upcoming high-resolution observations requires highly accurate numerical solutions and photometrically precise observations. To this end, we present an assessment and solution to numerical diffusion common to certain radiative transfer solvers used to synthesize the emergent intensity from simulations. These results retain the spatial resolution of the synthesized emergent intensity, with applications beyond solar radiative transfer. Further-

more, we assess the photometric precision of post-facto image reconstruction techniques applicable for four-meter solar telescopes. We find sufficient precision to observe radiative output variations found in the magnetohydrodynamic models. The improvement to the numerical radiative transfer method and increased certainty in the photometric precision of upcoming high-resolution observations provide the necessary tools to further enhance our understanding of solar radiative variability at the smallest spatial scales.

Acknowledgements

This thesis represents the culmination of support and mentorship from many amazing people throughout my education. First and foremost, I am greatly indebted to my research advisor, Mark Rast, whose countless hours of mentorship and encouragement have made me the scientist I am today. He has inspired me to continue to push the boundaries of my knowledge even though I often get "lost in the weeds". I also thank my colleagues Serena Criscuoli, Han Uitenbroek, Friedrich Wöger, and Jose Marino for many insightful conversations on solar physics, radiative transfer, and adaptive optics. I look forward to many future discussions and collaborations.

I would also like to acknowledge those who encouraged me to pursue a career in physics. First, the unconventional teaching style, quirky experiments, and mentorship I received from David McDonald led me to initially choose physics for my undergraduate degree. Additionally, many wonderful people at Montana State University influenced my decision to attend graduate school. In particular, I would like to thank Angela Des Jardins, who has been a valuable undergraduate mentor and a continued role model.

Finally, none of this would have been possible without my friends and family who have helped make graduate school more enjoyable. I am deeply grateful for the unwavering support from my sisters, Alyssa Peck and Briana Jones, and the love and encouragement from my partner Cameron Straatsma. I also extend my gratitude to Sarah Black, Baylee Bordwell, Jennifer Ellis, Rachel Plesha, Andrew Sturner, and Carrier Weidner who have been generous and caring friends throughout graduate school.

Contents

Chapter

Tables

Table

Figures

Figure

Chapter 1

Introduction

1.1 The Solar Magnetic Field

The Sun, a G2 type star, displays complex interactions between fluid dynamics and magnetism that influence the Earth's atmosphere and habitability. The core of the star occupies the inner 0.25 $R_\odot$[1] where nuclear fusion generates the solar luminosity. The temperature and density decrease throughout the entire solar interior and eventually no longer sustain nuclear fusion, defining the end of the solar core and the start of the radiative zone. In the radiative zone from around 0.25 $R_\odot$ to 0.70 $R_\odot$ the luminosity produced in the core is transported via radiation. At approximately 0.70 $R_\odot$ the temperature and density have reduced sufficiently such that the opacity increases, reducing the efficiency of radiative heat transport. Here the thermal stratification becomes unstable to convection, thus defining the convection zone where solar luminosity is transported through large-scale convective motions. In the upper most regions of the convection zone, the opacity becomes very small due to the low plasma density and radiative losses dominate over convective energy transport. This region, known as the photosphere, is the region where radiation escapes the solar atmosphere. Beyond the photosphere in the outer atmosphere of the Sun lie the optically thin chromosphere and corona.

The plasma motions in the interface region between the radiative and convection zones, called the tachocline, are thought to produce the large scale magnetic field in the Sun through a process called the solar dynamo (see e.g., Miesch & Toomre 2009; Charbonneau 2014, for reviews).

[1] $R_\odot$ is the solar radius

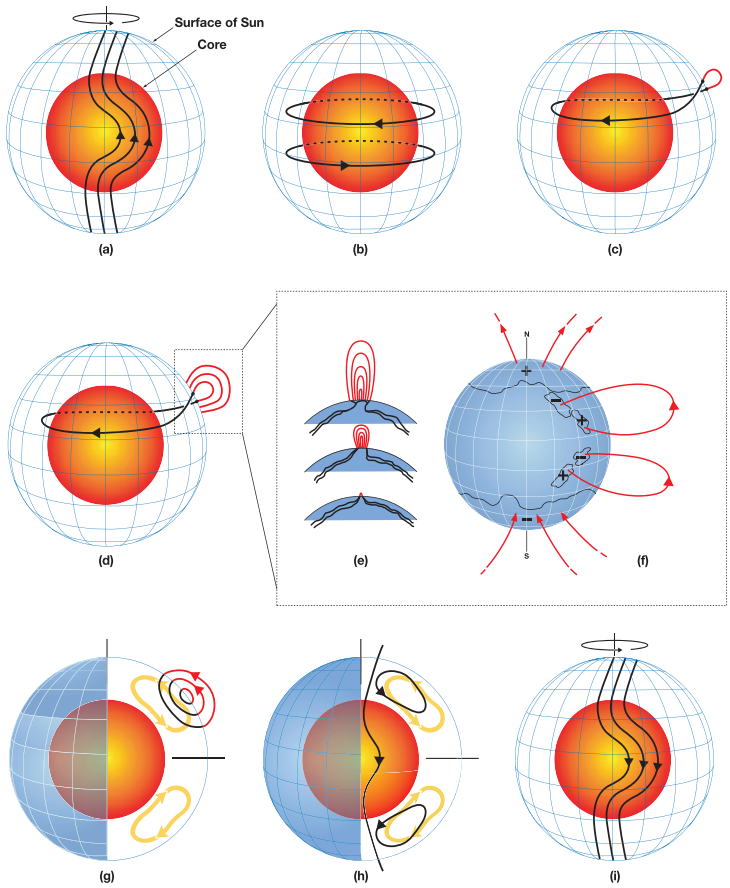

Figure 1.1: Simplified process of the solar dynamo. (a) The solar magnetic field begins as a dipole. (b) The differential rotation pulls the magnetic field faster at the equator than the poles resulting in a torroidal component of the magnetic field. (c) The complex twisting motions of the plasma wind magnetic fields, which occasionally form bundles of magnetic flux that buoyantly emerge in the photosphere. (d) The magnetic flux forms an active region, which continues to rise and grow (e) and the polarities across the equator are such that the flux cancels across the equator (f). (g) Meridional flows drag magnetic flux towards the poles. (h) The accumulation of magnetic flux acts to cancel the polar magnetic field, (i) eventually reversing the polarity of the poles. Figure adapted from Dikpati & Gilman (2006).

Figure 1.1 depicts a cartoon model describing the solar dynamo and the resulting solar magnetic activity cycle based on the pioneering work by Babcock (1961). Beginning with a dipolar magnetic field generated in the solar interior, differential rotation from the rotating non-solid body shears the polloidal magnetic field, generating a torroidal component of the magnetic field. As this process continues, magnetic fields begin to wind together to form magnetic flux bundles which become buoyant. This flux eventually buoyantly reaches the photosphere and forms a magnetic active

region, such as a sunspot, characterized by a leading and following polarity with an equator-ward tilt. The tilts of these active regions follow Joy's law (Hale et al. 1919) and the leading polarity in each hemisphere follows Hale's law (Hale & Nicholson 1925), such that the leading polarities in each hemisphere are opposite and tilted towards the equator. As the active region decays, meridional flow and supergranular motions transport the magnetic flux towards the poles. Due to some magnetic flux cancellation of the leading polarity across the equator, the net polarity transport to the poles is that of the following polarity. Through this process, the magnetic field at the poles is slowly reduced from the opposite polarities and the sign of the field at the pole ultimately reverses. This pole reversal process on the Sun is observed to repeat every 11 years, with a full cycle completed every 22 years, in what is known as the solar magnetic activity cycle (see e.g., Hathaway 2010, for a review on the solar magnetic activity cycle.)

Figure 1.2 shows observations of the solar magnetic flux over latitude and time, known as the solar magnetic butterfly diagram. The 22 year solar cycle is clearly apparent with periods of greatest

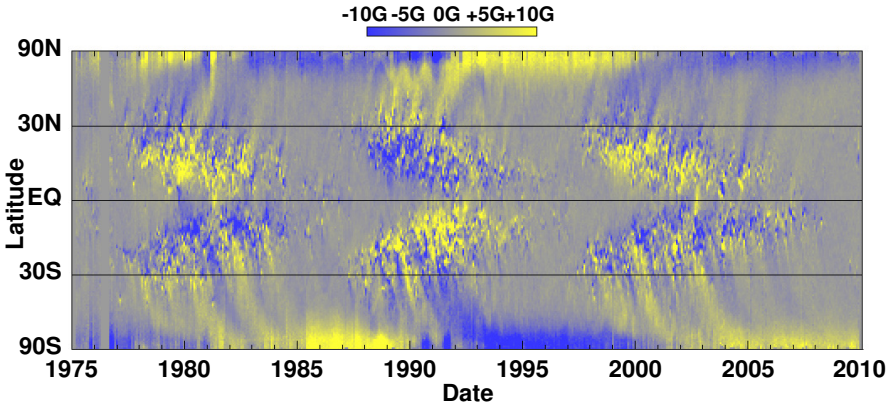

Figure 1.2: Solar magnetic butterfly diagram obtained from the Kitt Peak Vector Spectromagnetograph (VSM) and the Michelson Doppler Imager (MDI) onboard the Solar and Heliospheric Observatory (SOHO). The line-of-sight magnetic flux is shown in colors. This depicts the solar magnetic field evolution qualitatively described in Figure 1.1. Figure adapted from Hathaway (2010).

magnetic activity corresponding to solar maximum (e.g., 1979, 1989, and 2001) and periods of very little magnetic activity corresponding to solar minimum (e.g., 1986, 1997, and 2010). Following

solar minimum, magnetic flux emerges at high latitudes, with the emergence latitude decreasing over the 11 year cycle. The leading and following polarities described by Hale's law can be seen, as well as the sweeping of the following polarity towards the poles. The leading polarity preferentially cancels across the equator with the opposite polarity due to Hale's law. The accumulation of flux at the poles results in the polarity reversals, marking solar minimum.

The magnetic field produced by the solar dynamo is responsible for a wide range of phenomena on the solar surface. Figure 1.3 depicts several solar surface features that are observed in the visible wavelengths and are a main focus of this thesis. Most notably are active regions characterized by the presence of dark sunspots and bright faculae, with the latter typically observable near the solar limb. These features are a direct manifestation of the buoyant magnetic flux produced by the solar dynamo. The top right image of Figure 1.3 shows a close-up view of an active region, demonstrating the variety of spatial scales at which magnetism manifests on the solar photosphere. Sunspots are generally characterized by the very dark umbra surrounded by the filament-structured penumbra, while pores are equivalently dark with no surrounding penumbra. The granulation due to convective motions is present across the entire solar surface, consisting of the warm granules, or upflows, surrounded by the cool narrow downflow lanes. As shown in the bottom right image, magnetic fields concentrate in the downflow lanes down to the smallest spatial scales resolved in the image. These small regions of large magnetic flux density (typically around a few kG) correspond to faculae, while regions of lower magnetic flux density are known as internetwork and network. In this thesis, the term 'quiet sun' is used to refer to any region of the solar surface outside of active regions. These regions include network field with typical magnetic flux densities of around 1 kG.

1.2 Solar Radiative Variability

A striking feature of Figure 1.3 is the differing brightnesses of the solar surface structures. In the granulation, the upflows have higher temperature resulting in their brighter appearance relative to the cooler downflow lanes. Additionally, the magnetic regions have substantially different brightness. Sunspots appear very dark while faculae and magnetic concentrations within the quiet

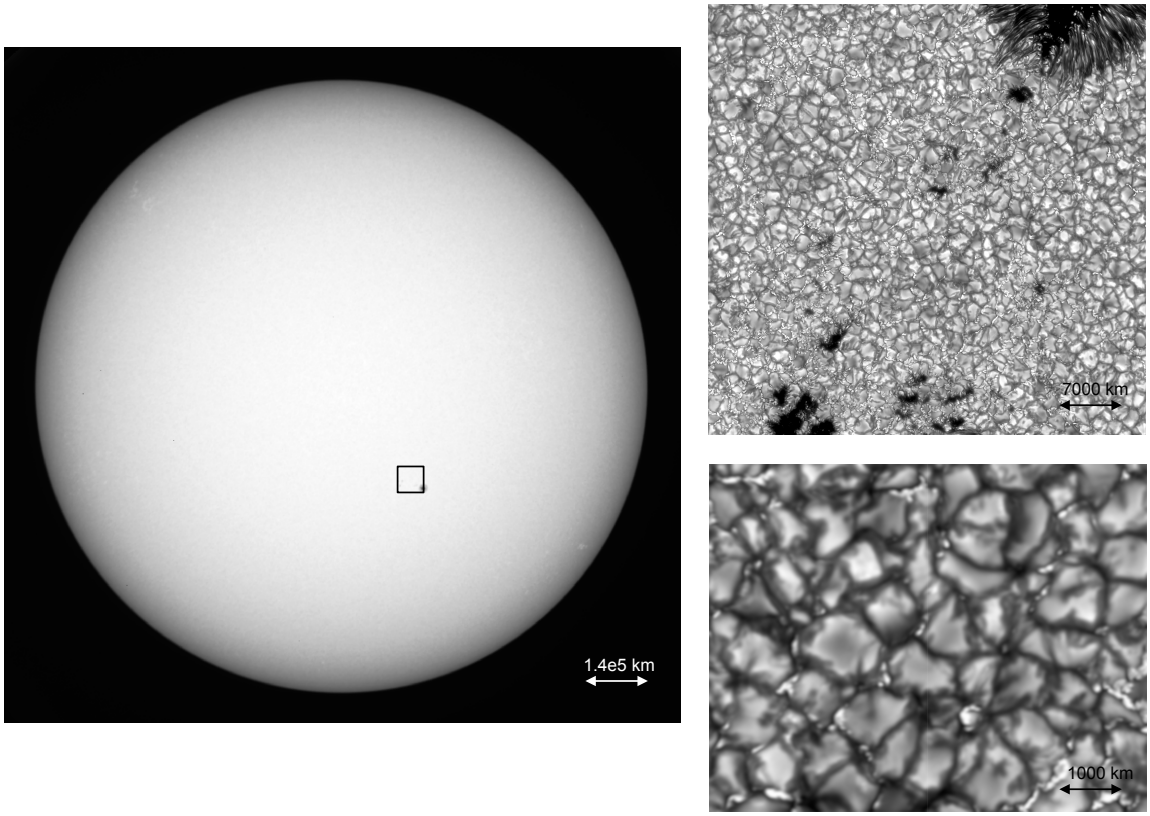

Figure 1.3: Left: Full solar disk observed by the Precision Solar Photometric Telescope (PSPT) at the Mauna Loa Solar Observatory (MLSO) at 409.4 nm. A dark sunspot and bright faculae (lower right of image) are shown. Top right: Calcium II line-wing image at 396.37 nm observed with the Swedish Solar Telescope (SST)[a] showing close-up view of magnetic active region. The background is dominated by the characteristic granulation due to convection, with magnetic field present in many narrow downflow lanes. Sunspots are characterized by the presence of a filament-structured penumbra surrounding a dark umbra, while pores have no such penumbra. Bottom right: Close-up view of a quiet sun region observed by the SST. Note that magnetic field exists in the downflow lanes of the granulation resulting in the bright magnetic structures. Approximate scales are shown in the lower right corner of each image.

[a] The Swedish Solar Telescope is operated on the island of La Palma by the Institute for Solar Physics in the Spanish Observatorio del Roque de los Muchachos of the Instituto de Astrofsica de Canarias. Observations and image processing performed by Vasco Henriques.

sun appear bright compared to the neighboring granulation. The magnetic field strength and the size of the structure play a large role in determining the relative brightness. Magnetic field suppresses the convective motions that dominate the transport of heat in the region just below the photosphere. Suppression of convection reduces heat transport within the magnetic structure

and results in a lower internal temperature compared to the external one. However, since the internal gas plus magnetic pressure must balance the external gas pressure, the presence of the magnetic field also acts to reduce the internal gas pressure which evacuates the structure relative to the surrounding plasma. The reduced gas pressure, and therefore particle density, decreases the internal opacity and allows for lateral radiative heating from the external plasma. The brightness of a structure is thought to be determined by the balance of these mechanisms, where structures with a solar surface radius greater than around 500 km appear dark whereas those with a smaller radius appear bright (Spruit 1976; Knölker & Schüssler 1988).

While the total luminosity generated at the core of the Sun varies on stellar evolutionary time scales, the presence of magnetism and its manifestation as magnetic structures on the surface acts to modulate the solar radiative output on much shorter timescales. In a sunspot, the magnetic field suppresses the convective energy flux resulting in locally reduced thermal energy flux. While some of this energy is redistributed in the surrounding plasma (Rast et al. 1999), some work suggests that energy not released due to the presence of a sunspot is stored within the convection zone and reemitted on thermal relaxation timescales (Spruit 1982a,b). This suggests that the solar luminosity is modulated by the magnetic field, where in general sunspots represent sinks and faculae represent sources of radiative losses. The combined effect of darkening due to sunspots and brightening due to faculae produces the observed enhancement of the solar radiative output with increasing magnetic field (see Section 1.2.1).

An important consequence of variations in the solar radiative output is the effect on Earth's atmosphere. Two measurements are essential to understand the mechanisms influenced by solar radiative variability: Total Solar Irradiance (TSI) and the Spectral Solar Irradiance (SSI). The TSI is the measure of the spectrally-integrated energy output of the Sun incident on Earth's atmosphere and is important to fully account for the total energy budget of the Earth's atmosphere. While the TSI value is necessary for global climate modeling, its variability has negligible impact on global climate change (see e.g., IPCC 2007; Gray et al. 2010). SSI is the measure of the solar radiative output as a function of wavelength. Because physical processes in Earth's atmosphere

depend strongly on interactions modulated by certain wavelengths, constraining the SSI magnitude and variations is necessary to understand the mechanisms that drive atmospheric photochemistry. Below we discuss the past and current understanding of solar irradiance variability.

1.2.1 Total Solar Irradiance (TSI)

Long term measurements of the frequency-integrated TSI began in 1978 with the Earth Radiation Budget (ERB) instrument onboard Nimbus-7 (Jacobowitz et al. 1978; Hickey et al. 1980), and subsequent missions have maintained a largely uninterrupted time series since then. Figure 1.4 shows measurements of the TSI from various instruments, which show a positive correlation with the solar cycle as indicated by the sunspot number. While sunspots appear more frequently near solar maximum, they are accompanied by the presence of the bright faculae. This results in the net increase in radiative output over the solar cycle despite the increased number of dark sunspots.

The variations in the TSI over the solar cycle were found to be on the order of 0.1% for all instruments, however the measured magnitudes of the TSI differed by nearly 1%. From approximately 1990 to 2003, the instrument results converged to the accepted mean value of 1365.4 $\pm$ 1.3 W m^{-2} (see e.g., Fröhlich 2006, for a review of instrument degradation and corrections). However the launch of the Total Irradiance Monitor (TIM) onboard the SOlar Radiation and Climate Experiment (SORCE) (Rottman et al. 2005; Kopp & Lawrence 2005; Kopp et al. 2005a,b) found a far lower mean value of 1361 W m^{-2}. Radiometric calibration tests revealed scattered-light effects in previous instruments, which corrected previous measurements down to the currently accepted value of 1360.8 $\pm$ 0.5 W m^{-2} (Kopp et al. 2012).

The lack of a long-term solar irradiance record, and the intermittency and degradation effects faced by TSI instrumentation have led to the development of irradiance models. Most irradiance models sum the contribution of bright and dark structures on the solar disk that are identified through available full-disk observations. Since many full-disk solar observations extend over longer time-scales than the TSI measurements, irradiance models are capable of reconstructing past irradiance over the time-series for which direct TSI observations are unavailable. Since the models

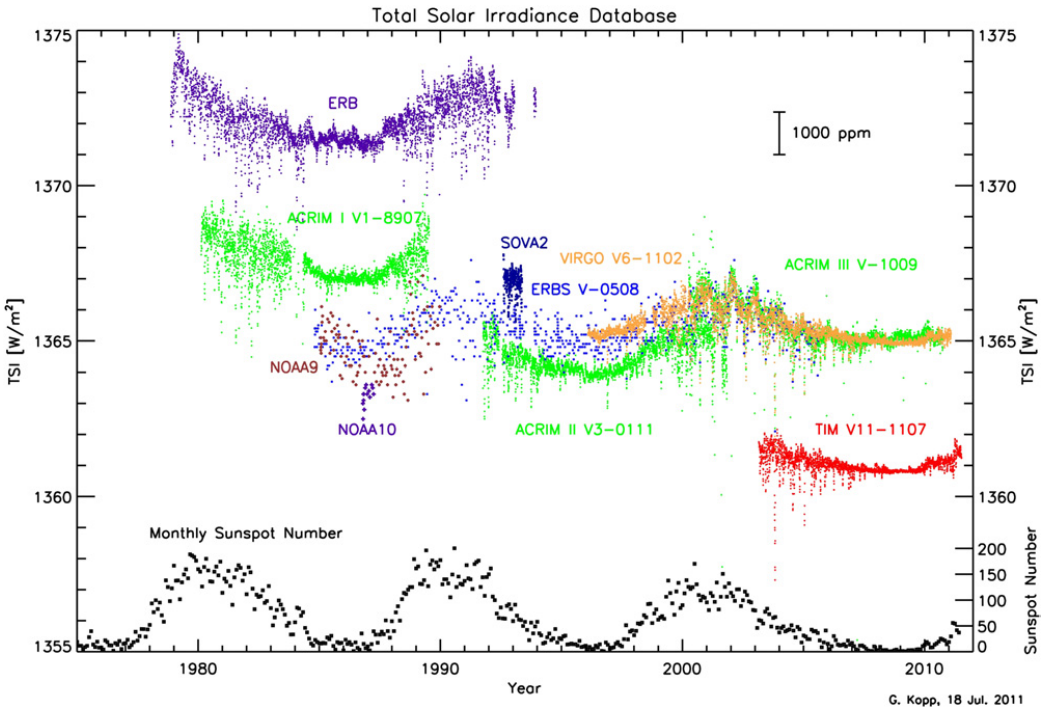

Figure 1.4: TSI measurements from various instruments over 35 years (colors) and the monthly sunspot number (black) used as a proxy for solar magnetic activity. The 11 year solar cycle is clearly visible in all measurements, which is responsible for changes of 0.1% in the TSI. Note the relative offsets of the measurements. Values from SORCE/TIM represent the currently accepted absolute value of 1360.8 $\pm$ 0.5 W m^{-2}. Figure adapted from Kopp et al. (2012).

typically tune the results to TSI measurements, they are ultimately limited to the relationship between magnetic structures and TSI for the time interval of the observations.

Modern irradiance models include COSI (Haberreiter et al. 2008), NRLTSI/SSI (Lean 2000), SATIRE (Fligge et al. 2000; Krivova et al. 2003), and SRPM (Fontenla et al. 2011, and references therein). Irradiance models can be classified as either semi-empirical or proxy models. Semi-empirical models include COSI, SATIRE, and SRPM. These models typically decompose the solar surface into a collection of structures — e.g., faculae, sunspot umbra and penumbra, and quiet sun — which have some observable signature in full-disk images such as magnetic field strength or intensity contrast. The models identify these structures on the solar disk using magnetograms or images from magnetically sensitive spectral lines and, for some models, continuum images. Each

structure has a single 1D atmospheric profile associated with it that is used to compute the radiative output of the structure based on disk position over all wavelengths. Once every pixel for a given image is assigned a structure, the irradiance is computed by summing the radiative output of every pixel on the solar disk. This is then repeated over the time-series of available observations. Since the models assume that all pixels associated with a given structure have the same radiative output, they require at least one free parameter to tune the model to the observed TSI. In several models, the free parameter is chosen as the filling factor of faculae in quiet sun regions, which saturates up to the assumed magnetic flux of facular structures (see e.g., Fligge et al. 2000; Wenzler et al. 2004). Proxy models, which include NRLTSI/SSI, use indirect measurements of the contribution of sunspots and faculae to irradiance. Such measurements include the Photometric Sunspot Index to estimate the disk coverage of sunspots and the Mg II core-to-wing ratio to estimate the contribution of faculae. These models tune the proxy measurements to the observed TSI through the use of free parameters, which quantify the relationship between the proxy measurement and observed radiative output.

Figure 1.5 shows the TSI reconstruction from 1978 to 2010 with the SATIRE and NRLTSI models compared to the PMOD composite (Fröhlich & Lean 1998), which compiles TSI measurements from multiple instruments into a single time series. The agreement between both models and the PMOD composite is around 90-95% over a single solar cycle (e.g., Ball et al. 2012, 2014). Because the models implicitly assume that magnetic structures drive irradiance variations, the close agreement between observations and irradiance models suggests that TSI variations are predominantly driven by changes in solar surface magnetism on the time scales of modern observations (Unruh et al. 1999; Krivova et al. 2003; Yeo et al. 2017). The agreement, however, is limited to the time periods of the observations, which may not represent TSI changes on longer timescales.

1.2.2 Spectral Solar Irradiance (SSI)

Measurements of the spectrally-resolved SSI in some portions of the spectrum have a similarly long history as TSI measurements (see e.g., Ermolli et al. 2013; Yeo et al. 2014a, for reviews

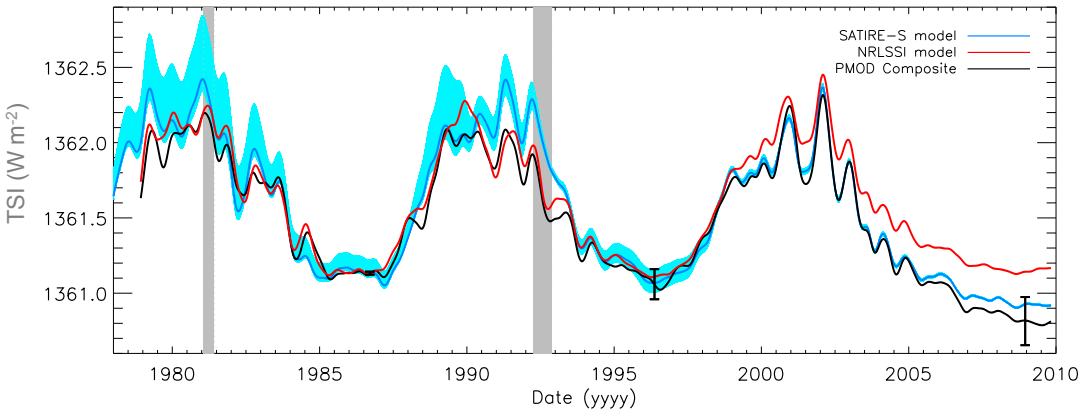

Figure 1.5: Reconstruction of TSI from SATIRE (blue) and NRLSSI (red) irradiance models. PMOD TSI time-series composite of observations (black). Blue bands around SATIRE shows the uncertainty in the reconstruction. Grey vertical bands indicate gaps in the TSI data. Adapted from Ball et al. (2014)

on SSI measurements). Due to interest in understanding the impact of UV variability on the chemistry in Earth's upper atmosphere, measurements in the range of 100 to 400 nm have a largely uninterrupted time series since 1978. As shown in Figure 1.6, the UV measured by various instruments varies in phase with the solar cycle with similar relative amplitudes. However, as

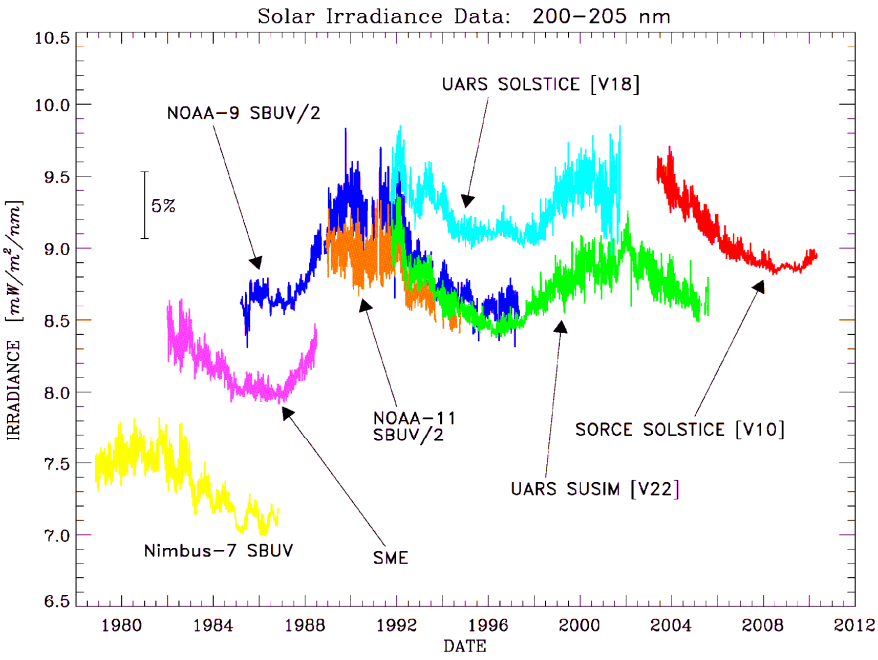

Figure 1.6: SSI measurements integrated from 200 - 205 nm. As in Figure 1.4, all measurements show that the UV varies in phase with the solar cycle. The absolute value of the measurements disagree up to approximately 20%. Adapted from Deland & Cebula (2008) updated to include SORCE/SOLSTICE measurements.

with the TSI measurements discussed previously, the measured absolute SSI values differ between instruments. Similar discrepancies are seen throughout the UV spectrum (e.g., Unruh et al. 2012; Ermolli et al. 2013).

The first radiometric measurements over the entire solar spectrum began in 2003 with the Spectral Irradiance Monitor (SIM) (Harder et al. 2005) and the SOLar STellar Irradiance Comparison Experiment (SOLSTICE) (McClintock et al. 2005) onboard SORCE, which collectively observe a broad range of wavelengths from 200 to 2400 nm, accounting for approximately 97% of the TSI. Both SIM and SOLSTICE measured a larger relative amplitude of the solar cycle variation in the

UV compared with previous instruments (Harder et al. 2009; DeLand & Cebula 2012), as shown for SOLSTICE in Figure 1.6.

The SIM and SOLSTICE measurements also produced unexpected results with respect to the irradiance models discussed in Section 1.2.1. Figure 1.7 shows the ratio of SSI to TSI variability, denoting the enhancement of each integrated wavelength region with the solar cycle. As shown,

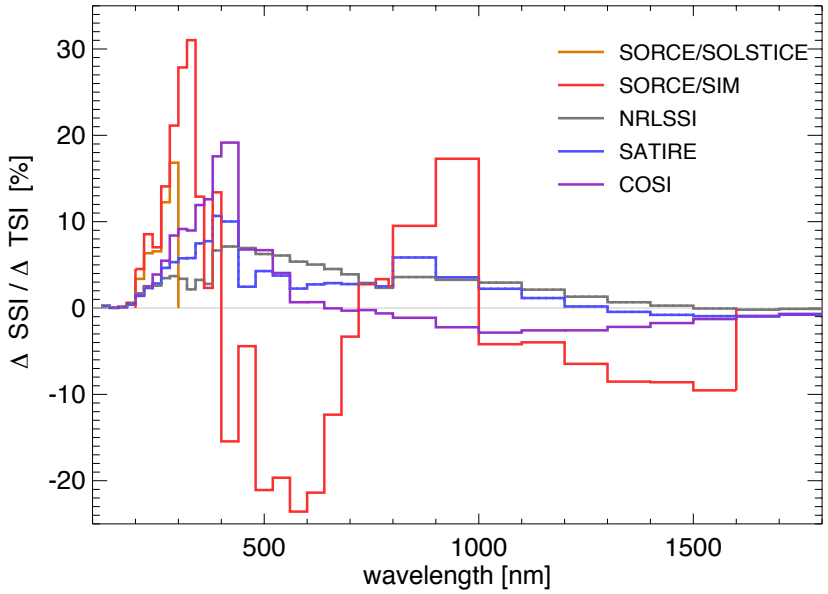

Figure 1.7: Ratio of SSI to TSI variability measured from SORCE (red) and SOLSTICE (orange) onboard SORCE and inferred from NRLSSI (gray), SATIRE (blue), and COSI (purple) irradiance models. Note the disagreement in the amplitude of the SSI variability between observations and models in the UV portion of the spectrum, and the disagreement in the sign in the visible and portions of the IR spectrum. Adapted from Ermolli et al. (2013).

the measurements from SIM and SOLSTICE produce larger enhancement of the UV over the timescales of the solar cycle compared with three irradiance models despite the measurements and models showing roughly equivalent measurements on solar rotational timescales (Unruh et al. 2008, 2012). In the visible portion of the spectrum, SIM measures an out-of-phase variation with the solar cycle while all models, with the exception of SRPM (Fontenla et al. 2011, not shown), predict an in-phase relationship although with differing amplitudes. Similar disagreement of the sign and amplitude of SSI variations measured by SIM and inferred from models are seen in the IR portion

of the spectrum.

The disagreeing results of SSI variability from SORCE measurements and irradiance models has sparked an ongoing effort to better understand irradiance variability and instrument degradation. Some studies comparing UV irradiance model trends to SIM measurements have suggested that the disagreements may be attributed to lack of accurate instrument calibration (e.g., Lean & DeLand 2012; DeLand & Cebula 2012; Yeo et al. 2014b). Alternatively, other studies have reproduced the visible wavelength SSI trends measured by SIM using ground-based photometry (Preminger et al. 2011) and 3D MHD simulations (Criscuoli & Uitenbroek 2014). Due to the importance of solar UV variability on upper atmospheric molecular concentrations, many authors have investigated the reliability of SORCE measurements and irradiance model results used as inputs to climate models in reproducing observed concentrations with contradictory results. In the comparison of stratospheric ozone concentrations some studies find that SORCE measurements produce inconsistent concentrations compared with observations (e.g., Ball et al. 2016), while others find SORCE measurements yield concentrations that agree better than those inferred using irradiance model SSI outputs (e.g., Haigh et al. 2010; Merkel et al. 2011). Similarly, SORCE measurements as input have been found to yield more accurate atmospheric OH concentrations than those found using irradiance model results (Wang et al. 2013).

While irradiance models successfully account for the majority of TSI variations, it is important to consider their limitations especially when evaluating their efficacy in reproducing SSI variations. First, the use of one or more free parameters in the models tunes the results to TSI observations, which may limit their ability to reproduce TSI variability on longer timescales. Additionally, the use of average 1D atmospheres in irradiance model calculations does not capture the 3D nature of the solar surface, and therefore the average radiative output of a 3D surface may not represent the radiative output of the average 1D atmosphere (Uitenbroek & Criscuoli 2011). This may explain why model results and observations of the intensity contrast over the solar disk disagree in some comparisons (Afram et al. 2011). Finally, irradiance models implicitly assume that changes in radiative output are due to the appearance and disappearance of magnetic struc-

tures on the solar disk. Due to the limited TSI and SSI datasets for making composite time series, any long term variability (longer than 11-years) not due to magnetism in the radiative output is currently not captured. Based on the lack of agreement between observations and models and the limitations of both, it is clear that our current understanding of the drivers of irradiance variations is somewhat limited.

1.3 Quiet Sun Magnetism and Irradiance Variability

From the previous discussion of solar variability and magnetism, magnetism appears largely responsible for at least short-term irradiance variations, while the source or existence of possible long term trends remains unknown. The appearance and disappearance of large magnetic structures — sunspots and faculae — on the solar disk account for a large fraction of observed irradiance variations, resulting in the success of irradiance models. Magnetic flux, however, is likely present at all spatial scales including within the quiet sun. Furthermore, the quiet sun covers around 90% of the solar disk and contributes substantially to the total magnetic flux (Sánchez Almeida 2004; Domínguez Cerdeña et al. 2006). Given that magnetism drives much of the solar radiative variability on the timescales of TSI observations, the underlying magnetism of the quiet sun likely contributes non-negligibly to both TSI and SSI variations.

The contribution of the quiet sun and its underlying magnetic substructure to irradiance variability has received limited attention, likely due to its low contrast and the limited spatial resolution of most available observations. Some studies have analyzed the variation in the quiet sun contrast with disagreeing results on the solar cycle radiative variability (Ortiz 2005; Ermolli et al. 2003). Using observations from Hinode and the Swedish Solar Telescope, Schnerr & Spruit (2011) found that the quiet sun can contribute a brightening of about 0.15% when the observations are corrected for resolution, a brightness larger than the TSI variation over the solar cycle. Furthermore, some studies suggest that the apparent brightness of quiet sun regions depends on the magnetic environment in which it is embedded. Observations show that the relative brightness of quiet sun magnetic fields is higher than that of equivalent magnetic fields observed in active regions (e.g.,

Lawrence et al. 1993; Kobel et al. 2011, 2012; Criscuoli et al. 2017). Similarly, results from Vögler (2005) found that the total emergent radiation in a local-box solar surface simulations depended on the average magnetic field within the domain, where a larger average vertical magnetic field resulted in a higher radiative output for regions consistent with quiet sun magnetic field strengths. The effect of quiet sun magnetism on radiative output is currently not well understood, and therefore not incorporated into irradiance modeling. In the following we discuss formation mechanisms of the quiet sun magnetic field and observed magnetic morphologies.

1.3.1 Origins of Quiet Sun Magnetism

Quiet sun magnetism includes magnetic fields with small enough spatial extent or flux densities such that they are not classified as faculae or sunspots. The magnetic regions within the quiet sun likely have unresolved magnetic substructure (Livingston & Harvey 1971), which has been seen in observations of quiet sun magnetism (e.g., Lin & Rimmele 1999; Domínguez Cerdeña et al. 2003; Harvey et al. 2007; Lagg et al. 2010). These magnetic fields are thought to originate through a variety of mechanisms, which likely coexist on the solar surface (see e.g., Wijn et al. 2009; Pillet 2013; Borrero et al. 2015, for reviews of quiet sun magnetism). For example, the quiet sun magnetic field could result from magnetic flux formed deep in the convection zone emerging at small spatial scales in the photosphere, or through the decay of magnetic active regions into small flux concentrations. As these magnetic fields are generally related to the global solar dynamo, the strength of the quiet sun magnetic field produced through these mechanisms likely contains signatures of the solar magnetic activity cycle.

Another magnetic field generation mechanism is a local turbulent dynamo, which produces magnetic field from the twisting and shearing motions in a fluid. This turbulent dynamo magnetic field was first suggested by Batchelor (1950), with the existence of this field in the solar context proposed by Petrovay & Szakaly (1993). The magnetic field is produced through chaotic motions of the plasma, such as turbulence, that generates and amplifies a magnetic field. This creates a mixed polarity magnetic field with spatial scales down to the integral length scale of the turbulent

flow. The turbulent flows generate isotropically oriented magnetic fields with mixed polarity over spatial scales down to the length scale of the flow. Since turbulent motions generate the magnetic fields in this process, the magnetic field strengths would be independent of the solar cycle.

Determining the source and filling factor of the quiet sun magnetic field resulting from these generation mechanisms is currently an active area of research. An assumed signature of the local turbulent dynamo is the presence of a strong horizontal magnetic field component, while the signature of magnetic field generated from deep in the convection zone or decaying active regions is assumed to be predominantly vertical. Measuring the weak signature of the quiet sun magnetic field, however, remains difficult particularly for mixed polarity and horizontal magnetic fields due to the limited sensitivity of Zeeman diagnostics. Recent studies have looked for observational signatures of quiet sun magnetic field produced through these mechanisms with varying results at least partially owing to the observational difficulties (e.g., Harvey et al. 2007; Lites et al. 2008; Asensio Ramos 2009; Ishikawa & Tsuneta 2009; Stenflo 2010; Danilovic et al. 2010a; Lites 2011). The solar cycle variation of the quiet sun magnetic field strength has been studied more recently using long time-series of magnetic field orientation in an attempt to determine the source of the quiet sun magnetic field. For example, Buehler et al. (2013) finds a portion of the quiet sun whose magnetic field strength does not vary with the solar cycle, while Lites et al. (2014) finds weak solar cycle dependence.

The quiet sun magnetic fields generated from various mechanisms likely coexist on the solar surface, and result in a wide variety of magnetic morphologies at small spatial scales. In fact, magnetic field generated by a local turbulent dynamo could appear predominantly vertical if the vertical extent of the field was large compared to the region observed. Similarly, large-scale solar magnetic fields are dipolar and the field lines must connect back to the surface. For highly entwined magnetic fields, the large-scale fields could appear nearly isotropic near the surface if the field lines connect back towards the surface nearby. Because there is currently no method to distinguish between the generation processes of the quiet sun magnetic field, the effect of the magnetic morphology on the radiative output remains unclear.

1.4 Aim of Thesis

While observational evidence suggests a variety of quiet sun magnetic morphologies, no studies to date have investigated the impact of the differing magnetic field morphologies on the radiative output of the quiet sun. Since quiet sun field covers approximately 90% of the solar surface, the integrated radiative output of these structures could have a large impact on irradiance variations. This thesis presents contributions to the study of the radiative output of the quiet sun using ground-based observations and highly realistic simulations of the solar surface. Chapter 2 demonstrates that ground-based observations alone are insufficient to deduce the influence of small scale magnetic field on the spectral radiative output of the quiet sun, due to the lack of high spatial resolution observations or spatially resolved absolute radiometric measurements. This motivates the use of highly realistic simulations of the solar photosphere to study the quiet sun radiative output.

Understanding the radiative output of the solar surface requires knowledge of the theory of radiative transfer, which is presented in Chapter 3. This chapter also discusses the assumptions used to synthesize the emergent intensity through a simulated solar atmosphere, including the treatment of local thermodynamic equilibrium and the dominant sources of opacity in the solar photosphere. Motivated by the need for efficient computational radiative transfer, Chapter 4 quantifies numerical artifacts in a commonly used numerical radiative transfer scheme and proposes a solution to avoid these artifacts. This work has applications to a broader range of computational problems to improve the numerical accuracy in some radiative transfer solvers, in particular as related to the preservation of intensity contrast when computing radiative transfer on a numerical grid.

Chapter 5 describes the 3D solar surface simulations used in this work, including the physics incorporated and the assumptions made. The simulations represent two quiet sun magnetic morphologies — one with a mean vertical field and the with an isotropic magnetic field distribution with zero mean field. We discuss the realism of the simulations as inferred from comparisons with observations. Chapter 6 then uses these simulations to analyze the effect of magnetic field morphology on radiative output by comparing the features of equivalent magnetic field strength and

size. Chapter 7 demonstrates the effect of the two magnetic morphologies on the inferred trends of irradiance models and potential errors introduced assuming an incorrect quiet sun atmosphere model.

Finally, Chapter 8 connects the observable differences due to magnetic morphology to upcoming observations from the high-resolution DKIST solar telescope by constraining the photometric precision error due resulting from the post-facto atmospheric degradation correction scheme. These observations coupled with the high resolution simulations of the solar surface may help improve understanding of the radiative behavior of the quiet sun.

Chapter 2

Photometric Trends in the Visible Solar Continuum and Their Sensitivity to the Center-to-Limb Profile

From the discussion in the previous chapter, the quiet sun radiative output and its dependence on the solar cycle may play an important role in irradiance variability. However, the quiet sun has received little attention due to the lack of sufficient spatial resolution. Currently, observing the solar cycle dependence of the quiet sun radiative output is limited to analyzing time series of full-disk images with a high photometric precision. Due to the lack of radiometrically accurate calibrations, such analyses require seeing or instrument degradation changes to be removed from each image. For solar observations, this is typically done by measuring the brightness of a pixel with respect to a center-to-limb profile definition — usually taken as the quiet sun. In this chapter, we demonstrate that the lowest contrast structures including the quiet sun are most sensitive to this profile definition, and the observed solar cycle trends lie within the error of determining this profile. This work utilizes ground-based observations from the Precision Solar Photometric Telescope at the Mauna Loa Solar Observatory to examine the sensitivity of continuum contrast measurements to the center-to-limb profile definition. We particularly demonstrate that the photometric trends of the lowest contrast structures (i.e., internetwork and network — comprising the quiet sun) are most sensitive to the definition.

This chapter is based on work previously published in Peck & Rast (2015)[1] . C. L. Peck was the primary author on the paper and performed the data analysis presented throughout. M. P.

[1] Peck, C. L., & Rast, M. P. 2015, Photometric Trends in the Visible Solar Continuum and Their Sensitivity to the Center-to-Limb Profile, The Astrophysical Journals, 808, 192

Rast provided project definition and guidance throughout the project.

2.1 Introduction

Solar irradiance studies to date have focused on disk-integrated radiometry and magnetic structure based irradiance reconstructions. Space-based measurements of the disk-integrated total solar irradiance (TSI) over the past several decades show $\sim 0.1\%$ variation on the timescales of solar rotation and the 11-year activity cycle (e.g., Fröhlich & Lean 2004, and references therein). More recent measurements of the disk-integrated solar spectral irradiance (SSI) have suggested that some wavelengths vary in phase with TSI while others do not (e.g., Harder et al. 2009). Ground based full-disk imaging has achieved relative photometric precision (pixel-to-pixel) of up to 0.1% (e.g., Rast et al. 2008), and these images have been used to understand the contribution of individual magnetic structures to the total and spectral irradiance (e.g., Fontenla et al. 2009).

The appearance and disappearance of magnetic structures can account for most of the variation in the TSI observed over the course of a solar cycle. Sunspots and pores have negative contrast against the background disk, while smaller scale magnetic elements generally contribute positively, and more so toward the limb, though whether the net contribution including a larger surrounding area is also positive has been recently brought into question by radiative magnetohydrodynamic simulations of small flux elements (Thaler & Spruit 2014). Empirical two-component models based on a sunspot deficit (from observed areas and locations) and a facular excess (determined using chromospheric proxies and/or the observed facular area from filter-gram images or longitudinal magnetograms) can account for up to 90% of the observed TSI variation (e.g., Fröhlich & Lean 2004; Krivova et al. 2006; Ball et al. 2012). These models do particularly well reproducing irradiance variations on solar rotation timescales, where deep drops in irradiance correspond to the passage of sunspots and enhanced irradiance results from large regions of faculae particularly at the limb. The positive facular contribution plays a dominate role on cycle timescales or longer. The existence of any longer-term secular variation, however, remains unknown. Suggestions for such a long-term component range from the enhancement by change in the number of small-scale elements (Ermolli

et al. 2003; Ortiz 2005) to underlying thermodynamic changes (Kuhn et al. 1998).

This work is concerned with wavelength resolved solar spectral irradiance variations, which are more complex due to the wavelength dependence of the solar opacity . The magnitude and even the sign of the spectral contribution of small scale magnetic structures depends critically on the wavelength being observed, the strength and distribution of the magnetic field within the structure, and the disk position at which the structure is found. Models of the solar spectral irradiance typically proceed semi-empirically, using a multi-component decomposition of solar images into structure classes, one-dimensional model atmospheres of each structure class, and spectral synthesis via a sum over contributions of each structure as a function of its disk position (e.g., Fontenla et al. 2011). Solar images are used in such analysis in two ways, for structure identification, usually employing Ca ll K emission or magnetic flux density measurements, and for empirical construction of the underlying one-dimensional model atmospheres based on the wavelength-dependent center-to-limb variations (CLV).

As there are no full-disk radiometric images available, photometric images from ground-based observations are employed in one or both of these steps. Unfortunately, analysis of the photometric image data requires a definition of the quiet sun intensity against which the contrasts of all structures on the disk are measured. This means that structure identification and contrast measurements are made relative to a somewhat arbitrary definition of the quiet sun CLV. Temporal variations in that CLV profile can result from error or inconsistencies in the identification of the quiet sun pixels, changes in the filling factor of unresolved magnetic flux elements, or true changes in the underlying thermodynamic structure of the star. These are difficult to separate, and any method using contrast images in the synthesis of the solar spectral output faces inherent difficulty in distinguishing actual trends in magnetic structure contributions from temporal variations in the CLV profile.

Work by Ermolli et al. (2003) and Ortiz & Rast (2005) investigated the possibility that small scale magnetic structures, particularly in the form of magnetic network, introduce long-term variability in the TSI and SSI. Using ground-based PSPT observations from the Osservatorio

Astronomico di Roma, Ermolli et al. (2003) found cycle-dependent enhancement of network contributions, while Ortiz & Rast (2005) using intensity images from Solar and Heliospheric Observatory (SOHO)/MDI, found no such enhancement. The balloon-borne Solar Bolometric Imager experiment (SBI, Foukal et al. 2004) found no indication of brightness variations in the quiet sun contributions. While Ortiz notes that the network discrepancy could result from the differing structure definitions, the limited spatial resolution of both the MDI and SBI instruments (4 and 5 arcsec, respectively) and the limited photometric precision (about 1%) of the MDI images may also have contributed. At low spatial resolution and photometric precision, network and quiet sun contributions are difficult to disentangle and depend sensitively on the CLV used in their identification.

There have also been efforts to use full-disk photometric imagery (contrast images) directly to understand irradiance trends without decomposing the images into magnetic components. Preminger et al. (2011) at the San Fernando Observatory computed disk-integrated red and blue continuum contrasts, finding them both to be slightly anti-correlated with solar magnetic activity. They concluded that the Sun's visible continuum is spot-dominated and therefore diminishes at solar maximum, a result contrary to SSI model reconstructions which suggest that the increased abundance of bright magnetic elements, such as faculae, with increased activity outweighs the sunspot deficit (e.g., Lean 2000). Preminger et al. (2011) concluded that the reduction in the continuum output with increased magnetic activity is in qualitative agreement with the SIM spectral irradiance measurements which suggest that these wavelengths respond out of phase over the solar cycle (Harder et al. 2009), however they are in disagreement with SOHO/VIRGO measurements which find the visible continuum to vary in phase (Wehrli et al. 2013).

These contradictory results, both that of the small magnetic structure contribution and the full-disk continuum trends, motivate our investigation of the role of the CLV in the measurements. We re-examine the disk-integrated continuum contrast as a function of solar cycle using two different definitions of the quiet sun reference. We find that the trends are highly dependent on the CLV profile employed, and that small changes in the profile shape can remove or reverse the observed trends. We also evaluate the role of the CLV in determining contrast trends of specific magnetic

structure classes. We find that the very abundant low contrast features, active network, network, and internetwork, are those most susceptible to variations in the CLV. This has implications for both relative photometric measurements of their variation and the disk integrated contrast which they dominate. We examine the effects of dramatically reducing the contribution of weak magnetic structures to the quiet sun CLV reference, and find that the strengths of the photometric trends depend critically on the magnetic flux density used in the quiet sun definition, both through the identification scheme and via weak field continuum contributions.

2.2 Photometric Trends Using PSPT Data

The Precision Solar Photometric Telescope (PSPT) at the Mauna Loa Solar Observatory (MLSO) produces daily seeing-limited full-disk images at blue continuum (409.4nm, FWHM 0.3nm), red continuum (607.1nm, FWHM 0.5nm), and CaII K (393.4nm, FWHM 0.3nm) wavelengths[2] with up to 0.1% pixel-to-pixel relative photometric precision (Rast et al. 2008). We use the red and blue images to measure the solar photospheric continuum contrasts and the CaII K images for magnetic structure identification (Fontenla et al. 2009), with sunspot umbra and penumbra identified by their red continuum deficit.

We employ two standard definitions of the quiet sun to compute the CLV, against which the contrast of each image pixel is measured. The first method employs the median intensity of all pixels in equal-area concentric annuli as a somewhat activity insensitive proxy for the quiet sun intensity. The details of this method are adopted from the work of Walton et al. (1998) and Preminger et al. (2002). The second uses the median intensity of internetwork pixels as identified by the Solar Radiation Physical Modeling (SRPM) semi-empirical thresholding scheme (Fontenla et al. 2009, and references therein) in aligned CaII K images. Both schemes employ 100 equal-area annuli between $\mu = 0.2$ and 1, where μ is the cosine of the heliocentric angle. We restrict our analysis to μ greater than 0.2, corresponding to $0.975 R_{\rm Sun}$, to lesson limb effects where structure identification becomes less robust due to the highly inclined viewing angle.

[2] filter profiles at http : //lasp.colorado.edu/pspt_access/

Subtracting the CLV profile from the image and normalizing by the CLV as a function of disk position creates a photometric map, identifying the relative contribution of each pixel to the disk-integrated contrast. Summing over all image pixels yields the photometric sum defined by Preminger et al. (2011) as

$$\Sigma = \frac{\sum_i \left(I_i - I(\mu_i)\right)}{\sum_i I(\mu_i)} \ , \tag{2.1}$$

where I_i is the observed intensity, μ_i is the cosine of the heliocentric angle, and $I(\mu_i)$ is the CLV profile as a function of μ determined using one of the two methods described above at the ith pixel location.

The photometric sums over the red and blue continuum images, Σ_R and Σ_B, are plotted in Figure 2.1 as a function of time for each of the CLV definitions. Short-term variations result from solar features, primarily sunspots and faculae, crossing the solar disk and changing the solar irradiance on timescales of a few days or weeks. Over-plotted are 81-day running mean values which highlight longer-term trends. As in previous work (Preminger et al. 2011), when employing the quiet sun proxy (median intensity of all pixels in annuli) in the construction of the CLV profile, Σ_R and Σ_B are out of phase with solar activity. However, when SRPM internetwork pixels alone are used in the CLV determination the photometric sums are in phase with solar activity. Long-term trends in the photometric sum are sensitive to the CLV profile employed. (Note: we will address the low amplitude annual variations seen in Figure 2.1 in Section 2.3.)

Using the SRPM image mask, we decompose the total photometric sum of Figure 2.1 into the contributions from magnetic structures: internetwork, network, active network, faculae, and sunspots. As shown in Figure 2.2 for the red continuum, the amplitude and phase dependence of sunspots and faculae contrasts show very little sensitivity to the CLV profiles. Using either profile, disk-integrated facular contrasts are in phase with the solar cycle while that of sunspots is out of phase. The active network contribution is similar to that of faculae, showing an in phase relationship to the solar cycle, but the magnitude of the variation with solar cycle is significantly larger when the determination of the CLV profile is based on quiet sun pixels only. The network contribution

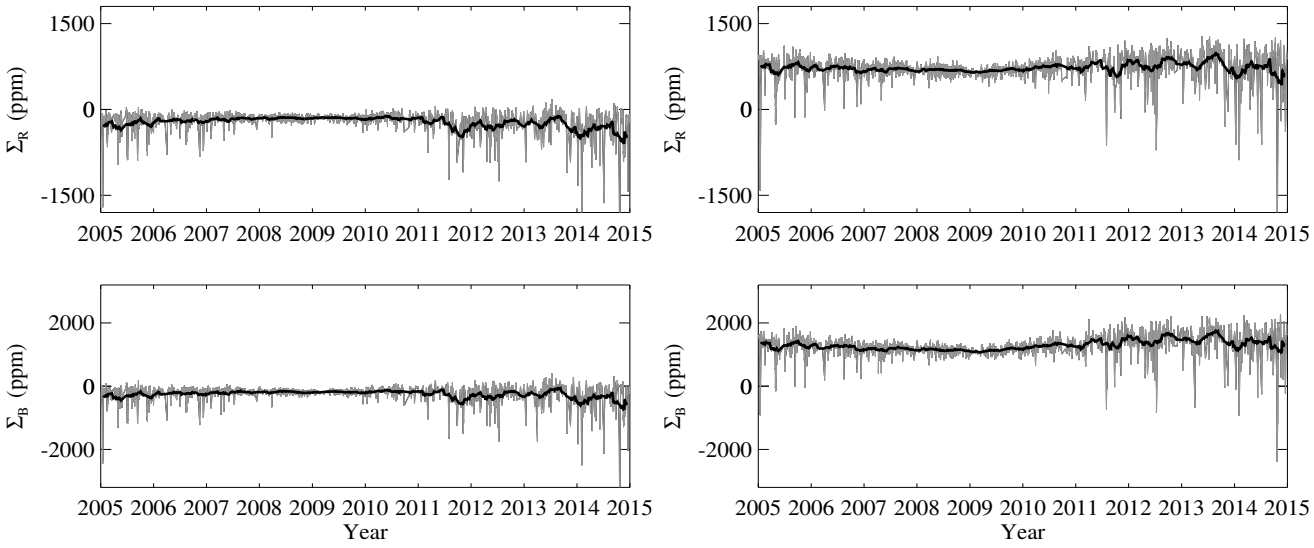

Figure 2.1: Left: photometric sum in red (top), Σ_{R}, and blue (bottom), Σ_{B}, using the median intensity as a proxy for quiet sun pixels in the CLV determination. Right: photometric sums using the median intensity of internetwork pixels only in the CLV. Bold lines are 81-day running averages to highlight longer-term trends. Note the trend reversal between the two processing schemes.

is out of phase with the solar cycle, with trends of approximately the same magnitude for the two CLV determination schemes. The internetwork dependence on cycle is flat when the quiet sun (internetwork) pixels are used to construct the CLV, since the internetwork pixels were used to construct the background reference. However, the internetwork shows an out of phase trend with the solar cycle when the median pixel value is employed. We note that the values presented here are total structure contributions normalized by the full disk area but not normalized to the number of pixels of each structure type, which changes with solar activity. Thus temporal variations in the photometric sums reflect two possible underlying causes, changes in the fractional area covered by the magnetic structure types and/or changes in the structure contrasts.

2.3 Contribution of the Selected Center-to-Limb Profile to Observed Photometric Trends

The differences between the right and left columns of Figures 2.1 and 2.2 reflect the sensitivity of the photometric measures to the CLV definition employed. Since the CLV is constructed using a 'quiet sun' reference and the contrast of each image pixel is measured against the chosen CLV, the quiet sun reference plays a significant role in the observed contrast trends. The quiet sun reference can vary over the solar cycle due to changes in the quiet sun identification, the filling factor of sub-pixel unresolved magnetic structures, or the underlying thermodynamic structure of the atmosphere.

While we can not differentiate between these underlying causes, we can evaluate how the CLV definitions of the previous section lead to the observed trends. The difference between the total photometric sum obtained when using the CLV constructed from the quiet sun median value proxy, $\Sigma_{\rm proxy}$, and the total photometric sum obtained when using the CLV constructed from internetwork pixels, $\Sigma_{\rm quietsun}$, can be written as

$$\Sigma_{\rm quietsun} - \Sigma_{\rm proxy} = -\delta(\Sigma_{\rm proxy} + 1) \ , \tag{2.2}$$

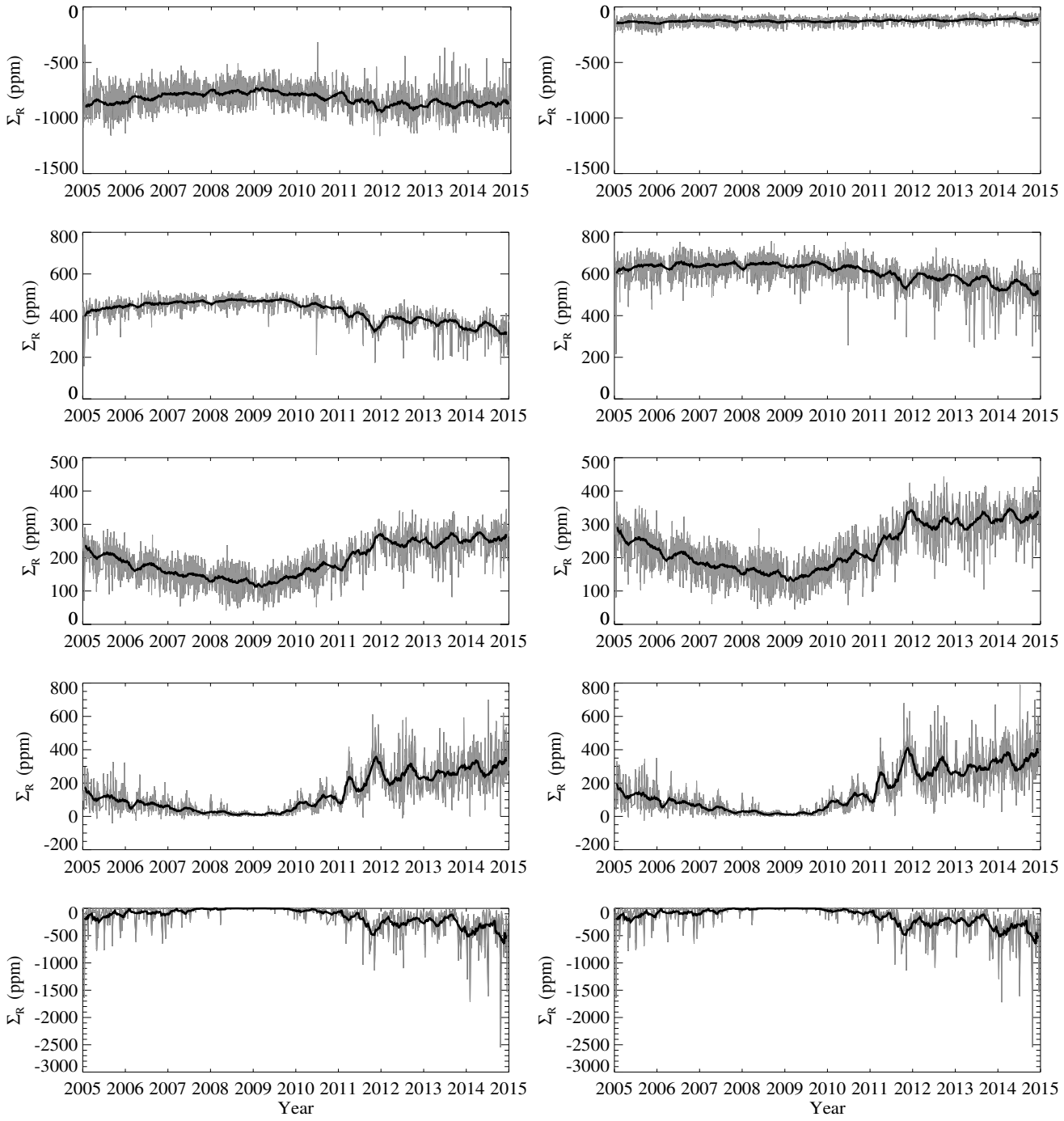

Figure 2.2: Effects of the CLV on photometric trends of SRPM identified features. Left: photometric sum, Σ_R, of solar elements using the median intensity as a proxy for quiet sun pixels. Right: photometric sum using the median intensity of only quiet sun pixels. From top to bottom: internetwork, network, active network, faculae, and sunspots. Bold lines are 81-day running averages to highlight longer-term trends. Note the trend reversal in the internetwork pixels only between the two processing schemes, which demonstrates the sensitivity of low contrast, high abundance features to the CLV.

where

$$\delta = \frac{\sum_i \left(I_{\mathrm{quietsun}}(\mu_i) - I_{\mathrm{proxy}}(\mu_i) \right)}{\sum_i I_{\mathrm{quietsun}}(\mu_i)} \tag{2.3}$$

is the disk-integrated difference in the two CLVs applied in this study. The difference in the total photometric sums thus depends linearly on the differences between the CLVs. This implies that the trend reversal in Figure 2.1 resulted from a cycle-dependent difference between the two CLVs of the same order of magnitude as the photometric trends themselves.

The disk-integrated relative difference between the CLVs (Equation 2.3) which gives rise to the trend reversal of Figure 2.1 includes both the cycle-dependent differences and a constant offset due to the mean intensity of the pixels used in the quiet sun reference. We are interested in cycle-dependent differences caused by the choice of the CLV profile and so define $\delta_{\mathrm{measured}}$ as δ minus its temporal average, and plot that disk-integrated quantity in Figure 2.3.

The disk-integrated CLV differences are out of phase with solar cycle and of the same magnitude of the total photometric trends of Figure 2.1. Since the only difference between the two CLV profiles is the number of resolved magnetic structures included in the quiet sun reference, the photometric sum deduced from one or both of the quiet sun references contains measurable cycle-dependent contamination which manifest in the photometric sum via the choice of CLV.

Evaluating the disk normalized changes between the two choices of CLV (quiet sun minus proxy) as a function of disk position illustrates how the underlying quiet sun references change the CLV shape with solar cycle (Figure 2.4). Only the 81-day running averages are plotted to emphasize the longer-term trends. The cycle dependency of the CLV difference in each annulus implies that one or both of the quiet sun references introduces contamination by magnetically enhanced structures in the CLV. The differences near the limb are out of phase with solar cycle, while those near disk center are in phase. This indicates that the CLV profiles are changing shape with respect to each other, and this in turn affects any measurement of the center-to-limb profile of magnetic structure contrast on the disk and the contribution of these structures to the photometric sums in Figure 2.2.

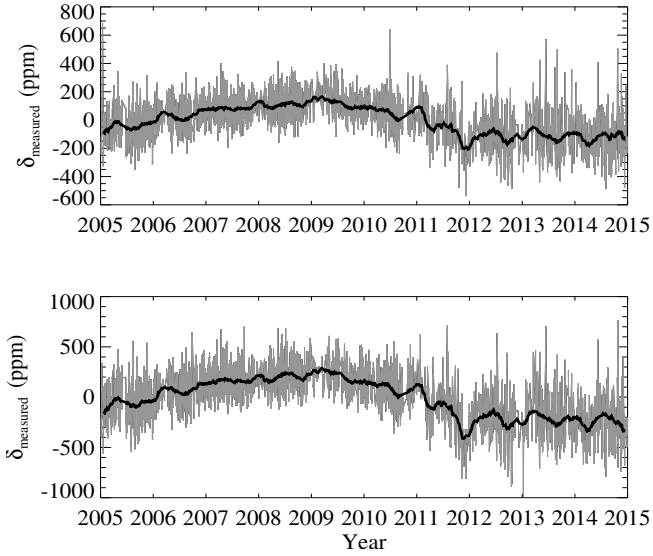

Figure 2.3: Relative difference between the disk integrated quiet sun CLV and quiet sun proxy CLV minus the temporal average, δ_{measured}, in red (top) and blue (bottom). Bold lines are 81-day running averages to highlight longer-term trends. Note the cycle dependence of the relative difference which changes in each annulus.

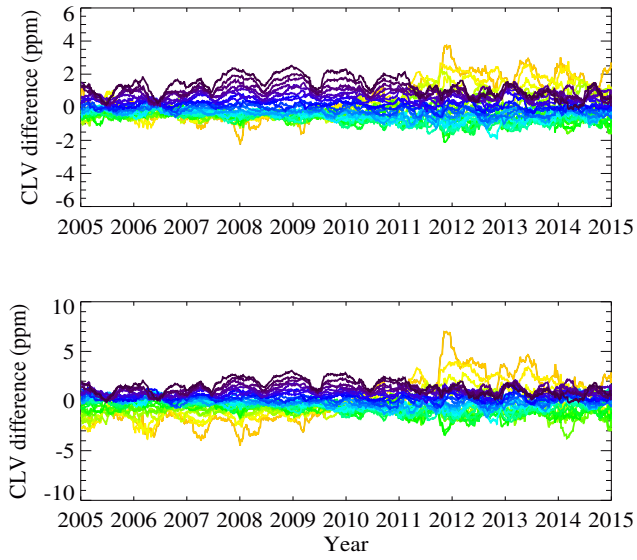

Figure 2.4: Disk normalized difference between the CLVs in each annulus in red (top) and blue (bottom) continuum from center (yellow) to limb (black) averaged over 81 days to highlight the longer-term trends. Each annulus responds differently to the solar cycle, indicating that the changing shape of the CLV gives rise to the photometric signal changes of Figure 2.1 and Figure 2.2.

We note the presence of annual variations in Figure 2.4, and attribute these to changes in the apparent size of the Sun over the Earth's orbital period. This causes a change in the resolution

of the full disk images, with the highest resolution occurring at perihelion, and in turn yields the annual variations in the CLV difference plots. Varying image resolution causes changes in quiet sun pixel identification and varying amounts of magnetic element contamination of these. We have verified this cause by degrading a high quality image by an amount comparable to that caused by the Earth's orbital motion and examining the effect on the CLV profile differences and the photometric sums. We find changes that are consistent with those observed in the time series, though seasonal seeing effects may also contribute.

Using the magnitudes of the long-term trends from Figure 2.2, we can estimate what cycle-dependent variability in the CLV would account for the observed trends in the structure specific photometric sums. This is a minimum uncertainty threshold for confidence that those trends are real and independent of the CLV algorithm employed. From Equation 2.2, the change in the integrated CLV necessary to account for the trends of the magnetic structures is

$$\delta_{\text{structure}} = \frac{1}{n_{\text{structure}}} \frac{\Sigma_{\text{max}}}{\Sigma_{\text{max}} + 1} \ , \tag{2.4}$$

where $n_{\text{structure}}$ is the fraction of disk pixels covered by the structure and Σ_{max} is the estimated maximum magnitude of the photometric trend for that structure in Figure 2.2 ignoring the mean offsets. For simplicity, this assumes that error in the CLV is distributed uniformly over disk position. Estimated values of Σ_{max}, $n_{\text{structure}}$, and the corresponding $\delta_{\text{structure}}$ from Equation 2.4 are shown in Table 2.1. The sensitivity of the measured long-term trends in the structure specific photometric sums to errors in the CLV profile depends on the structure contrast, with high-abundance low-contrast structure trends being most uncertain.

2.4 Effect of Further Removing Magnetic Activity in the quiet sun Reference

A cycle-dependent change on the order of a few hundred ppm in the integrated CLV is sufficient to account for the long-term variation of the total disk, internetwork, and network photometric sums, illustrating the sensitivity of the low contrast, high abundance full disk, internetwork, and network trends to uncertainty in the CLV profile. Much larger errors in the CLV are required to

Structure	$n_{\text{structure}}$	Σ_{max}	$\delta_{\text{structure}}$
Total Disk	1.0	500 ppm	500 ppm
Internetwork	0.75	250 ppm	330 ppm
Network	0.20	100 ppm	500 ppm
Active network	0.04	200 ppm	5000 ppm
Faculae	0.01	300 ppm	30000 ppm
Sunspots	0.001	500 ppm	500000 ppm

Table 2.1: Magnetic structure fraction of solar disk pixels, $n_{\text{structure}}$, estimated magnitude of photometric trends, Σ_{max}, and estimations of required error in CLV to remove trends, $\delta_{\text{structure}}$. The highest abundance structures are most sensitive to CLV error.

account for long-term trends of the high contrast active network, faculae, and sunspot components. As we have seen, the differences between the CLV profiles based on median or SRPM quiet sun intensities suggests that one or both of the quiet sun proxies used in construction of the CLV profile is likely contaminated by cycle-dependent magnetic activity. This motivates further masking of the magnetic activity, below that of the SRPM quiet sun definition, as a means of reducing cycle-dependent variability in the reference CLV.

Using co-aligned red and Ca II K images, we compute the CLV for the red continuum images using the internetwork pixels with the least magnetic flux; we employ co-temporal and co-aligned Ca II K images as a proxy for magnetic flux density (Ortiz 2005). We compute ten different CLV profiles as in Section 2.2, but constructed using the median continuum intensity of the internetwork pixels after applying Ca II K thresholds of increasing severity, including from 90% to the 1% of the darkest Ca II K internetwork pixels.

The resulting 81 day running average photometric sums (minus their temporal mean values) Σ_{trend} are plotted in Figure 2.5. The internetwork and network trends are out of phase with solar cycle independent of the threshold level applied. As the magnetic flux of the quiet sun reference is decreased by increasing the severity of the Ca II K mask, the trends become more pronounced. Active network and faculae remain in phase with the solar cycle, and these trends increase with decreasing magnetic flux in the quiet sun reference. The sunspot trends display little sensitivity to the thresholds employed in the CLV definition, consistent with Equation 2.4 and Table 2.1

indicating that very large changes in the CLV are necessary to change the trends of sunspots.

It is important to note that, while the amplitude of the long-term trends of the individual magnetic structures are enhanced with increasingly severe magnetic masking in construction of the CLV, the cycle related trend in the total photometric sum decreases with increasing severity of the mask. This is again due to the greater sensitivity of the low contrast structures; the change of the internetwork and network trends is larger in magnitude than the oppositely signed change in the active network and faculae contributions.

As in Section 2.3, we examine the changes in the continuum CLV shape that leads to the enhanced trends with decreasing internetwork Ca II K intensity defining the reference pixels. This is shown in Figure 2.6 as the disk-normalized difference between the 50% internetwork threshold CLV and the 100% internetwork pixel CLV. Unlike in Figure 2.4, which compares the difference between the median value and 100% internetwork CLV results, the difference between the 50% threshold CLV and the 100% internetwork constructed CLV shows little solar cycle dependence. Instead it shows large offsets, increasing with decreasing μ (toward limb) but nearly constant in time (aside from annual variability discussed below). This behavior is observed for all threshold levels, with the magnitude of the offsets increasing with decreasing magnetic flux levels. The center-to-limb profile becomes increasingly more limb darkened as the masking becomes more severe; the darkest internetwork pixels are more limb darkened than the median internetwork.

The increasingly limb darkened CLVs when applied to the image data yield the structure trends of Figure 2.5. Faculae are increasingly limb brightened, while the network and internetwork, inherently of more uniform intensity across the disk, have enhanced contrast at the limb but slightly lower contrast near at the center relative to the CLV profile. This yields the enhanced out of phase trends in the photometric sum. The magnitudes of photometric sum trends, excluding that of sunspots, are highly dependent on the center-to-limb profile of the somewhat arbitrary quiet sun reference. The true center-to-limb profiles of magnetic structures, their contributions to solar cycle irradiance trends, and the role of the quiet sun itself can only be determined via absolute imaging radiometry.

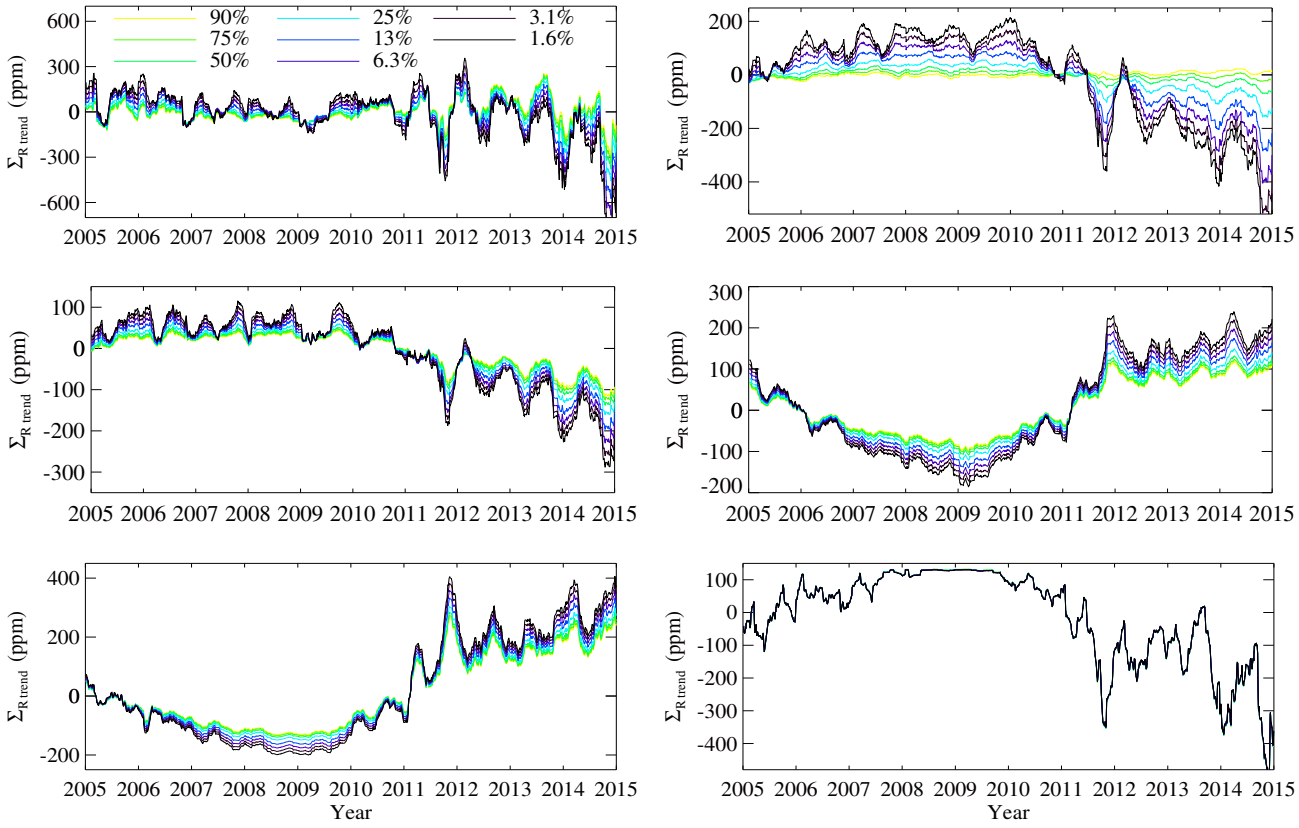

Figure 2.5: Photometric sums minus their temporal averages, Σ_{Rtrend}, averaged over 81 days using various levels of magnetic thresholding from Calcium images in the CLV to remove magnetically enhanced pixels from the quiet sun reference. Trends are shown for the total photometric sum (top left), internetwork (top right), network (middle left), active network (middle right), faculae (bottom left), and sunspots (bottom right). Note the enhancement of all structure trends as more magnetic flux is masked, while the total photometric trend diminishes.

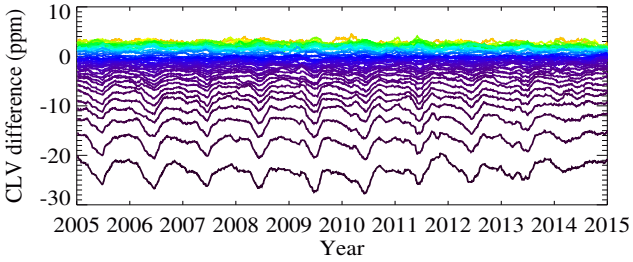

Figure 2.6: Disk normalized difference between the 50% internetwork magnetic threshold and the internetwork CLV in each annulus from center (yellow) to limb (black) averaged over 81 days to highlight the longer-term trends. Note how the annuli differences have little dependency on solar cycle and the 50% threshold CLV is strongly limb-darkened compared to the internetwork CLV.

We again note the annual variations in Figure 2.6. These have the same cause as that described in Section 2.3. Image blurring acts to reduce limb darkening by contaminating the CLV with magnetically bright structures on the limb. This blurring is most prominent during apoapsis and results in brightening of the CLV from neighboring pixels, and more so for the more severely thresholded CLVs which are more sensitive to contamination from blurring. The enhancement of the annual variations in the time series of low contrast structures in Figure 2.5 demonstrates that the CLV sensitivity to image blurring effects the low contrast structures most, which are most sensitive to variations in the CLV.

2.5 Conclusion

We examined the influence of the choice of CLV profile on contrast trends deduced from red and blue continuum PSPT images, and found that the observed cycle-long trends are sensitive to underlying assumptions in the construction of the center-to-limb profile against which the contrast is measured. Using the method of Preminger et al. (2011), taking the median value of all pixels on the disk as a proxy for the quiet sun intensity in the construction of the CLV, we obtain results that agree with those published; the resulting integrated continuum contrast is out of phase with solar activity. However, using a CLV which fits the SRPM identified quiet sun pixels yields the opposite result, an in phase variation of the continuum contrast with the solar cycle. Moreover, the amplitude of the signal decreases with increasingly severe masking in the quiet sun definition.

Thus, the integrated contrast (photometric sum) is highly sensitive to the CLV profile employed, and variations in the integrated contrast with solar cycle depend on the CLV definition and its consequent variation in time. Measurements of temporal variation in the photometric sum can not contribute to the resolution of the discrepancy between VIRGO and SIM assessments of the phase of solar spectral irradiance variations as there is no unique or robust way to define the CLV profile against which the photometric sum measurements are made.

The photometric contributions of specific magnetic structures also vary with the CLV profile employed. Internetwork and network contributions are most sensitive to variations in the CLV due to their low contrast and high abundance, and this sensitivity underlies the opposing photometric trends obtained with the two processing schemes. The photometric contribution of active network, faculae, and sunspots are less sensitive to the underlying CLV profile used. The contrast trends of the dimmest magnetic features are thus the least well determined, yet, as they are the most abundant, they are key to understanding long-term irradiance variability.

Differences between two CLV choices result in linear differences in the photometric trends over the solar cycle. Cycle-dependent changes in the quiet sun reference from which the CLVs are constructed introduced cycle-dependent differences in the CLVs of the same magnitude as the photometric trends, which resulted in the observed trend contradictions. Additionally, we found that the CLVs changed shape relative to each other over the solar cycle suggesting that the quiet sun references upon which the CLV profiles are based are likely contaminated by magnetic structures in the reference pixels. Employing a quiet sun reference that reduces the contribution of magnetic flux by increasingly severe masking based on Ca II K intensity reduces solar cycle dependent magnetic contamination of the center-to-limb profile and changes its shape in a way that yields a) an enhancement of individual structure trends and b) a cancelation between them that diminishes the disk-integrated contrast (photometric sum) trend.

Analyzing the veracity of a selected quiet sun reference and its corresponding CLV is non-trivial. The CLV can change with the solar cycle because of contributions from resolved or unresolved magnetic structures; it includes the center-to-limb variation of structures included intention-

ally or unintentionally in the quiet sun reference definition. As manifested by the annual variations apparent in Figure 2.4 and Figure 2.6, small changes in image resolution can result in significant changes in the CLV profile. These changes are caused by consequent quiet sun reference identification errors and continuum intensity values that include at lower resolution greater contribution from unresolved magnetic flux elements. While we demonstrated that the contrast trends found using severe thresholding in the CLV construction are less contaminated by cycle-dependent magnetic flux variations, we caution that the observed trends can still not distinguish underlying physical causes, most importantly the possible role of any true quiet sun in spectral irradiance variations, particularly long-term variations.

The contrast trends of the internetwork, network, active network, and the full disk sums are most susceptible to changes in the definition of the CLV. Determining whether cycle related changes are due to changes in the radiative output or filling factor of these components cannot be determined using relative photometric measurements alone, since all such measures are dependent on a arbitrary definition of a quiet sun reference component. We stress the need for space-based absolute spectral irradiance imaging to determine the radiative contributions of low contrast components such as internetwork and network to solar spectral irradiance variability. Observations of this kind will enable studies of the radiative properties of magnetic structures and their surroundings as a function of disk position and thus viewing angle without contamination from an uncertain CLV.

This material is based upon work supported by the National Science Foundation Graduate Research Fellowship Program under Grant No. DGE 1144083 and by NASA award number NNX12AB35G.

Chapter 3

Theory of Radiative Transfer

Radiative transfer describes the transport of energy via radiation, and is important both for comparing simulations with observations of the emergent intensity and for simulating the dynamics of a radiating fluid. It couples particles in a fluid to the photons produced both locally and nonlocally. In the Sun, radiative transfer plays a crucial role in the complex transition between the convection zone and the photosphere, where the majority of radiation escapes the solar atmosphere. Beyond the photosphere, it provides the physical understanding of the formation of spectral lines in the high temperature and low density regions of the chromosphere and corona. The scientific results presented later in this thesis heavily utilize the theory of radiative transfer and numerical solutions to the radiative transfer equation. The primary goal of this thesis is to investigate the effect of magnetic morphology on the radiative output of the quiet sun and determine its measurability in the absence of radiometers. To explore this topic requires a thorough background on the theory of radiative transfer and the numerical techniques to solve the transfer equation, which are detailed in this chapter.

The treatment of radiative transfer in this thesis is limited to the case of local thermodynamic equilibrium (LTE) with an emphasis on wavelengths which form in the continuum. In this chapter, we approach the theory of radiative transfer from a general standpoint. Here we present the terms and definitions used in radiative transfer. We then derive the radiative transfer equation, and demonstrate an approximation to the solution to the radiative transfer equation. Following this, we examine the conditions required for thermodynamic equilibrium, and present the crucial

arguments for assuming LTE in the solar photosphere. For a general overview of radiative transfer, the reader is referred to Gray (2005). The derivations presented here follow from the works of Cox & Giuli (1968), Mihalas (1978), and Mihalas & Mihalas (1984).

3.1 Radiative Transfer Terms and Definitions

We begin the derivation of the radiative transfer equation by considering a radiating surface shown in Figure 3.1. Consider the energy, dE_ν, transported from surface dS in the direction $\hat{n}$

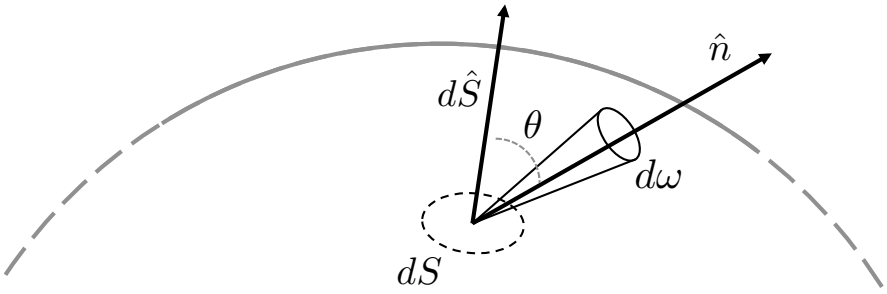

Figure 3.1: Energy transported by radiation of frequency ν across surface dS in time dt into solid angle $d\omega$ in the direction $\hat{n}$.

through solid angle $d\omega$ in time dt and frequency range $d\nu$. The energy is given as

$$\begin{aligned} dE_\nu &= I_\nu(\vec{x}, t; \vec{n}) d\vec{S} \cdot d\hat{n} d\omega d\nu dt \\ &= I_\nu(\vec{x}, t; \vec{n}) \cos\theta dS d\omega d\nu dt \ , \end{aligned} \tag{3.1}$$

where $I_\nu(\vec{x}, t; \vec{n})$ is the specific intensity. This equation represents the macroscopic version of the radiation field. The microscopic version can found by assuming a photon number density $\psi_\nu(\vec{x}, t; \vec{n})$ with velocity c. Since each photon has energy $h\nu$, the energy transported by the photons is given as

$$dE_\nu = ch\nu\psi_\nu(\vec{x}, t; \vec{n}) \tag{3.2}$$

This yields for the specific intensity,

$$I_\nu(\vec{x}, t; \vec{n}) = ch\nu\psi_\nu(\vec{x}, t; \vec{n}, \nu) \ , \tag{3.3}$$

which has SI units of W m^{-2} sr^{-1} nm^{-1}. The specific intensity is the quantity measured in spectrally resolved observations, and is therefore the quantity of interest in studying the transport of radiation. The value of I_ν is obtained from the radiative transfer equation in Section 3.2.

We derive several important quantities in radiative transfer starting from Equations 3.1 – 3.3. The first two moments of the radiation field over solid angles are of particular importance, J_ν and F_ν. The mean intensity, J_ν, is the angle-averaged specific intensity over a unit sphere surrounding the point of interest and is given by,

$$J_\nu(\vec{x}, t) = \frac{1}{4\pi} \oiint_\Omega I_\nu(\vec{x}, t; \vec{n}) \ d\Omega \ . \tag{3.4}$$

If the radiation field is isotropic — I_ν has no directional dependence — then $I_\nu = J_\nu$. The flux, F_ν, measures the net energy flow across a surface and is given by

$$F_\nu(\vec{x}, t; \vec{n}) = \oiint_\Omega I_\nu(\vec{x}, t; \vec{n}) \cos\theta \ d\Omega \ , \tag{3.5}$$

where θ is the angle measured with respect to the normal of the surface. The integration over solid angle gives F_ν and J_ν the same units of W m^{-2} nm^{-1}.

The monochromatic radiation energy density is the integral over all directions of the number density of photons, ψ, multiplied by their energy $h\nu$:

$$\begin{aligned} u_\nu(\vec{x}, t) &= h\nu \oiint_\Omega \psi_\nu(\vec{x}, t; \vec{n}) \ d\Omega \\ &= \frac{1}{c} \oiint_\Omega I_\nu(\vec{x}, t; \vec{n}) \ d\Omega \ , \end{aligned} \tag{3.6}$$

which implies

$$u_\nu(\vec{x}, t) = \frac{4\pi}{c} J_\nu(\vec{x}, t). \tag{3.7}$$

The energy density has units of J m^{-3} nm^{-1}. In the following, we drop the explicit notation indicating dependence of these quantities on $\vec{x}, t$, and $\vec{n}$.

3.1.1 Emission and Absorption

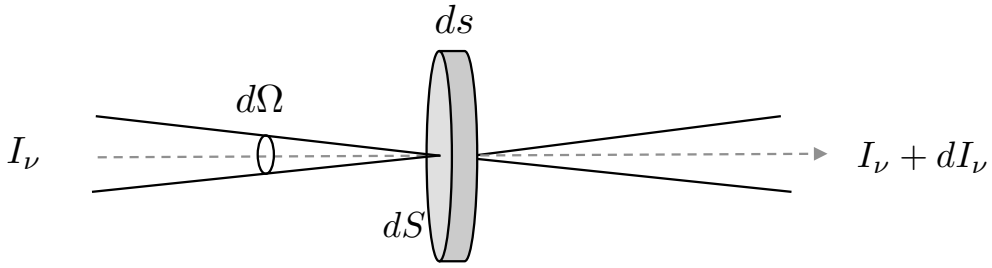

Figure 3.2: Radiation propagating through a thin slab of material of thickness ds through solid angle $d\Omega$. The effect of absorption and emission of the material changes the emergent intensity of the beam by an amount dI_ν.

Consider the specific intensity incident from a beam on a thin layer of material of thickness ds shown in Figure 3.2, where the beam is a collection of rays subtending a solid angle $d\Omega$ around direction $\hat{n}$. Upon passage through the material, the specific intensity will decrease by dI_ν, given by

$$dI_\nu = -\chi_\nu \; I_\nu \; ds \; , \tag{3.8}$$

where χ_ν is the frequency dependent absorption coefficient, or opacity. Note that χ_ν has units of m^{-1}.

The opacity, χ_ν includes two processes that remove radiation from the beam: true, or thermal, absorption and scattering. True absorption occurs when a photon interacts with the material in a way that it exchanges energy with the material, i.e., the energy loss from the radiation is converted to thermal energy of the material. This includes, for example, absorption of a photon by an atom or molecule which excites it into a higher energy state followed by collisional de-excitation, or photo-ionization resulting in the release of a free electron from an atom or molecule that subsequently interacts with the surrounding material. Scattering processes, on the other hand, exchange little or no energy with the material. In these processes, the photons interact with the material and scatter into another direction — removing the photons from the directionally dependent specific intensity.

Similarly, an increase in the specific intensity can occur in Figure 3.2 due to emission from

the material. The increase is given by

$$dI_\nu = \eta_\nu \; ds \; , \tag{3.9}$$

where η_ν is the frequency dependent emission coefficient, or emissivity, and has units of W m^{-3} sr^{-1} nm^{-1}. Again, η_ν includes emissivity contributions from both true emission and scattering. Processes of true emission include the inverse processes of those discussed for absorption (spontaneous de-excitation and radiative recombinations), while the scattering processes are the same between absorption and emission. We can separate χ_ν and η_ν into the absorption and scattering processes as

$$\begin{aligned} \chi_\nu &= \kappa_\nu + \sigma_\nu \\ \eta_\nu &= \eta_\nu^t + \eta_\nu^s \; , \end{aligned} \tag{3.10}$$

where κ_ν and η_ν^t are the true opacity and emissivity, respectively, and σ_ν and η_ν^s are the corresponding scattering terms. We will consider these terms in more detail in the following section.

3.2 The Radiative Transfer Equation

From the previous section, the net effect of absorption and emission processes on the emergent intensity through the thin slab ds is given by

$$dI_\nu = I_\nu(s + ds) - I_\nu(s) = \eta_\nu \; ds - \chi_\nu \; I_\nu \; ds \; . \tag{3.11}$$

It follows that

$$\frac{dI_\nu}{ds} = \eta_\nu - \chi_\nu \; I_\nu \; . \tag{3.12}$$

It is convenient to define the frequency-dependent optical depth τ_ν, where

$$\begin{aligned} \tau_\nu(s) &= -\int_{s_0}^{s} \chi_\nu ds \\ d\tau_\nu &= -\chi_\nu ds \; . \end{aligned} \tag{3.13}$$

The optical depth is a unit-less quantity that specifies the integrated absorption along a path ds as viewed by an observer at $\tau_\nu(s = s_0)$. This quantity is therefore defined in the opposite direction of the beam, rather than optical thickness which is measured along the beam path. The optical depth convention is typically taken in astrophysics since radiation is typically observed where $\tau_\nu = 0$. Expressing the radiative transfer equation in terms of τ_ν yields

$$\frac{dI_\nu}{d\tau_\nu} = I_\nu - S_\nu \ , \tag{3.14}$$

where S_ν is the source function and is the ratio of emissivity to the opacity given by Equation 3.10 as

$$S_\nu = \frac{\eta_\nu}{\chi_\nu} = \frac{\eta_\nu^t + \eta_\nu^s}{\kappa_\nu + \sigma_\nu} \ . \tag{3.15}$$

Through the application of an integrating factor, the implicit solution to the radiative transfer equation is given by,

$$I_\nu(\tau_\nu) = \int_{\tau_\nu}^{\tau_{\nu,0}} S_\nu(t_\nu) e^{-(t_\nu - \tau_\nu)} dt_\nu + I_\nu(\tau_{\nu,0}) e^{-(\tau_{\nu 0} - \tau_\nu)} \ . \tag{3.16}$$

Equation 3.16 states that the intensity at a given optical depth is the intensity at the initial location $\tau_{\nu,0}$ attenuated by the integrated absorption and scattering along the path, plus the contribution of sources of radiation (both scattered and thermal) attenuated by the integrated absorption along the path from their origination to τ_ν. The solution to the radiative transfer equation requires knowledge of both the opacities and emissivities in Equation 3.10 through the source function and the optical depth.

It is important to note that the source of radiation from the fluid will necessarily depend on the state of particles in the fluid, namely the level populations and ionization states of the material, and the radiation field directly via scattering processes. These are themselves dependent on the radiation field, which excites radiative transitions and ionization. It is clear then that, in general, the solution to the radiative transfer equation is not explicit — the source function depends on the excitation and ionization populations which themselves depend on the radiation field. An important

simplification arises if the fluid is in thermal equilibrium since then the populations depend on the local temperature rather than the radiation field.

3.2.1 The Eddington-Barbier Approximation

We take a moment to note an important approximation of the solution to the radiative transfer equation in Equation 3.16 known as the Eddington-Barbier Relation. Consider the semi-infinite plane-parallel atmosphere geometry shown in Figure 3.3. Let us define τ_ν^z as the optical depth

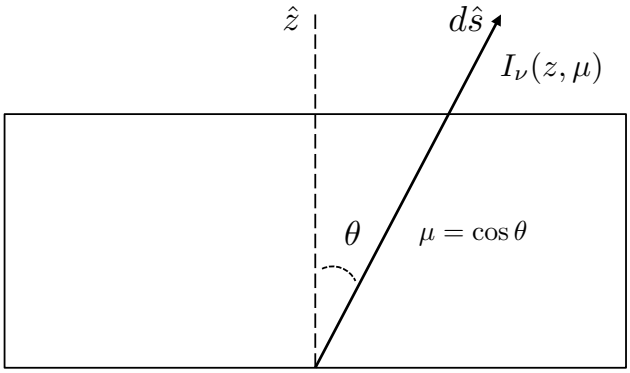

Figure 3.3: Plane parallel atmosphere geometry.

along the vertical direction z. Rewriting Equations 3.13 and 3.14 and assuming χ_ν is directionally independent gives

$$d\tau_\nu^z = -\chi_\nu dz = \mu d\tau_\nu \tag{3.13a}$$

and

$$\mu \frac{dI_\nu}{d\tau_\nu^z} = I_\nu - S_\nu \ , \tag{3.14a}$$

where $\mu = \cos\theta$ is the heliocentric angle. Solving Equation 3.14a as before and integrating over all optical depths from the observer at $\tau_\nu^z = 0$ yields

$$I_\nu(\tau_\nu^z = 0) = \frac{1}{\mu}\int_0^\infty S_\nu(t_\nu^z) e^{-t_\nu^z/\mu} dt_\nu^z \ , \tag{3.15a}$$

where we have assumed that the boundary condition, $I_\nu(\tau_\nu = \infty)e^{-\infty}$ goes to zero. Equation 3.15a then represents the emergent intensity emerging from all depths as seen by an observer outside the atmosphere.

Representing S_ν as a power series in τ_ν^z gives

$$S_\nu(\tau_\nu^z) = \sum_{n=0}^{N} a_n(\tau_\nu^z)^n \ . \tag{3.17}$$

Substituting this in Equation 3.15a yields,

$$\begin{aligned} I_\nu(\tau_\nu^z = 0) &= \frac{1}{\mu}\int_0^\infty a_0 \ e^{-t_\nu^z/\mu} dt_\nu^z + \frac{1}{\mu}\int_0^\infty a_1 t_\nu^z \ e^{-t_\nu^z/\mu} dt_\nu^z + ... \\ &= a_0 + \mu a_1 + ... \\ &\approx S_\nu(\tau_\nu^z = \mu) \ , \end{aligned} \tag{3.18}$$

where we have used $\int_0^\infty e^{-t} t^n dt = n!$.

The Eddington-Barbier relation describes two notable features in the study of stellar atmospheres. First, $S_\nu(\tau_\nu^z = \mu) \approx I_\nu(0)$ implies that the emergent intensity as viewed away from the vertical originates from a higher geometric location in the atmosphere. For a stellar atmosphere in which the temperature decreases with height, the observed intensity away from the center of the stellar disk decreases. This results in the center-to-limb darkening discussed in the previous chapter. Second, for $\mu = 1$, $S_\nu(\tau_\nu^z = 1) \approx I_\nu(0)$ indicates that the majority of the radiation seen by an observer originates at optical depth unity for the given frequency. Since the opacity, and therefore optical depth, is frequency dependent, the observed radiation field is a composite of radiation emerging from different heights so the emergent intensity reflects conditions at differing heights in the solar atmosphere.

3.3 Thermodynamic and Local Thermodynamic Equilibrium

Thermodynamic equilibrium is an important concept in many systems, including stellar interiors. Consider a cavity that contains any species of atoms or molecules and radiation. Initially, the contents of the cavity have some non-zero temperature which may not be uniform throughout

the cavity. After some time, the interactions of the matter and radiation results in a redistribution such that the entire contents reach some equilibrium temperature, T. The material reaches thermal equilibrium where the particle velocity distributions are Maxwellian and the excitations and ionization level populations follow Saha-Boltzmann statistics. The photons in the cavity also reach equilibrium with the material, and are then considered to be in thermodynamic equilibrium. From the density of states of bosons in thermal equilibrium, the energy density is given as

$$u_\nu(T) = \frac{8\pi h\nu^3}{c^3}\frac{1}{e^{hc/\lambda kT} - 1} \ . \tag{3.19}$$

Since radiation in thermodynamic equilibrium is isotropic ($I_\nu = J_\nu$), Equation 3.7 and 3.19 give the frequency dependent intensity of the radiation in the cavity as

$$I_\nu = B_\nu(T) = \frac{2h\nu^3}{c^2}\frac{1}{e^{h\nu/kT} - 1} \ . \tag{3.20}$$

which is recognized as the Planck function. This implies that regardless of the material contained, the radiation field within a cavity in thermodynamic equilibrium is given by the Planck function. Therefore in thermodynamic equilibrium, the photon distribution, the particle velocity distributions, atomic level populations, and ionization fractions are all determined by the single local value of the temperature, T.

A necessary and sufficient condition of a system in thermodynamic equilibrium is that of 'detailed balance'. Inside the cavity, the radiation field interacts with the matter even in this equilibrium. However, any emission of radiation by the matter must be exactly balance by absorption of radiation, otherwise the system would begin to set up temperature changes that deviate from the equilibrium, and this would violate the second law of thermodynamics. The principle of detailed balance states that for a closed system in thermodynamic equilibrium, every interaction process is balanced by the reciprocal process. Because of this, the relation between emission and absorption must be given by

$$\eta_\nu^{t*} = \kappa_\nu^* \ B_\nu(T) \ , \tag{3.21}$$

which is the Kirchoff-Planck relation where the asterisks denote thermodynamic equilibrium. In other words, the source function in thermodynamic equilibrium is given by the Planck function.

Therefore, if radiation leaks out of a small hole of the blackbody cavity such that the cavity maintains thermodynamic equilibrium, the emergent intensity as viewed by an observer would be described by the radiative transfer equation (Equation 3.16) with the source of photons closely approximated by the Planck function such that $S_\nu \approx B_\nu(T)$

Thermodynamic equilibrium provides a powerful simplification where the particle and photon distributions can be described by a single temperature. Stellar atmospheres, however, have varying temperature throughout the interior and therefore cannot be described by a single temperature. The material and radiation can locally achieve thermodynamic equilibrium so long as their equilibrium distributions are not disrupted by non-local processes. This is known as Local Thermodynamic Equilibrium (LTE) and is satisfied when the collisional timescales that maintain thermal equilibrium in the matter are much shorter than the timescales for which external processes (e.g., radiative heating) drive the local distributions out of equilibrium. Such a situation arises in regions of stellar atmospheres where the thermal gradients are small compared to the photon mean free path. Therefore, the radiation field originating from the solar atmosphere in LTE is described by the Planck function. Under this approximation, the source function at a given location in the atmosphere is represented by the Planck function for the fluid at that temperature. We will show in the following section that LTE is a valid assumption for the formation of continuum wavelengths in the solar photosphere.

3.4 Radiative Transfer in the Solar Atmosphere

With the derivation of the radiative transfer equation and the conditions for the assumption of LTE, we now focus on the solar opacity, χ_ν, and the regions in the solar atmosphere where LTE is valid. These two components are essential to solve the radiative transfer equation in a modeled solar atmosphere to ultimately compare with observations. In this section, we describe the physical origins of the solar opacities with an emphasis on the dominant source of the continuum wavelengths studied in this thesis. We then describe the conditions in the solar atmosphere under which the assumption of LTE is valid and demonstrate the validity using the 1D quiet sun solar

model atmosphere (FALC) (Fontenla et al. 1991) and the RH radiative transfer solver (Uitenbroek 2001).

Figure 3.4 shows the temperature and Hydrogen density in the FALC model solar atmosphere as a function of height where z = 0 km is defined by the optical depth unity at 500 nm, the τ_{500} = 1 surface. Negative values of height represent those into the photosphere towards the upper convection zone, while positive heights represent those above the photospheres towards the towards the chromosphere and eventually the corona. As shown, the photosphere is the region around τ_{500} = 1 and up to the temperature minimum around 500 km. Note that both the temperature and density decrease throughout the photosphere. Continuum wavelengths and weak spectral lines form in the photosphere. The chromosphere is the region above approximately 500 km where the temperature

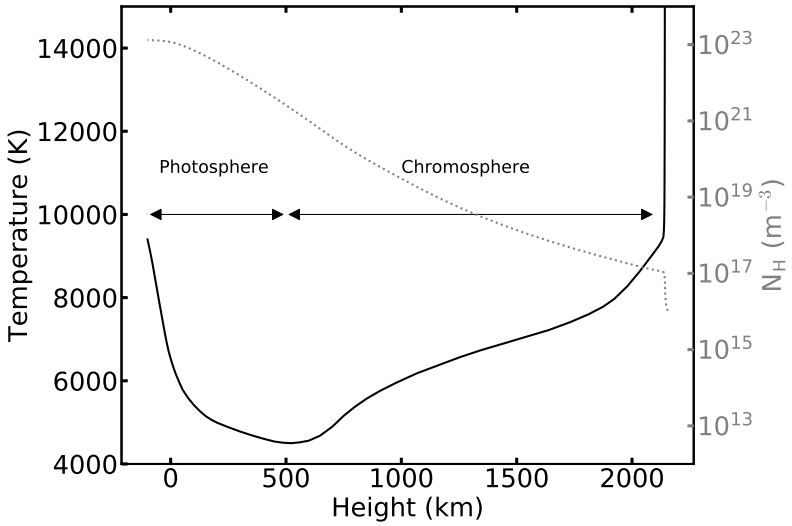

Figure 3.4: Temperature (black) and total Hydrogen density (gray dotted) stratifications in the solar atmosphere using the FALC quiet sun atmosphere of Fontenla et al. (1991). Negative heights are into the photosphere and positive are out towards the chromosphere and corona. Height at z = 0 km is defined at τ_{500} = 1 as computed by RH.

increases while density continues to decrease. Beyond the chromosphere, above approximately 2000 km, the temperature rises drastically defining the transition region to the corona. Strong spectral lines form in the chromosphere, transition region, and corona.

3.4.1 The Solar Opacity, χ_ν

Solving the radiative transfer equation (Equation 3.16) requires knowledge of the source function, S_ν, and the optical depth, τ_ν which both in general depend on the opacity, χ_ν. In the case of LTE, when the source function can be approximated by the Planck function, only the optical depth determination requires the opacity. The dominant opacity producing processes in the solar atmosphere include bound-free (bf) transitions in which an atom is ionized absorbing a photon in the process, free-free (ff) transitions in which an electron absorbs a photon when passing close to an ion, and scattering processes which act to change the direction of a photon. In numerical radiative transfer solvers, these opacities are computed either explicitly or using lookup tables of measured quantities based on the state variables from the MHD simulations. Bound-free and free-free transitions for some atoms can be calculated from classical or quantum treatments of the atom electron system as an oscillator driven by an electromagnetic field. Both methods are described in detail in Mihalas (1978). Bound-free transitions represent atomic transitions from a bound state to a free state with the absorption of a photon. Free-free transitions represent unbound transitions between states. The dominant opacities in the solar photosphere are discussed in the following. We ignore bound-bound transitions where an atom absorbs a photon resulting in excitation of an electron to a higher energy level which form spectral lines. The opacities of spectral lines are typically determined through quantum mechanical calculations, laboratory measurements, or semi-empirically using atomic database sets and comparing spectra synthesized from model atmospheres with observed values.

3.4.1.1 Hydrogen

As the most abundant particle in the solar atmosphere, Hydrogen represents the dominant source of opacity (see e.g., Asplund et al. 2009, for a review on the chemical composition of the Sun). Bound-free transitions of neutral Hydrogen are determined by the ionization potentials and the relative number of Hydrogen in a given excitation state. Since a photon with higher energy than

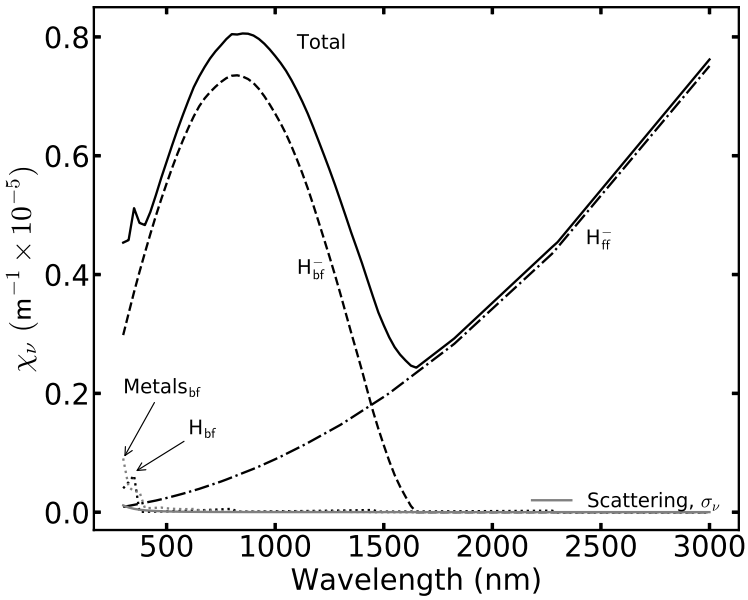

Figure 3.5: Dominant sources of opacities for the solar continuum computed by RH using the FALC quiet sun model atmosphere from Fontenla et al. (1991) at a temperature of 5790 K and Hydrogen density of 9.44e22 m^{-3}. Note that the solar opacity is dominated by H^- opacity sources (bound-free and free-free). Ionization of metals and molecules becomes important in the UV.

the ionization potential will be absorbed upon ionization, the opacity has a sharp drop-off at the ionization frequency and was shown by Gaunt (1930) to fall off as $1/\nu^3$ for higher frequencies. Since most Hydrogen is in the ground and first excited states, the n=1 and n=2 to n = ∞ transitions are strongest. The opacity due to bound-free transitions of Hydrogen in the solar photosphere are shown in Figure 3.5. Free-free transitions of neutral Hydrogen occur when an electron passes near a proton, the electron direction is altered and a photon may be absorbed or emitted in the process. The opacity depends again on the relative number of protons and electrons available for the collision (see e.g., Mihalas 1978).

Due to the polarization of the electron-proton system and the abundance of electrons from ionized metals, Hydrogen is capable of loosely binding an electron to create H^- with an ionization energy of 0.755 eV. Therefore, ionizing H^- requires a photon with wavelength less than 1642 nm. The opacity for this bound-free absorption has been calculated by Geltman (1962) and John (1988). Similarly, an electron passing near a neutral Hydrogen can result in H^- free-free transitions. Cal-

culations of free-free transition opacity are given by Stilley & Callaway (1970), Bell & Berrington (1987), and John (1988). Despite the relatively low abundance of electrons in the solar photosphere compared to Hydrogen (roughly 10^{-4} electrons per neutral Hydrogen), the large cross-section of H^- results in it being the dominant source of opacity in the solar photosphere as shown in Figure 3.5, with bound-free transitions dominating for wavelengths between 400 and 1500 nm and free-free transitions dominating for wavelengths larger than 1500 nm. .

3.4.1.2 Helium and Metals

While Hydrogen represents the largest source of opacity in the upper solar atmosphere, a few other sources are worth noting. Helium is the second most abundant element. Its tightly bound electrons, however, require photons with wavelengths below approximate 50 nm to ionize it from the ground state. Helium opacity near the visible portion of the spectrum from higher excited states only plays a role in stars much hotter than the Sun. Free-free transitions of Helium play a marginally larger role and their contributions have been calculated by John (1994).

Bound-free transitions of metals — any element above Helium — play a large role in the solar photospheric opacity particularly in the UV portion of the spectrum. Determination of the contribution to opacity from metals is nontrivial and the lack of proper abundance and cross-sections have led to the 'missing opacity' problem in stellar atmospheres (e.g., Allende Prieto et al. 2003; Asplund et al. 2009). Cross-sections of metals are determined from experimentally derived values for those available, treating the ionization as Hydrogenic with modifications to account for the differing structures, or from quantum calculations. The contribution of metals to opacity as a function of wavelength in the solar photosphere is shown in Figure 3.5. The contribution of metals exceeds that of H^- for wavelengths below around 250 nm (not shown in Figure 3.5).

3.4.1.3 Scattering

The two most important continuum scattering processes in the visible continuum of the solar photosphere are Thomson and Rayleigh scattering. Thomson scattering describes the elastic

scattering of radiation by free electrons, and is the angle-averaged low energy limit of Compton scattering. The scattering opacity is given by

$$\sigma_T = n_e \frac{8\pi}{3} \left(\frac{e^2}{4\pi\epsilon_0 m c^2} \right)^2 \tag{3.22}$$

where n_e is the electron density. Note that Thomson scattering is frequency independent. Rayleigh scattering, in contrast, describes the elastic scattering of radiation by a polarized system such as an atom or molecule where the radiation frequency is off-resonance from the transition frequencies of the atom or molecule. Like Thomson scattering, Rayleigh scattering can be described analytically and is given by

$$\sigma_R = \sigma_T \, \frac{\omega^4}{(\omega_o^2 - \omega^2)^2} \, , \tag{3.23}$$

where ω_o is the transition frequency of the atom or molecule and ω is the radiation frequency. Unlike Thomson scattering, the amplitude of Rayleigh scattering is a strong function of frequency. The summed contributions of Thomson and Rayleigh scattering in the solar photosphere are shown in Figure 3.5.

3.4.2 LTE Validity in the Solar Atmosphere

The analysis in this thesis assumes LTE in the solar photosphere. We therefore aim to demonstrate the validity of this assumption. There are two possible mechanisms under which the LTE assumption can break down. One is that the local particle velocity distributions and atomic level populations are not described by the local temperature and therefore the radiation field is not described by the Planck function at the local temperature. The other is that the photons from the region being observed do not reflect the local properties of the medium. For the continuum, such a situation arises when the dominant source of radiation from that region predominantly results from radiation scattering into the line of sight rather than locally produced thermal radiation. We demonstrate that neither of these situations is significant in the solar photosphere using the RH radiative transfer solver and the solar atmosphere model shown in Figure 3.4.

3.4.2.1 Particle Equilibrium Populations

A qualitative argument for thermal equilibrium populations is given below followed by a calculation using the atmosphere presented in Figure 3.4. In the solar interior, large particle densities result in very large opacities. Here, the vast majority of radiation produced locally cannot escape due to the large optical depths. If the mean free path of the photons is small compared with the temperature gradient (around 20 K/km for the Sun), then photons trapped at this location would be in LTE with the material. Moving out towards the photosphere, the particle density and opacity decrease. The presence of spectral lines increases the opacity, which effectively reduces the mean free path of the corresponding wavelengths. This results in radiative energy exchange occurring on spatial scales shorter than the mean free path of the continuum wavelengths, and acts to maintain LTE despite the continuum mean free path being roughly equivalent to the scale over which the temperature gradient changes. Eventually the photon mean free path becomes large compared to the thermal gradient. Therefore, some of the photons at this location may no longer reflect the local temperature. Despite the presence of non-local photons, the material will generate a Planck distribution of photons so long as the collisional processes that maintain equilibrium conditions amongst the particles occur on shorter timescales than the radiative processes that drive the material out of this equilibrium.

Higher in the solar atmosphere, near the chromosphere, the particle densities have dropped by several orders of magnitude. This reduction in density leads to fewer thermalizing interactions between the particles. The interaction of the non-local radiation field with the particles alters the equilibrium distribution of the particles at faster timescales than they can equilibrate to maintain their equilibrium populations. The non-local radiation field can therefore drive the particle populations out of their equilibrium distributions described by Saha-Boltzmann statistics, and in extreme cases drive the particle velocity distributions out of their Maxwellian distributions. Instead, these distributions will depend explicitly on the radiation field. In such a case, the material and radiation must be treated in non-local thermodynamic equilibrium (nLTE). These conditions prevail in the

regions above the solar photosphere where the particle densities have greatly reduced and there is a significant radiation field emanating from the lower regions.

The preceding arguments for the relevance of LTE or nLTE provided only a qualitative description of the validity. We now demonstrate which regions of the solar atmosphere have particle populations that are described by thermodynamic equilibrium distributions. This is done by comparing the atomic level populations assuming LTE where the populations are given by the local temperature, and nLTE where the populations are determined based on the radiation field. We compute the populations using the RH radiative transfer solver with the 1D quiet sun model atmosphere from Figure 3.4. We assume both LTE and nLTE and compare the equilibrium particle distributions of Hydrogen, the dominate source of density and opacity near the solar photosphere. For regions where the particle distributions are in thermodynamic equilibrium, the LTE and nLTE populations will be equivalent. The population results in nLTE and LTE for ionized Hydrogen and the first two excitation levels are shown in Figure 3.6, where the vertical grey band represents the approximate region of formation heights of wavelengths between 400 and 3000 nm. The neutral

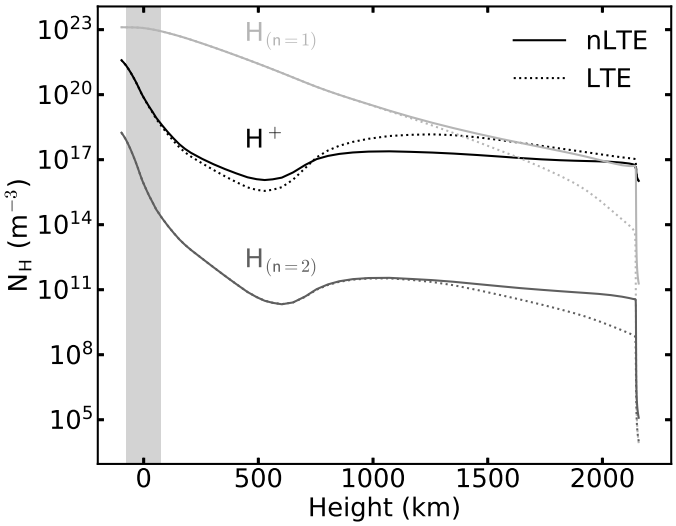

Figure 3.6: Hydrogen populations in nLTE (solid) and LTE (dashed). Grey band represents approximate formation heights of continuum wavelengths between 400 and 3000 nm. Note that the ionization population (H^+) begins to diverge from the LTE value in the low to mid photosphere. The two excitation levels diverge in regions above 1000 km. Populations computed using RH (Uitenbroek 2001) and model C quiet sun 1D atmosphere from Fontenla et al. (1991).

Hydrogen populations maintain their equilibrium values within 1% up to the temperature minimum at 500 km. The ionized Hydrogen populations, however, deviate by approximately 10% at 50 km above the $\tau_{500} = 1$ formation height, with deviations up to 70% around the temperature minimum. Within the formation heights of the continuum wavelengths between 400 and 3000 nm, the populations agree closely, allowing the source function to be closely approximated by the Planck function. Above this, the LTE validity begins to break down for some populations. In these cases, the radiative transfer must be treated in nLTE.

3.4.2.2 Photon Scattering

Finally, we analyze the relative importance of continuum scattering in regions where the material is in LTE. Scattering results when the radiation field from another region interacts with the local material in such a way that little to no energy is exchanged. When scattering processes dominate, the local radiation field will no longer be described by the Planck function at the local temperature even when the local material maintains thermal equilibrium. Consider the source function from Equation 3.24. If the true absorption and emission processes result from regions in LTE, then through the Kirchoff-Planck relation in Equation 3.21, the source function can be given as

$$S_\nu = \frac{\eta_\nu}{\chi_\nu} = \frac{\eta_\nu^t + \eta_\nu^s}{\kappa_\nu + \sigma_\nu} = \frac{\kappa_\nu B_\nu(T)}{\kappa_\nu + \sigma_\nu} + \frac{\eta_\nu^s}{\kappa_\nu + \sigma_\nu} \ . \tag{3.24}$$

Generally, the scattering terms can be related through redistribution functions, which specify the spatial and frequency dependent scattering of photons

$$\eta_\nu^s = \sigma_\nu \int_0^\infty \oiint_{4\pi} R(\nu, \nu', \vec{\Omega}, \vec{\Omega'}) I_{\nu'}(\vec{\Omega'}) d\vec{\Omega'} d\nu' \tag{3.25}$$

where the R is the redistribution function specifying the fraction of photons that will be scattered from direction $\vec{n'}$ into $\vec{n}$ (corresponding to solid angles Ω' and Ω, respectively), including a change in frequency from ν' to ν.

Outside of spectral lines, scattering can generally be treated as coherent, such that $\nu' = \nu$. Furthermore, the angular effects from continuum scattering can be treated as isotropic. This results

in a simplified emissivity given as

$$\eta_\nu^s = \sigma_\nu \; J_\nu \; . \tag{3.26}$$

Substituting this into Equation 3.24 gives

$$S_\nu = \frac{\kappa_\nu B_\nu(T)}{\kappa_\nu + \sigma_\nu} + \frac{\sigma_\nu J_\nu}{\kappa_\nu + \sigma_\nu} \; = \epsilon_\nu B_\nu(T) + (1 - \epsilon_\nu) J_\nu \; , \tag{3.27}$$

where ϵ_ν is $\kappa_\nu/(\kappa_\nu + \sigma_\nu)$ represents the relative contribution of true absorption to extinction.

If the scattering term is small, Equation 3.27 reduces to $S_\nu \approx B_\nu(T)$ and the system is closely approximated by LTE. If the material is in thermal equilibrium then the radiation field is given by the Planck function at the same temperature. If scattering dominates, then the source function is determined entirely by the radiation field, specifically J_ν, rather than the local plasma properties. In this case, the radiation field can no longer be assumed to be in LTE even if the particle distributions are in thermal equilibrium. Figure 3.7 shows the value of $1 - \epsilon_\nu$ for the atmosphere shown in Figure 3.4 as computed using RH. The scattering remains below 1% the regions of the photosphere where the continuum wavelengths between 400 and 3000 nm form, and only becomes

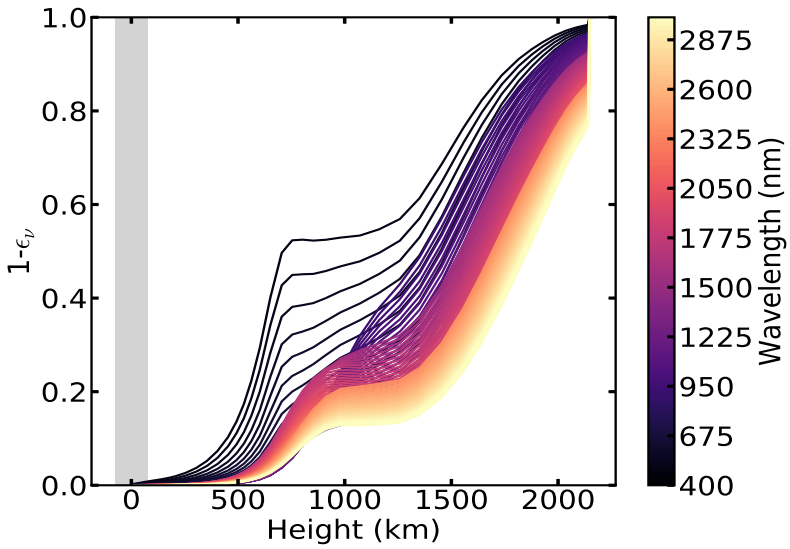

Figure 3.7: Dominance of photon scattering (1- ϵ_ν) as a function of wavelength. Grey band represents approximate formation heights of continuum wavelengths between 400 and 3000 nm. Scattering plays a negligible role in the continuum formation heights of the solar photosphere. Scattering computed using RH (Uitenbroek 2001) and model C quiet sun 1D atmosphere form Fontenla et al. (1991).

non-negligible in the upper photosphere and chromosphere. Therefore for continuum wavelengths formed in the photosphere, the final term in Equation 3.27 can be neglected and $S_\nu = B_\nu(T)$. We therefore conclude that the formation of continuum intensity in the solar photosphere can largely be treated in LTE.

3.5 Conclusions

This chapter reviewed the theory of radiative transfer and the assumptions made in the treatment of stellar atmospheres, in particular the application to the solar atmosphere. We discussed the case of thermodynamic and local thermodynamic equilibrium which permits the approximation of the source function as the Planck function. This simplifies the treatment of radiative transfer considerably since the distribution of photons and particles are therefore described by the local temperature.

We showed that from the Eddington-Barbier approximation, the emergent intensity for a given frequency seen by an observer is roughly value of the source function at optical depth unity at that frequency. Therefore for the solar continuum spectrum which is closely approximated by LTE, the observed spectrum is a combination of Planck functions of differing temperatures reflecting the temperature of the optical depth unity height at each frequency. This explains why the solar spectrum can not be fully described by the Planck function at a single temperature. We then described the physical origins of the solar opacity with an emphasis on formation of continuum wavelengths which are the focus of this thesis. We showed that in the continuum wavelengths at the temperature and density of the solar photosphere, Hydrogen dominates the solar opacity.

We further discussed the two conditions where LTE assumptions break down — lack of thermal equilibrium of the material and photon scattering. We demonstrated that the Hydrogen populations are closely approximated by their thermal equilibrium values in the regions of the photosphere where continuum wavelengths form, while they diverge above the temperature minimum (approximately 500 km above the photosphere). We also showed that scattering in the continuum wavelengths from 400 to 3000 nm remains negligible below the temperature minimum, but

becomes dominant in the chromosphere. This relation should be interpreted cautiously as it has been implicitly assumed that the scattered photons escape without thermal interactions (as this would begin to drive the material out of equilibrium). The arguments made in this chapter focused only on Hydrogen populations for continuum arguments since it is the dominant source of the solar opacity. Other atomic and molecular lines must be treated accordingly to determine whether LTE is a valid assumption. Additionally, lines which form near the temperature minimum and above (strong lines) must be treated in nLTE both due to the equilibrium distributions of the particles and the effects of scattering in the lines themselves as well as in the continuum.

Chapter 4

An Assessment of and Solution to the Intensity Diffusion Error Intrinsic to Short-characteristic Radiative Transfer Methods

Numerically solving the radiative transfer equation is crucial to properly simulate the radiative energy transport in a modeled solar photosphere, as well as synthesizing the emergent intensity for the analyses presented in the remainder of this thesis. Numerical solutions, however, are always an approximation and the degree of approximation can adversely affect the results. The purpose of this work is to quantify the specific intensity diffusion error known to be introduced by a common numerical radiative transfer technique, the method of short-characteristics. This is accomplished by deriving an analytical model for the diffusion, followed by an assessment of the apparent spatial smearing in 3D radiative magnetohydrodynamic (MHD) simulations compared with the model results. We then propose a method to avoid this diffusion error that may be efficiently implemented into existing MHD solvers, and demonstrate its efficacy to avoid the numerical diffusion. The full derivation of the analytical model is placed in Appendix A so as to not distract from the main arguments of the work.

This chapter is based on work previously published in Peck et al. (2017a)[1] and is a restatement of that paper. The project was independently formulated by C. L. Peck who derived the analytical solution presented here and in the Appendix, and carried out the analysis. The coauthors provided guidance on the analyses and advice on how to demonstrate the conclusions.

[1] Peck, C. L., Criscuoli, S., & Rast, M. P. 2017, An Assessment of and Solution to the Intensity Diffusion Error Intrinsic to Short-Characteristic Radiative Transfer Methods, The Astrophysical Journals, 850, 9

4.1 Introduction

Computational radiative transfer is critical to inferring the physical properties of astrophysical objects from observed spectra. Moreover, radiation is often a key energy transport mechanism and radiative transfer modeling plays an important role in hydrodynamic and MHD simulations of a wide range of phenomena from planetary and stellar atmospheres to accretion disks around compact objects. Reliable solution of the radiative transfer equation is required to both determine the radiative heating rate in the solution of the energy equation and synthesize spectra for comparison with observations.

Several techniques have been developed to numerically solve the radiative transfer equation. Most often the solution is sought along rays by evaluating the formal solution

$$I_\nu(\tau_{\nu,f}) = \int_{\tau_{\nu,f}}^{\tau_{\nu,i}} S_\nu(t_\nu)\, e^{-(t_\nu - \tau_{\nu,f})}\, dt_\nu + I_\nu(\tau_{\nu,i})\, e^{-(\tau_{\nu,i} - \tau_{\nu,f})} \tag{4.1}$$

with

$$\tau_\nu = -\int_{s_f}^{s_i} \chi_\nu \, ds \ , \tag{4.2}$$

where I_ν is the specific intensity at frequency ν, τ_ν is the optical depth along ray path ds, χ_ν is the frequency specific opacity, and S_ν is the source function (the ratio of the thermal emissivity to the opacity), which in local thermodynamic equilibrium is taken to be the Planck function (see Mihalas & Mihalas 1984 for details and Carlsson 2008 for a short review of solution methods as applied to a three-dimensional radiative transfer in stellar atmospheres of cool stars). Moments of the radiation field are then evaluated by numerical quadrature (Carlson 1963; Lathrop & Carlson 1965; Carlson 1970) using a limited number of ray directions.

Numerical integration of the formal solution (Equation 4.1) along rays typically employs one of two strategies: the long-characteristic (Mihalas et al. 1978) or the short-characteristic (Kunasz & Auer 1988) method. These are illustrated in Figure 1 for radiation propagating from the bottom of the domain, where $I_\nu(0)$ is specified, to a point within the domain. The long-characteristic method solves the radiative transfer equation along rays connecting downwind grid points in the domain

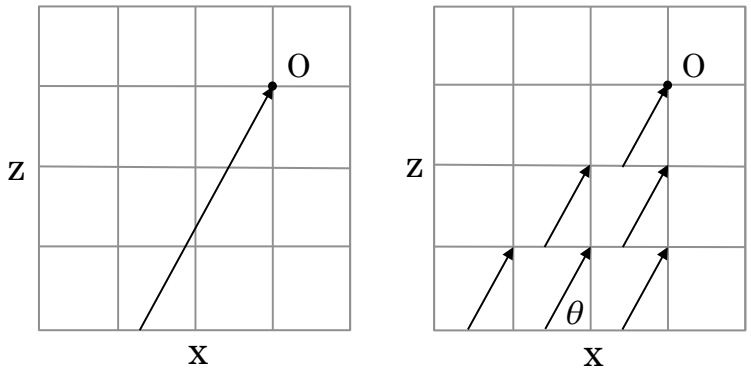

Figure 4.1: Ray propagation in the long-characteristic (left) and short-characteristic (right) methods.

(the points for which the specific intensity is computed directly from the transfer equation, position O in the left panel of Figure 4.1) to the last upwind point where the ray originates. Because the ray does not necessarily intersect the numerical grid except at the upwind point, this method requires interpolation of the plasma properties (κ_ν, ρ, and S_ν) at ray intersections with the grid rows or columns when evaluating the transfer equation, as well as interpolation of the specific intensity along the computed rays to neighboring grid points which do not lie directly on the ray paths. The long-characteristic method faces some challenges when, for large problems, domain decomposition is needed to distribute the computation among many processors (e.g., Carlsson 2008).

The short-characteristic method, on the other hand, updates the specific intensity row-by-row by solving the radiative transfer equation for each grid point along rays starting from interpolated values on the previous row (right panel in Figure 4.1) or column, depending on the ray direction. Sweeping the grid in this way allows for somewhat more straightforward domain decomposition, since the radiative transfer solution along the short rays depends only on the local plasma properties and the value of the specific intensity must be communicated only at the grid locations. The short-characteristic method is routinely employed in radiative MHD solvers (e.g., Vögler et al. 2005; Hayek et al. 2010; Gudiksen et al. 2011; Davis et al. 2012) and stand-alone radiative transfer solvers (e.g., Uitenbroek 2001; Criscuoli & Rast 2009; Leenaarts & Carlsson 2009; Štěpán & Bueno 2013; Ibgui et al. 2013; Pereira & Uitenbroek 2015; Zhu et al. 2015).

The most significant drawback of the short-characteristic method is that for non vertical or non grid-point intersecting ray directions the specific intensity suffers diffusion because it is successively interpolated as it is propagated. In the long-characteristic method only the plasma properties and not the specific intensity itself need to be interpolated to integrate along the ray path. The diffusive error introduced by the short-characteristics method has been known since the foundational work of Kunasz & Auer (1988), who demonstrated the occurrence of angular dispersion of the radiation for non grid-aligned propagation directions. The error of the scheme decreases with increasing order of interpolation scheme, but at the cost of ringing in regions with steep specific intensity gradients. This can lead to negative intensity values, which in turn can be mitigated by monotonic interpolation schemes (e.g., Auer & Paletou 1994; Criscuoli 2007; Hayek et al. 2010; Ibgui et al. 2013), but a consequence of these is the non conservation of the radiative energy (Criscuoli 2007). For this reason, and for its computational efficiency, many widely used radiative transfer solvers rely on the short-characteristic method with linear interpolation despite the diffusive error introduced (e.g., RH Uitenbroek (2001), PORTA Štěpán & Bueno (2013), RH1.5 Pereira & Uitenbroek (2015), MULTI3D Leenaarts & Carlsson (2009)).

The diffusive errors inherent in short-characteristic solvers leads to viewing angle dependent inaccuracies in the calculated emergent intensity, whether the emergent intensity is computed directly within the MHD simulation or post-facto using a stand-alone radiative transfer solver for spectral synthesis. Moreover, it can affect the numerical solution of the radiative MHD equations through the radiative heating rate in the energy equation. Some work has been done to demonstrate and quantify the errors (e.g., Kunasz & Auer 1988; Bruls et al. 1999), but a more detailed understanding is needed. This is particularly true in light of the upcoming large aperture telescopes, such as the NSF's Daniel K. Inouye Solar Telescope (DKIST) (Elmore et al. 2014; Tritschler et al. 2016) and the planned European Solar Telescope (EST) (Collados et al. 2013; Matthews et al. 2016), for which the diffraction limit is nearing the resolution of radiative MHD simulations of the solar surface (e.g., Rempel 2014; Freytag et al. 2002; Galsgaard & Nordlund 1996). In these circumstances comparisons between observations and simulations become sensitive to the diffusive

errors in the calculation of the emergent intensity.

Here we quantify the effective reduction in spatial resolution that results when employing the short-characteristic radiative transfer method to calculate the emergent intensity at inclined viewing angles. We derive a closed form analytical model for the specific intensity of a beam at each point of the grid as a function of beam angle when the beam is initiated as a delta function at the bottom of the computation domain. The emergent intensity at the top of the domain is the effective point spread function (PSF) of the numerical scheme. We validate the model by comparing the intensity obtained by a numerical short-characteristic solution of the radiation emerging from a 3D MHD simulation snapshot with that predicted by the analytic model. Finally, we demonstrate that the diffusive error is readily avoided by interpolating the simulation atmosphere onto a viewing-angle aligned grid prior to computing the radiative transfer solution. Section 2 describes the analytical model. Section 3 assesses the effect of short-characteristic intensity diffusion on the spatial resolution of the emergent intensity, and demonstrates that pre-tilting the simulation atmosphere avoids the diffusive error. Section 4 examines the effect of a higher-order interpolation on both the diffusive error and the total emergent intensity as functions of ray inclination.

4.2 Analytical Model of the Short-characteristic Diffusive Error

To derive an analytic expression for the effective diffusion introduced by the short-characteristic radiative transfer method, we consider a single delta-function point source of radiation at the bottom of a 3D domain and the subsequent propagation of the specific intensity through the domain along inclined ray directions (i.e., the search-beam problem, Kunasz & Auer 1988). To maintain analytic tractability, we examine only linear interpolation on a regular rectangular grid and assume that the beam propagates through vacuum, so that only interpolation of the specific intensity (and not that of the plasma properties) contributes to diffusion effects. The emergent intensity at the top of the domain is then effectively the PSF of the short-characteristic solution. Moreover, since, as we will see in more detail, specific intensity interpolation errors are compounded with height, they dominate the error budget even in non-vacuum calculations.

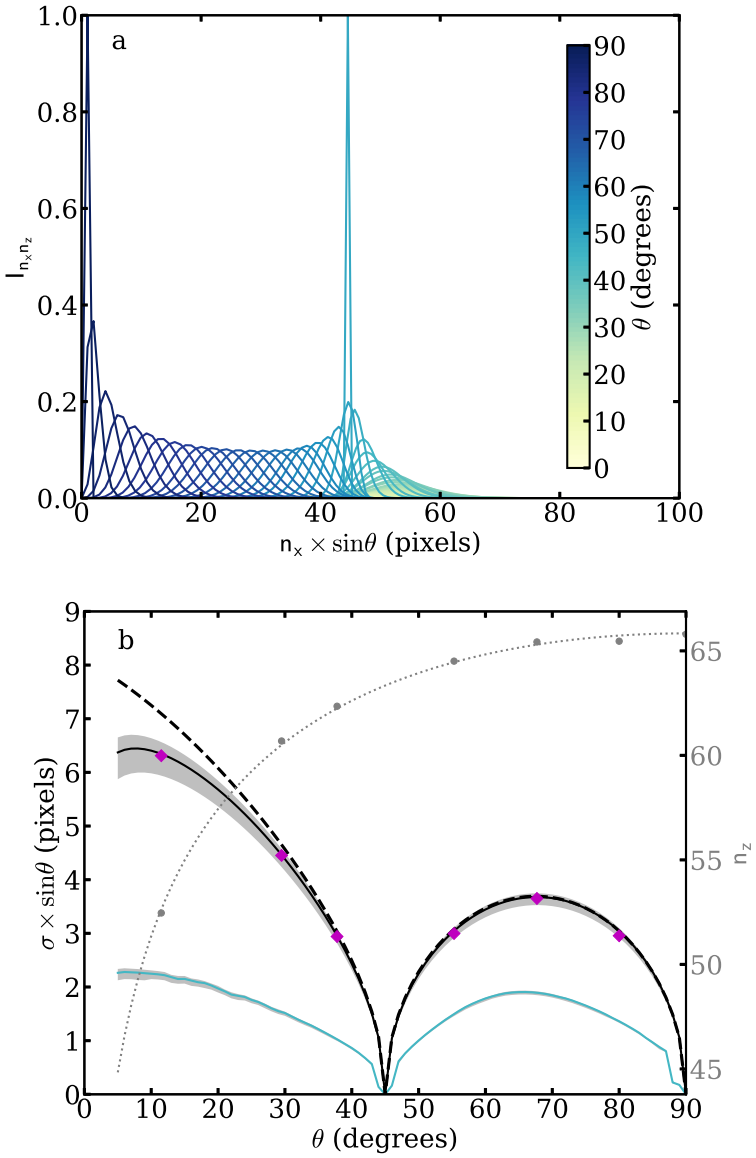

Figure 4.2: In (a), intensity distributions from Equations 4.3 and 4.4 with $n_z = 65$. In (b), the effective image smearing computed as the standard deviation of the model (Equation 4.5) for $n_z = 65$ (dashed black curve) and for n_z computed using the mean $\tau = 1$ formation depths in the MHD snapshot when accounting for viewing angle (solid black curve). Both n_x and σ are scaled by $\sin\theta$ to account for apparent foreshortening caused by viewing the emergent intensity at inclined angles. The mean $\tau_{500} = 1$ formation depths were explicitly computed for viewing angles plotted with filled gray circles and determined by a logarithmic fit otherwise (dotted gray curve). The gray band indicates the σ range for n_z between the mean $\tau = 0.5$ and 1.5 formation depths. Pink diamonds represent the standard deviation of the binomial convolution kernel applied to the pre-tilt amplitude spectrum that best fits the standard short-characteristic spectrum. The solid blue curve and accompanying gray band indicates the standard deviation for the same mean τ formation depths when employing cubic monotonic interpolation in the short-characteristic solution.

Depending on the ray propagation direction, the short characteristic method interpolates the specific intensity either on horizontal (xy) or vertical (xz or yz) planes. The full derivation of the general 3D solution for arbitrary ray direction is given in Appendix A. Here, for simplicity of presentation, we discuss the solution for the special case where $\phi = 0°$. This corresponds to ray propagation in the xz plane (as shown in the right panel of Figure 4.1). Interpolation then occurs on horizontal (in x) or vertical (in z) grid lines only, depending on the ray propagation direction θ. Note that θ, the search-beam inclination angle, is defined with respect to the horizontal so that $\theta = 90°$ for a vertical propagating ray.

When $\phi = 0°$, the 3D solution (Equations A.2 and A.6 in Appendix A) reduces to a PSF in x only, as no diffusion occurs in the y direction for a ray confined to the xz plane. For ray angles $\text{atan}(\frac{dz}{dx}) < \theta < 90°$ (interpolation on horizontal grid lines) the intensity at any grid point can be written as

$$I^{\mathrm{h}}_{\mathrm{n_x n_z}} = I_{\text{source}} \times \frac{n_z!}{n_x!(n_z - n_x)!}\left(1 - \frac{dz}{dx\tan\theta}\right)^{n_z - n_x}\left(\frac{dz}{dx\tan\theta}\right)^{n_x}, \tag{4.3}$$

where I_{source} is the initial point source intensity, and n_x and n_z are the integer number of grid point displacements in the ray direction from the source location. For ray angles $0° < \theta < \text{atan}(\frac{dz}{dx})$ (interpolation on vertical grid lines) the expression becomes

$$I^{\mathrm{v}}_{\mathrm{n_x n_z}} = I_{\text{source}} \times \frac{n_x - 1!}{(n_x - n_z)!(n_z - 1)!}\left(1 - \frac{dx\tan\theta}{dz}\right)^{n_x - n_z}\left(\frac{dx\tan\theta}{dz}\right)^{n_z}. \tag{4.4}$$

The intensity distributions (as a function of n_x) in Equations 3 and 4 represent the one-dimensional PSFs introduced by the short-characteristic method, which depend on the ray inclination angle θ and the number of horizontal grid plane displacements n_z above the initial source height. One advantage of writing the intensity distributions in terms of discrete grid point displacements is that they become recognizable as standard and negative binomial distributions in n_x for fixed n_z with

standard deviations

$$\sigma = \sqrt{\pm\, n_z \frac{dz}{dx \tan\theta}\left(1 - \frac{dz}{dx \tan\theta}\right)}, \tag{4.5}$$

where the plus and minus signs apply to the horizontal (Equation 4.3) and vertical (Equation 4.4) grid line interpolation solutions, respectively, and dz/dx is the ratio of the grid spacing. These standard deviations are one measure of the spatial smearing or diffusion introduced by the short-characteristic method.

The intensity distributions and their standard deviations are plotted in Figure 4.2 as a function of θ for the case of a square grid ($dx = dz$). In the plots, n_x and σ have been scaled by the sine of the inclination angle to account for foreshortening when the emergent intensity is viewed at inclined angles. This allows for direct comparison with simulations (Section 4.3). For illustrative purposes, the distributions (Figure 4.2a) and standard deviations (thick dashed curve in Figure 4.2b) are shown at multiple ray angles for fixed $n_z = 65$ (the depth of the mean vertical ray $\tau = 1$ surface in the MHD simulation described in Section 3). The short-characteristic ray direction is grid aligned at $\theta = 90°$ and $45°$, and the specific intensity distribution collapses to a delta function at those angles (no diffusive error). While $\theta = 0°$ is grid aligned as well, that case is pathological because a strictly horizontal ray never reaches the upper boundary. Moreover, when interpolation occurs on vertical grid lines, as it does for $0° < \theta < 45°$, an increasing number of interpolations are required (to cross an equal number of horizontal grid lines, n_z) with decreasing inclination angle. Thus the diffusive error increases monotonically as $\theta \to 0°$. For horizontal grid interpolation ($45° < \theta < 90°$), the maximum diffusive error σ occurs at $67.5°$, half-way between the grid aligned directions.

The specific intensity distributions given by the analytic solutions of Equations 4.3 and 4.4 (more generally by Equations A.2 and A.6 in Appendix A) and plotted in Figure 4.2a represent the PSFs of the short-characteristic solution for any ray propagation angle θ through a vacuum domain. The width of the distribution σ (Equation 4.5 and Figure 4.2b thick dashed curve) captures the effective image smearing introduced when computing the emergent intensity. It depends

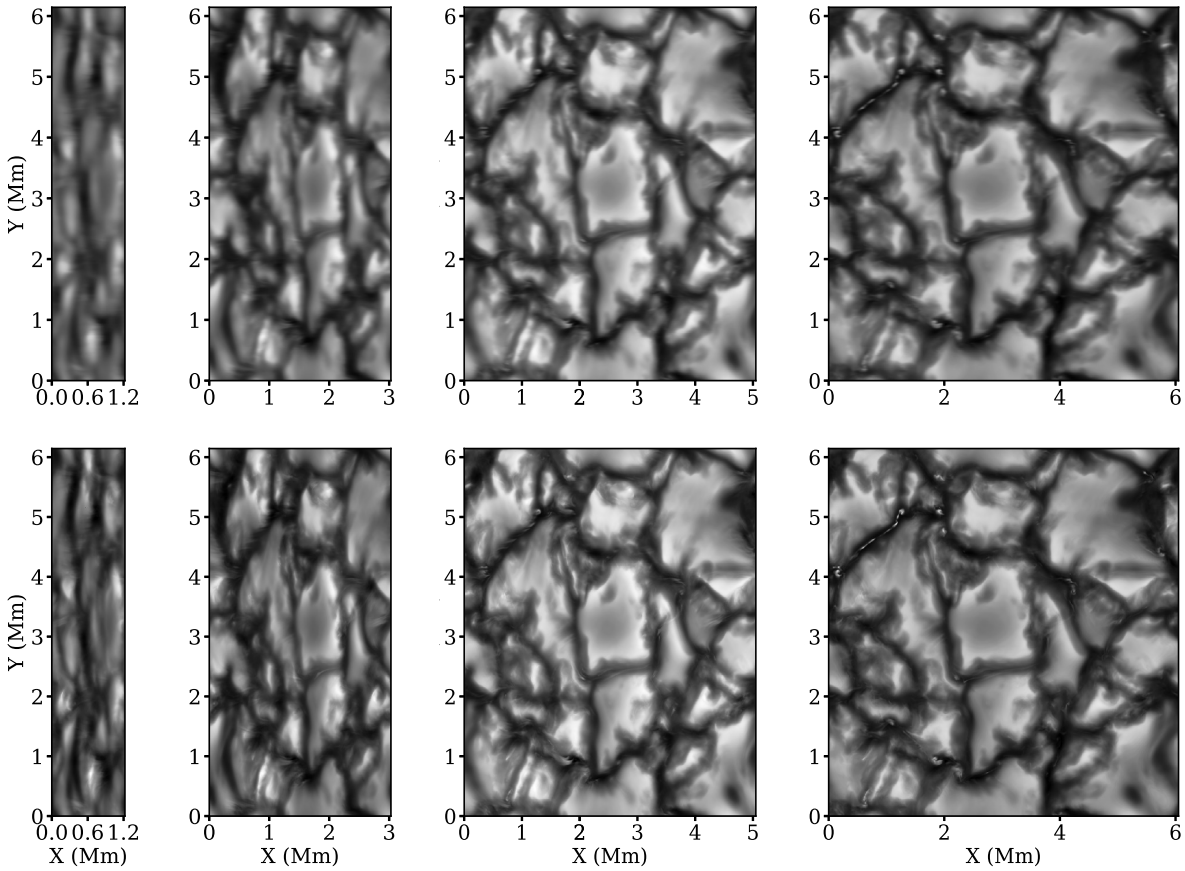

Figure 4.3: Emergent intensity synthesized in the standard short-characteristics method at inclinations values $\mu = 0.20, 0.49, 0.82, 0.99$ (top row from left to right) . Note the smearing in the direction of the tilt due to the short-characteristic intensity diffusion. Bottom row shows the emergent intensity for the same inclination angles when synthesized on a pre-tilted domain (grid-aligned with the ray propagation direction). Note how the pre-tilted images better maintain the spatial resolution of small scale structures.

explicitly on n_z, the number of interpolations above the source point. Since the model assumes ray propagation through a vacuum, the analytic solution captures image degradation in a realistic 3D solution due to radiation propagation above the optically thick to optically thin transition. Below the $\tau = 1$ transition, the medium is optically thick and the diffusive error of the short-characteristic method, while it may contribute to the accuracy with which the divergence of the radiative flux is determined in the radiative MHD simulation, does not contribute significantly to degradation of the emergent intensity. Thus the specific intensity error made depends on the depth within the domain from which the radiation escapes. Since the optical depth surfaces are not aligned with the numerical grid, that depth depends not only on the simulation solution, but on the viewing angle and the wavelength of the radiation. This must be accounted for when evaluating the short-characteristic error in the emergent intensity from a simulation solution.

4.3 Diffusive Error in the Emergent Intensity from 3D MHD Simulations

To assess the amount of image degradation in the emergent intensity images computed from 3D MHD simulations, we examine a snapshot from a MURaM (Vögler et al. 2005) simulation of a $6 \times 6 \times 1.2$ Mm region of solar granulation including magnetic field generation by small-scale dynamo processes (Rempel 2014). The solution has 8 km grid spacing in both the vertical and horizontal directions, the latter comparable to high resolution images that will be forthcoming with the DKIST. It thus provides a good test bed for future comparisons between simulations and observations. The synthesized emergent intensity was computed using the RH radiative transfer solver (Uitenbroek 2001) for viewing angles between μ of 0.2 and 1 ($\mu = \sin\theta$, with θ as defined previously) and at $\lambda = 500$ nm. For comparison with Section 2, we confine the viewing angles to the xz plane ($\phi = 0°$).

We perform the radiative transfer in two ways. In the first, we solve the radiative transfer equation using the standard short-characteristics scheme, linearly interpolating the specific intensity along the inclined rays. The resulting emergent intensity images, for $\lambda = 500$ nm and viewing angles $\mu = 0.20, 0.49, 0.82, 0.99$ are shown along the top row of Figure 4.3. The effect of numerical diffusion

in the direction of inclination is visually apparent in the images. In the second, we compute the radiative transfer on the same atmosphere by pre-tilting the atmosphere to the required viewing angle, interpolating the atmospheric properties along the viewing angles, and solving the transfer equation, using the same short-characteristic scheme, along the now grid-aligned rays. We perform the interpolation such that dz in the ray-aligned atmosphere remains unchanged from its value in the original atmosphere. The interpolation is therefore not restricted to horizontal or vertical planes of the atmosphere, and a bilinear interpolation scheme is used. This method allows for calculation of the emergent intensity at highly inclined angles without causing very sparse grids that would result from interpolation restricted to grid planes. In this way we avoid the compounded specific intensity interpolation error of the short characteristic method, though the plasma properties are still interpolated as required for all radiative transfer solvers. Similar approaches to avoid diffusion error in the emergent intensity have been used in other works (e.g., Koesterke et al. 2008; Hayek et al. 2011; Amarsi et al. 2016). The important point is that the pre-tilting procedure eliminates the compounded specific intensity interpolation error without adding additional sources of error. The bottom row of Figure 4.3 shows the emergent intensity that results when the pre-tilted scheme is employed. It is visually apparent that the images retain higher spatial resolution than those obtained with the standard short-characteristic method.

Quantifying this difference, and its agreement with the model of Section 2, requires that n_z be determined for use in Equations 4.3 and 4.4. As discussed previously, n_z is the number of horizontal grid plane displacements above the source height. This is the vertical displacement between the height from which the radiation escapes and the observer's position (approximately the number of horizontal grid levels crossed along the ray between the mean $\tau = 1$ surface and the top of the domain). Since we are examining the emergent intensity at $\lambda = 500$ nm, we measure, for select viewing angles, the depth of the mean $\tau_{500} = 1$ surface in the simulation. We determine that $n_z = 53$ to 66 for lines-of-sight between 10° and vertical, and plot those values as filled circles in Figure 4.2b. For other angles we use a logarithmic fit to the measured points (dotted gray curve in Figure 2b), and use these to calculate σ from Equations 4.3 and 4.4. This is as plotted a

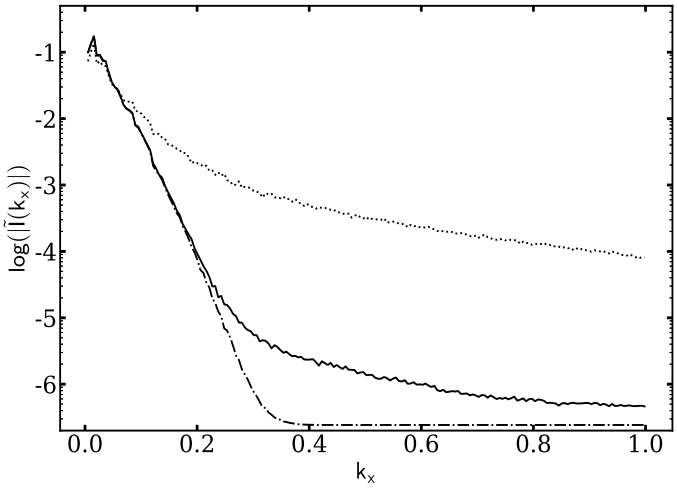

Figure 4.4: Average (over image rows) intensity amplitude spectrum for $\mu = 0.49$ after employing the standard (solid curve) and pre-tilted (dotted curve) short-characteristic methods. Dot-dashed curve shows averaged spectra of the pre-tilted image rows convolved with a binomial convolution kernel with width that yields the best-fit to the standard spectrum. Spectra are normalized to share the same integrated amplitude.

solid black curve in Figure 4.2b. A comparison between the σ values computed from the 3D MHD snapshot, for which n_z is a function of the inclination angles (solid black curve), and those found for the case of a ray propagating in vacuum (Section 4.2) for which n_z is not a function of θ (dashed black curve), shows the dependence of the smearing on the formation height of radiation. In this example, for which we have chosen the value n_z in the vacuum calculation to coincide with the depth of the $\tau_{500} = 1$ surface in the vertical direction, the amounts of smearing differs significantly for angles smaller than $\theta \lesssim 30^\circ$.

We compare the effective smearing from the analytic model directly with the measured reduction in spatial resolution induced by the standard short-characteristic method in the images themselves. In this way, we can demonstrate agreement with the model of Section 2, and show that the error can be eliminated in real model analysis by pre-tilting and interpolating before computing the radiative transfer. To make this comparison, we examine the amplitude spectra of the two image sets. Since the error occurs only in the inclined direction of the viewing angle prescribed, we compute the average 1D spatial amplitude spectra along the direction of the tilt (x-dimension). We

then convolve the rows of the pre-tilted image with the generic analytic solution (Equations 4.3 or 4.4), and use a least-squares measure of the difference between the average of those convolutions and the average 1D spectrum of the standard short-characteristic image to determine the standard deviation of the best-fit binomial convolution kernel. Examples of the average 1D spectra used in this procedure are plotted in Figure 4.4, and the estimates of the standard deviation σ of the binomial convolution kernel are shown in Figure 4.2b with pink diamonds. The error in those measures, estimated as the uncertainty in the fit between the spectra, is smaller than the symbol size, and the values agree with the image degradation caused by inclined ray interpolation in the short-characteristic method. The agreement demonstrates that the model correctly captures the image degradation induced by the short-characteristic computation of the emergent intensity, and that the degradation can be avoided by pre-tilting the solution before computing the short-characteristic radiative transfer.

4.4 Extension to Higher-Order Interpolation

As discussed in Section 1, the interpolation error introduced by the short-characteristics method can be reduced by employing a higher-order monotonic interpolation scheme (e.g., Kunasz & Auer 1988; Hayek et al. 2010). To assess the effectiveness of this approach, we revisit the search beam problem, this time employing cubic monotonic interpolation (Fritsch & Carlson 1980) in the short-characteristic solution. Unlike the linear interpolation solution, we were unable to derive an analytical solution for the intensity on the grid, and so instead propagated the search beam through the vacuum domain numerically. For direct comparison with the linear interpolation results as applied to the MHD simulations, the short-characteristic solution was iterated through n_z heights on a uniform grid $dx = dz$, where n_z was taken to be the depth of the τ surfaces measured as a function of angle in the previous section. The width of the emergent intensity distribution was determined by a skew-normal fit, and the resulting values are shown as solid blue line in Figure 4.2b. Numerical diffusion is significantly reduced (by a factor of up to about three) by employing the higher order interpolation scheme, but because of the monotonicity constraint

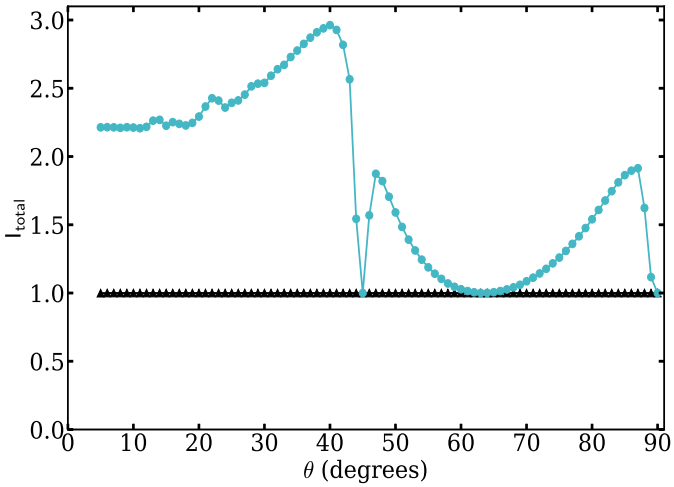

Figure 4.5: Normalized integrated intensity for linear (black triangles) and cubic monotonic (blue circles) interpolation. Note how the integrated intensity is conserved using linear interpolation, but not using cubic monotonic interpolation.

needed to avoid negative specific intensity values, energy is not conserved. The integrated intensity at the top of the domain (normalized by the source value) as a function of beam angle is plotted for both linear and cubic monotonic interpolation in Figure 4.5. While the total intensity is conserved by linear interpolation for all inclination angles (black triangles), cubic monotonic interpolation (blue circles) conserves intensity only at 45°, 90°, and near 62°. For all other beam inclinations, the total emergent intensity is overestimated.

4.5 Discussion and Conclusion

We have quantified the effect of interpolation errors inherent in the short-characteristic radiative transfer method, deriving an analytical model of the diffusion of a point source through a grid at arbitrary viewing angle and comparing that with the spatial resolution degradation of the emergent intensity calculated using a 3D MHD snapshot. We have shown that due to the compounding nature of the error, intensity interpolation accounts for most, if not all, of the reduction in resolution introduced by the short-characteristic method. Interpolation of the plasma properties along the ray path, common to both short- and long- characteristic methods, likely contributes negligibly to resolution reduction. While higher-order interpolation schemes reduce the diffusion

error in the short-characteristic method, they do not conserve energy. We have demonstrated that both the numerical diffusion and energy conservation problems can be circumvented by pre-tilting the computational domain to a ray-aligned grid and performing the short-characteristic radiative transfer vertically through this domain. This requires only that the interpolation of the atmospheric properties along the ray directions occurs prior to the ray propagation, rather than after it.

Without such pre-tilting, the short-characteristic scheme introduces errors that challenge comparisons between numerical solutions and observations. The errors are a strong function of viewing angle, the image and simulation resolutions, and the formation height of the wavelength of interest. For simulations and observations with matching native resolution, any non grid-aligned viewing angle yields a fundamental mismatch in the effective spatial resolution. For example, the simulation used in this work has a resolution of 16 km at best (assuming Nyquist sampling) which is reduced to 80 km when viewed at 30°. The change is equivalent to the difference in spatial resolution of observations obtained in the visible with telescope apertures of 4 m (e.g., DKIST and EST) and $\sim$ 0.8 m (e.g., the NSF's Dunn Solar Telescope). We note that since the PSF of the short-characteristic diffusion error is now known analytically for linear interpolation, the emergent intensity could simply be de-convolved to obtain the fully resolved image. This is true in the case of local thermodynamic equilibrium where the specific intensity along a ray depends only on the local plasma properties, but is likely much more difficult for non-local thermodynamic equilibrium solutions for which the radiation field is iteratively solved and the error may propagate non-linearly through the domain. Employing higher-order interpolation schemes yields an improvement (to 28 km resolution when viewed at 30° for the cubic monotonic interpolation in the example above) at the expense of specific intensity non-conservation. This non-conservation of energy does not affect the emergent intensity image contrast at any given viewing angle, but does affect the relative intensity at differing angles, again likely posing difficulties for non-local thermodynamic equilibrium solutions.

Similarly, since some radiative MHD solvers use short-characteristic radiative transfer in combination with discrete angle-weighted quadrature schemes to evaluate the divergence of the

radiative flux in the solution of the energy equation, angle dependent specific intensity errors may introduce computational artifacts in the radiative MHD solutions themselves. The effects of numerical diffusion on the moments of the radiative transfer equation were discussed in Bruls et al. (1999) for the case of specific triangular grids. Similarly, angle dependent artifacts have been noted in solutions for the photon density in cosmological solutions for optically thin radiative transfer (Finlator et al. 2009). A detailed analysis of how short-characteristic error propagates through the quadrature schemes employed by MHD solvers in the optically thick to optically thin transition of the solar photosphere is warranted, and the subject of future work.

Finally, we reiterate that the diffusive errors introduced by the short-characteristic method can be avoided by interpolating the atmosphere onto a ray-aligned grid before computing the radiative transfer. Since the total number of interpolations incurred by pre-tilting is less than that for the standard short-characteristic method (only the plasma properties not the specific intensity values must be interpolated if pre-tilting is employed), the pre-tilting method may save computational time in the solution of the radiative transfer equation. However, if the specific intensity is needed on the original grid, for quadrature calculation of the flux divergence for example, interpolation of the specific intensity back to the original grid is also required at the expense of some diffusion. This makes the total interpolation cost the same without propagating the diffusive error, though careful comparison between the computational speed of these methods on multiprocessor hardware must be made. The advantage of pre-tilting compared to the standard short-characteristic method is that the interpolation of the specific intensity back to the original grid does not compound the error. Other solutions to the numerical diffusion problem have been explored. Long-characteristic solvers are routinely employed (e.g., Bifrost (Gudiksen et al. 2011), CO5BOLD (Freytag et al. 2012), Stagger (Magic et al. 2013) StellarBox (Wray et al. 2015)), and these fundamentally avoid the intensity diffusion error. Hybrid radiative transfer schemes using adaptive mesh refinement have also been developed (Rijkhorst et al. 2006) and help mitigate the error. Which approach proves most accurate and computationally efficient is still an open question, but pre-tilting is simple, highly effective, and can perhaps be seamlessly integrated into existing radiative MHD solvers.

This material is based upon work supported by the National Science Foundation Graduate Research Fellowship Program under grant No. DGE 1144083 and the National Science Foundation under grant No. 1616538. The National Solar Observatory is operated by the Association of Universities for Research in Astronomy under a cooperative agreement with the National Science Foundation. This work utilized the Janus supercomputer, which is supported by the National Science Foundation (award number CNS-0821794) and the University of Colorado Boulder. The Janus supercomputer is a joint effort of the University of Colorado Boulder, the University of Colorado Denver and the National Center for Atmospheric Research. The authors are grateful for the International Space Science Institute in Bern for hosting the International Team 335 "Towards New Models of Solar Spectral Irradiance Based on 3D MHD Simulations" which resulted in fruitful discussions. The authors thank Matthias Rempel for providing the MHD snapshot, and both Han Uitenbroek and the referee for useful feedback to improve the quality of the work.

Chapter 5

MHD Simulations of Quiet Sun Magnetic Morphologies

5.1 Introduction

This thesis focuses on understanding the radiative output of the quiet sun under differing magnetic field morphologies. From the discussion in Chapter 2, current ground- and space-based photometric observations are insufficient to deduce radiative behavior of the low contrast quiet sun due to the sensitivity to the construction of the center-to-limb profile. In order to understand the quiet sun radiative behavior in the absence of sufficiently accurate photometric and high spatial resolution observations, we require realistic simulations of the solar photosphere and the resulting emergent intensity. The simulations must therefore include the relevant physical processes which produce the conditions consistent with observations, including the interaction of a magnetic field with a partially ionized fluid and the transport of energy via radiation. Such conditions are governed by the equations of radiative magnetohydrodynamics (MHD).

Radiative MHD simulations solve the coupled conservation equations of mass, momentum, and energy, as well as the induction equation for the magnetic field (see Section 5.2 for the equations or Nordlund et al. 2009; Stein 2012, for reviews on radiative MHD in the solar surface). The equations include the effects of radiation which influences excitation populations, ionization fractions, and energy transport. Because of the frequency dependence of the opacity, numerically solving the radiative transfer equation in the MHD solution requires a solution at every frequency. As this is computationally prohibitive, most MHD solvers limit the number of calculated frequencies by computing the radiative transfer over a small number of frequency bins which are taken to represent

a larger subset of frequencies in a method known as opacity binning (Nordlund 1982).

Modern MHD solvers for solar surface simulations include Bifrost (Gudiksen et al. 2011), CO5BOLD (Freytag et al. 2012), Stagger (Magic et al. 2013), and MURaM (Vögler et al. 2005). The solution of the MHD equations results in a statistically steady state of the simulated domain, which approximates the physical conditions of the plasma at the solar surface. Comparison of the results from MHD simulations with observations of the solar photosphere requires the emergent intensity from the simulated surface at the frequency of the observation. Since the MHD simulations utilize an approximation to the full frequency spectrum in the calculation of the radiative transfer, the solution to the radiative transfer equation must be recomputed at the frequencies of interest with the steady state MHD simulation solution as the input. This is achieved by synthesizing the emergent intensity using a standalone radiative transfer solver incorporating the relevant sources of opacity and the elemental and molecular abundances. Unlike typical MHD solvers, most standalone radiative transfer solvers are capable of solving the radiative transfer equation at all frequencies including those which fall in spectral lines. Examples of such radiative transfer solvers include RH and RH1.5 (Uitenbroek 2001; Pereira & Uitenbroek 2015) which are used throughout this thesis, PORTA (Štěpán & Bueno 2013), and MULTI3D (Leenaarts & Carlsson 2009).

To study the effect of magnetic field morphology on radiative output, we employ two sets of radiative MHD simulation solutions of the quiet sun; one representing a nearly isotropic magnetic field configuration and the other with a predominantly vertical magnetic field. The simulations are computed at high spatial resolution to mimic upcoming observations from DKIST. In this chapter, we discuss the radiative MHD equations and the simulations used throughout remainder of this thesis. We also demonstrate their realism in reproducing the observed quiet sun magnetic field.

5.2 Radiative MHD Simulations

The simulations used in this thesis represent a 'box-in-a-star' setup with a 3D cartesian domain that simulates the uppermost portion of the convection zone up to the top of the photosphere. The simulation solutions return the statistically equilibrated state variables of the domain, as well

as the velocities and magnetic field profiles at all points throughout the domain. In this section, we present an overview of the MHD equations solved in simulations of the solar photosphere, the treatment of energy transport by radiation, the boundary conditions imposed, and the realism as compared with observations of the solar surface.

5.2.1 MHD Equations

Radiative MHD simulations require solution of the equations for the conservation of mass, momentum, energy, and magnetic induction. The equations can be written as,

$$\frac{\partial \rho}{\partial t} = -\nabla \cdot (\rho \mathbf{v}) \tag{5.1}$$

$$\frac{\partial \rho \mathbf{v}}{\partial t} = -\nabla \cdot (\rho \mathbf{v}\mathbf{v}) - \nabla P - \rho \nabla \Phi - \nabla \cdot \tau_{visc} + \boldsymbol{J} \times \boldsymbol{B} \tag{5.2}$$

$$\frac{\partial e}{\partial t} = -\nabla \cdot (e\mathbf{v}) - P(\nabla \cdot \mathbf{v}) + Q_{rad} + Q_{visc} + \eta J^2 \tag{5.3}$$

$$\frac{\partial \boldsymbol{B}}{\partial t} = \nabla \times (\mathbf{v} \times \boldsymbol{B} - \eta \nabla \times \boldsymbol{B}) \,. \tag{5.4}$$

Here ρ, P, $\mathbf{v}$, e, and $\boldsymbol{B}$ represent the mass density, pressure, velocity, internal energy density, and magnetic flux density, respectively. Furthermore, $\boldsymbol{J} = \nabla \times \boldsymbol{B}$ is the current density, τ_{visc} is the viscous stress tensor, $-\nabla\Phi$ is the gravitational acceleration, η is the magnetic diffusivity, and Q_{rad} and $Q_{visc} = \vec{\mathrm{v}} \cdot \nabla \tau_{visc}$ are the heating by radiative and viscous dissipation, respectively.

The continuity equation (Equation 5.1) represents the mass conservation equation and states that any changes in the density in time result from the divergence of flow. The momentum equation (Equation 5.2) captures the forces exerted on the fluid. This includes the effect of the magnetic field through the Lorentz force, which acts to suppress plasma motions perpendicular to the magnetic field, describing the suppression of convection by magnetism. The energy equation (Equation 5.3) describes the conservation of energy in the plasma and includes the effects of energy transport by work, radiative and viscous heating, and resistive heating from the magnetic field. The solution to the coupled equations requires two equations of state closures that relate the pressure and temperature to the density and internal energy.

5.2.2 Radiative Heating

The radiative heating rate Q_{rad} in Equation 5.3 couples the radiation field to the MHD equations where

$$Q_{rad} = -\int_{\nu} \nabla \cdot F_{\nu} d\nu \ , \tag{5.5}$$

and the radiative flux F_{ν} is defined in Equation 3.5. Radiative MHD simulations of the solar photosphere typically assume LTE in the solution of the radiative transfer equation, which reduces the complexity of the problem. The calculation of the radiative heating rate presents two computational challenges in MHD simulations. The first that computing the divergence of the flux requires the integrated emergent intensity over all solid angles for each grid point in the computational domain. Numerical quadrature is used to approximate the integral where the contribution to the flux from all directions is approximated by weighting the contribution from discrete angles. The second challenge is that the flux must be computed over all frequencies. This is typically avoided by reducing the number of frequencies over which the flux is calculated. The opacity binning method developed by (Nordlund 1982) is commonly used in solar surface simulations to reduce the number of frequencies calculated in the radiative heating rate. In this method, the opacity is grouped into bins based on the formation heights of the frequencies and assigned a single opacity for the entire bin. The solution to Equation 3.5 is then computed only over those discrete bins. Depending on the sophistication of the scheme, the number of bins can range from a single-valued average opacity (a grey atmosphere) to a nearly fully-resolved spectrum. Many state-of-the-art MHD simulations use between 4 and 12 frequency bins, which has been shown to closely approximate the radiative interactions compared to a larger number of bins (Vögler et al. 2004).

5.2.3 Boundary Conditions

While the boundary conditions between various simulations differ, several generalizations can be made for simulations of the solar photosphere. The simulation domains use periodic boundary conditions in the horizontal directions for all physical quantities. The bottom boundary is located

in the convection zone and remains open to allow fluid to inflow and outflow. The inflow of fluid from the bottom boundary is set to mimic the conditions of the deeper convection zone that is not simulated. The treatment of the upper boundary varies between MHD solvers, but are typically set open to allow fluid to flow outward and prevent reflection of waves and shocks off the upper boundary. Magnetic fields can also be imposed on the boundaries as an initial condition to investigate the role of magnetic fields on the simulation solutions.

5.2.4 Realism of Simulations Compared with Observations

Modern MHD solvers reproduce many observed features and signatures of the solar surface (see e.g., Nordlund et al. 2009; Stein 2012). We focus here on those which compared MURaM simulations to observations of the solar photosphere. Danilovic et al. (2008) compared the granular contrast of Hinode with MURaM solutions spatially degraded to the resolution of Hinode. They found that the addition of a slight defocus in the spatial degradation resulted in 7.5% granulation contrast compared to the observed value of 7.0%. Afram et al. (2011) demonstrated the agreement between MURaM simulations and Hinode observations of intensity distributions and center-to-limb variations in the visible continuum. As the differences between simulations and observations were more pronounced in the blue continuum compared to green and red, they attributed this difference to the use of LTE and not synthesizing spectral lines which both have larger effects closer to UV wavelengths. Results from Hirzberger et al. (2010) and Riethmüller et al. (2014) showed agreement in the emergent intensity of MURaM simulations of quiet sun magnetic field with the high-resolution observations from SUFI onboard Sunrise. These results demonstrate the realism of the solar surface simulations compared to observations.

Beeck et al. (2012) showed agreement between three different radiative MHD simulations from the codes CO5BOLD, MURaM, Stagger, which have differing numerical schemes and approximations, domain sizes, grid resolutions, and boundary conditions. Using 'standard' simulations produced from the three MHD solvers, they found agreement of the average temperature profiles as a function of height of less than 2% with differences of approximately 1% near $\tau_{500} = 1$. Similarly,

the center-to-limb profiles across continuum wavelengths agree within approximately 2%, with the exception of 400 nm with deviations of around 4%. They attributed slight deviations to differences in the spatial resolutions and opacity binning schemes. Their result demonstrates confidence in the different simulation setups and results from the various MHD solvers.

5.3 MURaM Simulations

The Max Planck Institute for Solar System Research/University of Chicago Radiation Magnetohydrodynamics (MURaM) code (Vögler et al. 2005; Rempel et al. 2009; Rempel 2014) solves the non-ideal MHD equations using a fourth-order finite difference scheme to discretize the MHD equations in space. The system of MHD equations is closed using the OPAL equation of state tables (Rogers & Iglesias 1996). MURaM employs the Carlson quadrature to calculate the angular integration of the intensity. This quadrature scheme is invariant over axes rotations which permits identical angles in 90 degree rotations and evenly spaces the angles over the sphere. Details of this method can be found in Carlson (1963), Lathrop & Carlson (1965), and Carlson (1970). MURaM uses the A4 quadrature which computes 12 rays on the unit sphere surrounding each grid point. The radiative transfer is computed using the method of short-characteristics (see Chapter 8 for a discussion of future work to estimate the error introduced by the short-characteristics method in radiative MHD simulations). For the simulations used in this work, the MURaM code implemented a 4-bin opacity based on continuum opacities from the ATLAS 9 model atmosphere package (Kurucz 1993). MURaM replaces the dissipative terms of the MHD equations (e.g., η and τ_{visc}) with a numerical diffusion, which acts to stabilize the numerical scheme. The numerical diffusion prevents buildup of high-frequency grid oscillations on the smallest scales. Details of the method can be found in Rempel et al. (2009) and Rempel (2014).

5.3.1 Simulation Setup

This thesis is concerned with the radiative behavior of the quiet sun under differing magnetic morphologies, and we therefore require simulations which closely approximate solar-like morpholo-

gies. We chose a simulation with a predominantly vertical magnetic field across the domain, which we call the mean field (MF) simulation. This magnetic field configuration is achieved by imposing a vertical magnetic field within the domain. The other simulation, in contrast, simulates an isotropic magnetic field with mixed polarity. This results in a nearly zero mean vertical magnetic field within the domain. We call this simulation the local dynamo (LD) simulation as it is meant to simulate the magnetic field generated by a local turbulent dynamo. Simulating such a local dynamo driven magnetic field has been the subject of previous work (Vögler & Schüssler 2007), however, the horizontal magnetic field was too weak to reproduce the observed magnetic field distribution seen by Danilovic et al. (2010b) and Orozco Suárez & Bellot Rubio (2012).

Recently, work by Rempel (2014) found that the observations of the strong horizontal magnetic field seen at small scales in the quiet sun (Danilovic et al. 2010b; Orozco Suárez & Bellot Rubio 2012) could be achieved using a modified magnetic bottom boundary. The bottom boundary allows for horizontal magnetic field to be advected into the domain, and effectively mimics the properties of the upper convective zone. Therefore, to test the realism of this bottom boundary and to understand the effects of a turbulent dynamo penetrating the convection zone, Hotta et al. (2015) simulated a larger portion of the convection zone, up to just below the photosphere, at high spatial resolution in order to resolve the dynamo action at small spatial scales. They found that not only did the bottom boundary of Rempel (2014) mimic that of the output of their global simulation, they also found that despite suppressing convection, the small-scale dynamo improved the efficiency of convective energy transport through reduction of horizontal mixing. This reduction in convective velocities partially closes the gap between the simulation and observed low wavenumber velocities in the convective zone, which may be overestimated in current convective simulations (Hanasoge et al. 2012; Lord et al. 2014).

The simulations used in this thesis were computed on a grid with dimensions $6.144 \times 6.144 \times 3.072$ Mm^3 and 8 km grid spacing (around 1-2 Mm vertical extent) and using the bottom boundary condition of Rempel (2014). The simulation was initialized with no magnetic field, simulating a pure hydrodynamic case, the HD simulation. In the LD simulations, a randomly oriented seed field

of 10^{-3} G was added to the thermally relaxed HD simulation with no net magnetic flux across the top and bottom boundaries. The simulation was then evolved until the field amplitude saturated. In the MF simulations an additional 80 G vertical mean magnetic field was imposed to the thermally relaxed hydrodynamic simulation, and again evolved until it reached steady state. For all three simulations (HD, MF, and LD), we use 10 snapshots at 4 minute cadence, which is used to increase the statistics of the analysis.

5.3.2 Steady-State Magnetic Field

Comparison between the MHD simulations with observations requires the values of the simulated magnetic field at the height where the majority of photons escape. As many magnetograms infer magnetic field strength using lines in the visible portion of the spectrum, the value of $\tau_{500} = 1$ is commonly used to approximate this height. To compare the observable values of the magnetic field of the MF and LD simulations described above, we use the RH radiative transfer solver (Uitenbroek 2001) to determine the $\tau_{500} = 1$ height and interpolate the magnetic field from the simulations onto this surface. The results for B_z, $|B|$, and $|B_h|$ in a snapshot of each atmosphere is shown in Figure 5.1. The MF simulation forms stronger and larger magnetic field concentrations (both $|B|$ and B_z) compared to those formed in the LD simulation. The LD simulation produces much smaller magnetic flux concentrations and structures with mixed polarities, whereas the MF simulation is dominated by the positive B_z polarity imposed. The vertical magnetic field in the MF simulations results in magnetic flux cancellation of negative polarities produced at smaller scales. In contrast to the MF, the LD simulation produces stronger horizontal unsigned flux $|B_h|$.

The average photospheric magnetic field distributions for the 10 snapshots of the MF and LD simulations used in this work, as well as the observational results of the small-scale dynamo quiet sun magnetic field, are shown in Table 5.1. The magnetic field values of the simulations were computed at the $\tau_{500} = 1$ surface and averaged over the 10 snapshots. As shown in Table 5.1, the LD simulation on average has a weaker vertical magnetic field strength and a stronger horizontal magnetic field strength than the MF. Note that the average unsigned magnetic flux $< |B| >$ for the

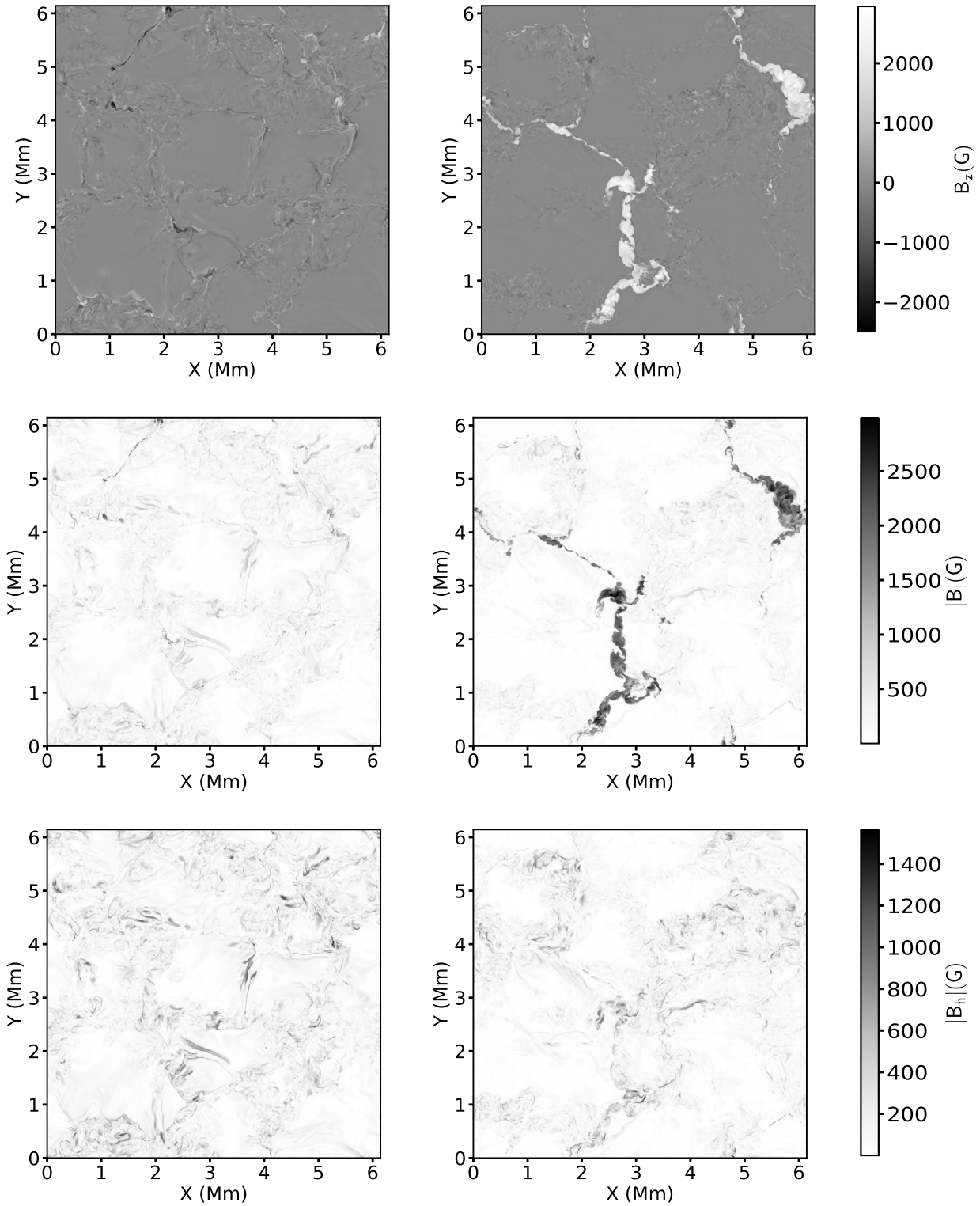

Figure 5.1: Vertical unsigned (top), unsigned (middle), and horizontal unsigned (bottom) magnetic field for a snapshot of the LD (left) and MF (right) atmospheres interpolated on the $\tau_{500} = 1$ surface as computed by RH.

	$< \|B\| >$	$< \|B_z\| >$	$< \|B_h\| >$	$< B_z >$
Simulations				
LD	180 G	91 G	138 G	0 G
MF	184 G	128 G	100 G	78 G
Observations				
Danilovic et al. (2010b)	170 G	84 G	147 G	—
Orozco Suárez & Bellot Rubio (2012)	220 G	64 G	198 G	—

Table 5.1: Average unsigned magnetic field $< |B| >$, vertical unsigned magnetic field $< |B_z| >$, horizontal magnetic field $< |B_h| >$, and vertical signed magnetic field $< B_z >$ for the 10 snapshots of the LD and MF simulations. Also shown are the properties of the small-scale dynamo field inferred from observations.

two simulations are roughly equivalent, saturating around 180 G, while the horizontal and vertical components differ substantially. The LD simulation agrees closely with the inferred magnetic field properties of Danilovic et al. (2010b), while the observations from Orozco Suárez & Bellot Rubio (2012) have a stronger overall field as well as transverse field.

5.4 Conclusions

In this Chapter, we discussed the equations that govern radiative MHD simulations of the solar photosphere, including the treatment of radiative transfer in the solution to the radiative heating rate, and the boundary conditions employed to mimic solar conditions. We then described the MURaM radiative MHD solver and the boundaries imposed to generate the simulations used throughout the remainder of this thesis, followed by the average magnetic properties of the two simulations over the 40 minute time series.

The two simulations approximate the quiet sun magnetic field under two different morphologies: one with a vertical magnetic field imposed (the MF simulation) and the other with a mixed polarity isotropic magnetic field with no mean vertical component (the LD simulation). The MF simulation is set up by imposing a mean field over the top and bottom boundary of the computational domain to simulate a large-scale vertical magnetic field embedded through the surface. The LD simulation represents quiet sun magnetic field formed by the small-scale dynamo process acting

locally, which manifests as a nearly isotropic magnetic field with mixed polarities. We showed that this LD simulation reproduced observed properties of the quiet sun magnetic field though to be due to the operation of a local turbulent dynamo. These simulations are used in the following chapters to analyze the effect of magnetic field morphology on the quiet sun radiative output.

Chapter 6

Effect of Magnetic Field Morphology on Simulated Quiet Sun Radiative Output

6.1 Introduction

In the previous chapters, we discussed quiet sun magnetic field generation processes that can result in different magnetic field morphologies (see e.g., Wijn et al. 2009; Pillet 2013; Borrero et al. 2015, for reviews of quiet sun magnetism). While many studies have searched for signatures of quiet sun magnetism resulting from these generation mechanisms, the quiet sun magnetism is likely composed of mixed contributions from various mechanisms. A goal of this thesis is to understand the effect of quiet sun magnetic field morphology on radiative output. Given that the quiet sun covers a large fraction of the solar disk and contributes substantially to the total magnetic flux, the radiative output of the quiet sun can have a large effect on solar irradiance and its variations. However, the quiet sun magnetic field distribution is not well resolved in the full-disk images used by many irradiance models or by high resolution spectropolarimeters due to the lack of sensitivity of the stokes profiles to mixed polarity and horizontal magnetic fields. This lack of resolution limits the ability to directly measure both the magnetic field distribution of the quiet sun and the resulting radiative output.

Magnetic field concentrations within the quiet sun have often been described as magnetic flux tubes, with their physical properties studied through the use of flux tube models (e.g., Spruit 1976; Knölker & Schüssler 1988; Deinzer et al. 1984). These models determine the thermal stratification of the tube interior by balancing the effects of suppressed convection due to the presence of the magnetic field within the tube with the enhanced lateral heating from the sidewalls of the tube due

to the reduced opacity. Tubes with small internal radii are predicted to have a higher temperature as a function of height compared to large ones since the horizontal radiative flux can heat the interior of the small tube more efficiently. The relative brightness of the flux tube compared to the surroundings depends then on the internal temperature at $\tau = 1$. Small flux tubes typically appear bright and large ones appear dark with the transition occurring around a diameter of 300 to 500 km (e.g., Knölker & Schüssler 1988; Keller 1992), where the transition results from the lateral heating from the sidewalls no longer being able to balance the reduced heating from convective suppression.

Some results suggest that the apparent brightness of a magnetic structure may also depend on the magnetic environment in which it is embedded. Observations show that the relative brightness of quiet sun magnetic fields is higher than that of equivalent magnetic fields observed in active regions (e.g., Lawrence et al. 1993; Kobel et al. 2011, 2012; Criscuoli et al. 2017). Similarly, work by Criscuoli (2013) used high-resolution MHD simulations with differing imposed vertical magnetic field to study the effect of average magnetic flux on the simulations. They showed that increased environmental magnetic flux resulted in reduced intensity contrast for magnetic structures of similar field strength and size. These results may be explained both by the reduced convective energy transport of the region and the generally larger magnetic structures (Kobel et al. 2012; Criscuoli 2013). These observations and simulations compared the brightness of small magnetic structures embedded in regions of differing vertical (line-of-sight) magnetic flux. Despite the recent observations suggesting the presence of a small-scale dynamo field in the quiet sun (Harvey et al. 2007; Lites et al. 2008; Ishikawa & Tsuneta 2009; Danilovic et al. 2010b; Lites 2011), no studies to date have analyzed the effect of differing magnetic morphologies on the brightness of quiet sun magnetic structures.

In this chapter, we analyze the effect of magnetic field morphology on the radiative output of quiet sun magnetic structures. We use two highly realistic solar surface simulations with one representing a region of predominantly vertical magnetic field, and the other representing an isotropic distribution in the absence of a mean vertical magnetic. The simulations were discussed in Chap-

ter 5 and shown to have equivalent average magnetic field strength but with differing morphologies. We analyze the regions responsible for the radiative differences between the two morphologies by comparing the radiative output of similar features, as well as the atmospheric properties of the two simulations.

6.2 Simulations and Analysis

We use the MURaM simulations discussed in the previous chapter. The simulations were computed on a grid with dimensions $6.144 \times 6.144 \times 3.072$ Mm^3 and 8 km grid spacing. The MF simulation displays a predominantly vertical magnetic field with a mean signed magnetic flux of approximately 80 G, and the LD simulation displays isotropic magnetic field of mixed polarities with zero mean signed magnetic flux. The magnetic field at $\tau_{500} = 1$ was shown in Figure 5.1 for a single snapshot of each simulation. The average properties over 10 snapshots with a 4 minute cadence for each simulation set was shown in Table 5.1. The two simulations have nearly equivalent magnetic field strength at $\tau_{500} = 1$, but differ in their morphologies. The average magnitude of the LD magnetic field also agrees well with observations of the quiet sun field in Danilovic et al. (2010b), which found signatures of a strong horizontal component of the magnetic field in the quiet sun.

To compare the radiative output of the two simulations, we compute the radiative transfer for the vertical viewing angle at $\lambda = 500$ nm using the RH radiative transfer solver (Uitenbroek 2001; Pereira & Uitenbroek 2015). The value of 500 nm was selected to represent the solar photosphere and continuum wavelengths. We study the vertical line-of-sight emergent intensity, corresponding to disk center on the solar surface. In addition to the emergent intensity, RH also computes the opacities as a function of depth at each grid point in the simulated atmospheres which is used to calculate the optical depth as a function of height through the atmospheres (Equation 3.13). To compare the results with previous observational studies, we require the vertical magnetic field at the optical depth unity surface as this is the typical observed signature from magnetograms. We therefore compute $\tau_{500} = 1$ for each simulation snapshot and interpolate the grid-defined magnetic

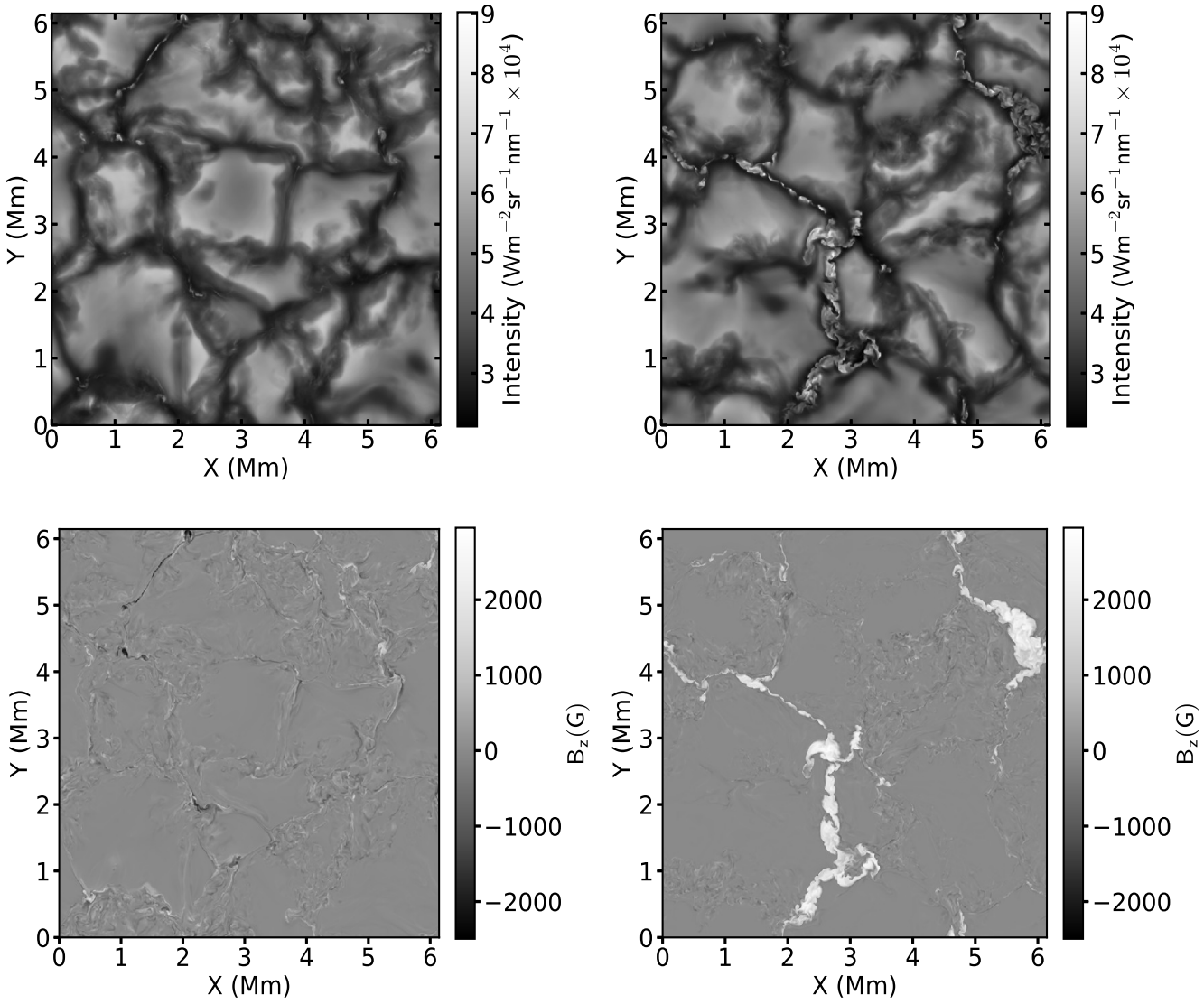

Figure 6.1: Top: Emergent intensity at $\lambda = 500$ nm for a snapshot of the LD (left) and MF (right) atmospheres. Bottom: Vertical magnetic field, B_z, computed at the $\tau_{500} = 1$ surface.

field vectors onto this surface. The emergent intensity for the vertical line-of-sight and the vertical magnetic field for a snapshot of the two simulations is shown in Figure 6.1. The similarities of the convective patterns and magnetic structures in the intensity images have qualitatively similar patterns to those seen in the bottom right of Figure 1.3.

To investigate the effect of the magnetic field morphology on the radiative output, we directly compare the emergent intensity at $\lambda = 500$ nm as a function of the pixel vertical magnetic

field strength. We then assess the sources of the radiative differences between the simulations by comparing the emergent intensity of upflows, downflows, and magnetic structures of differing sizes.

6.3 Results

6.3.1 Dependence of Intensity on Magnetic Field

To test if there exists a difference in the radiative output of the two atmospheres due to the magnetic field morphology, we directly compare the emergent intensity for the vertical viewing angle (disk center) of the two atmospheres as a function of the vertical magnetic field strength at $\tau_{500} = 1$. For every pixel in all 10 snapshots of the two simulations, we plot the emergent intensity as a function of the signed line-of-sight magnetic flux density. The result is shown in Figure 6.2. The average and standard deviation over 50 equally-spaced magnetic field bins is shown as solid lines. The dotted grey line represents the average emergent intensity over all the simulation sets, where the LD and MF have nearly equivalent mean intensity (see Table 6.1).

The shape of the curves can be explained as follows. Pixels with $|B_z| \approx 0$ G represent the centers of granules, and are on average slightly brighter than the average pixel. The pixels with larger $|B_z|$ correspond to the magnetic pixels that begin to accumulate in the downflow lanes. As seen here and in Figure 6.1, the downflow lanes are darker on average than the granule tops. This results from downflows being the regions where cool plasma descends and the granule centers being the regions where warm plasma rises. For pixels with magnetic flux density larger than approximately $|B_z| = 750$ G, the average emergent intensity increases with increasing magnetic field strength. These correspond to pixels found in the magnetic structures seen in Figure 6.1. The presence of the magnetic field in the structure reduces the opacity, allowing radiation to escape from deeper in the atmosphere where the temperature is higher resulting in a higher emergent intensity. Following the flux tube model, thermal structure within the magnetic structure itself depends on the balance of lateral heating from the sidewalls of the tube and the suppression of convective flux by the magnetic field.

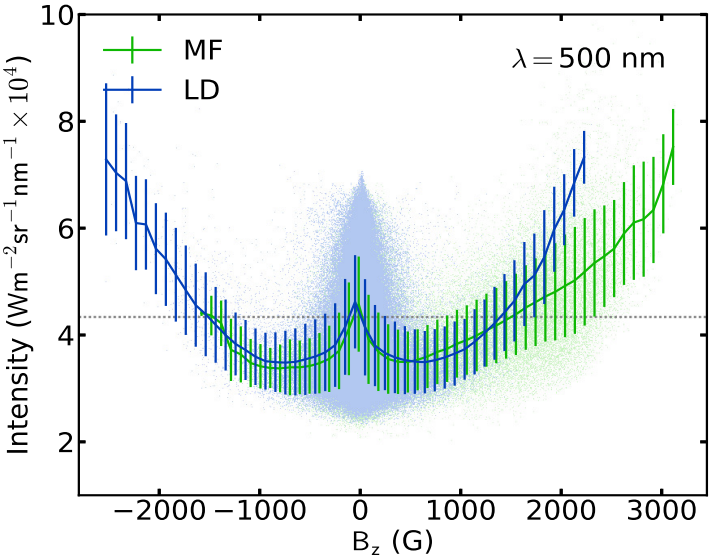

Figure 6.2: Emergent intensity at $\lambda = 500$ nm as a function of magnetic field $\mu = 1.0$. The average and standard deviation over 50 equally-spaced magnetic field bins is shown as solid lines. Dotted line denotes the average intensity of the two simulations. Note that the LD has a higher emergent intensity than the MF for $B_z > 1200$ G.

There are several notable features in Figure 6.2. First, for negative magnetic field pixels, the MF simulation has no pixels with negative field greater than roughly -1500 G while the LD simulation extends to nearly -3000 G. This is a result of the magnetic field imposed on the MF simulation, which enforces a net positive vertical field over the domain and cancels a large portion of the negative polarity field generated locally. Since the LD simulation has no imposed vertical field, these negative fields remain in this simulation. Second, note that for pixels with $|B_z| < 750$ G the two simulations on average have the same emergent intensity. Finally, for B_z greater than approximately 1200 G the LD pixels have a higher radiative output for identical vertical magnetic field strength than the MF simulation. The differences are as large as 50% for the highest magnetic field pixels.

6.3.2 Isolating Sources of Radiative Differences

The enhanced intensity in the high positive magnetic field pixels (i.e., aligned with the field introduced in the MF simulation) in the LD compared to the MF simulations in the previous section (Figure 6.2) suggests that the radiative differences between the atmospheres lie in the magnetic structures, which have a stronger magnetic flux density. To investigate this further, we separate the atmospheres into structures and analyze their radiative output. The structures are upflows, downflow lanes, and magnetic elements.

The structure identification begins with magnetic elements. First, we apply a mask to all simulation pixels with an unsigned vertical magnetic flux greater than 750 G at the $\tau_{500} = 1$ surface. This threshold was chosen based on the location of the minimum mean intensity in Figure 6.2, which represents the region where magnetic flux begins to concentrate in the downflow lanes and enhance the pixel brightness relative to the downflow lanes. Using this mask, we identify a magnetic structure as any pixels within the mask that are spatially adjoined. Since the LD simulations produce small magnetic elements compared to the MF, we bin magnetic elements into small and large elements. Small elements are those which have a total pixel area smaller than the largest LD magnetic element (650 pixels or roughly 150 km effective radius assuming circular cross-sections),

while large elements are those with a larger total pixel area. Once all magnetic elements are identified, we then identify upflows and downflow lanes. Upflows are identified as any non-magnetic structure pixels with a positive vertical velocity at the $\tau_{500} = 1$ surface and downflows are identified as the remaining pixels. The results of the masks for a snapshot of each atmosphere are shown in Figure 6.3.

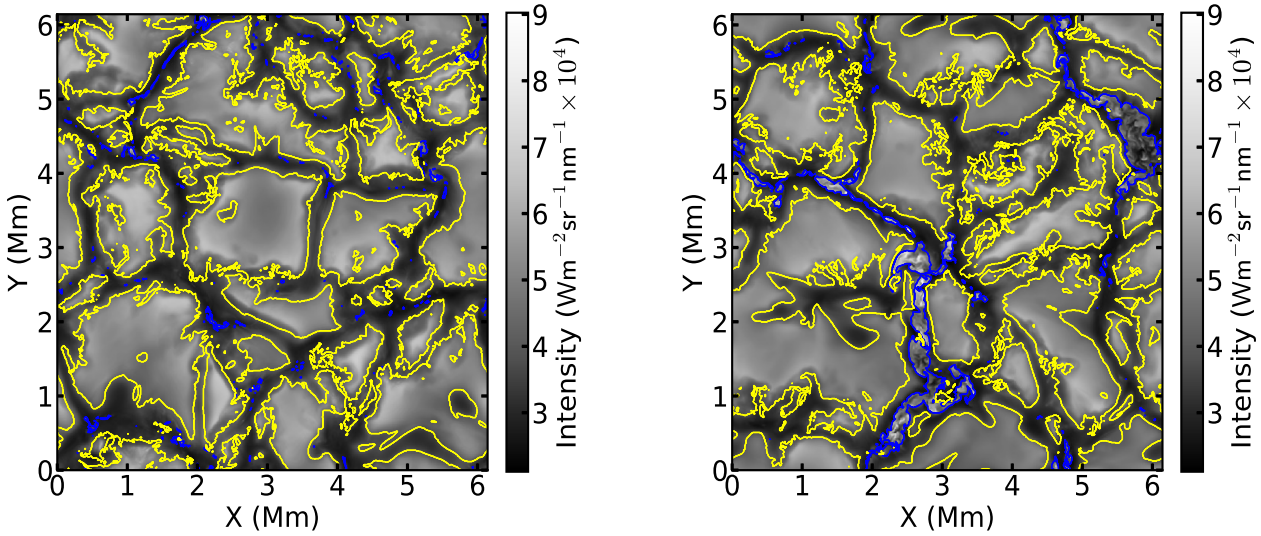

Figure 6.3: Top: Emergent intensity at $\lambda = 500$ nm for a snapshot of the LD (left) and MF (right) atmospheres with contours showing magnetic structures (blue) and upflows (yellow). All remaining pixels were identified as downflow lanes.

Using these identifications for upflows, downflow lanes, small and large magnetic structures, we compute the average intensity and number densities of these structures and the average over the full simulation for the three atmospheres. The results are shown in Table 6.1. The average intensity for all pixels, upflows, and downflow lanes in the the three simulations agree closely (corresponding to a few Kelvin temperature differences), suggesting that the magnetic morphology of the atmospheres plays little role in modifying the radiative output of the weakly magnetized regions. The differences in output between the LD and MF atmospheres are primarily restricted to magnetic structures.

The average intensity of both small and large magnetic structures in the MF simulations is

	Intensity ($W\ m^{-2}\ sr^{-1}\ nm^{-1} \times 10^4$)			Number density of pixels		
	HD	LD	MF	HD	LD	MF
All pixels	4.313 ± 0.928	4.340 ± 0.927	4.334 ± 0.927	1.000	1.000	1.000
Upflows	4.905 ± 0.661	4.950 ± 0.678	4.924 ± 0.687	0.584	0.572	0.554
Downflow lanes	3.482 ± 0.526	3.518 ± 0.479	3.504 ± 0.584	0.416	0.419	0.401
Small structures	—	3.833 ± 0.802	4.202 ± 1.037	—	0.009	0.007
Large structures	—	—	4.518 ± 0.939	—	—	0.038

Table 6.1: Average intensity with standard deviation at $\lambda = 500$ nm and number densities of pixels for the full simulation, upflows, downflow lanes, and small and large magnetic structures in the HD, LD, and MF atmospheres.

on average higher than that of the LD magnetic structures. This may seem contradictory to the results shown in Figure 6.2, however it is important to note that the averages presented in Table 6.1 represent pixels of any B_z value within the small or large magnetic structures. The distribution of pixels in B_z for the LD and MF atmospheres for small and large magnetic structures are shown in Figure 6.4. From this figure it is apparent that small magnetic structures within the LD simulations

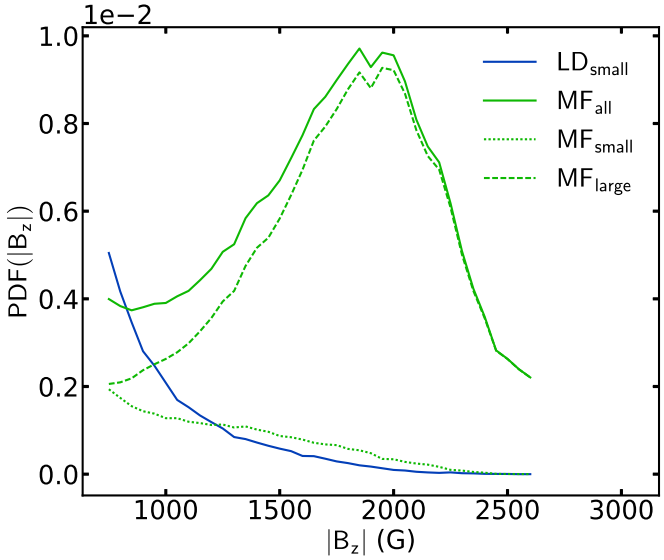

Figure 6.4: PDF of the large and small magnetic structures normalized to sum of all image pixels. Note that pixels in large magnetic structures of the MF simulation have field strengths centered around 2000 G, which results in the higher radiative output of large structures despite the perceived lower radiative output from Figure 6.2.

have on average smaller values of B_z than those in the MF simulation. Similarly, the pixels in the large magnetic structures in the MF simulation largely have field strengths around 2000 G, which have a higher radiative output than pixels with field strengths closer to 1000 G.

6.3.3 Radiative Behavior of Magnetic Structures

Given the previous results suggesting that differences in the emergent intensity as a function of magnetic field strength lie within the magnetic structures, we examine the radiative output of structures as a function of their size. The size of the structure can help determine the balance of the efficiency of lateral heat flux from the sidewalls compared with the suppression of convective flux. Due to limited resolution of simulations and observations, many analyses of the intensity of magnetic elements assume that magnetic structures are tubes (known as flux tubes) embedded in the photosphere. Therefore, the size of a magnetic structure is taken as the effective radius of the roughly circular cross-section at the photosphere. As seen in Figure 6.1, the magnetic structures simulated at high spatial resolution range form tubes to elongated sheets within the downflow lanes. Therefore, the assumption of a flux tube breaks down at high resolution and the effective radius approach would incorrectly estimate the size of the elongated structures if the cross-sectional size is important.

For long sheet-like magnetic structures, we are interested in the width perpendicular to the midline of the downflow lane, which we will call the characteristic width. This width indicates the space between adjacent granules occupied by the structures. We therefore take an alternative approach to estimating the characteristic width by using two easily-measured quantities of a magnetic structure — the perimeter, P, and area, A. We then apply a simple argument to determine the effective width of a structure based on these quantities. If the structures are roughly represented by circles, one can determine the simple relationship for the characteristic width of the photospheric cross section, $w_c = 4\mathrm{A}/\mathrm{P}$, while the effective radius would derive $w = 2r = 2\sqrt{A/\pi}$. While this estimation is somewhat crude, it does introduce another measurable parameter (the perimeter) to constrain the width unlike the effective radius method which only uses the area. The advantage of

introducing the perimeter in this method is that it returns a value heavily weighted towards the smallest dimension, which in general gives the width of the magnetic structure within the downflow lane. Furthermore, if the structure cross-section is better approximated by a long rectangle, the maximum error made in the characteristic width would be a factor of 2 whereas the effective radius method has an unbounded error.

Using the structure identification scheme described previously, shown in Figure 6.3, we identify large and small magnetic structures and compute the area as the sum of pixels contained in a single structure. We compute the perimeter using the same structure identification and applying a binary erosion[1] algorithm to each structure individually. Using a mask image of each structure, the algorithm removes all adjoined pixels on the mask border where the number of removed pixels approximates the perimeter in pixels. We show the average magnetic structure intensity and vertical magnetic field for all magnetic structures in the LD and MF and show them as a function of w_c in Figure 6.5. The vertical dashed line represents the characteristic width of the downflow lanes. Since the downflow lanes appear as elongated structures, we estimate the characteristic width as w_c = 2A/P as would be derived for a long rectangle. Note for small magnetic structures in both the MF and LD simulations that the intensity increases with increasing width. This also corresponds to an increase in the magnetic flux of the element. As the characteristic width of the magnetic structure increases further, the average intensity of the structure begins to reduce while the average magnetic flux of the structure continues to increase.

Despite the crudeness of this estimation, it is interesting to note that the downturn in average magnetic structure intensity occurring at roughly w_c = 150 km coincides with the value of the average characteristic width of the downflow lanes calculated with the area and perimeter scheme. This suggests that once the characteristic width of the magnetic structures are roughly the width of the downflow lanes, the presence of the magnetic field begins to modify the surrounding convection patterns. In Figure 6.5, the behavior of the LD and MF small magnetic structures agree closely with both the average intensity and magnetic flux, showing an increase in average intensity with

[1] From the Scipy ndimage package: docs.scipy.org/doc/scipy/reference/ndimage.html

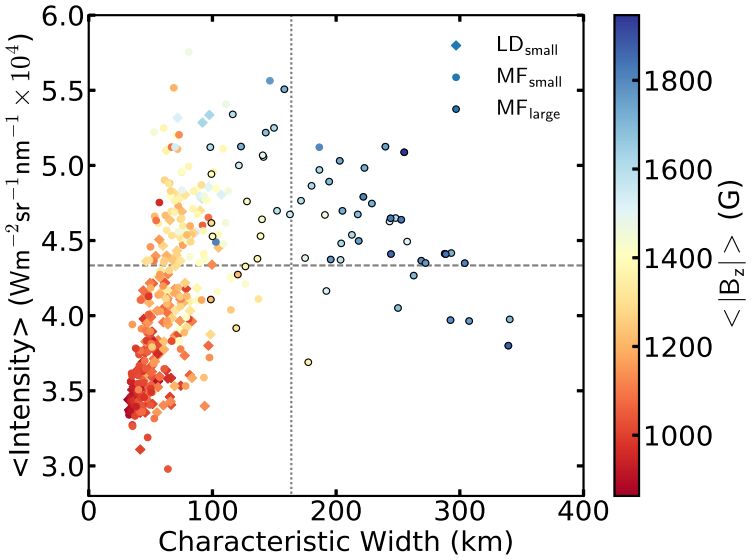

Figure 6.5: Average intensity of a magnetic structure as a function of characteristic width. The color bar denotes the magnetic flux of the element (average magnetic field of the element at τ_{500} = 1). LD small and MF small and large elements are denoted by triangles, circles, and outlined circles, respectively. Horizontal dashed line represents the average intensity of the LD and MF atmospheres, while the vertical dashed line represents the characteristic width of a downflow lane. Note that the downturn of the intensity corresponds roughly with the size of the characteristic width of downflow lanes.

increasing width and magnetic flux. The large MF structures, however, decrease in intensity with increasing size and flux. This suggests that the radiative differences between the atmospheres results from the presence of large magnetic structures in the MF simulations which do not exist in the LD simulations.

We examine this further by removing the large structures from the analysis of pixel intensity with B_z. We recreate the plots of Figure 6.2 excluding the large magnetic structures in the MF simulation which is shown in Figure 6.6. As shown, removal of the large magnetic structures from the MF simulations results in the emergent intensity as a function of B_z for the LD and MF simulations to exhibit the same trend, confirming that the reduction in the average intensity for large B_z in Figure 6.2 is due to the large structures, which have a different dependence of intensity with magnetic field compared to small magnetic structures.

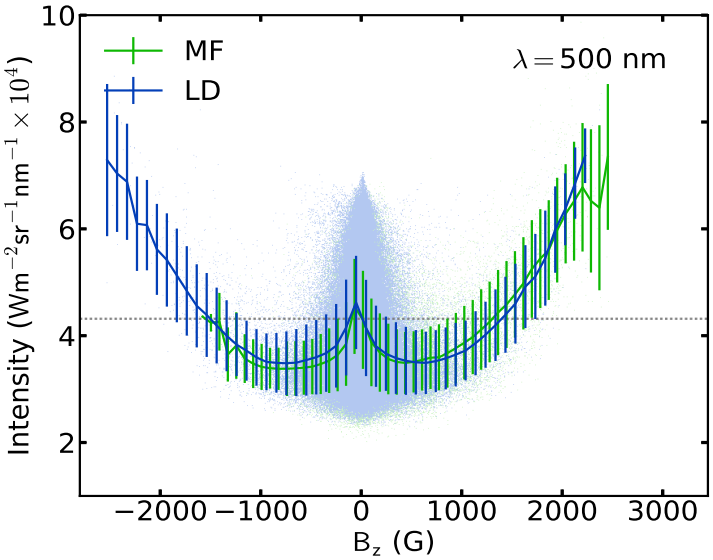

Figure 6.6: Emergent intensity as a function of vertical magnetic field strength for all pixels in the LD (blue) and MF (green) simulations except those corresponding to large magnetic structures (greater than 560 pixels). Note that removing the large magnetic structures results in improved agreement between the MF and LD simulations compared to Figure 6.2.

6.4 Atmospheric Profiles

We now turn our attention to understanding the physical properties that result in differences between large and small magnetic structures seen in Figure 6.5. In particular, we are interested in understanding the role of suppression of convection due to the presence of the magnetic field, as this has been attributed to the reduced brightness of magnetic elements in environments with differing average magnetic field strength (Kobel et al. 2012; Criscuoli 2013). In this section, we compare the atmospheric stratifications of small and large magnetic structures in the two simulations. We primarily analyze temperature and velocity profiles as these roughly indicate the thermal heating and the strength of convection, respectively.

6.4.1 Properties of Weakly Magnetized Structures

Prior to comparing the atmospheric profiles of the magnetic structures, we first analyze the behavior of the weakly magnetized regions surrounding the magnetic structures — the upflows and

downflow lanes. This step is necessary to verify that the magnetic structures are not influenced by different environments. We compute the vertical stratifications of the temperature and vertical velocity from the LD and MF simulations as a function of the optical depth τ_{500} given by RH. The results are shown in Figure 6.7. As shown, the temperature and velocity profiles of the granule upflows and downflow lanes, excluding magnetic structures, in the two atmospheres are nearly identical. This is consistent with the results of the previous section showing that the radiative

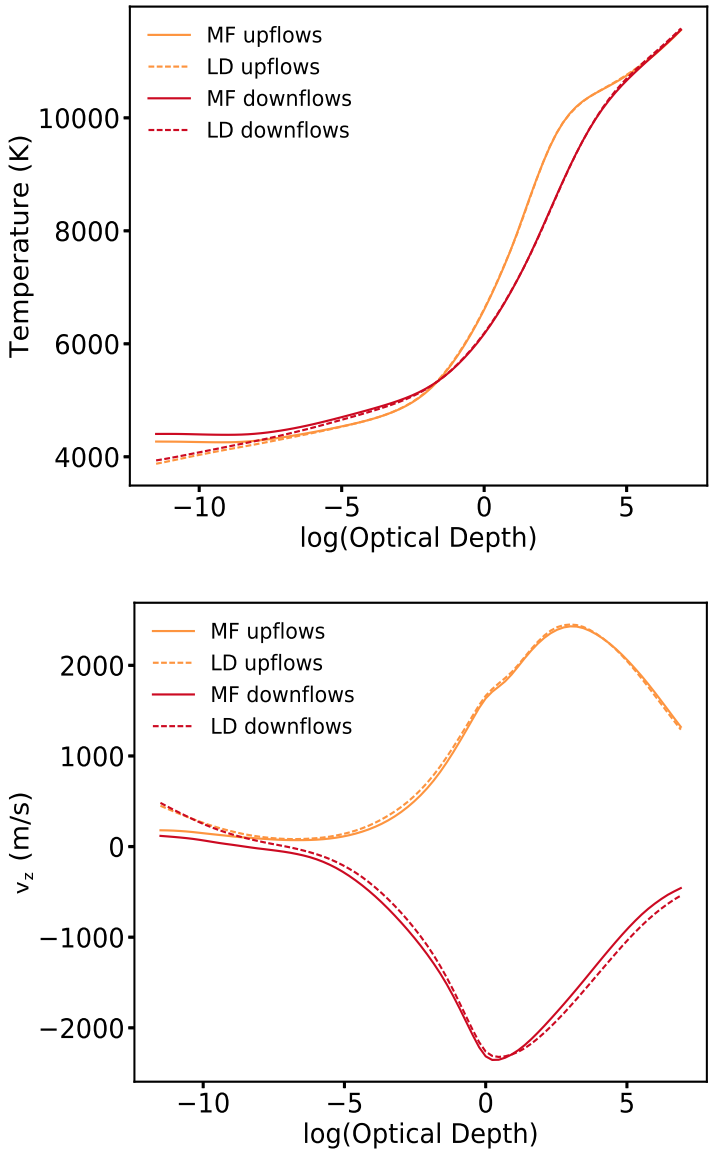

Figure 6.7: Temperature (top) and vertical velocity (bottom) stratifications in upflows (orange) and downflow lanes (red) for the MF (solid) and LD (dashed) simulations.

output of weakly magnetized regions similar in the two atmospheres. The differences in the thermal properties of magnetic structures is not due to differences in the average properties of their weakly magnetized surroundings.

6.4.2 Properties of Magnetic Elements

In the previous section, we demonstrated that the formation of magnetic structures with larger characteristic width in the MF simulation is responsible for the differences in radiative output of high magnetic field pixels between the two simulations. We now compare the differences in the atmospheric profiles of pixels with equivalent magnetic field strength embedded in large and small magnetic structures. As in Section 6.4.1, we compare the temperature and vertical velocity with optical depth for the LD small and MF small and large magnetic elements. To isolate the radiative differences at large B_z seen in Figure 6.2, we further bin the magnetic elements into $|B_z|$ bins ranging from 750 G to 2000 G. The results are shown in Figure 6.8.

As shown in the top panel of Figure 6.8, the temperature near the photosphere of the small LD and MF magnetic elements agree closely for pixels with similar magnetic flux density. The large magnetic structures, on the other hand, have a lower temperature, and a shallower gradient near the photosphere. Note that for all $|B_z|$ bins, the temperature gradient flattens near $\tau_{500} = 1$ for pixels of increasing $|B_z|$. This flattening of the gradient in the photosphere is consistent with the results of Criscuoli & Uitenbroek (2014) showing decreased temperature gradients with increased magnetic flux in a simulation atmosphere.

The bottom panel of Figure 6.8 shows pronounced differences in the vertical velocity for pixels in small and large magnetic elements. For pixels with low $|B_z|$ in both large and small magnetic structures, the vertical velocity profiles are roughly equivalent. For pixels with higher $|B_z|$, the profiles differ in their trends. For large magnetic elements, the downflow velocity is significantly reduced in pixels of increasing vertical unsigned magnetic field strength at all depths whereas small MF elements have reduced vertical velocity only near $\tau_{500} = 1$. The small LD elements have the opposite trend where the vertical velocity is enhanced with increased $|B_z|$, likely suggesting that

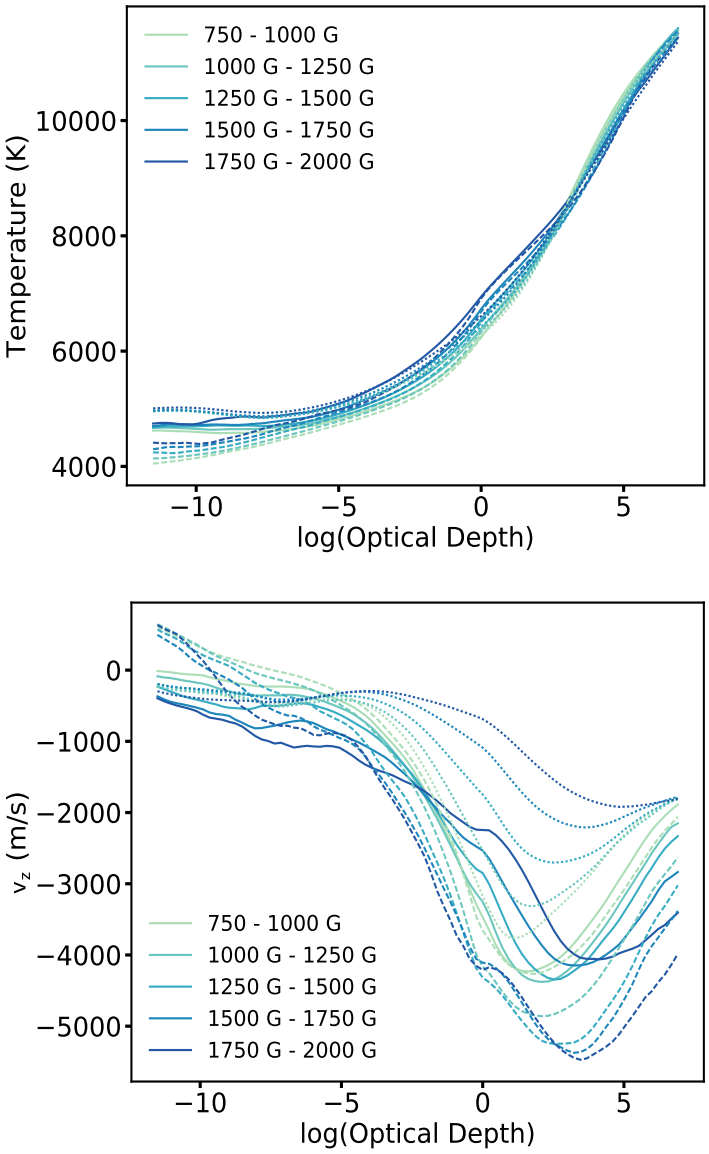

Figure 6.8: Temperature (top) and vertical velocity (bottom) stratifications in LD small (dashed), MF small (solid), and MF large (dotted) structures binned by magnetic field strength.

the higher magnetic field pixels are more likely to accumulate in stronger downflows. These trends indicate that the small magnetic structures in both the MF and LD simulations have a negligible role on the suppression of convection, while the suppression of convection in large magnetic structures increases with increasing pixel magnetic field strength.

The top panel of Figure 6.9 shows the unsigned vertical magnetic field as a function of depth for the same bins of magnetic field in large and small magnetic structures. At large optical depth, the unsigned vertical magnetic field in the large structures remains much larger than that in small structures of equivalent magnetic field strength in the photosphere. This indicates that the magnetic field of the large magnetic structures permeates deeper into the domain, and further supports the notion that convection is more suppressed in large magnetic structures compared to small ones. The bottom panel of Figure 6.9 shows the τ_{500} formation height as a function of depth for the magnetic field bins of large and small structures. The formation heights of the small MF and LD structures closely agree at optical depth unity and deeper. The large magnetic structures, however, have a deeper formation height for all optical depths.

6.4.3 Estimating the Role of Convective Flux

Finally, we further investigate the role of the suppression of convection on the reduced intensity in large magnetic structures compared to small ones. To achieve this, we estimate the convective flux and compare this for different the magnetic elements using the characteristic width derived in Section 6.3.3. The convective flux is the internal energy of a system plus work as transported by the convective motions. To estimate the convective flux, we start from Equation 5.3. Rewriting this equation in terms of the internal energy density plus the kinetic and magnetic energy densities yields:

$$\frac{\partial}{\partial t}\left(\frac{1}{2}\rho\mathbf{v}^2 + e + \boldsymbol{B}^2/2\mu\right) = -\nabla\cdot\left[\left(\frac{1}{2}\rho\mathbf{v}^2 + e + P + \boldsymbol{B}^2/2\mu\right)\mathbf{v} + \boldsymbol{E}\times\boldsymbol{B}/\mu\right] - \nabla\cdot\boldsymbol{F}_{\rm rad} - \nabla\cdot\boldsymbol{F}_{\rm visc} + \rho\mathbf{v}\cdot\boldsymbol{g}, \tag{6.1}$$

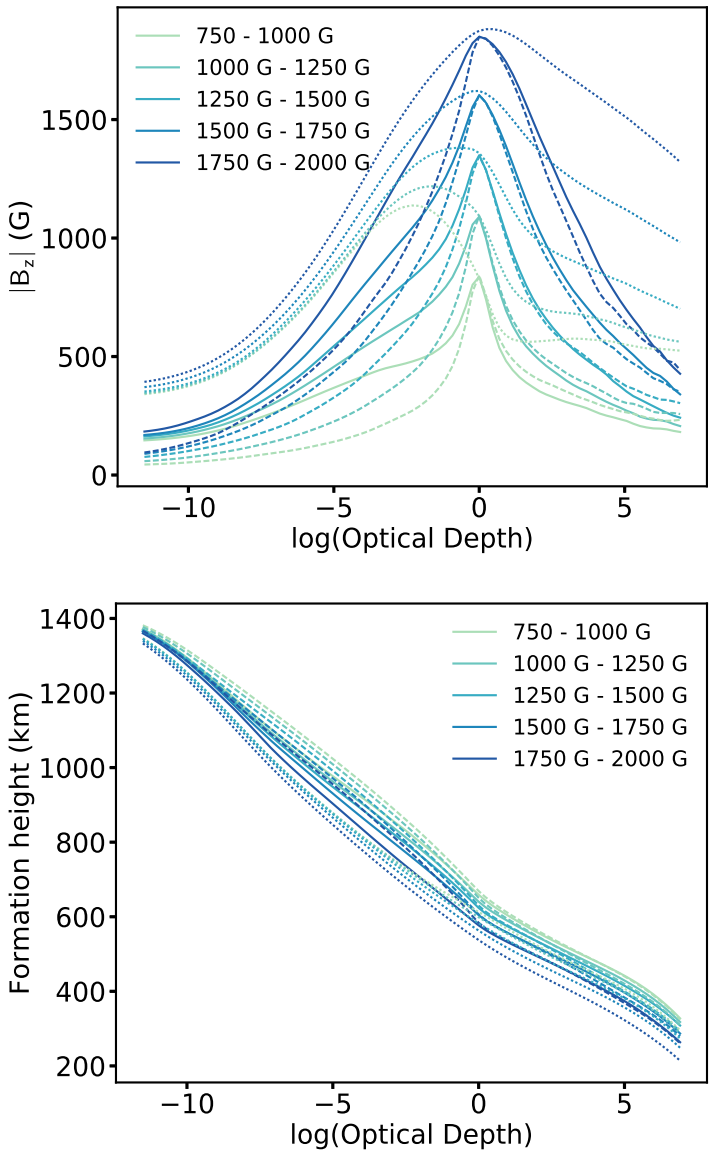

Figure 6.9: Vertical magnetic field (top) and τ_{500} formation height (bottom) stratification in LD small (dashed), MF small (solid), and MF large (dotted) structures binned by magnetic field strength.

where μ is the permeability. Since enthalpy, h, is the internal energy density plus P, one obtains:

$$\begin{aligned}\frac{\partial}{\partial t}\left(\frac{1}{2}\rho\mathbf{v}^2 + e + \boldsymbol{B}^2/2\mu\right) &= -\nabla\cdot\left(\frac{1}{2}\rho\mathbf{v}^2\mathbf{v} + h\mathbf{v}\right) - \nabla\cdot\boldsymbol{F}_{\rm rad} - \nabla\cdot\boldsymbol{F}_{\rm visc} + \rho\mathbf{v}\cdot\boldsymbol{g} \\ &= -\nabla\cdot\left(\boldsymbol{B}^2\mathbf{v}/2\mu\right) - \nabla\cdot\boldsymbol{F}_{\rm conv} - \nabla\cdot\boldsymbol{F}_{\rm rad} - \nabla\cdot\boldsymbol{F}_{\rm visc} + \rho\mathbf{v}\cdot\boldsymbol{g}, \qquad (6.2)\end{aligned}$$

where

$$\boldsymbol{F}_{\rm conv} = \frac{1}{2}\rho\mathbf{v}^2\mathbf{v} + h\mathbf{v}. \qquad (6.3)$$

Next, we derive an expression for enthalpy. In the solar photosphere, the internal energy of the fluid carried by convection is the thermal energy of the particles plus their ionization potential. For a partially ionized fluid consisting of N_p ionized Hydrogen, N_H total Hydrogen atoms, and N $= N_H + N_e$ total particles, the enthalpy density is given as,

$$\begin{aligned}h = e + P &= \frac{n_H}{N_H}\left[\frac{3}{2}NkT + N_p\varepsilon_H + PV\right] \\ &= n_H\left[\frac{3}{2}(1+x)kT + x\varepsilon_H + (1+x)kT\right] = n_H\left[\frac{5}{2}(1+x)kT + x\varepsilon_H\right], \qquad (6.4)\end{aligned}$$

where $x = n_p/(n_H + n_p)$ is the ionization fraction, n_H is the Hydrogen density, and ε_H is the ionization energy of Hydrogen. From the Saha ionization equation for an ionized plasma, x is given by

$$\frac{x^2}{1-x} = \frac{1}{n_H}\left(\frac{2\pi m_e kT}{h^2}\right)^{3/2} e^{\varepsilon_H/kT}. \qquad (6.5)$$

Combining Equations 6.4 and 6.5 results in a solution to the enthalpy flux (Equation 6.3).

Figure 6.10 shows the perturbation of the vertical convective flux estimate relative to the geometric mean binned by the characteristic width of the structure as was done in Figure 6.5. After computing the perturbation to the vertical component of the convective flux at geometric layers, the values were interpolated onto the $\tau_{500} = 1$ surface. As shown, the average vertical convective flux perturbation from the mean for small structures has a large spread in values compared to that of large structures. As the characteristic width of the magnetic structure increases, the convective flux tends towards zero, indicating that the convection is less effective compared to that of small

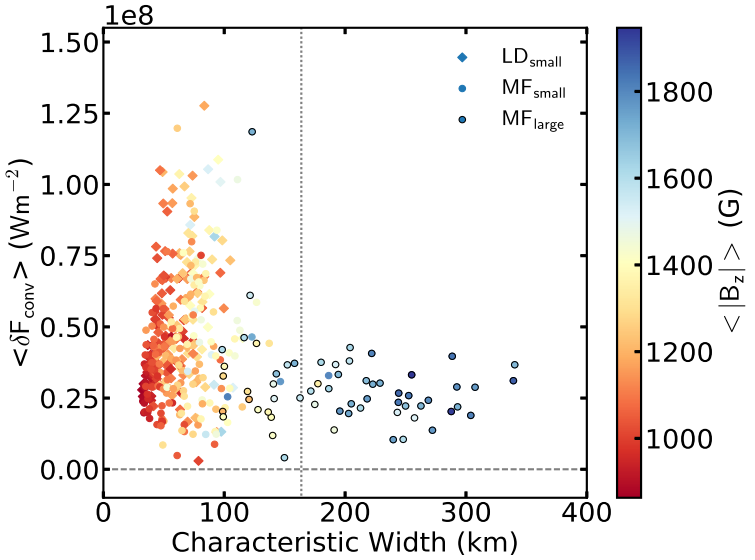

Figure 6.10: Average perturbation of the vertical convective flux of a magnetic structure as a function of characteristic width. The color bar denotes the magnetic flux of the element. LD small and MF small and large elements are denoted by triangles, circles, and outlined circles, respectively. The vertical dashed line represents the characteristic width of a downflow lane. Note that the convective flux tends towards zero as the characteristic width of the magnetic structure increases.

structures. While the values shown are estimations of the convective flux, the trends shown indicate that suppression of convective flux is more prevalent in larger structures compared with smaller ones.

6.5 Discussion and Future Outlook

In this chapter, we used two simulations of equivalent magnetic field strength but differing morphologies to analyze the effect of magnetic field morphology on the radiative output of quiet sun magnetic structures. The MF simulation represents predominantly vertical magnetic field strength, whereas the LD simulation represents an isotropic magnetic field of mixed polarity. We synthesized the emergent intensity in the simulations at $\lambda = 500$ nm for the vertical line-of-sight and compared this to the magnetic flux density at τ_{500} =1. We demonstrated that the radiative output for high magnetic field pixels differed between the two simulations, and that this difference can be attributed to the presence of large magnetic structures in the MF simulation which are absent from the LD

simulation.

Comparing the emergent intensity as a function of vertical magnetic field strength in Figure 6.2 indicated that the MF and LD simulation differed in their high magnetic field pixels, where the LD was on average brighter than that of the MF. We then showed in Figure 6.5 that this difference is attributed to the large magnetic structures which form in the MF simulation but not in the LD simulation. We further demonstrated that the radiative behavior of the LD and MF atmospheres were equivalent if the large magnetic structures were excluded from the analysis (Figure 6.6). These results suggest that the magnetic field strength of a given pixel is less important than the size of the structure in which it is embedded, which is in agreement with proposed causes of enhanced quiet sun magnetism compared to that within an active region (Kobel et al. 2011; Criscuoli 2013). These results strongly support that the size of a magnetic structure (width perpendicular to the downflow spine) is an important feature in contributions to irradiance

The shape of the average magnetic structure intensity as a function of the characteristic width within the downflow lanes may provide further insight into the behavior of magnetic structures based on size. For example, the location of the knee in Figure 6.5 may demonstrate a characteristic of when convective suppression begins to overtake the brightness of a magnetic structure. Given that the knee in this figure corresponded with the width of the downflow lane, it may indicate that convection remains vigorous until the magnetic structure fills the downflow lane and begins to act on the neighboring granules. Similarly, the rate that intensity decreases with increasing characteristic width may also indicate a property of the magnetic structures, such as how deep they permeate into the downflow lane. A more careful analysis of the correlation of radiative output with structure size is warranted under a broader range of simulated atmospheres and is the subject of future work. Such a study could help us understand the relationship between size and intensity of magnetic elements particularly in the low resolution limits that are used to infer irradiance trends from irradiance models.

The turnover of the emergent intensity as a function of magnetic structure size in Figure 6.5 has not been clearly seen in simulations or observations, and can help improve our understanding of

the drivers of changes in radiative output. Spruit & Zwaan (1981) showed the reduction in intensity with increasing magnetic structure size for structures larger than roughly 100 km, however other results do not show this reduction (Wiehr et al. 2004; Viticchié et al. 2010). The rise in intensity for small magnetic structures has been observed in G-band bright points (Viticchié et al. 2010), although without the corresponding reduction seen here. This may result from differing wavelengths analyzed. Criscuoli (2013) showed qualitatively similar results, but with much lower resolution of the structure sizes and using a circular cross-section approximation for the magnetic structure sizes. However, caution must be exercised in evaluating the intensity as a function of characteristic width particularly in the limit of structures with small areas. For example, some work has shown magnetic structures viewed on the photosphere to have patterns consistent with fractals (see e.g., Balke et al. 1993; Meunier 1999; Abramenko 2005; Criscuoli et al. 2007). The characteristic width method would break down if this were true, particularly at increasing resolution. Similarly, some work has shown that the estimated size of the smallest structures (below roughly 500 pixels^2) may include effects from pixelization that makes the inferred size susceptible to large errors (Criscuoli et al. 2007). Similarly, the threshold used to identify a structure as well as spatial resolution could play a non-neglible role in the inferred width as well. These potential issues should be analyzed in detail using shapes with known perimeters and widths.

Finally, we analyzed the atmospheric profiles within magnetic structures to understand the source of the different behaviors with increasing structure size. We showed that the temperature and velocity stratifications of the weakly magnetized regions (upflows and downflow lanes) were equivalent between the two simulations. This indicates that the differences in radiative behavior of the magnetic structures in the two atmospheres is not likely resulting from differences in their interaction with the neighboring plasma. We compared the vertical velocity profiles of small and large magnetic structures as a function of unsigned vertical magnetic field strength. We showed that the vertical velocities of the small structures in the MF and LD simulations had qualitatively similar behavior of the profiles with optical depth and increased magnetic flux, however the profiles for large magnetic structures showed a clear dampening of the vertical velocity with increased magnetic field

strength. This strongly suggests that suppression of convective flux plays a large role in the large magnetic structures and results in the reduced intensity as a function of increased characteristic width. Similarly, the unsigned vertical magnetic field in the large structures permeates deeper into the photosphere than for that of the small structures. This suggests that as magnetic field concentrates into magnetic elements, they eventually become large enough to suppress convective flux resulting in their reduced intensity.

The results of this work suggest that the magnetic morphology for equivalent magnetic field simulations likely plays a negligible role in modifying the radiative output, and that the formation of magnetic structures of varying sizes is more important. In this work, we estimated the convective flux in a given structure showing that the size of the structure reduced the convective flux. To further understand the balance of convective flux and radiative heating laterally from the sidewalls of the magnetic structures, these quantities should be analyzed more rigorously using the parameters calculated directly in the solution to the MHD equations. This is the subject of future work. In particular, this may help understand the meaning of the turnover in the intensity as a function of width and the balance of the convective and radiative fluxes. This may provide further understanding of the role of magnetic structure size and radiative output beyond the flux tube model.

Chapter 7

Effect of Magnetic Field Morphology on Inferred Irradiance Trends

7.1 Introduction

Spectral solar irradiance (SSI) and its variations play an important role in the chemistry and absorption processes of Earth's atmosphere. Due to the strong wavelength dependence of interactions in Earth's upper atmosphere especially near the UV portion of the spectrum, monitoring SSI variations is necessary to constrain atmospheric climate models. While intensity variations in the UV portion of the spectrum have been measured regularly since 1978 (see e.g., Deland & Cebula 2008), measurements over a large range of wavelengths (300 to 2400 nm) only recently began with observations by the Spectral Irradiance Monitor (SIM) (Harder et al. 2005) onboard the Solar Radiation and Climate Experiment (SORCE) (Rottman et al. 2005). Monitoring these wavelengths is necessary to quantify the solar energy that reaches Earth's surface and its influence on, for example, oceanic heating. The lack of spectral and temporal coverage of SSI observations has led to the development of semi-emperical irradiance models, which relate SSI variability to the passage of bright and dark magnetic structures across the solar disk.

Measurements and model results demonstrate that the SSI variability with the 11 year solar magnetic activity cycle depends strongly on the wavelength observed. UV wavelengths, for example, are generally seen to vary in phase with the solar cycle, while IR wavelengths vary out of phase. The relative variability of these wavelengths as well as the sign of the variability in the visible wavelengths, however, remains a point of disagreement between the measurements and models (see e.g., Ermolli et al. 2013, for a review of SSI measurements, models, and their discrepancies).

Measurements from SIM suggest that the visible wavelengths vary out of phase with solar cycle, which has been corroborated by simulation results by Criscuoli & Uitenbroek (2014). While ground-based observations by Preminger et al. (2011) demonstrated an out-of-phase variation of the visible continuum, results from Peck & Rast (2015) presented in Chapter 2 showed that such trends lie within the sensitivity of the quiet sun background reference. Results from the spectral irradiance models SATIRE (Krivova et al. 2003; Ball et al. 2011) and NRLSSI (Lean 2000; Lean & DeLand 2012), however, find these wavelengths to vary in phase with the solar cycle. These results in turn have been corroborated by space-based observations by Wehrli et al. (2013). The disagreements between models and measurements demonstrate the limitations of the current understanding of the drivers of SSI variations.

Semi-emperical irradiance models reconstruct the solar irradiance based on the passage of magnetic structures across the disk using either magnetogram images or proxy measurements. Each identified structure (e.g., faculae, sunspots, and quiet sun) is assigned a 1D atmospheric model which is used to synthesize the emergent intensity. The contribution based on the number density of each structure is summed to infer the SSI over a time series, where the spectrally integrated irradiance is tuned to match observations of the total solar irradiance (TSI). This method inherently assumes that variations in the photospheric magnetic flux is the underlying cause of solar irradiance variations. Magnetic flux is likely present at all spatial scales, where the smallest concentrations of magnetic flux may not be accurately accounted for in irradiance models. The low contrast magnetic regions within the quiet sun likely have unresolved magnetic substructure (Livingston & Harvey 1971), which has been seen in observations of quiet sun magnetism (e.g., Lin & Rimmele 1999; Domínguez Cerdeña et al. 2003; Harvey et al. 2007; Lagg et al. 2010). Given that the quiet sun contributes substantially to the total solar surface magnetic flux (Sánchez Almeida 2004; Domínguez Cerdeña et al. 2006), the underlying contribution from the quiet sun magnetism may play a role in SSI variations that are currently not captured by irradiance models.

The radiative variability of the quiet sun has been examined in previous studies. Ortiz (2005) studied the visible continuum variability of the quiet sun using MDI onboard SOHO, finding no

change in the radiative output over time, while (Ermolli et al. 2003) found signature of variability using ground based measurements from PSPT. Results from Peck & Rast (2015) presented in Chapter 2 demonstrated that the contribution of the quiet sun magnetic field to solar cycle irradiance variations is difficult to constrain in photometric measurements due to both its intrinsic low contrast and influence on the background center-to-limb variation (CLV) profile against which the contrast is measured. Furthermore, recent observations indicate the likely presence of various magnetic morphologies within the quiet sun (Harvey et al. 2007; Lites et al. 2008; Ishikawa & Tsuneta 2009; Danilovic et al. 2010b; Stenflo 2010; Lites 2011). The effect of the quiet sun magnetic morphology on radiative output may not be captured by a single atmospheric profile ascribed by irradiance models.

In the previous chapter we analyzed the effect of magnetic field morphology on the radiative output for the vertical line-of-sight of quiet sun magnetism. We used a mean field (MF) simulation with predominantly vertical magnetic field and a local dynamo (LD) simulation with isotropic magnetic field of mixed polarity. The LD simulation reproduces properties consistent with observations of quiet sun magnetic field thought to be generated by a local turbulent dynamo (see Danilovic et al. 2010b; Rempel 2014, and Table 5.1). Despite having equivalent magnetic field strength but differing morphologies, we demonstrated that the radiative output of the two simulations differed between pixels of equivalent magnetic flux density, with the radiative output at 500 nm of the LD simulation higher than that of the MF simulation. The differences were attributed to the presence of larger magnetic structures in the MF simulation. Pixels of equivalent magnetic field strength in large magnetic structures have reduced radiative output compared to those found in smaller magnetic structures. This is likely due to enhanced suppression of convective energy flux by the larger magnetic structures.

Given an understanding of the sources of radiative differences, we now aim to assess the potential impacts of magnetic field morphology on the inferred radiative output of the disk-integrated quiet sun. We analyze the effect of magnetic field morphology on the center-to-limb contrast of quiet sun magnetic structures pre- and post-image degradation, using the same simulations as in

the previous chapter and discussed in Chapter 5. We then analyze the potential impact of the two quiet sun magnetic field morphologies on inferred irradiance by comparing the relative differences in the disk-integrated spectral irradiance derived from the two simulations and from two quiet sun atmospheres used in some irradiance models.

7.2 Simulations and Spectral Synthesis

To understand the radiative output of the two simulated atmospheres, we synthesize the emergent intensity across continuum wavelengths over the solar disk. The spectral synthesis is performed using the RH radiative transfer solver (Uitenbroek 2001; Pereira & Uitenbroek 2015). For computational tractability, we select 17 wavelengths ranging from the visible to the UV and corresponding to the SORCE/SIM bandpass. The selected wavelengths (λ = 400, 500, 514, 629, 743, 858, 972, 1104, 1235, 1367, 1498, 1630, 1789, 1947, 2106, 2264, and 2423 nm) were also used in Criscuoli & Uitenbroek (2014). We focus on these continuum wavelengths which form in LTE as they correspond to the wavelengths where SORCE/SIM disagrees with models and contribute roughly 50% to the TSI and 30% to its solar cycle variations (e.g., Krivova et al. 2006). For comparison of the magnetic field strength in the simulations with those derived from observations, we compute the line-of-sight magnetic field at the $\tau_{500} = 1$ surface, which roughly corresponds to the height at which magnetometers observe the magnetic field components.

In order to compute the center-to-limb intensity and disk-integrated spectral irradiance, the spectral synthesis must be computed across the solar disk. We selected 10 viewing angles of $\mu = 1.0$, 0.945, 0.887, 0.825, 0.757, 0.683, 0.600, 0.503, 0.383, and 0.2 — where μ is the cosine of the viewing angle known as the heliocentric angle. These values were chosen such to represent 10 equal-area annuli across the solar disk between $0 < R_\odot < 0.980$. The use of equal-area annuli ensures straightforward intensity integration across the disk where all viewing angles contribute equal weight to the sum. The spectral irradiance for a given wavelength is then computed as the average emergent intensity of all 10 viewing angles for each atmosphere scaled by the angle subtended by the solar disk as seen at Earth. This summation implicitly assumes that the quiet sun covers the full solar

disk in order to assess the irradiance implications of differing magnetic substructures.

From the analysis by Peck et al. (2017a) presented in Chapter 4, the short-characteristics method results in spatial smearing of the emergent intensity solution. Since RH utilizes the short-characteristics method and we are interested in comparing high-resolution simulations to observations, this diffusion error must be avoided by pre-tilting the atmosphere prior to computing the radiative transfer solution. In contrast to a radiative transfer using the method of long-characteristics, pre-tilting is advantageous for large simulations since RH1.5 in its current form is capable of efficient domain decomposition by computing the radiative transfer for vertical rays through an atmosphere (see Chapter 8 for a discussion of implementing pre-tilted atmospheres directly into MHD solvers).

To pre-tilt the atmosphere, we chose to keep the z dimension grid spacing and the number of horizontal pixels in the tilted atmosphere unchanged from the untilted atmosphere. This was primarily done for simplicity in the analysis, where any grid spacing could in theory be chosen (although large grid spacings could result in under-sampling the atmospheric parameters). We use a bilinear interpolation to generate the tilted atmospheres. Such an approach makes this method fundamentally different from many long-characteristics solvers which typically restrict interpolation to the horizontal or vertical grid lines. We also restricted the tilting to a single axis, which allows for easy parallelization to compute the tilted atmosphere. Due to the large domain size of the atmospheres, the interpolation was divided onto multiple processors. An example of the original and pre-tilted grid (for temperature) is shown in Figure 7.1 for an angle of $\mu = 0.6$.

Using the pre-tilted atmospheres, we synthesize the emergent intensity at all wavelengths and viewing angles of interest. The emergent intensity for $\lambda = 500$ nm is shown in Figure 7.2 for 5 viewing angles (0.383, 0.600, 0.757, 0.887, and 1.000) for a snapshot of the LD and MF simulations. The limb darkening due to observing the optical depth unity surface higher in the atmosphere for inclined viewing angles discussed in Chapter 3 is visually apparent. Note that the emergent intensity for inclined viewing angles preserves the spatial resolution.

To compare our simulations with full-disk observations of the quiet sun, we require that the magnetic field strength be measured at the resolution of the magnetograms used by irradiance

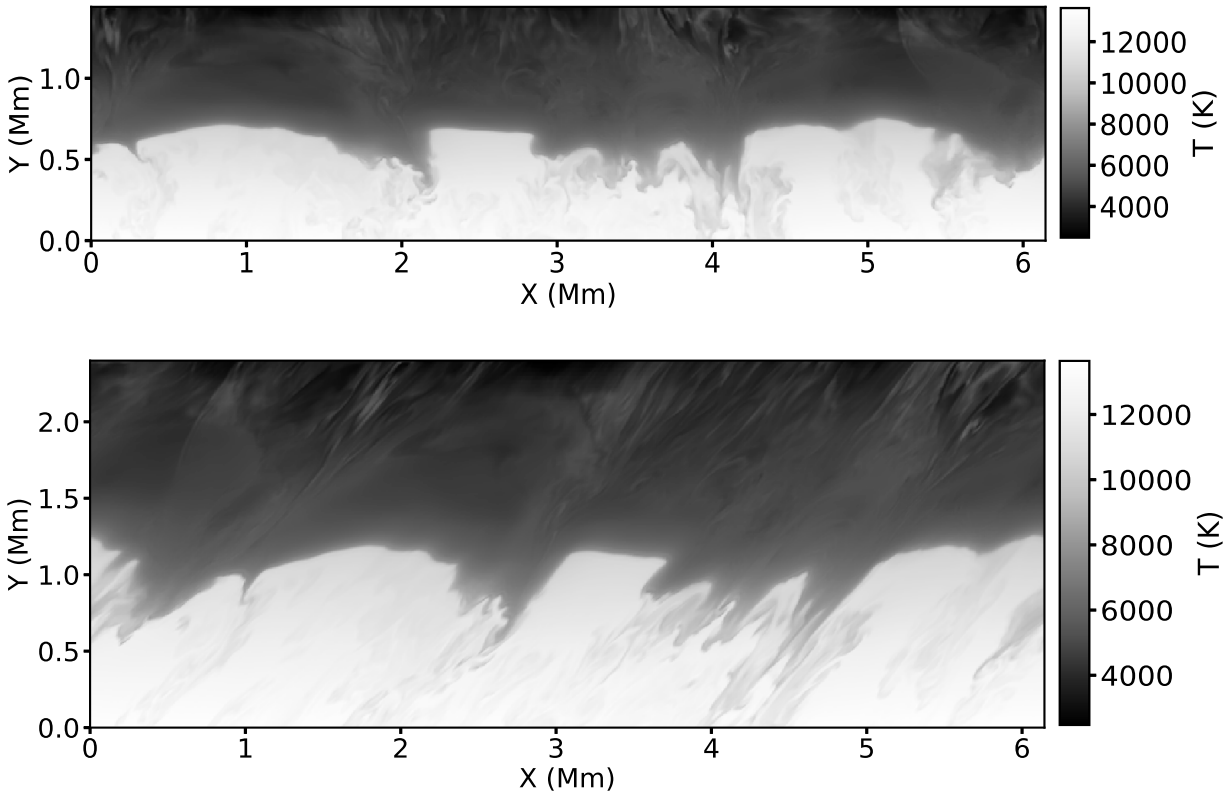

Figure 7.1: Example of a 2D vertical slice of the temperature profile with height in an MHD simulation. Top: Original un-tilted atmosphere. Bottom: Pre-tilted atmosphere inclined to mimic a viewing angle of $\mu = 0.6$.

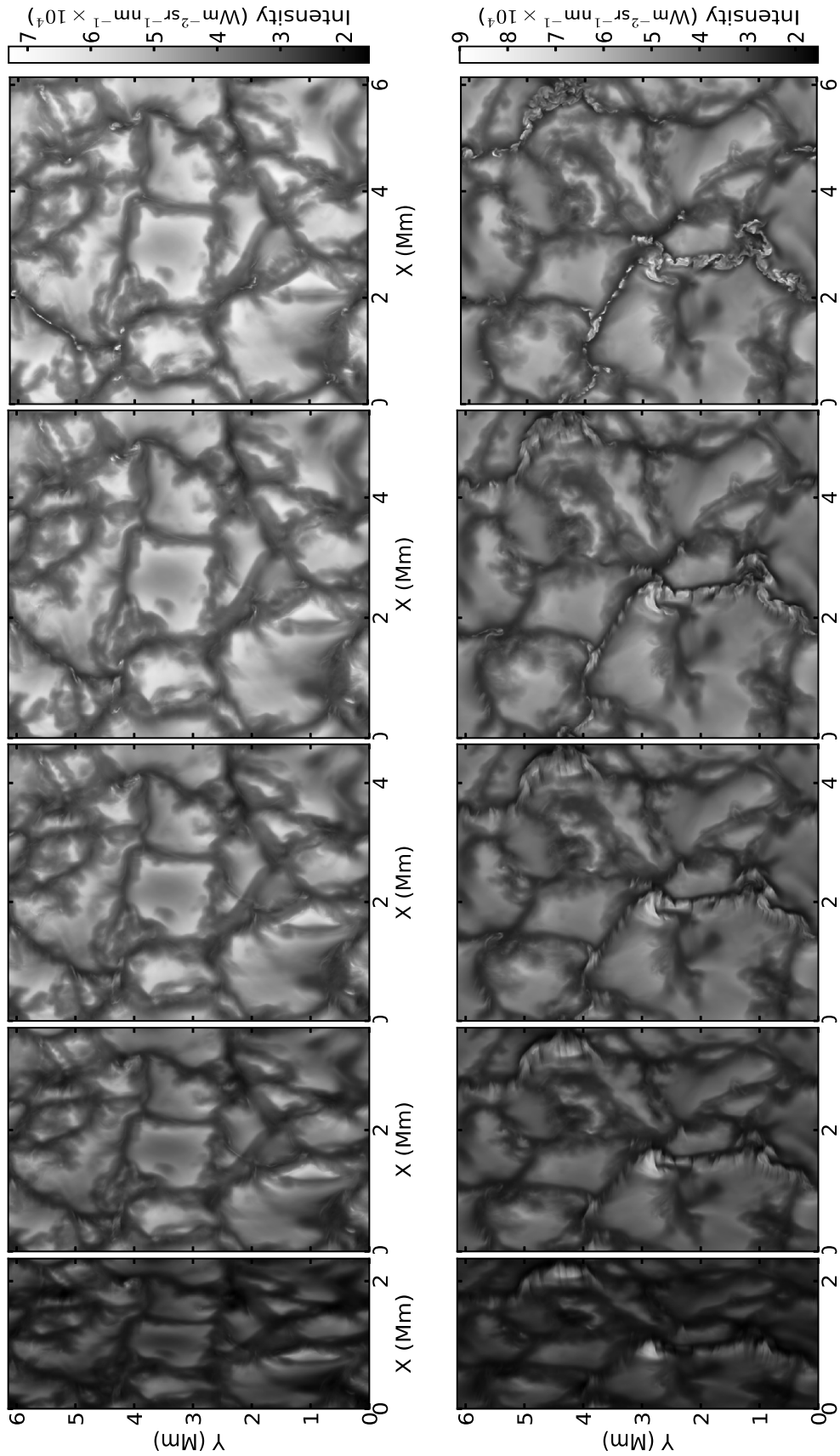

Figure 7.2: Emergent intensity for LD (top) and MF (bottom) for heliocentric angles of $\mu = 0.383$, 0.600, 0.757, 0.887, and 1.000 (from left to right, respectively). The limb darkening discussed in Chapter 3 is visually apparent in these images.

models. We therefore convolve the magnetic field of our simulations with the point-spread-function of a 1 arcsecond resolution telescope. The convolution is performed on the line-of-sight magnetic field for all viewing angles. The results for a snapshot representing $\mu = 1.0$ of the LD and MF simulations are shown in Figure 7.3. Magnetic structures are not well-resolved by full-disk images. In the LD simulations, the magnetic structures are not resolved due to both the presence of the

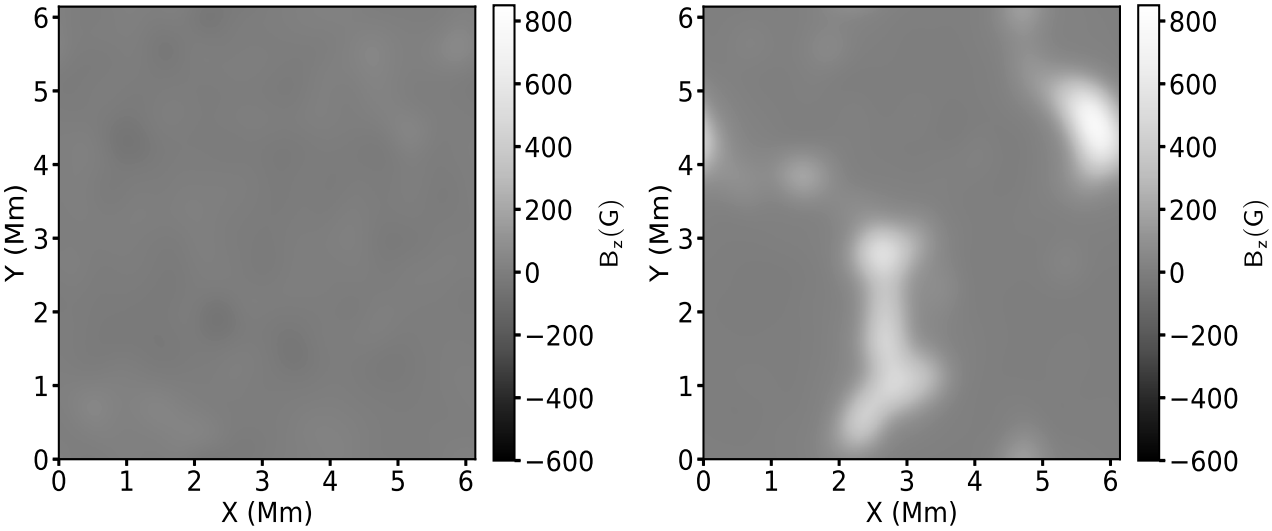

Figure 7.3: Signed line-of-sight magnetic field for $\mu = 1.0$ for a snapshot of the LD (left) and MF (right) atmospheres at the $\tau_{500} = 1$ surface convolved to 1 arcsecond resolution consistent with full-disk observations.

mixed polarity field and the small size of the magnetic structures. The MF magnetic structures are partially resolved, but their spatial extent increases under the convolution. In this work, we identify the quiet sun as all pixels in the convolved magnetic field image with $|B_z| < 50$ G. We then use the fully-resolved underlying intensity of these pixels to calculate the radiative output of the quiet sun pixels.

Due to the lack of radiometrically accurate measurements, observations use intensity contrast measurements to compare the emergent intensity of features on the solar disk for different spatial and temporal images. The contrast measurements require a definition of a background to measure each intensity image against, which is assumed to be unchanged between observations (see Chap-

ter 2). The emergent intensity of the background as a function of disk position (or CLV) is used to normalize the emergent intensity of the observation. In full-disk observations, the CLV is typically computed using the most weakly magnetized pixels on the disk. As an analog for simulations, we measure contrast relative to the non-magnetic hydrodynamic (HD) simulation center to limb profile. Therefore, the average intensity contrast of each atmosphere is

$$C(\lambda, \mu) = \frac{< I_{MF/LD}(\lambda, \mu) >}{< I_{HD}(\lambda, \mu) >} - 1 \ , \tag{7.1}$$

where the average is taken over all pixels in all 10 snapshots of each simulation for a given wavelength and viewing angle.

7.3 Results

7.3.1 Center-to-Limb Contrast at High and Low Spatial Resolution

To understand the effect of convolution on the center-to-limb variation of the quiet sun, we compare the center-to-limb radiative outputs of pixels designated as quiet sun in the two simulations pre- and post-convolution of the magnetic field observed at the $\tau_{500} = 1$ surface. Figure 7.4 shows the intensity and intensity contrasts averaged over all 10 snapshots for the LD and MF atmospheres as a function of wavelength and viewing angles for the original image and the pixels identified using the convolved line-of-sight magnetic field threshold of 50 G. While the differences in the absolute intensities between the two atmospheres are small, the intensity contrast shows the differences between the intensities more clearly.

There are several notable features in the center-to-limb variations of the fully resolved simulations (left panels). First, is the variation as a function of viewing angle. As shown for all wavelengths in the bottom panel of Figure 7.4, the LD atmospheres have a shallower intensity contrast as a function of viewing angle than the MF atmospheres. This is in agreement with simulation results from Criscuoli & Uitenbroek (2014), who found steeper intensity contrast for higher $< B_z >$ (where we showed previously that LD has 0 G and MF has 78 G in Table 5.1). The increase in intensity contrast from the center-to-limb is also in qualitative agreement with observations of low

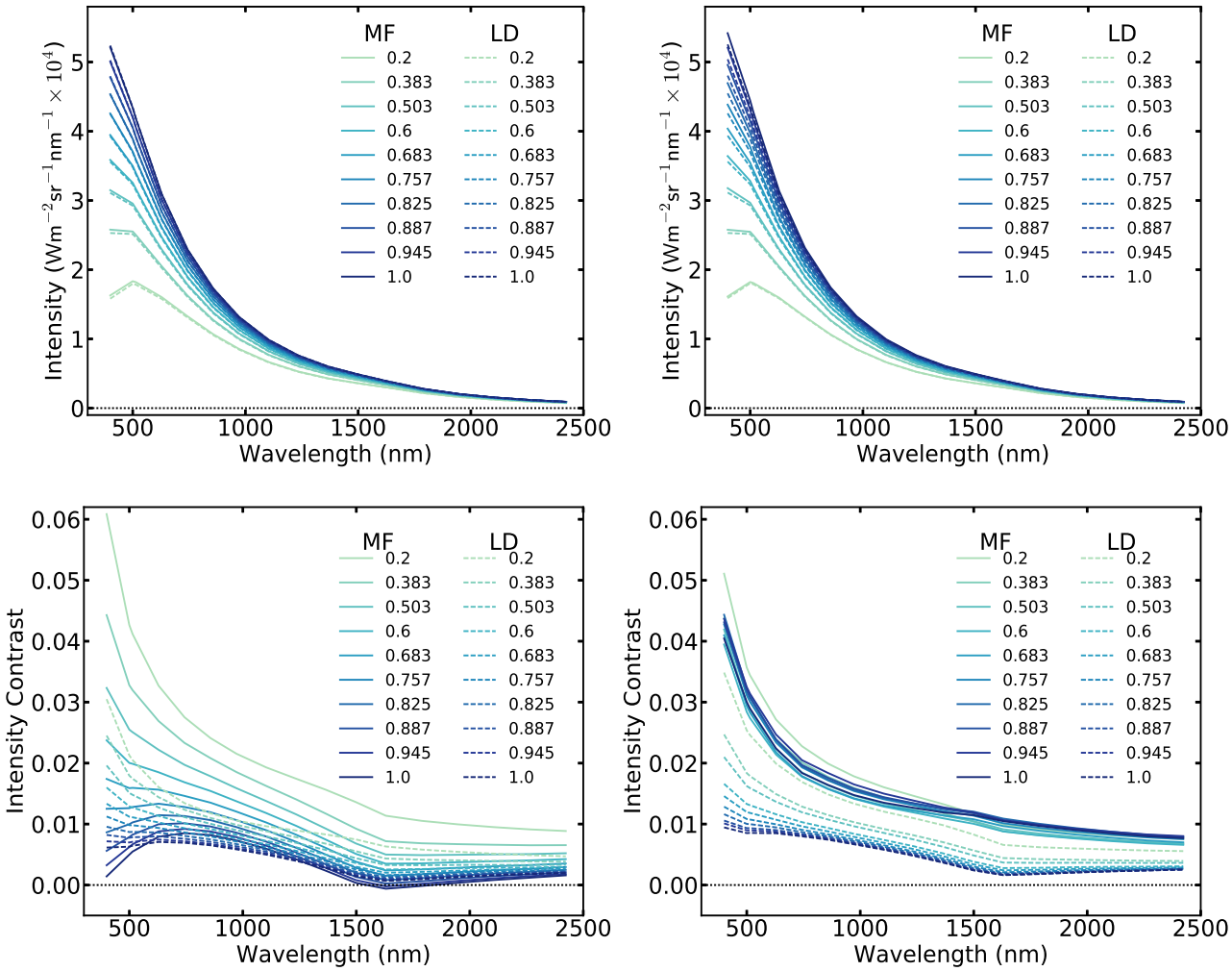

Figure 7.4: Emergent intensity (top) and intensity contrast (bottom) as a function of wavelength and viewing angle for the LD (dashed) and MF (solid) atmospheres. Left: Pre-convolution center-to-limb variation using all pixels in the domain. Right: Post-convolution center-to-limb variation using only pixels with a convolved line-of-sight magnetic field less than 50 G.

magnetic flux pixels (Ortiz et al. 2002; Afram et al. 2011; Yeo et al. 2013; Criscuoli et al. 2017). Second, is the center-to-limb variation as a function of wavelength. The shape of the intensity contrast for each viewing angle as a function of wavelength for the LD and MF simulations differ, where the MF simulation roughly mimics the shape of the H^- opacity curve (see Figure 3.5). Since the intensity contrast is measured relative to the HD simulation, the lack of a clear H^- opacity curve in the LD simulation when measured relative to the HD simulation indicates that the two atmospheres have more similar thermal properties compared with the MF simulations (as differences in temperature result in changes in the H^- opacity). In contrast to the results from Criscuoli & Uitenbroek (2014), the intensity contrasts of all wavelengths shorter than 1500 nm are positive where their results found negative contrast for wavelengths below 500 nm.

The intensity contrasts for pixels identified as quiet sun using the convolved line-of-sight unsigned magnetic field threshold of less than 50 G are shown on the right of Figure 7.4. While the change in the intensity again appears small, there is a large change in the intensity contrast under the magnetic threshold. Note that the convolution of the MF simulation near the vertical line-of-sight results in a higher intensity contrast compared to the fully-resolved intensity contrast. The effect of the magnetic field threshold also results in a shallower center-to-limb contrast compared to the fully-resolved contrast for the MF simulation. These effects are due to the removal of the bright magnetic structures which reduces the intensity contrast, however the preferential removal of the neighboring downflow lanes due to the convolution process results in a net increase in contrast. The LD, in contrast, shows little change under the convolution except at highly inclined viewing angles. This is caused by the presence of smaller magnetic structures in the LD simulation compared to the MF simulation, which do not greatly increase the spatial extent of the magnetic structures under convolution. This results in fewer pixels removed when applying the magnetic field threshold after convolution from the LD simulation for near vertical lines-of-sight compared to the MF simulation. The fraction of pixels removed as a function of viewing angle for the two simulations is shown in Figure 7.5. The MF simulation has a larger fraction of pixels removed near the vertical lines-of-sight compared to the LD due to the presence of large structures in the MF simulation. With

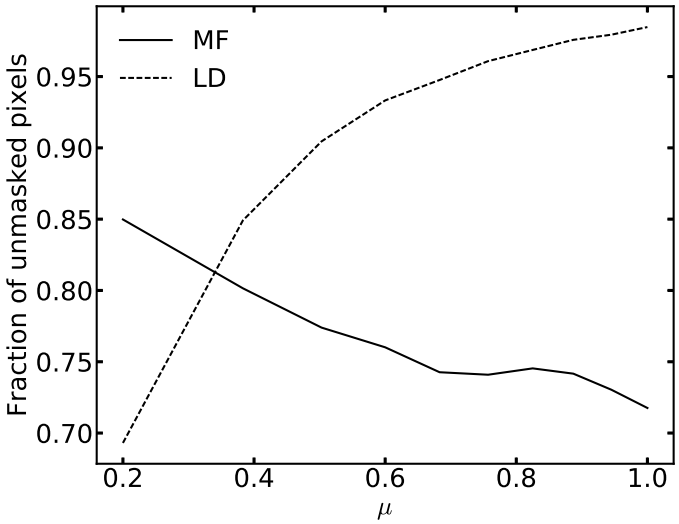

Figure 7.5: Quiet sun identified pixels as a function of viewing angle for LD (dashed) and MF (solid) atmospheres. These pixels were those identified as having a unsigned line-of-sight magnetic field lower than 50 G when the magnetic field at $\tau_{500} = 1$ was convolved to 1 arcsecond resolution. Note that MF simulation has fewer unmasked (quiet sun identified) pixels near $\mu = 1$ compared to the LD. Viewed away from disk center, the fraction of unmasked pixels in the MF simulation increases while the LD simulation decreases.

increasingly inclined viewing angle, the fraction of pixels removed between the two simulations have opposing trends. The increase in the fraction of pixels removed in the LD simulation results from the stronger horizontal magnetic field compared to the MF simulation, which is projected along the line-of-sight for inclined viewing angles.

7.3.2 Comparison of Spectral Irradiance Calculated from Simulations and Irradiance Model Atmospheres

The differences in the intensity contrasts for the quiet sun identified pixels (using the convolved line-of-sight magnetic field threshold of 50 G) shown on the right of Figure 7.4 suggests that the spectral irradiance inferred for the quiet sun likely differs between the two simulations. We therefore analyze the effect of the two magnetic morphologies on the inferred spectral irradiance and compare the results with those obtained from the 1D quiet sun atmospheres used in irradiance models and measurements from SORCE/SIM. We use the pixels in the LD and MF simulations

identified as quiet sun from the convolved magnetic field threshold and compute the average quiet sun emergent intensity for each simulation at each viewing angle and wavelength. For the quiet sun irradiance derived from models, we selected the Kurucz quiet sun model used in SATIRE (Kurucz 1992; Unruh et al. 1999) and the FALC model used in SRPM (Fontenla et al. 1991). The temperature as a function of optical depth of the model atmospheres are shown as the dotted and dashed black lines, respectively in Figure 7.6. The average temperature as a function of optical

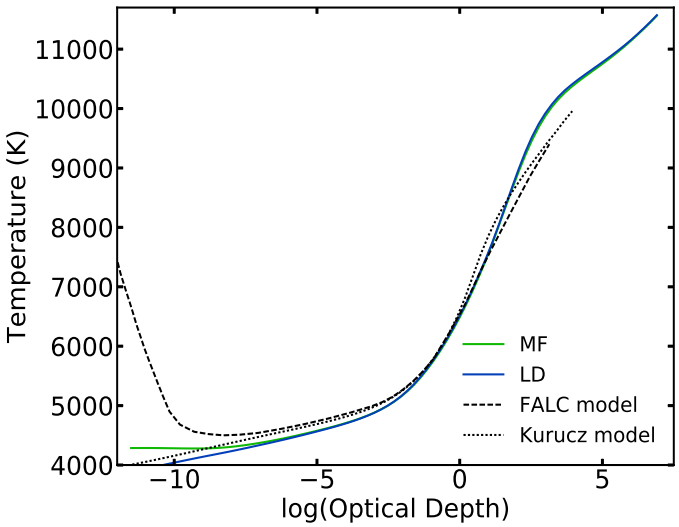

Figure 7.6: Temperature stratifications for quiet sun pixels identified in the LD (blue) and MF (green) simulations convolved to 1 arcsecond resolution. The threshold magnetic field strength for quiet sun pixels was $|B_z| < 50$ G. Also shown are the Kurucz quiet sun (dotted black) and FALC (dashed black) 1D model atmospheres. FALC model includes a chromosphere, resulting in the increase in temperature at small optical depths.

depth for the pixels identified as quiet sun using the convolved magnetic field threshold are also shown for the MF (green) and LD (blue) simulations. As shown, the $\tau_{500} = 1$ temperature for all atmospheres are roughly the same, but the models have differing temperature gradients into the photosphere. The increase in temperature at small optical depths in the FALC model is due to inclusion of a chromosphere in the model. To compare the simulation results with the quiet sun model atmospheres used in these irradiance models, we synthesize the emergent intensity using RH from the 1D quiet sun model atmospheres at the same wavelengths and viewing angles described previously. We then sum the contribution of the emergent intensity across the disk for the simula-

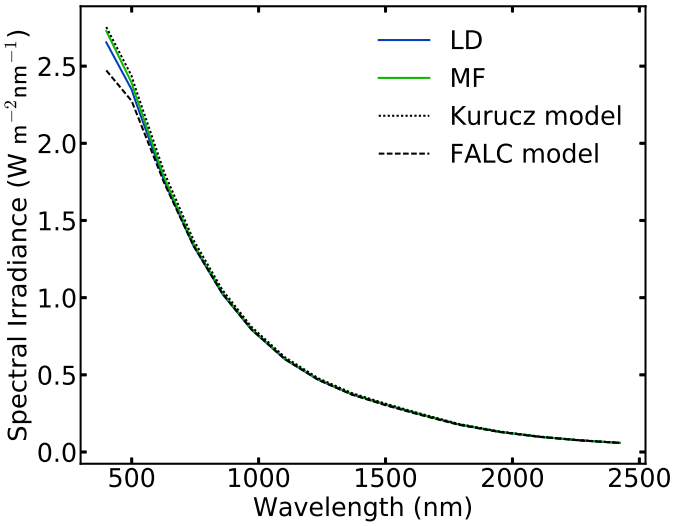

Figure 7.7: Spectral irradiance computed for LD (blue) and MF (green) quiet sun pixels compared with the Kurucz (dotted black) and FALC (dashed black) 1D quiet sun models. The spectral irradiance as shown here assumes that the entire solar disk is covered in quiet sun.

tion and model results to obtain the spectral irradiance that would be measured at Earth. This is shown as a function of wavelength in Figure 7.7 for the quiet sun identified pixels in the LD and MF simulations and the two irradiance model atmospheres. As shown, the spectral irradiance of the simulations and models differ most at wavelengths in the visible portion of the spectrum and shorter. The spectral irradiance derived from the LD and MF quiet sun identified pixels lie within the range of the results from the two quiet sun models.

Note that the differences between the models and simulations are all wavelength dependent. The wavelength dependence differences in the spectral irradiance inferred from the simulations and models indicate that wavelength dependent error could be introduced into the inferred spectral irradiance variability through the use of an incorrect quiet sun model. To test this, we estimate the potential error in SSI variability introduced through a given atmosphere (model or simulation) assuming that the solar cycle variability of the quiet sun results only from changes in number density of the quiet sun pixels. We assume the change in number density increases by roughly 10% from solar maximum to solar minimum (see e.g., Fontenla et al. 2011), and estimate the absolute error as the difference between the 'truth' and model SSI multiplied by the fractional

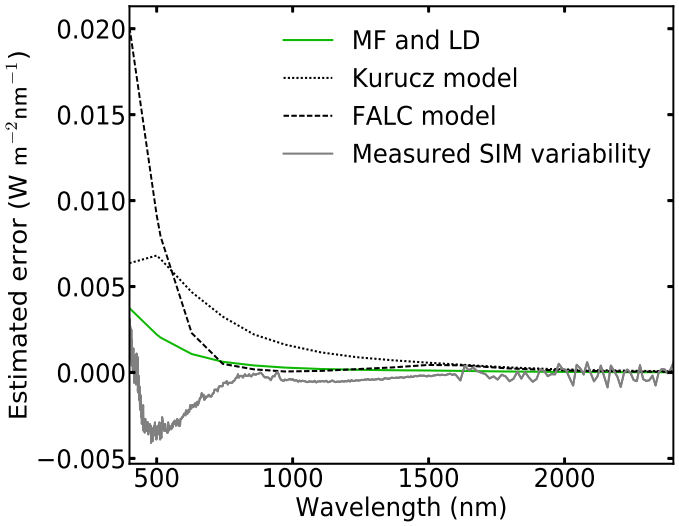

Figure 7.8: Estimated absolute error in SSI variability (solar maximum - solar minimum) between simulations and models. The estimation assumes the solar surface changes filling factor of quiet sun by 10% between solar maximum and solar minimum. Error computed relative to the average of LD and MF simulation results. Green line shows the error when using either the MF or LD simulation compared with their average.

change in number density. For simplicity, we assume the 'truth' is given by the average spectral irradiance of the LD and MF simulations. The results are shown in Figure 7.8 including the SSI variability measured by SIM [1] . As shown, all error estimates are wavelength dependent. The FALC model shows the largest variability over the solar magnetic activity cycle, but the amplitude of the difference between it and that derived from the average of the MURaM simulations is comparable to the solar cycle variability measured by SORCE/SIM. The latter is also true of the Kurucz model. Thus, the difference between spectral irradiance trends inferred using models and those measured by SORCE/SIM may lie within the uncertainty of the quiet sun contribution to the spectral irradiance.

7.4 Discussion and Conclusions

We have compared the center-to-limb distributions of the LD and MF simulations, as well as the integrated spectral irradiance for pixels in the simulations identified as quiet sun. To identify the quiet sun pixels in the two simulations, we convolved the line-of-sight magnetic field with

[1] Variability measured for solar cycle 23 using SIM version 22 data. Data courtesy of Jerry Harder.

the point-spread-function of a 1 arcsecond resolution telescope. Quiet sun pixels are taken to be those with an unsigned line-of-sight magnetic flux less than 50 G, as is typical when analyzing observations. Using these pixels, the spectral irradiance of the quiet sun from the LD and MF simulations was then compared to the spectral irradiance derived from the quiet sun atmospheres used in the SRPM and SATIRE irradiance models, and the wavelength-dependent error introduced into the SSI variability was estimated.

The results in Figure 7.4 demonstrated the effect of image convolution, through the identification of pixels considered to be part of the quiet sun, on the inferred center-to-limb contrast of the quiet sun. They show that the center-to-limb profile of the MF simulation changes significantly as a result of the convolution. This is caused by the removal of pixels corresponding to the magnetic regions and the surrounding downflow lanes. The removal results in an increased brightness of the MF simulation due to preferentially removing more downflow lanes. The presence of larger magnetic structures would likely have a larger effect on the center-to-limb contrast as the structures would appear darker and their stronger magnetic fields would result in removing more downflow lanes in the convolved magnetic field threshold. While the results of the convolved center-to-limb variation qualitatively agrees with observations (Ortiz et al. 2002; Afram et al. 2011; Yeo et al. 2013; Criscuoli et al. 2017), the shapes of the full-resolution center-to-limb variation do not agree well with simulation results from Criscuoli & Uitenbroek (2014). Further investigation is necessary to understand the source of the differences in the profile, whether they lie in the difference in MHD codes used for the simulated solar surface or a difference in number density of bright and dark structures due to differing mean vertical magnetic field in the simulation domains.

We showed that the LD and MF atmospheres had differing temperature stratifications compared with the 1D quiet sun atmospheres used in two irradiance models, particularly in the region just below optical depth unity. The results in Figure 7.8 indicate that irradiance models could potentially introduce error in the variability of the spectral irradiance with the solar cycle through the use of an incorrect quiet sun model atmosphere. The differences introduced due to the two magnetic morphologies also introduce differences in the spectral irradiance variability on the order

of the total variability measured by SORCE/SIM. Increasing the vertical magnetic field in the domain would likely enhance these differences between the morphologies due to both the formation of larger magnetic structures with a reduced intensity compared to smaller structures and the larger spatial extent of the quiet sun mask under convolution. The spectral variability of the quiet sun must be investigated in more detail. Upcoming observations from DKIST may help understand the physical properties of the quiet sun (temperature, B_z, etc.), which are currently unresolved. This will provide a means to further understand the filling factor of different magnetic morphologies, as well as refine irradiance modeling techniques through the use of more physically realistic model atmospheres.

To improve the realism of irradiance modeling, some effort has focused on using 3D MHD simulations rather than 1D models (Yeo et al. 2017). This requires creating a lookup table of 3D MHD atmospheres convolved to the resolution of the magnetogram used to identify magnetism on the surface (typically 1 arcsecond for HMI). The spectrally resolved emergent intensity for the MHD simulation matched to the observed magnetic field over the solar disk are then integrated to give the spectral irradiance. Such an approach is more realistic than 1D atmospheric models since it takes the multicomponent nature of the atmosphere into account (Uitenbroek & Criscuoli 2011). However, such a model still relies on the assumption that magnetism on the solar disk fully accounts for irradiance trends. This has been shown to be adequate for total solar irradiance on timescales of approximately a solar cycle where magnetism reproduces 95% of the irradiance variations (e.g., Ball et al. 2012), but it is not known if this holds for spectral irradiance variations or for long-term irradiance variations, for which measurements are limited. To avoid bias from a priori assumptions about the effect of magnetism, irradiance must be understood from a physical standpoint rather than an observational one. This requires understanding the physical processes which underly irradiance variations. This work demonstrates that magnetic morphology and the density of magnetic structures of various spatial extend may play a role in spectral irradiance variations that are not accounted for in irradiance modeling. Future work should analyze this effect further under a larger array of 3D simulations of differing magnetic field morphologies.

Chapter 8

Influence of Speckle Image Reconstruction on Photometric Precision for Large Solar Telescopes

Our work in the previous chapters suggests that radiative differences in the quiet sun are likely due to the formation of magnetic structures of various sizes. Current solar observations, however, lack sufficient spatial resolution to observe the magnetic field or photometric properties of quiet sun magnetic structures smaller than approximately 100 km observed at $\lambda = 500$ nm. Understanding the effect of the quiet sun magnetic field on the solar radiative output shown in the simulations analyzed in the previous chapters therefore requires sufficiently high resolution observations and photometric precision to observe the quiet sun magnetic field and infer the radiative output. Observations from the upcoming 4 meter Daniel K. Inouye Solar Telescope and the European Solar Telescope will provide images of the solar surface and magnetic field with roughly 16 km spatial resolution in the visible continuum. These observations can be used to compare the emergent intensity synthesized from MHD models and improve our understanding of the radiative output of the quiet sun.

This work analyzes the expected photometric precision of amplitude reconstructed solar images calibrated using models for the on-axis speckle transfer functions with input parameters derived from adaptive optics (AO) control data. This study provides the first assessment of the anticipated photometric precision of images to be obtained with 4-meter class solar telescopes using an AO system and post-facto image reconstruction techniques. A formal derivation and description of imaging through a turbulent atmosphere is provided in Appendix B. This chapter is based on work

published in Peck et al. (2017b)[1] and is a restatement of that paper. C. L. Peck improved the accuracy of the reconstruction algorithm by identifying sources of error in the numerical solution, performed the simulation calculations, and analyzed the results. The coauthors provided guidance during the project and feedback on the paper. The reconstruction algorithm as presented in this chapter was written by F. Wöger and the atmospheric simulations were generated by J. Marino.

8.1 Introduction

The next generation of solar telescopes, including the currently under-construction 4 m Daniel K. Inouye Solar Telescope (DKIST, Elmore et al. 2014; Tritschler et al. 2016) and the upcoming 4 m European Solar Telescope (EST, Collados et al. 2013; Matthews et al. 2016), will observe the solar surface with unprecedented ∼15 km resolution in the visible spectrum, constituting a near threefold improvement over current solar telescopes. Achieving diffraction-limited resolution requires correction of seeing degradation due to Earth's turbulent atmosphere using an AO system. AO correction, however, remains only partial due to the limited bandwidth of the AO system's control loop and the finite number of sensing and correcting elements in the system. Furthermore, outside the isoplanatic path, the wavefront remains largely uncorrected because of the spatial decorrelation of atmospheric turbulence at different viewing angles. Multi-conjugate adaptive optics (MCAO) offer the potential to overcome the latter issue (e.g., von der Lühe et al. 2005; Berkefeld et al. 2006; Schmidt et al. 2017), but residual errors will always be present to some degree. Reaching the diffraction limit both inside and outside the isoplanatic patch, therefore requires post-facto image reconstruction techniques such as Multi-Object Multi-Frame Blind Deconvolution (e.g., van Noort et al. 2005) and speckle interferometry, the latter of which is the focus of this work.

Speckle image reconstruction utilizes a sequence of short exposure images – a speckle burst – to reconstruct the unperturbed source image. Since the atmosphere typically evolves on much smaller timescales than solar structures (∼10 ms and 100 s, respectively), image exposures on the

[1] Peck, C. L., Wöger, F., & Marino, J. 2017, Influence of Speckle Image Reconstruction on Photometric Precision for Large Solar Telescopes, Astronomy and Astrophysics, 607, A83

order of atmospheric evolution timescales capture the turbulent motion of the atmosphere over the stationary source. Each burst image contains some information on small-scale atmospheric structures, which is severely attenuated for long-exposure images. Using a collection of short-exposure burst images, the small-scale structure of the source can be recovered by separately reconstructing the source's Fourier phases and amplitudes. The Fourier phases are estimated using the Knox-Thompson cross-spectrum (Knox & Thompson 1974) or triple-correlation bispectra (Lohmann et al. 1983), which show good convergence for the solar case (de Boer et al. 1992; Wöger et al. 2008). The Fourier amplitudes are reconstructed using Labeyrie's method (Labeyrie 1970), and are the focus of this work.

Fourier amplitude reconstruction requires knowledge of the speckle transfer function (STF), which includes individual contributions from the telescope, AO system, and atmosphere over the speckle burst. Generally, the telescope can be well-characterized, but the atmospheric and AO system contributions to the STF must be estimated or measured directly. Since solar observations cannot make use of calibration stars as done in night-time astronomy, the atmospheric contribution to the STF is estimated by modeling the index of refraction fluctuations due to turbulence and their effects on image quality. These turbulence effects can be characterized by a single parameter known as the Fried parameter (Fried 1966a), r_0, which quantifies the strength of the atmospheric turbulence. Given an estimate of r_0, the atmospheric STF can be solved analytically (Korff 1973). For observations using an AO system, the atmospheric STF is modified to include the partial wavefront compensation through AO performance characteristics that estimate the wavefront correction (Wang & Markey 1978; Wöger & von der Lühe 2007).

To estimate r_0, von der Lühe (1984) proposed the spectral ratio method, which uses the ratio of the equivalent long-exposure power spectrum to the average short-exposure power spectrum of the images that constitute the speckle burst. This method is currently used in speckle reconstruction algorithms at several ground-based solar observatories with good success (e.g., Mikurda & von der Lühe 2006; Denker et al. 2007; Wöger et al. 2008) and with modifications to include a fixed estimate for partial compensation by an AO system and to account for anisoplanatism (Puschmann & Sailer

2006; Wöger & von der Lühe 2007). However, a systematic study of the influence of the STF input parameters (r_0 and AO performance parameters) on the photometric precision of the reconstructed image is still lacking. Such a study is of particular relevance in light of results from Denker et al. (2007) showing that the estimation of r_0 is impacted by the morphological structure of the scenery observed through azimuthal asymmetry in the image power spectrum and is potentially inaccurate. This image-scene dependence will likely have a greater impact on upcoming high-resolution observations, since the ratio of r_0 to the telescope aperture is smaller and therefore requires a more accurate measurement of r_0.

This paper presents a speckle reconstruction model that estimates r_0 from the AO system control data, which removes the potential of image scene bias in the estimation of r_0. We performed an in-depth study of the sensitivity of the modeled on-axis STF to the r_0 estimate and AO performance parameters applicable for four-meter class solar telescopes. Using simulations of atmospheric turbulence of a known r_0 and a simulated AO system, we computed r_0 and the AO performance parameters using AO system measurements. We then separately varied the input parameters and computed the resulting model STFs. We deduced the sensitivity of the photometric precision to the input parameters by convolving high-resolution solar surface images with the simulated atmosphere-telescope STF and subsequently deconvolving with a model STF and comparing the results with the original image. Section 2 describes the details of the simulations used in this study. Section 3 details the methods used to construct and test the transfer functions. Section 4 describes the results of the sensitivity analysis. Finally, Section 5 discusses the results in the context of future high-resolution observations including extension to MCAO systems.

8.2 Simulations and Analytical Models

In this section, we describe the atmospheric and AO system simulations, as well as the analytical STF model. The atmospheric simulation implements the Kolmogorov power spectrum to simulate wavefront distortions through Earth's atmosphere. The simulated AO system subsequently measures these wavefront distortions with a wavefront sensor (WFS) and creates a post-AO

compensated, or residual, wavefront using a model for the deformable mirror (DM). The WFS measurements and DM actuator commands are used to compute r_0 and the AO performance parameters, which are then input to the model STF.

8.2.1 Atmospheric Simulation

The AO simulations rely on an atmospheric model to reproduce the effects of atmospheric turbulence. The atmospheric model used in our simulations was a simple model composed of a single turbulent layer located at the telescope entrance pupil, which was scaled for Fried parameters of r_0 = 10 cm and 15 cm. The layer is represented by a large phase screen of 8192×8192 pixels that slides across the telescope aperture from right to left to simulate the effect of wind with a constant speed of 5 m s^{-1}. For simplicity, we assumed a constant wind speed throughout the full simulation. The phase screen was computed using a FFT-based method (Johansson & Gavel 1994), which combines a known power spectrum of the phase (Kolmogorov power spectrum) with a random Fourier phase.

This computation method is known to under-represent low spatial frequencies, corresponding to low order Zernike or Karhunen-Loève (KL) modes (for the definition of Zernike or KL modes see e.g., Wang & Markey (1978); Dai (1995)). This effect can be compensated by the addition of low spatial frequency sub-harmonics to the phase. In our case, it was determined that this correction to the phase screen was not necessary because of the small size of the pupil (512×512 pixels) in comparison to the full size of the phase screen. By not adding sub-harmonics to the phase screen we ensured that it remained cyclically continuous and can be tiled to produce an effectively infinite phase screen. These infinite phase screens, where the phase wraps around at the edges indefinitely, can be used to produce very long time series of continuous AO simulations.

8.2.2 Adaptive Optics Simulation

We used a solar AO simulation tool developed at the National Solar Observatory (Marino 2012) to simulate the operation of the AO system currently under development for the DKIST. The AO simulation package provides a flexible environment to simulate any configuration of classical or

multi-conjugate AO systems. It allows an arbitrary number of WFS and active mirrors that can accommodate almost any system configuration. The AO simulation package fully simulates field dependent effects like anisoplanatism. Although, it should be noted that for this study we only considered the on-axis performance of the simulated AO system. The results of this study are then only valid inside the isoplanatic patch, which is typically of the order of 5 to 10″ (Denker et al. 2007).

The simulated AO system for this work replicates the design of the actual DKIST AO system. It consists of a WFS and two active mirrors: a dedicated tip-tilt mirror and a DM. The simulated WFS is a cross-correlating Shack Hartmann (SH) WFS with 1429 sub-apertures placed in a 43×43 square grid. The simulated DM is a continuous face plate mirror with a total of 1516 actuators located in a 44×44 square grid. The DKIST DM is equipped with 1600 actuators, some of which fall outside the DM aperture and are slaved to their nearest neighbors (see e.g., Johnson et al. 2014, and references therein). For simplicity, we ignored these slaved actuators and only included actively controlled actuators. The WFS and DM are placed in the Fried geometry where the actuators of the DM are aligned with the corners of the WFS sub-apertures. Due to the computationally intensive nature of the problem, the code that simulates the solar cross-correlating SH WFS does not actually perform the cross-correlations between the WFS sub-aperture images. Instead, the AO simulation tool computed the average tip and tilt from the phase screen portion in each WFS subaperture to calculate the shift value for that subaperture. Numerical tests validated that this algorithmic simplification produces very similar results to a typical extended source SH WFS.

The simulated AO system must be calibrated before it can be operated. Calibration was performed by measuring the response of the WFS to a set of known inputs placed on the active mirrors, as is normally done in real AO systems. In our simulations, we used KL modes to perform the calibration and built a least-squares wavefront reconstructor using the Moore-Penrose pseudo-inverse (Gavel 2003). The AO control matrix obtained by this process was used to reconstruct the wavefront measured by the WFS. The wavefront was reconstructed as a linear combination of 500 KL modes, which are projected onto the DM actuators. A simulated servo loop integrated the

reconstructed residual wavefront at each iteration to produce an optimal update to the shape of the mirrors.

The simulated AO system operates nominally at a frequency of 2 kHz. We ran our simulated AO system for a total of 10,000 iterations, corresponding to a total simulated time of 5 s. At each iteration we recorded the distorted uncorrected wavefront phase produced by the atmosphere model and the residual phase after correction by the AO system. The uncorrected atmospheric phases provide information about the exact seeing conditions the AO system was attempting to correct, while the residual phases provide information about the quality of the correction supplied by the simulated AO system. The data from the residual phase facilitate the direct computation of the STF and therefore set the 'ground truth' for a test of the analytical STF models and their input.

8.2.3 Analytical Model for Fourier Amplitude Reconstruction

The STF is used in post-facto image reconstruction techniques that require the calibration of the spatial Fourier amplitudes as a step in the reconstruction process. In particular, the Fourier amplitude recovery in a solar speckle image reconstruction is performed using Labeyrie's method (Labeyrie 1970) applied to post-AO corrected burst images $I_j(\vec{s})$ where

$$\langle |I_j(\vec{s})|^2 \rangle = |O(\vec{s})|^2 \times \langle |S_j(\vec{s})|^2 \rangle. \tag{8.1}$$

The spatial power spectrum of the object $|O(\vec{s})|$ can therefore be determined if the STF $\langle |S_j(\vec{s})|^2 \rangle$ is known. Using the definition of the optical transfer function $S(\vec{s})$ and the abbreviation

$$g^{[\prime]+} := g(\vec{r}^{[\prime]} + \frac{1}{2}\vec{s}) \qquad \text{and} \qquad g^{[\prime]-} := g(\vec{r}^{[\prime]} - \frac{1}{2}\vec{s}), \tag{8.2}$$

where g is an arbitrary function, the STF is defined by taking the time average over the residual phase after AO correction, as follows:

$$\begin{aligned} \langle |S(\vec{s})|^2 \rangle = & \int\int d\vec{r}' d\vec{r} W^+ W^- W'^+ W'^- \\ & \times \left\langle \exp\left[-i \left\{ \left(\varphi^+ - \phi^+\right) - \left(\varphi^- - \phi^-\right) \; - \left(\varphi'^+ - \phi'^+\right) - \left(\varphi'^- + \phi'^-\right) \right\} \right] \right\rangle. \end{aligned} \tag{8.3}$$

The phase terms can be represented in terms of basis functions, $M_i(\vec{r})$, that are mutually orthogonal on the (non-complex) aperture function $W(\vec{r})$ as

$$\varphi(\vec{r}) = \sum_{i=2}^{\infty} a_i M_i(\vec{r}) \qquad \text{and} \qquad \phi(\vec{r}) = \sum_{i=2}^{N} \beta_i a_i M_i(\vec{r}). \tag{8.4}$$

Here $\varphi(\vec{r})$ is the phase disturbance of the atmosphere and $\phi(\vec{r})$ is the AO partial compensation to that phase disturbance. The term $a_{\rm i}$ represents the expansion coefficient of the ith mode M_i, and β_i describes the degree of compensation by the AO system, typically with $-1 < \beta_i < 1$. For example, $\beta_i = 0$ represents a mode that is entirely uncorrected, while $\beta_i = 1$ represents a mode that is fully corrected by the AO system. A negative value for β_i can occur for modes that are not well sampled by the WFS and in anisoplanatic conditions for which the atmospheric modes decorrelate with increasing off-axis viewing angles.

Following the notation of Wöger et al. (2008) and using KL modes – that by definition have a diagonal covariance matrix for the atmospheric expansion coefficients a_i – as the M_i, we obtain as the model STF:

$$\begin{aligned}\langle |S(\vec{s})|^2 \rangle = \int\int d\vec{r}' d\vec{r} W^+ W^- W'^+ W'^- \times \exp\Bigg[&- \mathscr{D}(\vec{s}) - \mathscr{D}(\Delta\vec{r}) + \frac{1}{2}\big\{\mathscr{D}(\Delta\vec{r}+\vec{s}) + \mathscr{D}(\Delta\vec{r}-\vec{s})\big\} \\ &+ K(\vec{r},\vec{s}) + K(\vec{r}',\vec{s}) - \tilde{K}(\vec{r},\vec{r}',\vec{s}) - \tilde{K}(\vec{r}',\vec{r},\vec{s})\Bigg],\end{aligned} \tag{8.5}$$

where

$$\begin{aligned} K(\vec{r},\vec{s}) &= \sum_{i=2}^{N} \beta_i \left(1 - \frac{1}{2}\beta_i\right) \langle a_i^2 \rangle (M_i^+ - M_i^-)(M_i^+ - M_i^-) \\ \tilde{K}(\vec{r},\vec{r}',\vec{s}) &= \sum_{i=2}^{N} \beta_i \left(1 - \frac{1}{2}\beta_i\right) \langle a_i^2 \rangle (M_i^+ - M_i^-)(M_i^{+'} - M_i^{-'}). \end{aligned} \tag{8.6}$$

As shown by Equations (8.5) and (8.6), the model STF depends only on two parameters. One is the Fried parameter, r_0, which appears in the well-known phase structure function $\mathscr{D}(\vec{s})$ and $\langle a_i^2 \rangle$ (e.g., Noll 1976), and the other is the AO correction efficiency array $\boldsymbol{\beta}$ for the N (partially) corrected KL modes. The four-dimensional integral in Equation (8.5) is evaluated using Monte Carlo integration; its convergence has been analyzed in Wöger et al. (2008). The values of r_0 and $\boldsymbol{\beta}$ are taken as the sole input parameters to the STF model. The sensitivity of the STF model

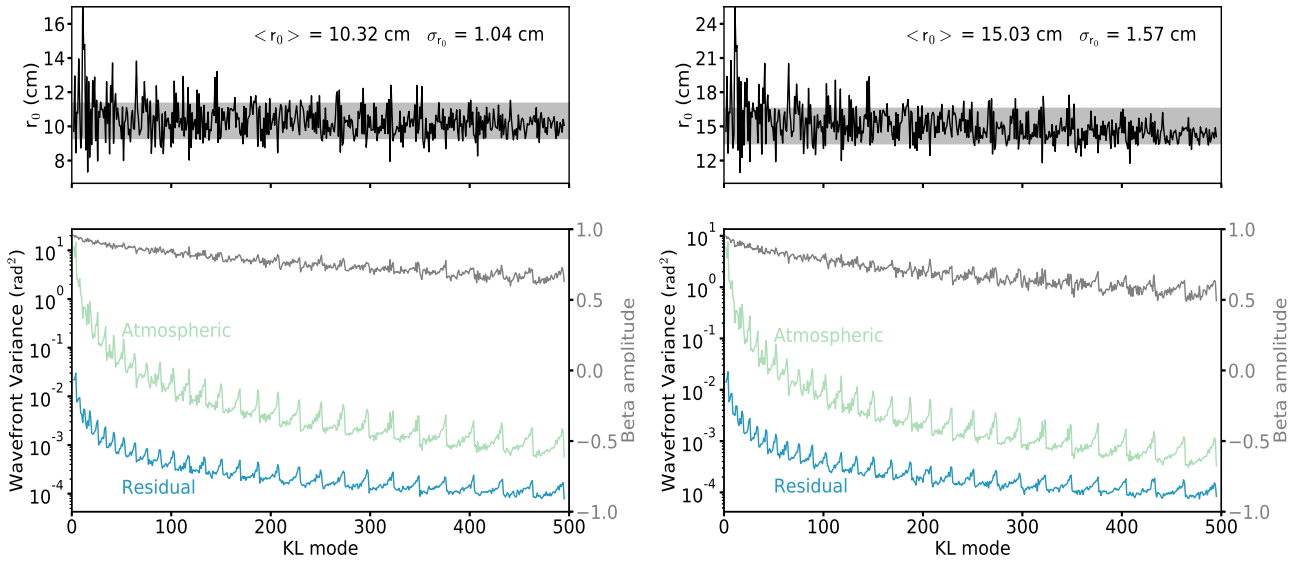

Figure 8.1: Top: Estimate of r_0 using the atmospheric variance measured from DM actuator commands for the 10 cm (left) and 15 cm (right) simulated atmospheres. The gray band represents the standard deviation, where both the mean and standard deviation are computed over all KL modes. We note that the two atmospheres are scaled versions of each other. Bottom: Atmospheric (green) and residual (blue) wavefront variances measured from the DM actuators and WFS shifts, respectively. The computed value of $\boldsymbol{\beta}$ from Equation (8.8) is shown in gray.

and the resulting photometric precision to these input parameters are discussed in the following sections.

8.3 Method

8.3.1 Estimation of Input Parameters

The analytical STF model from the previous section takes two input parameters, r_0 and the array $\boldsymbol{\beta}$. For solar observations, r_0 has typically been estimated using the spectral ratio method (von der Lühe 1984):

$$\epsilon(\vec{s}) = \frac{|\langle I(\vec{s})\rangle|^2}{\langle |I(\vec{s})|^2\rangle} = \frac{|\langle O(\vec{s}) \cdot S(\vec{s})\rangle|^2}{\langle |O(\vec{s}) \cdot S(\vec{s})|^2\rangle} = \frac{|\langle S(\vec{s})\rangle|^2}{\langle |S(\vec{s})|^2\rangle} = \frac{\mathrm{LETF}^2}{\mathrm{STF}}, \tag{8.7}$$

where LETF is the long exposure transfer function. In the absence of AO correction, r_0 is found by fitting a model to the azimuthal average of $|\langle I(\vec{s})\rangle|^2/\langle |I(\vec{s})|^2\rangle$. In the presence of AO correction, estimating r_0 becomes more complicated because it is difficult to differentiate between wavefront

improvements from the AO correction and increased r_0; this has motivated the introduction of a 'generalized Fried parameter' (Cagigal & Canales 2000). While in theory the object's Fourier signal in Equation (7) should cancel, Denker et al. (2007) has shown that $\epsilon(\vec{s})$ is not independent of the morphological structure in the object and can introduce asymmetries in the spectral ratio – and therefore errors in the estimation of r_0.

We took a different approach to estimate r_0 and $\vec{\beta}$ that utilizes AO system measurements of the atmospheric and residual wavefront covariances. Since the covariance of a Kolmogorov power spectrum is well known and scales with r_0 (Noll 1976), the atmospheric covariance measures r_0 and the residual covariance measures the AO system performance. The covariances are found respectively as $\mathscr{C}_{\rm atm} = \mathscr{H}_{\rm DM}\mathbf{M_{DM}}(\mathscr{H}_{\rm DM}\mathbf{M_{DM}})^{\rm T}$ and $\mathscr{C}_{\rm res} = \mathscr{H}_{\rm WFS}\mathbf{M_{WFS}}(\mathscr{H}_{\rm WFS}\mathbf{M_{WFS}})^{\rm T}$. The matrices $\mathscr{H}_{\{\rm DM,WFS\}}$ convert DM actuator and WFS shift values to KL modal coefficients, respectively, and are determined from the AO-system calibration. The matrices $\mathbf{M}_{\{\mathbf{DM,WFS}\}}$ contain the set of all DM actuator and WFS shift values measured during the image burst acquisition, respectively. We estimated WFS noise as the high-frequency offset in the power spectral density of the WFS shifts averaged over all sub-apertures and subtract it from $\mathbf{M}_{\{\mathbf{WFS}\}}$. Noise in cross-correlating SH WFS shift measurements is caused by several sources. Besides photon and detector read noise in the sub-aperture images themselves, other noise contributors are the contrast (and structure) of the imaged source, severity of the seeing conditions, anisoplanatism in individual sub-aperture images, and the cross-correlation peak finding algorithm. Due to the fact that the KL modes are statistically independent, the atmospheric and residual modal variances, $\sigma^2_{i,\rm atm}$ and $\sigma^2_{i,\rm res}$, are simply the diagonal values of the respective covariance matrices. The atmospheric modal variance of Kolmogorov turbulence can be modeled as a function that depends only on the scaling parameter $(D/r_0)^{5/3}$ (Noll 1976), where D is the telescope aperture diameter. Therefore, the value of r_0 is estimated by comparing the measured atmospheric variance, $\sigma^2_{\rm atm}$, to the theoretical variance and finding the best-fit scaling factor. This approach removes the dependence of r_0 on the image scene or AO correction.

The AO performance array, $\vec{\beta}$, is also estimated from $\sigma^2_{\rm atm}$ and $\sigma^2_{\rm res}$. From Wöger & von der

Lühe (2007), β_i is computed as

$$\beta_i = 1 - \sqrt{\frac{\sigma^2_{i,\mathrm{res}}}{\sigma^2_{i,\mathrm{atm}}}}. \tag{8.8}$$

The top panels of Figure 8.1 shows the r_0 estimate for the 10 cm (left) and 15 cm (right) atmospheres using σ^2_{atm} derived from the DM actuator commands and the theoretical KL values for atmospheric turbulence. The mean and standard deviation are taken over the first 500 KL modes. The larger standard deviation in low order modes is due to the fact that these modes evolve on longer timescales than high order modes. This results in fewer sampling statistics of these low order modes, and therefore a larger standard error of the sample mean over the 5 s time series. The bottom of Figure 8.1 shows the values of σ^2_{atm} and σ^2_{res} from the DM actuator commands and WFS shifts, respectively, as well as the corresponding value of $\boldsymbol{\beta}$ computed using Equation (8.8).

8.3.2 Estimation of Photometric Precision

To evaluate photometric precision, we use high spatial resolution images from numerical simulations consistent with four-meter solar telescope observations. The images are computed with the MURaM code with 16 km resolution (e.g., Rempel 2014) synthesized at 500 nm using a radiative transfer code (Uitenbroek 2001). We used one simulation of network and one of internetwork fields so that the simulations have differing intensity amplitude spectra. We convolved the image with the simulated STF of the atmosphere-telescope system, $\mathrm{STF}_{\mathrm{sim}}$, computed directly from the residual phase screens using Equation (3). We then deconvolved with a model STF computed with a set of input parameters to obtain the reconstructed image. Both $\mathrm{STF}_{\mathrm{sim}}$ and the model STF include the telescope aperture modulation transfer function that cancels out in the convolution and deconvolution process.

We directly compared the original image with the reconstructed image and calculate the photometric precision as the standard deviation of the normalized difference image (original minus reconstructed divided by the original image for all pixels). We repeated this for both image scenes. A burst image, original image, and reconstructed image for each image scene is shown in Figure 8.2 using the 10 cm atmospheric simulations and values of r_0 and $\boldsymbol{\beta}$ from the left of Figure 8.1. The

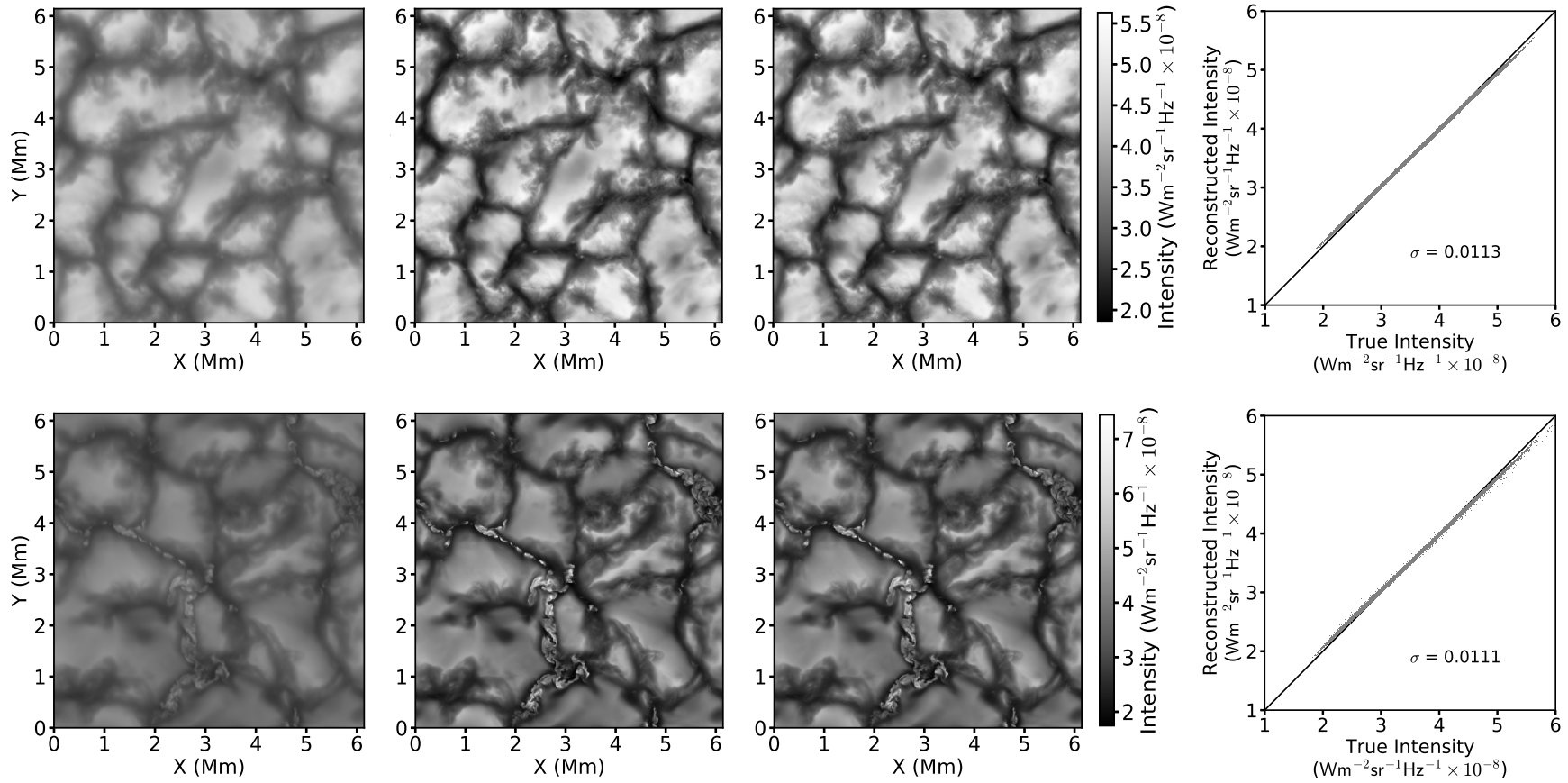

Figure 8.2: From left to right: post-AO burst image, original image, reconstructed image, and reconstructed vs. original image precision for the 10 cm atmosphere. The images were reconstructed with the STF using r_0 and $\boldsymbol{\beta}$ from Figure 8.1. Top: Internetwork image. Bottom: Network image.

improvement in the Fourier amplitudes by using the reconstruction can be seen by comparing the burst image with the reconstructed image. We note how the burst image appears to resolve small-scale structures, but does not accurately measure the image Fourier amplitudes due to the turbulent atmosphere. The photometric precision is shown on the right of Figure 8.2 and is the standard deviation of the intensity difference from the black line.

8.4 Results

In this section, we separately analyze the impact of errors introduced through the parameters r_0 and $\boldsymbol{\beta}$ on photometric precision. Using the AO-derived values of r_0 and $\boldsymbol{\beta}$ shown in Figure 8.1, we computed the model STFs under three different conditions; varying the Fried parameter input r_0, varying the number of KL modes included in $\boldsymbol{\beta}$, and fluctuating the KL mode correction by applying a per mode pseudo-random factor to the β_i values in $\boldsymbol{\beta}$. The results are shown below.

8.4.1 Variations of the Fried Parameter r_0

We tested the sensitivity of the analytical STF model to uncertainties in the estimation of r_0, which could result from errors in the WFS measurements or divergence of the atmospheric turbulence from a Kolmogorov spectrum. We varied the input value of r_0 within 20% of the AO-derived values of 10.32 and 15.03 cm. We computed the model STFs and determined the resulting photometric precision, shown in Figure 8.3 for the two image scenes. Also shown are the measured pre- and post-AO corrected $\mathrm{STF}_{\mathrm{sim}}$ and the diffraction-limited squared modulation transfer function, MTF.

As shown, the photometric precision remains within 2% photometric error for values of r_0 that are within approximately 10% and 20% for the 10 and 15 cm atmosphere, respectively, where 2% precision is a requirement of the DKIST Visible Broadband Imager (VBI) (Wöger et al. 2012). We note a systematic overestimation in the model STFs with respect to $\mathrm{STF}_{\mathrm{sim}}$ at normalized spatial frequencies $\gtrsim 0.4$. This effect likely contributes to the limit of photometric accuracy achieved in this study. Also shown by the vertical dashed line in the bottom of Figure 8.3 is the r_0 parameter

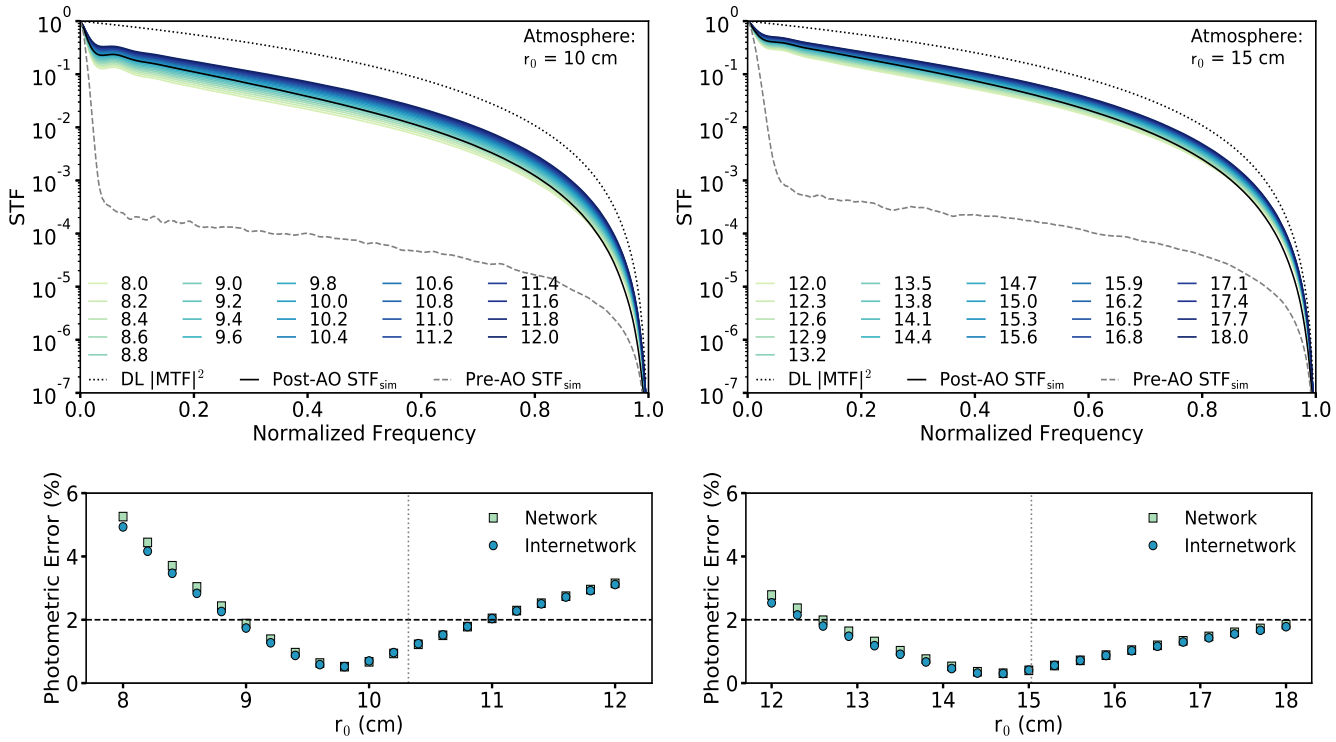

Figure 8.3: Top: Model STFs computed using $\boldsymbol{\beta}$ from Figure 8.1 under different input values of r_0 in cm (colored) for the 10 cm (left) and 15 cm (right) atmospheric simulations. Also shown: Diffraction-limited squared MTF (dotted), pre-AO atmospheric STF_{sim} (dashed), and post-AO corrected STF_{sim} (solid black). Bottom: Resulting image photometric error for the two image scenes. The AO-estimated value of r_0 is shown as the dashed vertical line. The 2% target value for DKIST is marked with the horizontal line.

determined from the AO system (from Figure 8.1). The derived value of r_0 for the 10 cm atmosphere is somewhat larger than the value set in the simulation. This effect could be caused by increased noise in the WFS measurement; the DKIST WFS is designed with a subaperture size of 9.3 cm. Therefore, measured values of $r_0 \lesssim 9.3$ cm could be attenuated by higher order optical aberrations. We note that the photometric precision is more sensitive to under-estimations of r_0 than to over-estimations since, due to the scaling of r_0, the STF is less sensitive to larger values of r_0. This is also responsible for the higher accuracy of the 15 cm atmosphere for similar relative variations in r_0.

8.4.2 Changes in the Number of Included KL Modes

We tested the dependence of the reconstruction on the number of AO-compensated KL modes used in the calculation of the model STFs. Using r_0 fixed to the AO-derived values (10.32 and 15.03 cm), we computed the STF for different numbers of modes included in the parameter array $\boldsymbol{\beta}$ computed from Equation (8) using the variances from Figure 8.1. The resulting model STFs and photometric precision are shown in Figure 8.4.

As expected, increasing the number of modes included in the model improves the accuracy of the model STF. As the number of corrected modes increases to several hundred, the improvement in the photometric precision reaches the 2% threshold. We note the increase in error from 400 to 500 KL modes in the 10 cm case, which indicates that the WFS had difficulty sensing the highest order modes and therefore worsened the reconstruction accuracy. In the 15 cm case, it is likely that the accuracy limit in this study is influenced by the number of corrected modes in the simulated AO system (500 KL modes). However, improvements in the photometric accuracy are likely to be relatively small and are achieved at the expense of increased computation time.

8.4.3 Fluctuations in KL Mode Corrections

Uncertainties in the WFS measurements, in addition to affecting the accuracy of the estimated r_0 values, may also influence the accuracy of the estimated β_i values. This effect is likely to be larger for higher-order modes, which have more small-scale structure and therefore have lower signal-to-noise ratio in the WFS measurement. To understand the contribution to photometric error, we computed the model STFs using pseudo-random fluctuations of the correction values for the KL modes. The error is modeled as a random error that increases linearly with increasing KL mode, therefore assuming that the WFS has increased difficulty measuring these modes. Each mode β_i adds an error with a random number u_i between -1 and 1 multiplied by a constant such that the highest order mode can not deviate more than 10% of a fully corrected mode:

$$\delta\beta_i = \left(\frac{u_i \times i}{N}\right) \times 0.1, \tag{8.9}$$

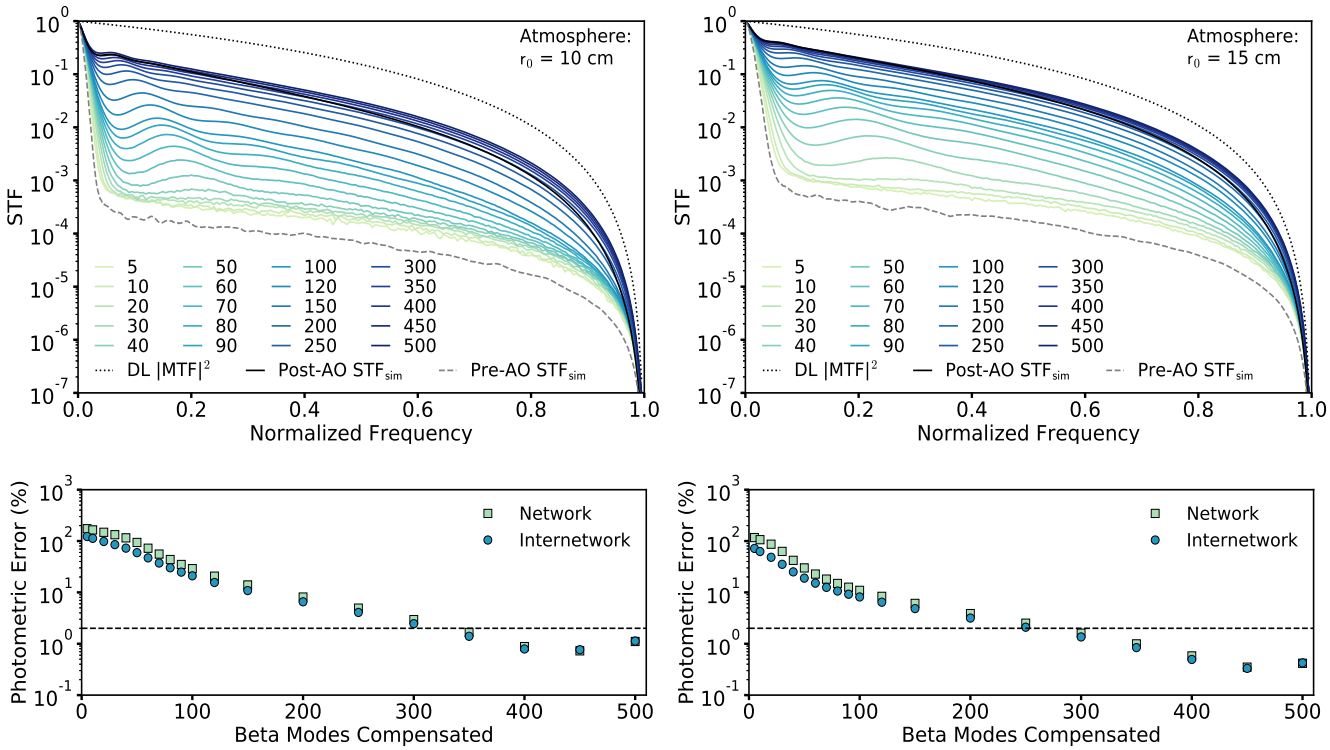

Figure 8.4: Top: Model STFs for r_0 and $\boldsymbol{\beta}$ from Figure 8.1 where $\boldsymbol{\beta}$ is truncated to the specified number of KL modes (colored). Bottom: Resulting image photometric error for the two image scenes. The target 2% value is marked with the dashed horizontal line.

where $N = 500$ in this study.

We generated 25 pseudo-random fluctuations, which are shown in Figure 8.5 overlaid with the original values of $\boldsymbol{\beta}$. We then computed the model STFs using each $\boldsymbol{\beta}$ set and the values of r_0 fixed to the AO-derived values (10.32 and 15.03 cm). The model STFs and corresponding photometric errors are shown in Figure 8.5. As shown, the STF changes very little under this random error fluctuation and all STFs are nearly identical. This indicates that random fluctuations in a given KL mode, β_i, have negligible effects on photometric precision.

8.5 Discussion

In this work, we analyzed the influence of the Fourier amplitude recovery algorithm and its inputs – in particular the on-axis STF model – on the photometric precision. In order to isolate

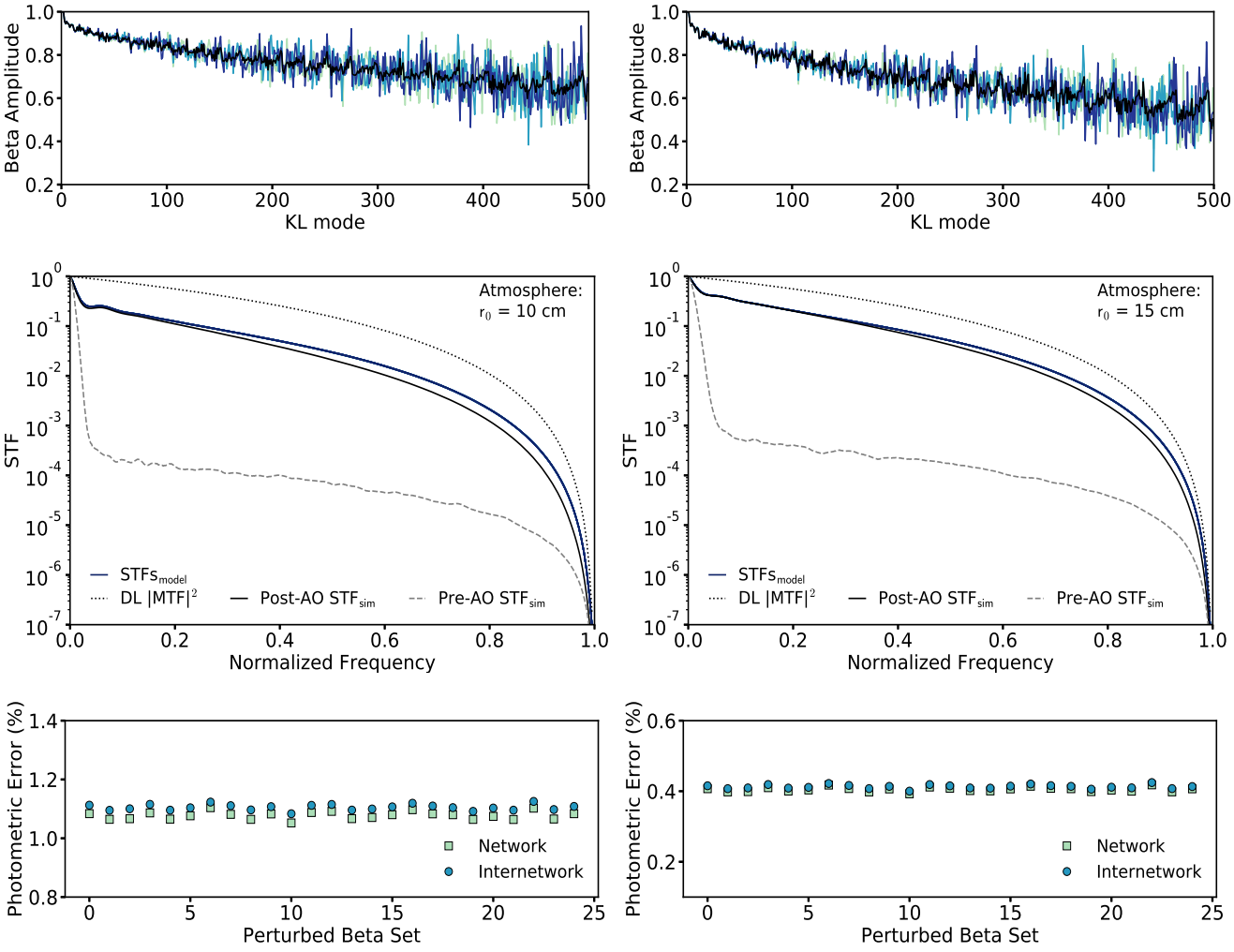

Figure 8.5: Top: Values of three sets of $\boldsymbol{\beta}$ with pseudo-random fluctuations added on each mode from Equation (9) and the original $\boldsymbol{\beta}$. Middle: Model STFs for r_0 from Figure 8.1 and the perturbed $\boldsymbol{\beta}$ sets (colored). Bottom: Resulting image photometric error for the two image scenes.

the effects of these input parameters, we based the work on several idealized assumptions of the telescope and AO system. A full evaluation of photometric precision in any observed image must be seen in the context of all sources of error that can impact it, including for example other steps in the reconstruction algorithm, source and detector noise, stray light, and off-axis performance of the AO system. These are discussed below and put into the context of the results in this work.

This study focuses on the Fourier amplitude reconstruction which determines the relative intensity weighting of structures at different spatial scales in the image. The photometric properties in the reconstructed image cannot be uncoupled from estimation of the Fourier phases for the reconstruction. In speckle interferometric algorithms, the image Fourier phases are typically estimated using recursive or iterative algorithms, or a combination of both (Matson 1991; de Boer et al. 1992; Wöger et al. 2008). The convergence of the Fourier phase reconstruction algorithms to a unique solution has been explored in the past, for example, in Matson (1991); Wöger et al. (2008). In general, the unique solution depends primarily on the chosen bispectrum parameters and can thus be influenced by the number of evaluated bispectrum positions and iterations. Pehlemann & von der Lühe (1989), however, demonstrated that Fourier phases can be recovered with high accuracy as long as a minimum of evaluated bispectrum positions are used. Therefore, in all practical situations, errors in the Fourier amplitude recovery dominate the photometric precision in a reconstructed image over errors in the Fourier phase estimation.

Measurements of the solar atmosphere are impacted by several sources of noise, which were deliberately not considered in this study beyond their potential to introduce error in the determination of the model STF input parameters. Detector noise in solar observations is dominated by photon noise, particularly when considering modern scientific CMOS sensors that can achieve less than two photo-electrons of read noise and are consequently more and more often used at telescope facilities such as DKIST. Additionally, detector noise can show characteristics that are particularly inconvenient for extended source imaging and reconstruction algorithms, for example fixed pattern noise which exhibits a non-white signature in the two-dimensional power spectrum of an image. In general, the treatment of noise through filtering in the reconstruction process is a very important

aspect that needs careful consideration. In most image reconstruction pipelines, noise is treated by applying a filter function that proportionally dampens amplitudes at those frequencies that have been identified to be affected by noise. Therefore, this process can significantly impact the photometric precision in the final image: for example, if noise in the input images is underestimated the contrast in the reconstruction will be overestimated, while in the opposite case it will be underestimated. Many noise filtering techniques, with a large range of complexity, have been proposed in the past. Some of these have been specifically suggested for solar image processing (e.g., de Boer 1996; DeForest 2017). An evaluation of the large variety of these techniques is outside the scope of this work. Nonetheless, we estimate that improper noise filtering, in particular due to a poor noise estimate affecting some or all spatial frequencies, can easily bias the photometric properties in reconstructed images by several percent.

A final and significant uncertainty that can affect the photometric precision in any image observed with an optical system is stray light. Identifying sources of stray light is often not trivial and measuring stray light can be difficult even with space-borne solar telescopes. The best option is often to measure stray light directly during a transit of a planet or occultation by the moon, and even in these cases a complete characterization is not simple (Wedemeyer-Böhm 2008). Past works (e.g., Danilovic et al. 2008; Wedemeyer-Böhm & Rouppe van der Voort 2009) have shown for example that for the Hinode space telescope the stray light contribution to granular contrast is likely of the order of a few percent, a reasonable number given its many potential sources.

The three major sources of photometric error discussed here – the applied STF, the noise filtering process, and stray light – need to be bounded to allow, for example, comparisons between observed and reconstructed images with radiative magneto-hydrodynamical simulations of the solar atmosphere. The results of this work demonstrate that the photometric errors introduced by the on-axis STF can be minimized to well below 1%, and therefore is not fundamentally a limitation to such a comparison. The additional sources of error are independent of a reconstruction algorithm and have to be carefully assessed and considered in data acquired by any telescope.

While this work focused on on-axis STFs, the field-dependence of conventional AO correction

has been modeled in the past (Wöger & von der Lühe 2007). Only turbulent layers located high above the telescope pupil contribute to field dependent variations of the point spread function. A full or partial correction of wavefront distortions conjugated to the telescope pupil – as performed by conventional AO systems – does not affect the spatial decorrelation of modal Zernike coefficients describing these distortions (Molodij & Rousset 1997) across the field, as described by Wöger & von der Lühe (2007). Future MCAO systems (e.g., von der Lühe et al. 2005; Berkefeld et al. 2006; Schmidt et al. 2017) aim to correct for discrete turbulent layers in earth's atmosphere using multiple correctors optically conjugated to the respective layer heights. Adapting this work to incorporate the correction by an MCAO system in the STF calculations requires knowledge of the remaining turbulence in the corrected and uncorrected layers so that the spatial decorrelation coefficients of the optical modes can be derived. Furthermore, to apply this particular work to off-axis STFs, whether a conventional AO or an MCAO system is assumed for correction, an analytical or numerical decorrelation model applicable to KL modes is needed. While this is beyond the scope of this study, it is highly desirable and will be a subject of the authors' future work.

The model STFs for this work were computed for an unobstructed circular telescope aperture such as that of the Goode Solar Telescope (Goode & Cao 2012), or DKIST. This was convenient for several reasons, in particular because it allowed easy and direct cross-verification of all results generated by the AO simulation tool and the computer code that calculated the analytical STF models. The model STFs can easily be computed for telescopes with a central obscuration incurred by on-axis Gregorian style telescopes, such as the GREGOR telescope (Schmidt et al. 2012), or EST. In fact, the implementation of KL modal functions for computation of model STFs in this work is based on Cannon (1996) which can accommodate a circular obstruction of any size with a single parameter, and can simultaneously calculate both the modal coefficient variances and modal functions for these cases. Furthermore, this algorithm can incorporate any atmospheric structure function if so desired, although we strictly used the original Kolmogorov structure function which has in practice been verified as being a good assumption for most telescope locations. In addition to errors introduced by the input parameters studied in this work, the sensitivity of the photometric

precision to the central obscuration parameter should be analyzed for model STFs applicable for telescopes like GREGOR or EST.

Finally, results from this work are relevant to investigations of photometric precision in images reconstructed using algorithms other than speckle including Multi-Object Multi-Frame Blind Deconvolution (van Noort et al. 2005) and Joint Phase Diverse Speckle (Paxman et al. 1992). Some research has been performed to analyze potential ways to improve on the photometric performance of reconstructed images using these algorithms (Scharmer et al. 2010). The authors of that work suggest to incorporate into the original reconstruction algorithms the application of a transfer function that is based on two components: a) an estimate of the low-order modal aberrations derived from the phase estimation algorithms themselves, and b) a statistical estimate of the (uncorrected) high-order modal aberrations derived from the prevailing seeing conditions. The latter requires an accurate estimation of r_0, but it remains unclear to what accuracy the value must be known to achieve a particular precision. We surmise that had the authors performed a similar sensitivity investigation of photometric precision versus r_0 value, they would have reached a similar conclussion.

8.6 Conclusion

In this work, we present the results of our analysis of the sensitivity of analytical models for the on-axis STF to their input parameters. These are the Fried parameter r_0 and the AO system performance as described by an efficiency array, $\boldsymbol{\beta}$. We estimated these parameters from the AO system control data. This study separates various mechanisms that can affect the model STF accuracy by comparing the model STFs with the post-AO STF of the atmospheric and AO system simulations. We analyzed the sensitivity of the model STF on the photometric properties of high spatial resolution images of the solar photosphere as they would be acquired with a 4 m aperture telescope such as DKIST.

We examined the sensitivity of the model STF to inaccuracies in determining r_0, and its impact on the photometric precision in images calibrated with this STF. Using the AO-derived

values of $\boldsymbol{\beta}$ from Figure 8.1, we varied r_0 up to 20% from the nominal values and found that deviations in r_0 greater than 10% and 20% in the 10 and 15 cm atmosphere, respectively, degraded the photometric precision to more than 2%. The ability to correctly determine r_0 is the most important factor in photometric precision as this parameter appears to have the largest impact on the shape of the STF. This result could prove to be useful for enhancing the expected photometric precision in images deconvolved with long-exposure point-spread functions derived from AO control data (e.g., Veran et al. 1997; Marino & Rimmele 2010).

We evaluated the effect of the number of KL modes included in the analytical model of the STF on the photometric precision. We computed the STFs with different numbers of KL modes by modifying the length of the input parameter array $\boldsymbol{\beta}$ and using the values of r_0 derived from the AO system. We find that several hundred KL modes are required to achieve the minimum precision requirements of the DKIST VBI. The results also indicate that the photometric precision could be improved with the inclusion of more than 500 corrected modes, but the improvements would be limited and at the expense of longer computation times.

Finally, to determine the effect of uncertainty in the measurement of the AO efficiency, we added pseudo-random noise to each entry in the original $\boldsymbol{\beta}$ array. We find that these fluctuations have negligible effect on the photometric precision and deduce that the shape of the $\boldsymbol{\beta}$ profile plays a larger role than the relative amplitudes of neighboring modes.

This study provides the first rigorous analysis of the process of utilizing AO system information to derive both an estimate for the Fried parameter, r_0, and $\boldsymbol{\beta}$ in order to support the speckle image reconstruction process. The main advantage of this method is that it removes the dependence of the r_0 estimate on the image scene (via non-azimuthally symmetric power spectra). For the nominal values of these parameters, we find a photometric error below 1% and with little dependence on image scene. Furthermore, this work provides for the first time direct evidence that the parameter $\boldsymbol{\beta}$ accurately encodes the impact of an AO system on the model STF, and that the analytical model described in Equation (8.5) can indeed be used to calibrate the Fourier amplitudes during the image reconstruction process. While previous works had already indicated

high accuracy of the applied calibration function (e.g., Wöger et al. 2008), this study was able to address several aspects of its sensitivity in more detail.

The authors would like to thank the anonymous referee whose comments contributed to significant improvements to the manuscript. The National Solar Observatory is operated by the Association of Universities for Research in Astronomy (AURA) Inc. under a cooperative agreement with the National Science Foundation. This material is based upon work supported by the National Science Foundation Graduate Research Fellowship Program under grant No. DGE 1144083 and NASA award number NNX12AB35G. This work utilized the Janus supercomputer, which is supported by the National Science Foundation (award number CNS-0821794), the University of Colorado Boulder, the University of Colorado Denver, and the National Center for Atmospheric Research. Janus is operated by the University of Colorado Boulder. CLP would like to thank Dr. Mark Rast for valuable discussions during the course of this research.

Chapter 9

Conclusions

9.1 Summary

The work presented in this thesis focused on the role of the quiet sun magnetic field on the solar radiative output and variability. We demonstrated the difficultly in constraining photometric trends of the low-contrast quiet sun, which motivated the use of high-resolution radiative magnetohydrodynamic (MHD) simulations. These simulations permit the study of the radiative output of the quiet sun magnetism in the absence of sufficiently high spatial resolution images and radiometric observations. The simulations focused on the influence of the magnetic field morphology on the radiative output of the quiet sun. This was motivated by recent observations suggesting the existence of various quiet sun magnetic morphologies (Harvey et al. 2007; Lites et al. 2008; Ishikawa & Tsuneta 2009; Danilovic et al. 2010b; Stenflo 2010; Lites 2011), which likely coexist on the solar surface.

Connecting the results from this study to upcoming observations requires both highly accurate numerical solutions of both the radiative MHD simulations and the synthesized emergent intensity using a radiative transfer solver, as well as sufficiently high confidence in the photometric accuracy of high-resolution observations. To this end, we have presented contributions to improvements in the numerical accuracy of radiative transfer solutions — with improvements proposed for radiative MHD simulations discussed in Section 9.2.1 — and constrained the photometric precision of the post-facto image reconstruction technique applicable to upcoming high resolution observations from the four-meter DKIST. These contributions will aid our understanding of the radiative output of

the quiet sun

9.1.1 Observational Limitations of Measuring Quiet Sun Radiative Output

This work analyzed the disagreement between studies using photometric observations of the quiet sun which yielded differing estimates for the enhancement of the quiet sun with solar cycle. The key component of this work is that analyzing photometric trends requires a reference against which all pixels are compared. Such a reference is typically defined as the low magnetic flux 'quiet sun', the definition of which differs between various analyses. This presents at least two problems. The first is that the defined background reference is not necessarily consistent between analyses and therefore the inferred photometric trends, whether of the full disk or structures, were demonstrated to depend sensitively on the background selected. The second is that the background reference is typically defined as the quiet sun, which is assumed to be constant in time. While there is little evidence to suggest an invariant nature of the quiet sun, we demonstrated that the photometric trends of the full-disk lie within the error in determining the photometric trends of the lowest-contrast structures, including the quiet sun.

The results of this work demonstrate the sensitivity of photometric measurements to the assumed quiet sun background, particularly when analyzing the photometric properties of low-contrast elements on the solar disk such as the quiet sun. Similarly, in full-disk photometric measurements with weak cycle enhancement or de-enhancement the trends are similarly sensitive to the background reference selected. Therefore, the uncertainty in the determination of the solar cycle variation of the quiet sun or the full-disk may lie within the cycle variability of the reference itself. Additionally, it should be stressed that there is not necessarily a correct background reference to use when examining photometric data. This work prompted the use of radiative MHD simulations to understand the source of brightness variations, rather than attempting to measure the brightness variations directly.

9.1.2 Improving Spatial Resolution with Grid Pre-Tilting

Due to the computational demands to solve the radiative MHD equation in simulations of the solar photosphere, all 3D MHD simulations utilize some estimation of the opacity of the fluid that is not spectrally resolved in the convergence to a statistically steady-state solution. Therefore, if the spectrally resolved radiative output is required, a standalone radiative transfer code must be utilized on the output of the MHD simulations. There are several computational techniques used to solve the radiative transfer equation in 3D simulations. The method of short-characteristics is often employed in the numerical solution to the radiative transfer equation due to its relative ease of parallelization on multiple processors, but is known to introduce numerical diffusion in the emergent intensity as an artifact. In this work, we quantified the numerical diffusion introduced by the short-characteristics method in the emergent intensity solution at inclined viewing angles. The amount of diffusion depends strongly on the viewing angle and interpolation scheme employed in the radiative transfer solver. We also demonstrated that while a higher-order interpolation scheme results in reduced diffusion, this is at the expense of conservation of the intensity through the domain where the degree of error in the conservation depends on the viewing angle analyzed.

To overcome the numerical diffusion while still maintaining the computational advantages of this method, we demonstrated that pre-tilting the atmosphere prior to computing the transfer resulted in no numerical diffusion. This pre-tilting method is computationally simple and may provide numerical advantages beyond calculation of the emergent intensity as discussed Section 9.2.1.

The numerical diffusion introduced by the method of short-characteristics would adversely affect comparisons between simulations and observations off of disk center unless the simulations were computed at much higher spatial resolution than the observations. The results of this work therefore have important implications for studies comparing simulations and observations that have utilized the short-characteristics method. Similarly, the potential effect on the radiative heating balance in the solution to MHD simulations must also be analyzed in detail (see Section 9.2.1).

9.1.3 Impact of Magnetic Morphology on Radiative Output

To understand the effect of magnetic field morphology on the radiative output of the quiet sun, we analyzed simulations representing two different morphologies likely present on the solar surface. We used simulations from the MURaM MHD code, which is capable of producing results consistent with observations of a strong horizontal magnetic field within the quiet sun, thought to result from a local turbulent dynamo (see e.g., Danilovic et al. 2010b; Rempel 2014). We utilized two sets of simulations with equivalent magnitude of the magnetic fields, but differing morphologies. We synthesized the radiative transfer using the pre-tilting method under various inclination angles and over continuum wavelengths. We showed that the radiative output of equivalent magnetic field pixels between the two quiet sun simulations, where the isotropic mixed polarity magnetic morphology had an output up to 50% higher than that of a predominantly vertical magnetic morphology. Initially, this appears to suggest that the radiative output between the two simulations differ due to the field morphology. However, the analysis of the radiative output of magnetic flux element sizes demonstrates that the radiative outputs of the two atmospheres would be equivalent if they included equivalent densities of magnetic structure sizes.

We further analyzed the emergent intensity of the magnetic structures from the two simulations as a function of their characteristic width. Using a simple area and perimeter ratio, we demonstrated that the intensity of small structures increases with increasing characteristic width. However, once the structures reach the approximate width of the downflow lanes, the intensity decreases. This suggests that the convective energy flux for small structures remained relatively unchanged until the structure reached the approximate size of the downflow lane, at which point the presence of the magnetic field begins to modify the surrounding convective flows, resulting in a lower emergent intensity. To demonstrate this, we estimated the convective flux as a function of structure size, finding results in agreement with the reduced convective flux for larger structures.

To determine the effect of the two simulations on the inferred irradiance, we compared the simulation results to those that would be obtained with irradiance models. To this end, we convolved

the line-of-sight magnetic field with the point-spread-function of a 1 arcsecond resolution telescope to mimic the magnetic field as would be measured by full-disk magnetograms for the purpose of irradiance models. We then identified the quiet sun pixels as those in the convolved magnetic field image with $|B_z| < 50$ G and compared the irradiance of the two simulations to that obtained with the quiet sun atmospheres used in two irradiance models. We demonstrated that the spectral irradiance of the quiet sun structures in the MHD simulations fell within the irradiance model results, but that the difference in spectral irradiance between the two simulations and models showed a wavelength dependence with intensity variations of a magnitude that could result in an error in the inferred solar irradiance variability on the order of the variability measured in observations. Therefore, the influence of the quiet sun on spectral irradiance should be examined in further detail, especially when considering the disagreement between model and observations of the spectral irradiance variability.

9.1.4 Connecting to Upcoming High-Resolution Observations

Finally, we connected these results of the source of quiet sun radiative differences lying in the differing structure sizes to upcoming observations from high resolution telescopes. The next generation of solar telescopes will resolve the quiet sun at spatial resolutions similar to those of the simulations used in this work. As these telescopes are ground-based, they will only be capable of photometric observations. Therefore, measuring the low contrast of the quiet sun magnetism to compare with the simulation results in this work will only be possible under sufficiently high photometric precision.

In this work, we studied the photometric precision of the upcoming DKIST 4 m solar telescopes. The telescope will utilize adaptive optics to overcome seeing through Earth's turbulent atmosphere, and post-imaging speckle reconstruction to remove degradation effects not captured by the adaptive optics system. The speckle algorithm is based on Kolmogorov statistics describing atmospheric turbulence, and the resulting effect on wavefront propagation. The details of this method are shown in Appendix B. We analyzed the sensitivity of the speckle reconstruction to the

scale-size of the turbulent atmosphere and the efficiency of the adaptive optics system.

The results of this work demonstrated that the estimation of the scale-size of the atmospheric turbulence is the most important input parameter to ensure accurate photometric precision. Assuming this parameter is well estimated, photometric precision within 2% is readily obtained. Compared with the results of the difference in radiative output of the two MHD simulations at full resolution, a photometric precision of this order is sufficient to identify the difference in radiative output of magnetic field pixels seen in this thesis.

9.2 Future Directions

9.2.1 Extension of Short-Characteristic Diffusion Solution

The analysis presented in Chapter 4 demonstrates the numerical diffusion in the emergent intensity when the method of short-characteristics is used in the solution to the radiative transfer equation. While we showed that the pre-tilting method overcomes the numerical diffusion introduced, the radiative transfer in the MHD simulations used throughout this thesis were computed using short-characteristics. In these simulations, the divergence of the radiative flux is required to calculate the radiative heating rate, which itself requires the intensity. This potentially leads to numerical diffusion introduced in the solutions through the energy equation (i.e., diffusion in the energy rather than the emergent intensity).

An important follow up is understanding the effect of short-characteristic numerical diffusion on the MHD simulation solutions themselves. The numerical diffusion introduced by the short characteristics method introduces angle-dependent error in the solution to the emergent intensity ,and therefore the calculation of the radiative flux. This diffusion may introduce errors in the solution to the energy equation. Furthermore, the numerical diffusion can also act to over- or under-account for a point source of intensity in a domain. Imagine a point source of intensity in a domain where a quadrature technique is used as shown in Figure 9.1. The use of a numerical quadrature weights the contribution from each ray, which may over- or under- account for a source

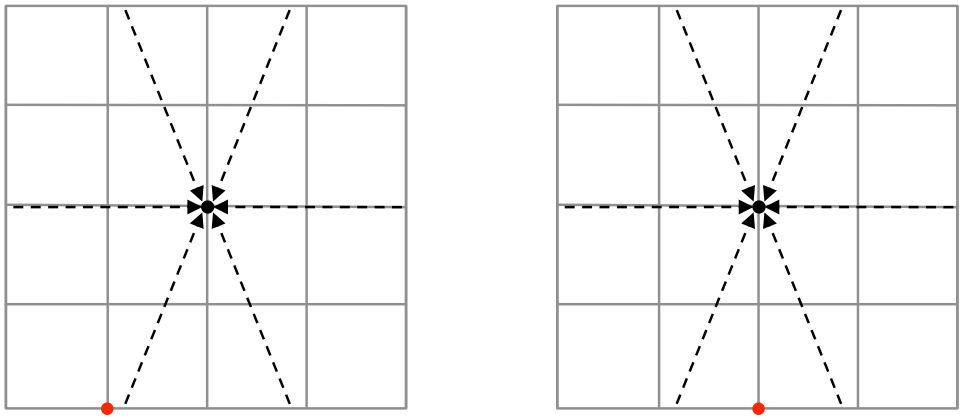

Figure 9.1: Simple model of the evaluation of the flux in 2D at a given point (black dot). The red dot represents a source of high temperature. Note that the weighting of the influence from the source depends on its location relative to the quadrature rays (dotted arrows).

of intensity depending on the location of the point source relative to the rays themselves. The short-characteristics method applied through the radiative heating rate would smear the intensity over the sphere. This effect may act to balance each other and result in negligible impact. However a thorough study is required.

Similarly, the calculation of the emergent intensity solution in the case of nLTE requires a simultaneous solution of the radiation field and the particle densities due to the presence of a non local radiation field. Solving for the source function in Equation 3.27 therefore requires an iterative solution which depends on the mean intensity of the non local radiation field. If the short-characteristics method introduces numerical diffusion that modifies the mean intensity solution, then the convergence of the nLTE solution may be erroneous or not converge at all. Considering that chemical abundances are determined from spectral lines, some of which are formed in nLTE, such errors could lead to incorrect inferences of the solar composition (see e.g., Asplund et al. 2009, and references therein for details on the solar abundance problems). Two tests must be made to understand the role of the numerical diffusion in nLTE calculations. The first would be testing the effect of numerical diffusion in a scattering dominated radiation field from Equation 3.27, where the mean intensity may introduce diffusion in the short-characteristics method. The second test

would be to analyze the effect of the intensity diffusion on the convergence of the local populations states. Both of these would play a role in the accuracy but the extent should be covered in more detail.

The improvement in spatial resolution using the pre-tilting method in the calculation of the emergent intensity warrants an investigation of the most computationally efficient radiative transfer method applied to these atmospheres. Simply pre-tilting the grid and applying the short-characteristics method is not likely a computationally efficient method since the number of calculations will depend directly on the grid points in the pre-tilted solution. The scheme used throughout this thesis (employed by RH) for tilted rays uses a series expansion to estimate the functional form of the opacity along the inclined ray path. The method implemented for vertical rays, however, may not require such an estimate as the grid spacing between subsequent points may be small enough to avoid the series expansion. Therefore, an important next step will be to investigate a computationally efficient method to solve the radiative transfer on a pre-tilted grid. A likely solution will be the Feautrier method (Feautrier 1964; Auer 1976; Mihalas et al. 1978) commonly employed in long-characteristics solutions. For both the MHD and nLTE solutions, the pre-tilting method may be computationally advantageous compared to the short-characteristics method. Calculation of the radiative heating rate when using short-characteristics can result in somewhat difficult domain decomposition for large arrays since the solution has to be communicated between grid-points and must be calculated over many angles in the quadrature scheme used. However, with the pre-tilting method, the arrays could be pre-tilted at the discrete quadrature angles of interest and the radiative transfer solution computed for each gird point, only communicating between the pre-tilted arrays for the following time step in the solution. This requires further investigation and is the subject of future work by the author.

9.2.2 Further Understanding the Effects of Morphology on Radiative Output

The work presented in Chapter 6 demonstrated that magnetic structures play a large role in the radiative output of the simulations, rather than the magnetic morphology. We demonstrated

that this is likely due to the suppression of convective flux resulting from the concentrations of the magnetic field. This work however utilized only two simulation setups, which may not adequately represent the variety of conditions under which magnetic structures can form. Therefore, further analysis of the impact of field morphology and the distribution of magnetic structures generated is required, as well as the intensity distributions as a function of size.

Additionally, a more thorough analysis of the convective flux and the balance with radiative flux should be carried out to fully understand their role in the radiative output of magnetic structures. This step will require the convective and radiative flux as computed directly from MURaM to determine the role of lateral heating from the sidewalls of a magnetic structures compared to the suppression of convection due to the magnetic field, particularly under differing magnetic field morphologies. This work will help further quantify the role of magnetism and magnetic structures in the radiative output of the quiet sun.

Furthermore, the results should be connected to upcoming observations with DKIST and EST, which requires inferring the atmospheric profiles of observed pixels based on their spectra. To do so, the first step will degrade the simulation results to the resolution of DKIST, which will perform spectropolarimetric measurements at the simulation resolution. Spectral inversions will then be performed on the degraded simulations to infer the temperature and pressure profiles using an inversion code. This step will require an analysis of spectral lines that are appropriately sensitive to the temperature or pressure in order to adequately infer the profiles. The inferred profiles compared to those directly obtained from the simulations will then indicate the observability of the thermodynamic property of interest. These results will determine if the profiles will be observable using DKIST or other existing instruments.

9.2.3 Speckle Image Reconstruction for Spectropolarimetric Observations

DKIST will observe the solar surface with an unprecedented $\sim$15 km resolution in the visible spectrum, constituting a near 3-fold improvement over current solar telescopes. This resolution can elucidate currently unknown properties of the magnetic fields from spectropolarimetric measure-

ments and the underlying atmospheric structure through inversion techniques. Several studies have used post-facto image reconstruction techniques for solar spectropolarimetric data. For example, Puschmann & Beck (2011) demonstrated the use of speckle and MOMFDB reconstructions on spectropolarimetric data and found good performance in cases of high signal-to-noise. Asensio Ramos et al. (2012) studied the influence of phase-diversity reconstruction on circular polarization using 3D MHD simulations and assumptions about the imaging conditions for the balloon-borne IMaX instrument. They found that although the reconstructions reduced spatial smearing, the appearance of spatially-correlated noise in phase-diversity measurements modified the profiles. These methods could benefit from AO derived input parameters, which were not used in the aforementioned studies.

Future work will investigate the effect of speckle image reconstruction on spectropolarimetric observations. The DL-NIRSP (Tritschler et al. 2007) instrument provides simultaneous spatial and spectral images to deduce the spectropolarimetric signals with observed wavelengths in the range of VBI. This simplifies the procedure as the VBI transfer functions can be applied to images obtained by DL-NIRSP directly without the need to observe the wavefront distortion at the wavelength observed. The first step could use the method of Keller & von der Lühe (1992) to apply the speckle transfer function (the same that will be applied to the VBI broadband speckle burst set) to the DL-NIRSP narrowband images in wavelength regions near the VBI broadband spectrum (such as the 630 nm Fe I lines). This permits the estimation of the required short-exposure 'speckle burst' from a combination of the VBI short exposure images and the comparatively long-exposure DL-NIRSP images. Determining the accuracy of this method would then require comparison of the reconstructed line profiles with the profiles directly obtained from the MHD simulations.

Bibliography

Abramenko, V. I. 2005, Solar Physics, 228, 29

Afram, N., Unruh, Y. C., Solanki, S. K., et al. 2011, Astronomy & Astrophysics, 526, A120

Allende Prieto, C., Hubeny, I., & Lambert, D. L. 2003, The Astrophysical Journal, 591, 1192

Amarsi, A. M., Asplund, M., Collet, R., & Leenaarts, J. 2016, Monthly Notices of the Royal Astronomical Society, 455, 3735

Asensio Ramos, A. 2009, The Astrophysical Journal, 701, 1032

Asensio Ramos, A., Martínez González, M. J., Khomenko, E., & Martínez Pillet, V. 2012, Astronomy and Astrophysics, 539, A42

Asplund, M., Grevesse, N., Sauval, A. J., & Scott, P. 2009, Annual Review of Astronomy and Astrophysics, 47, 481

Auer, L. 1976, Journal of Quantitative Spectroscopy and Radiative Transfer, 16, 931

Auer, L. H. & Paletou, F. 1994, Astronomy and Astrophysics, 285, 675

Babcock, H. W. 1961, The Astrophysical Journal, 133, 572

Balke, A. C., Schrijver, C. J., Zwaan, C., & Tarbell, T. D. 1993, Solar Physics, 143, 215

Ball, W. T., Haigh, J. D., Rozanov, E. V., et al. 2016, Nature Geoscience, 9, 206

Ball, W. T., Krivova, N. A., Unruh, Y. C., Haigh, J. D., & Solanki, S. K. 2014, Journal of the Atmospheric Sciences, 71, 4086

Ball, W. T., Unruh, Y. C., Krivova, N. A., Solanki, S., & Harder, J. W. 2011, Astronomy & Astrophysics, 530, A71

Ball, W. T., Unruh, Y. C., Krivova, N. A., et al. 2012, Astronomy and Astrophysics, 541, A27

Batchelor, G. K. 1950, Proceedings of the Royal Society of London Series A, 201, 405

Beeck, B., Collet, R., Steffen, M., et al. 2012, Astronomy and Astrophysics, 539, A121

Bell, K. L. & Berrington, K. A. 1987, Journal of Physics B: Atomic and Molecular Physics, 20, 801

Berkefeld, T., Soltau, D., & von der Lühe, O. 2006, in Proc. SPIE, Vol. 6272, Society of Photo-Optical Instrumentation Engineers (SPIE) Conference Series, 627205

Borrero, J. M., Jafarzadeh, S., Schüssler, M., & Solanki, S. K. 2015, Space Science Reviews, 1

Bruls, J. H. M. J., Vollmöller, P., & Schüssler, M. 1999, Astronomy and Astrophysics, 348, 233

Buehler, D., Lagg, A., & Solanki, S. K. 2013, Astronomy and Astrophysics, 555, A33

Cagigal, M. P. & Canales, V. F. 2000, Journal of the Optical Society of America A, 17, 903

Cannon, R. C. 1996, Journal of the Optical Society of America A, 13, 862

Carlson, B. 1963, in Methods in Computational Physics, Vol. 1, ed. B. Alder & S. Fernbach, 1–42

Carlson, B. 1970, Transport Theory: Discrete Ordinates Quadrature Over the Unit Sphere, Tech. Rep. LA-4554, Los Alamos National Laboratory, Los Alamos, NM

Carlsson, M. 2008, Physica Scripta Volume T, 133, 014012

Charbonneau, P. 2014, Annual Review of Astronomy and Astrophysics, 52, 251

Collados, M., Bettonvil, F., Cavaller, L., et al. 2013, Memorie della Societa Astronomica Italiana, 84, 379

Cox, J. P. & Giuli, R. T. 1968, Principles of Stellar Structure (Gordon and Breach)

Criscuoli, S. 2007, PhD thesis, University of Rome Tor Vergata

Criscuoli, S. 2013, The Astrophysical Journal, 778, 27

Criscuoli, S., Norton, A., & Whitney, T. 2017, The Astrophysical Journal, 847, 93

Criscuoli, S. & Rast, M. P. 2009, Astronomy and Astrophysics, 495, 621

Criscuoli, S., Rast, M. P., Ermolli, I., & Centrone, M. 2007, Astronomy and Astrophysics, 461, 331

Criscuoli, S. & Uitenbroek, H. 2014, The Astrophysical Journal, 788, 151

Dai, G.-M. 1995, Journal of the Optical Society of America A, 12, 2182

Danilovic, S., Beeck, B., Pietarila, A., et al. 2010a, The Astrophysical Journal Letters, 723, L149

Danilovic, S., Gandorfer, A., Lagg, A., et al. 2008, Astronomy and Astrophysics, 484, L17

Danilovic, S., Schüssler, M., & Solanki, S. K. 2010b, Astronomy and Astrophysics, 513, A1

Davis, S. W., Stone, J. M., & Jiang, Y.-F. 2012, The Astrophysical Journal Supplement Series, 199, 9

de Boer, C. R. 1996, Astronomy and Astrophysics Supplement Series, 120, 195

de Boer, C. R., Kneer, F., & Nesis, A. 1992, Astronomy and Astrophysics, 257, L4

DeForest, C. E. 2017, The Astrophysical Journal, 838, 155

Deinzer, W., Hensler, G., Schüssler, M., & Weisshaar, E. 1984, Astronomy and Astrophysics, 139, 426

Deland, M. T. & Cebula, R. P. 2008, Journal of Geophysical Research (Space Physics), 113, A11103

DeLand, M. T. & Cebula, R. P. 2012, Journal of Atmospheric and Solar-Terrestrial Physics, 77, 225

Denker, C., Deng, N., Rimmele, T. R., Tritschler, A., & Verdoni, A. 2007, Solar Physics, 241, 411

Dikpati, M. & Gilman, P. A. 2006, The Astrophysical Journal, 649, 498

Domínguez Cerdeña, I., Kneer, F., & Sánchez Almeida, J. 2003, The Astrophysical Journal Letters, 582, L55

Domínguez Cerdeña, I., Sánchez Almeida, J., & Kneer, F. 2006, The Astrophysical Journal, 636, 496

Elmore, D. F., Rimmele, T., Casini, R., et al. 2014, in Proc. SPIE, Vol. 9147, Ground-based and Airborne Instrumentation for Astronomy V, 914707

Ermolli, I., Berrilli, F., & Florio, A. 2003, Astronomy & Astrophysics, 412, 857

Ermolli, I., Matthes, K., Dudok de Wit, T., et al. 2013, Atmospheric Chemistry & Physics, 13, 3945

Feautrier, P. 1964, Comptes Rendus Academie des Sciences (serie non specifiee), 258

Finlator, K., Özel, F., & Davé, R. 2009, Monthly Notices of the Royal Astronomical Society, 393, 1090

Fligge, M., Solanki, S. K., & Unruh, Y. C. 2000, Astronomy and Astrophysics, 353, 380

Fontenla, J. M., Avrett, E. H., & Loeser, R. 1991, The Astrophysical Journal, 377, 712

Fontenla, J. M., Curdt, W., Haberreiter, M., Harder, J., & Tian, H. 2009, The Astrophysical Journal, 707, 482

Fontenla, J. M., Harder, J., Livingston, W., Snow, M., & Woods, T. 2011, Journal of Geophysical Research: Atmospheres, 116, D20108

Foukal, P., Bernasconi, P., Eaton, H., & Rust, D. 2004, The Astrophysical Journal Letters, 611, L57

Freytag, B., Steffen, M., & Dorch, B. 2002, Astronomische Nachrichten, 323, 213

Freytag, B., Steffen, M., Ludwig, H.-G., et al. 2012, Journal of Computational Physics, 231, 919

Fried, D. L. 1966a, Journal of the Optical Society of America, 56, 1380

Fried, D. L. 1966b, Journal of the Optical Society of America, 56, 1372

Fritsch, F. & Carlson, R. 1980, SIAM Journal on Numerical Analysis, 17, 238

Fröhlich, C. 2006, Space Science Reviews, 125, 53

Fröhlich, C. & Lean, J. 1998, Geophysical Research Letters, 25, 4377

Fröhlich, C. & Lean, J. 2004, Astronomy and Astrophysics Review, 12, 273

Galsgaard, K. & Nordlund, Å. 1996, Journal of Geophysical Research, 101, 13445

Gaunt, J. A. 1930, Proceedings of the Royal Society of London. Series A, 126, 654

Gavel, D. T. 2003, in Proc. SPIE, Vol. 4839, Adaptive Optical System Technologies II, ed. P. L. Wizinowich & D. Bonaccini, 972–980

Geltman, S. 1962, The Astrophysical Journal, 136, 935

Goode, P. R. & Cao, W. 2012, in Astronomical Society of the Pacific Conference Series, Vol. 463, Second ATST-EAST Meeting: Magnetic Fields from the Photosphere to the Corona., ed. T. R. Rimmele, A. Tritschler, F. Wöger, M. Collados Vera, H. Socas-Navarro, R. Schlichenmaier, M. Carlsson, T. Berger, A. Cadavid, P. R. Gilbert, P. R. Goode, & M. Knölker, 357

Goodman, J. W. 2005, Introduction to Fourier Optics (Roberts and Company Publishers)

Gray, D. F. 2005, The Observation and Analysis of Stellar Photospheres (Cambridge University Press)

Gray, L. J., Beer, J., Geller, M., et al. 2010, Reviews of Geophysics, 48, RG4001

Gudiksen, B. V., Carlsson, M., Hansteen, V. H., et al. 2011, Astronomy and Astrophysics, 531, A154

Haberreiter, M., Schmutz, W., & Hubeny, I. 2008, Astronomy and Astrophysics, 492, 833

Haigh, J. D., Winning, A. R., Toumi, R., & Harder, J. W. 2010, Nature, 467, 696

Hale, G. E., Ellerman, F., Nicholson, S. B., & Joy, A. H. 1919, The Astrophysical Journal, 49, 153

Hale, G. E. & Nicholson, S. B. 1925, The Astrophysical Journal, 62, 270

Hanasoge, S. M., Duvall, T. L., & Sreenivasan, K. R. 2012, Proceedings of the National Academy of Science, 109, 11928

Harder, J., Fontenla, J., White, O., Rottman, G., & Woods, T. 2005, Memorie della Societa Astronomica Italiana, 76, 735

Harder, J. W., Fontenla, J. M., Pilewskie, P., Richard, E. C., & Woods, T. N. 2009, Geophysical Research Letters, 36, L07801

Harvey, J. W., Branston, D., Henney, C. J., Keller, C. U., & SOLIS and GONG Teams. 2007, The Astrophysical Journal Letters, 659, L177

Hathaway, D. H. 2010, Living Reviews in Solar Physics, 7, 1

Hayek, W., Asplund, M., Carlsson, M., et al. 2010, Astronomy & Astrophysics, 517, A49

Hayek, W., Asplund, M., Collet, R., & Nordlund, Å. 2011, Astronomy and Astrophysics, 529, A158

Hickey, J. R., Stowe, L. L., Jacobowitz, H., et al. 1980, Science, 208, 281

Hirzberger, J., Feller, A., Riethmüller, T. L., et al. 2010, The Astrophysical Journal Letters, 723, L154

Hotta, H., Rempel, M., & Yokoyama, T. 2015, The Astrophysical Journal, 803, 42

Ibgui, L., Hubeny, I., Lanz, T., & Stehlé, C. 2013, Astronomy and Astrophysics, 549, A126

IPCC. 2007, Climate Change 2007 - The Physical Science Basis: Working Group I Contribution to the Fourth Assessment Report of the IPCC, ed. S. Solomon, D. Qin, M. Manning, Z. Chen, M. Marquis, K. B. Averyt, M. Tignor, & H. L. Miller (Cambridge University Press)

Ishikawa, R. & Tsuneta, S. 2009, Astronomy and Astrophysics, 495, 607

Jacobowitz, H., Stowe, L. L., & Hickey, J. R. 1978

Johansson, E. M. & Gavel, D. T. 1994, in Proc. SPIE, Vol. 2200, Amplitude and Intensity Spatial Interferometry II, ed. J. B. Breckinridge, 372–383

John, T. L. 1988, Astronomy and Astrophysics, 193, 189

John, T. L. 1994, Monthly Notices of the Royal Astronomical Society, 269, 871

Johnson, L. C., Cummings, K., Drobilek, M., et al. 2014, in Proc. SPIE, Vol. 9148, Adaptive Optics Systems IV, 91481S

Judge, P. G., Kleint, L., Uitenbroek, H., et al. 2015, Solar Physics, 290, 979

Keller, C. U. 1992, Nature, 359, 307

Keller, C. U. & von der Lühe, O. 1992, Astronomy and Astrophysics, 261, 321

Knölker, M. & Schüssler, M. 1988, Astronomy and Astrophysics, 202, 275

Knox, K. T. & Thompson, B. J. 1974, The Astrophysical Journal Letters, 193, L45

Kobel, P., Solanki, S. K., & Borrero, J. M. 2011, Astronomy and Astrophysics, 531, A112

Kobel, P., Solanki, S. K., & Borrero, J. M. 2012, Astronomy and Astrophysics, 542, A96

Koesterke, L., Allende Prieto, C., & Lambert, D. L. 2008, The Astrophysical Journal, 680, 764

Kopp, G., Fehlmann, A., Finsterle, W., et al. 2012, Metrologia, 49, S29

Kopp, G., Heuerman, K., & Lawrence, G. 2005a, Solar Physics, 230, 111

Kopp, G. & Lawrence, G. 2005, Solar Physics, 230, 91

Kopp, G., Lawrence, G., & Rottman, G. 2005b, Solar Physics, 230, 129

Korff, D. 1973, Journal of the Optical Society of America, 63, 971

Krivova, N. A., Solanki, S. K., Fligge, M., & Unruh, Y. C. 2003, Astronomy and Astrophysics, 399, L1

Krivova, N. A., Solanki, S. K., & Floyd, L. 2006, Astronomy and Astrophysics, 452, 631

Kuhn, J. R., Bush, R. I., Scherrer, P., & Scheick, X. 1998, Nature, 392, 155

Kunasz, P. & Auer, L. H. 1988, Journal of Quantitative Spectroscopy and Radiative Transfer, 39, 67

Kurucz, R. 1993, ATLAS9 Stellar Atmosphere Programs and 2 km/s grid. Kurucz CD-ROM No. 13. Cambridge, Mass.: Smithsonian Astrophysical Observatory, 1993., 13

Kurucz, R. L. 1992, Revista Mexicana de Astronomia y Astrofisica, vol. 23, 23, 181

Labeyrie, A. 1970, Astronomy and Astrophysics, 6, 85

Lagg, A., Solanki, S. K., Riethmüller, T. L., et al. 2010, The Astrophysical Journal Letters, 723, L164

Lathrop, K. & Carlson, B. 1965, Discrete Ordinates Angular Quadrature of the Neutron Transport Equation, Tech. Rep. LA-3186, Los Alamos National Laboratory, Los Alamos, NM

Lawrence, J. K., Topka, K. P., & Jones, H. P. 1993, Journal of Geophysical Research, 98, 18

Lean, J. 2000, Geophysical Research Letters, 27, 2425

Lean, J. L. & DeLand, M. T. 2012, Journal of Climate, 25, 2555

Leenaarts, J. & Carlsson, M. 2009, in Astronomical Society of the Pacific Conference Series, Vol. 415, The Second Hinode Science Meeting: Beyond Discovery-Toward Understanding, 87

Lin, H. & Rimmele, T. 1999, The Astrophysical Journal, 514, 448

Lites, B. W. 2011, The Astrophysical Journal, 737, 52

Lites, B. W., Centeno, R., & McIntosh, S. W. 2014, Publications of the Astronomical Society of Japan, 66, S4

Lites, B. W., Kubo, M., Socas-Navarro, H., et al. 2008, Astrophysical Journal, 672, 1237

Livingston, W. & Harvey, J. 1971, in Solar Magnetic Fields, Vol. 43, IAU Symposium, 51

Lohmann, A. W., Weigelt, G., & Wirnitzer, B. 1983, Applied Optics, 22, 4028

Lord, J. W., Cameron, R. H., Rast, M. P., Rempel, M., & Roudier, T. 2014, The Astrophysical Journal, 793, 24

Magic, Z., Collet, R., Asplund, M., et al. 2013, Astronomy and Astrophysics, 557, A26

Marino, J. 2012, Optical Engineering, 51, 101709

Marino, J. & Rimmele, T. 2010, Applied Optics, 49, G95

Matson, C. L. 1991, Journal of the Optical Society of America A, 8, 1905

Matthews, S. A., Collados, M., Mathioudakis, M., & Erdelyi, R. 2016, in Proc. SPIE, Vol. 9908, Ground-based and Airborne Instrumentation for Astronomy VI, 990809

McClintock, W. E., Rottman, G. J., & Woods, T. N. 2005, Solar Physics, 230, 225

Merkel, A. W., Harder, J. W., Marsh, D. R., et al. 2011, Geophysical Research Letters, 38, L13802

Meunier, N. 1999, The Astrophysical Journal, 515, 801

Miesch, M. S. & Toomre, J. 2009, Annual Review of Fluid Mechanics, 41, 317

Mihalas, D. 1978, Stellar Atmospheres, 2nd edn. (W. H. Freeman and Company)

Mihalas, D., Auer, L. H., & Mihalas, B. R. 1978, The Astrophysical Journal, 220, 1001

Mihalas, D. & Mihalas, B. W. 1984, Foundations of Radiation Hydrodynamics (Oxford University Press)

Mikurda, K. & von der Lühe, O. 2006, Solar Physics, 235, 31

Molodij, G. & Rousset, G. 1997, Journal of the Optical Society of America A, 14, 1949

Noll, R. J. 1976, Journal of the Optical Society of America, 66, 207

Nordlund, A. 1982, Astronomy and Astrophysics, 107, 1

Nordlund, Å., Stein, R. F., & Asplund, M. 2009, Living Reviews in Solar Physics, 6, 2

Orozco Suárez, D. & Bellot Rubio, L. R. 2012, The Astrophysical Journal, 751, 2

Ortiz, A. 2005, Advances in Space Research, 35, 350

Ortiz, A. & Rast, M. 2005, Memorie della Societa Astronomica Italiana, 76, 1018

Ortiz, A., Solanki, S. K., Domingo, V., Fligge, M., & Sanahuja, B. 2002, Astronomy & Astrophysics, 388, 1036

Paxman, R. G., Schulz, T. J., & Fienup, J. R. 1992, Journal of the Optical Society of America A, 9, 1072

Peck, C. L., Criscuoli, S., & Rast, M. P. 2017a, The Astrophysical Journal, 850, 9

Peck, C. L. & Rast, M. P. 2015, The Astrophysical Journal, 808, 192

Peck, C. L., Wöger, F., & Marino, J. 2017b, Astronomy & Astrophysics, 607, A83

Pehlemann, E. & von der Lühe, O. 1989, Astronomy and Astrophysics, 216, 337

Pereira, T. M. D. & Uitenbroek, H. 2015, Astronomy & Astrophysics, 574, A3

Petrovay, K. & Szakaly, G. 1993, Astronomy and Astrophysics, 274, 543

Pillet, V. M. 2013, Space Science Reviews, 178, 141

Preminger, D. G., Chapman, G. A., & Cookson, A. M. 2011, The Astrophysical Journal Letters, 739, L45

Preminger, D. G., Walton, S. R., & Chapman, G. A. 2002, Journal of Geophysical Research (Space Physics), 107, 1354

Puschmann, K. G. & Beck, C. 2011, Astronomy and Astrophysics, 533, A21

Puschmann, K. G. & Sailer, M. 2006, Astronomy and Astrophysics, 454, 1011

Rast, M. P., Fox, P. A., Lin, H., et al. 1999, Nature, 401, 678

Rast, M. P., Ortiz, A., & Meisner, R. W. 2008, The Astrophysical Journal, 673, 1209

Rempel, M. 2014, The Astrophysical Journal, 789, 132

Rempel, M., Schüssler, M., & Knölker, M. 2009, The Astrophysical Journal, 691, 640

Riethmüller, T. L., Solanki, S. K., Berdyugina, S. V., et al. 2014, Astronomy & Astrophysics, 568, A13

Rijkhorst, E.-J., Plewa, T., Dubey, A., & Mellema, G. 2006, Astronomy and Astrophysics, 452, 907

Roddier, F. 1981, Progress in optics. Volume 19. Amsterdam, North-Holland Publishing Co., 1981, p. 281-376., 19, 281

Rogers, F. J. & Iglesias, C. A. 1996, in Bulletin of the American Astronomical Society, Vol. 188, American Astronomical Society Meeting Abstracts #188, 58.04

Roggemann, M. C., Welsh, B. M., & Hunt, B. R. 1996, Imaging Through Turbulence (CRC Press)

Rottman, G., Harder, J., Fontenla, J., et al. 2005, Solar Physics, 230, 205

Sánchez Almeida, J. 2004, in Astronomical Society of the Pacific Conference Series, Vol. 325, The Solar-B Mission and the Forefront of Solar Physics, 115

Scharmer, G. B., Löfdahl, M. G., van Werkhoven, T. I. M., & de la Cruz Rodrguez, J. 2010, Astronomy and Astrophysics, 521, A68

Schmidt, D., Gorceix, N., Goode, P. R., et al. 2017, Astronomy and Astrophysics, 597, L8

Schmidt, W., von der Lühe, O., Volkmer, R., et al. 2012, Astronomische Nachrichten, 333, 796

Schnerr, R. S. & Spruit, H. C. 2011, Astronomy and Astrophysics, 532, A136

Spruit, H. C. 1976, Solar Physics, 50, 269

Spruit, H. C. 1982a, Astronomy and Astrophysics, 108, 348

Spruit, H. C. 1982b, Astronomy and Astrophysics, 108, 356

Spruit, H. C. & Zwaan, C. 1981, Solar Physics, 70, 207

Stein, R. F. 2012, Living Reviews in Solar Physics, 9, 4

Stenflo, J. O. 2010, Astronomy and Astrophysics, 517, A37

Štěpán, J. & Bueno, J. T. 2013, Astronomy & Astrophysics, 557, A143

Stilley, J. L. & Callaway, J. 1970, The Astrophysical Journal, 160, 245

Thaler, I. & Spruit, H. C. 2014, Astronomy and Astrophysics, 566, A11

Tritschler, A., Rimmele, T. R., Berukoff, S., et al. 2016, Astronomische Nachrichten, 337, 1064

Tritschler, A., Sankarasubramanian, K., Rimmele, T., Gullixson, C., & Fletcher, S. 2007, in Bulletin of the American Astronomical Society, Vol. 210, American Astronomical Society Meeting Abstracts #210, 26.03

Uitenbroek, H. 2001, The Astrophysical Journal, 557, 389

Uitenbroek, H. & Criscuoli, S. 2011, The Astrophysical Journal, 736, 69

Unruh, Y. C., Ball, W. T., & Krivova, N. A. 2012, Surveys in Geophysics, 33, 475

Unruh, Y. C., Krivova, N. A., Solanki, S. K., Harder, J. W., & Kopp, G. 2008, Astronomy & Astrophysics, 486, 311

Unruh, Y. C., Solanki, S. K., & Fligge, M. 1999, Astronomy and Astrophysics, 345, 635

van Noort, M., Rouppe van der Voort, L., & Löfdahl, M. G. 2005, Solar Physics, 228, 191

Veran, J.-P., Rigaut, F., Maitre, H., & Rouan, D. 1997, Journal of the Optical Society of America A, 14, 3057

Viticchié, B., Del Moro, D., Criscuoli, S., & Berrilli, F. 2010, The Astrophysical Journal, 723, 787

Vögler, A. 2005, Memorie della Societa Astronomica Italiana, 76, 842

Vögler, A., Bruls, J. H. M. J., & Schüssler, M. 2004, Astronomy and Astrophysics, 421, 741

Vögler, A. & Schüssler, M. 2007, Astronomy & Astrophysics, 465, L43

Vögler, A., Shelyag, S., Schüssler, M., et al. 2005, Astronomy & Astrophysics, 429, 335

von der Lühe, O. 1984, Journal of the Optical Society of America A, 1, 510

von der Lühe, O., Berkefeld, T., & Soltau, D. 2005, Comptes Rendus Physique, 6, 1139

Walton, S. R., Chapman, G. A., Cookson, A. M., Dobias, J. J., & Preminger, D. G. 1998, Solar Physics, 179, 31

Wang, J. Y. & Markey, J. K. 1978, Journal of the Optical Society of America, 68, 78

Wang, S., Li, K.-F., Pongetti, T. J., et al. 2013, Proceedings of the National Academy of Sciences, 110, 2023

Wedemeyer-Böhm, S. 2008, Astronomy and Astrophysics, 487, 399

Wedemeyer-Böhm, S. & Rouppe van der Voort, L. 2009, Astronomy and Astrophysics, 503, 225

Wehrli, C., Schmutz, W., & Shapiro, A. I. 2013, Astronomy and Astrophysics, 556, L3

Wenzler, T., Solanki, S. K., Krivova, N. A., & Fluri, D. M. 2004, Astronomy and Astrophysics, 427, 1031

Wiehr, E., Bovelet, B., & Hirzberger, J. 2004, Astronomy and Astrophysics, 422, L63

Wijn, A. G. d., Stenflo, J. O., Solanki, S. K., & Tsuneta, S. 2009, Space Science Reviews, 144, 275

Wöger, F., McBride, W., Ferayorni, A., et al. 2012, in Astronomical Society of the Pacific Conference Series, Vol. 463, Second ATST-EAST Meeting: Magnetic Fields from the Photosphere to the Corona., ed. T. R. Rimmele, A. Tritschler, F. Wöger, M. Collados Vera, H. Socas-Navarro, R. Schlichenmaier, M. Carlsson, T. Berger, A. Cadavid, P. R. Gilbert, P. R. Goode, & M. Knölker, 431

Wöger, F. & von der Lühe, O. 2007, Applied Optics, 46, 8015

Wöger, F., von der Lühe, O., & Reardon, K. 2008, Astronomy and Astrophysics, 488, 375

Wray, A. A., Bensassi, K., Kitiashvili, I. N., Mansour, N. N., & Kosovichev, A. G. 2015, arXiv:1507.07999 [astro-ph], arXiv: 1507.07999

Yeo, K. L., Krivova, N. A., & Solanki, S. K. 2014a, Space Science Reviews, 186, 137

Yeo, K. L., Krivova, N. A., Solanki, S. K., & Glassmeier, K. H. 2014b, Astronomy and Astrophysics, 570, A85

Yeo, K. L., Solanki, S. K., & Krivova, N. A. 2013, Astronomy and Astrophysics, 550, A95

Yeo, K. L., Solanki, S. K., Norris, C. M., et al. 2017, Physical Review Letters, 119

Zhu, Y., Narayan, R., Sadowski, A., & Psaltis, D. 2015, Monthly Notices of the Royal Astronomical Society, 451, 1661

Appendix A

Analytical Derivation of the Short-Characteristic Diffusion in 3D

The work presented here is the appendix for the published paper Peck et al. (2017a) presented in Chapter 4. We derive the analytical form of the numerical diffusion introduced by the method of short-characteristics radiative transfer for a ray propagating in a 3D cartesian domain. To isolate the effects of numerical diffusion, the numerical diffusion is calculated assuming a single delta-function point source at the bottom of the domain. The ray propagates through vacuum so there is no need to interpolate the plasma properties. To maintain analytical tractability, we assume linear interpolation and a regular spatial grid with sampling dx by dy and dz in the horizontal and vertical directions respectively.

In the short-characteristic method, rays are propagated differently depending on whether the upwind intensity is interpolated in a vertical or horizontal plane. We present the two cases separately. For the ray orientations shown in Figure 4, the intensity for both cases is updated from left to right and then from front to back. The solution is applicable to other ray orientations as the indices used represent the number of grid points away from the I_{source} location (e.g., I_{000} represents the source location and $I_{\mathrm{n_x n_y n_z}}$ represents the point n_x, n_y, and n_z grid steps from I_{source} in the x,y, and z directions). The domain is taken to have sufficient horizontal extent such that the fully dispersed beam intersects the upper domain boundary before exiting the sides. If this is not the case, horizontal periodicity must be imposed on the solution.

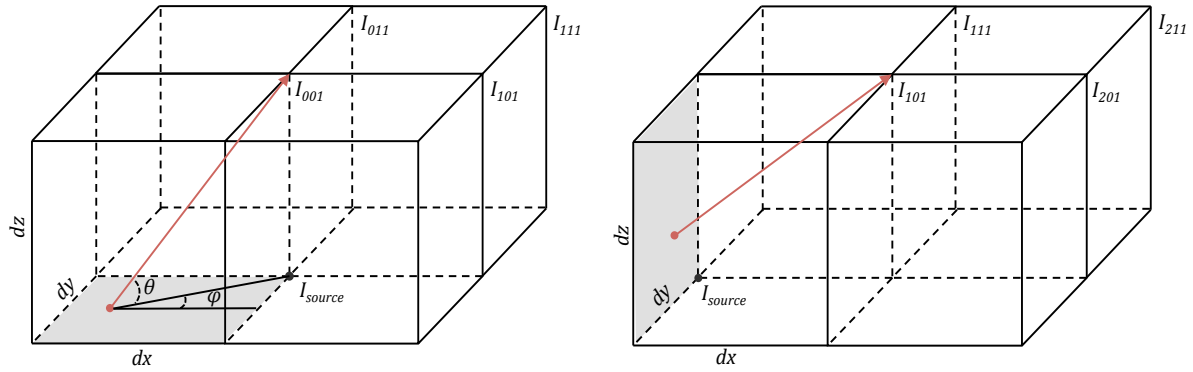

Figure A.1: Short-characteristic intensity interpolation in a 3D domain. Left: Interpolation on the xy plane. Right: Interpolation on the yz plane. Interpolation on the xz plane is not shown, but follows that on yz. Angles defined as shown in the left image.

A.1 Solution for Ray Directions for Interpolation on Horizontal Planes

The ray propagation for this subset of angles is shown on the left of Figure A.1. In 3D geometry, the boundary condition I_{source} on the upwind xy-plane results in four intensity values at the downwind grid points that are linearly interpolated as:

$$
\begin{aligned}
I_{001} &= I_{\text{source}} \left(1 - \frac{dz}{dx}\frac{\cos\phi}{\tan\theta}\right)\left(1 - \frac{dz}{dy}\frac{\sin\phi}{\tan\theta}\right), \\
I_{101} &= I_{\text{source}} \left(\frac{dz}{dx}\frac{\cos\phi}{\tan\theta}\right)\left(1 - \frac{dz}{dy}\frac{\sin\phi}{\tan\theta}\right), \\
I_{011} &= I_{\text{source}} \left(1 - \frac{dz}{dx}\frac{\cos\phi}{\tan\theta}\right)\left(\frac{dz}{dy}\frac{\sin\phi}{\tan\theta}\right),
\end{aligned}
$$

and

$$
I_{111} = I_{\text{source}} \left(\frac{dz}{dx}\frac{\cos\phi}{\tan\theta}\right)\left(\frac{dz}{dy}\frac{\sin\phi}{\tan\theta}\right). \tag{A.1}
$$

Repeating the interpolation at each subsequent plane (and thus compounding the interpolation error) yields the emergent intensity for point $I_{\mathrm{n_x n_y n_z}}$:

$$
I_{\mathrm{n_x n_y n_z}} = I_{\text{source}} \times I_{\mathrm{n_x n_z}} \times I_{\mathrm{n_y n_z}} ,
$$

with

$$I_{\mathrm{n_x n_z}} = \frac{n_z!}{(n_x)!(n_z - n_x)!}\left(1 - \frac{dz}{dx}\frac{\cos\phi}{\tan\theta}\right)^{n_z - n_x}\left(\frac{dz}{dx}\frac{\cos\phi}{\tan\theta}\right)^{n_x}$$

and

$$I_{\mathrm{n_y n_z}} = \frac{n_z!}{(n_y)!(n_z - n_y)!}\left(1 - \frac{dz}{dy}\frac{\sin\phi}{\tan\theta}\right)^{n_z - n_y}\left(\frac{dz}{dy}\frac{\sin\phi}{\tan\theta}\right)^{n_y}. \tag{A.2}$$

$I_{\mathrm{n_x n_z}}$ and $I_{\mathrm{n_y n_z}}$ are binomial distributions with variances

$$\sigma_x = \sqrt{nz\ \frac{dz}{dx}\frac{\cos\phi}{\tan\theta}\ \left(1 - \frac{dz}{dx}\frac{\cos\phi}{\tan\theta}\right)}$$

and

$$\sigma_y = \sqrt{nz\ \frac{dz}{dy}\frac{\sin\phi}{\tan\theta}\ \left(1 - \frac{dz}{dy}\frac{\sin\phi}{\tan\theta}\right)}. \tag{A.3}$$

For interpolation in horizontal planes the two-dimensional PSF (Equation A.2) has widths (Equation A.3) that are independent functions which depend on the propagation angle and the number of horizontal planes n_z through which the beam has propagated.

It is straightforward to show that source intensity is conserved with height. At any given height $n_z = N_z$ the total intensity is shown to be

$$\begin{aligned} I_{\mathrm{total}} &= \sum_{n_y=0}^{N_z}\sum_{n_x=0}^{N_z} I_{\mathrm{n_x n_y N_z}} \\ &= I_{\mathrm{source}}\left(1 - \frac{dz}{dx}\frac{\cos\phi}{\tan\theta}\right)^{N_z}\left(1 - \frac{dz}{dy}\frac{\sin\phi}{\tan\theta}\right)^{N_z}\left[\sum_{n_x=0}^{N_z}\frac{N_z!}{(n_x)!(N_z - n_x)!}\left(\frac{\frac{dz}{dx}\frac{\cos\phi}{\tan\theta}}{1 - \frac{dz}{dx}\frac{\cos\phi}{\tan\theta}}\right)^{n_x}\right] \\ &\quad \times\left[\sum_{n_y=0}^{N_z}\frac{N_z!}{(n_y)!(N_z - n_y)!}\left(\frac{\frac{dz}{dy}\frac{\sin\phi}{\tan\theta}}{1 - \frac{dz}{dy}\frac{\sin\phi}{\tan\theta}}\right)^{n_y}\right] \\ &= I_{\mathrm{source}}\,, \end{aligned} \tag{A.4}$$

where we have used the binomial series expansion $(1+x)^\alpha = \sum_{k=0}^{\alpha}\binom{\alpha}{k}x^k$ with $\alpha = N_z$.

The PSFs for three viewing angles are shown in Figure A.2 after being scaled to account for apparent foreshortening (x and y in Figure A.2 have been defined so that the images display the intensity as it would be observed from an inclined angle, not the solutions to Equation A.2 on the xy grid plane).

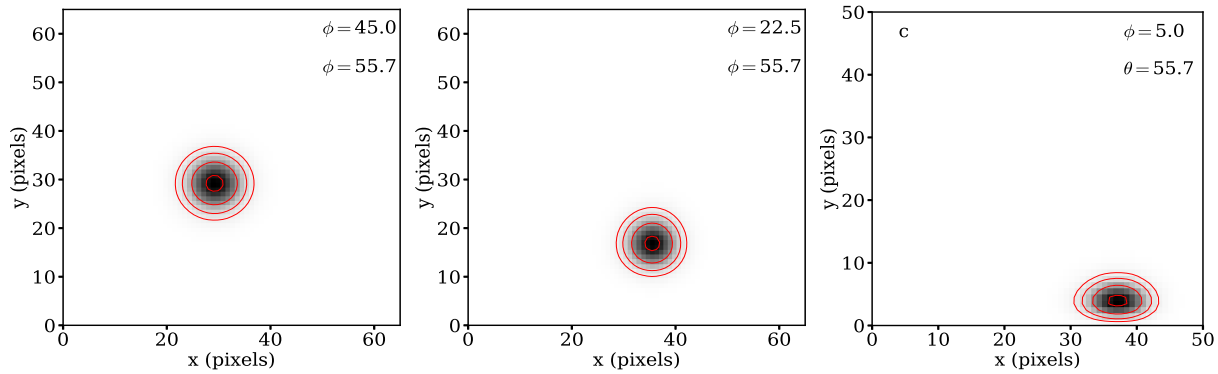

Figure A.2: PSFs derived from Equation A.2. Note that the position of the PSF at the top of the domain simply reflects the propagation angle. (*a*) Centered interpolation in the *xy* grid. The PSF is circular with $\sigma_x = \sigma_y$. (*b* and *c*) Non-centered interpolation in the *xy* grid, resulting in increasingly oblate PSF with decreasing ϕ. Contours denote the reduction in peak amplitude of 10%, 50%, 75% and 87.5%.

A.2 Solution for Ray Directions for Interpolation on Vertical Planes

Using the same method as in the previous subsection, we derive the beam diffusion for when the incident angle is such that the interpolation occurs in *xz* or *yz* planes. Here we explicitly present the solution for interpolation in *yz* planes, as illustrated by the right hand panel of Figure A.1. As indicated below, the solution can be readily generalized for the alternative case (interpolation in *xz* planes).

In most short-characteristic schemes, the first grid point value is solved employing a long-characteristic ray, and we assume the that is true here for the first upwind grid point to avoid complication and without loss of exactness. Unlike for interpolation on horizontal planes, for which only four grid points on the first horizontal plane downwind of I_{source} are illuminated, interpolation on vertical planes populates the entire horizontal plane down wind of the source. This is because each subsequent downwind interpolation, as one sweeps left to right, relies on the previous grid point solution. Thus sweeping from left to right each successive row front to back (in the direction

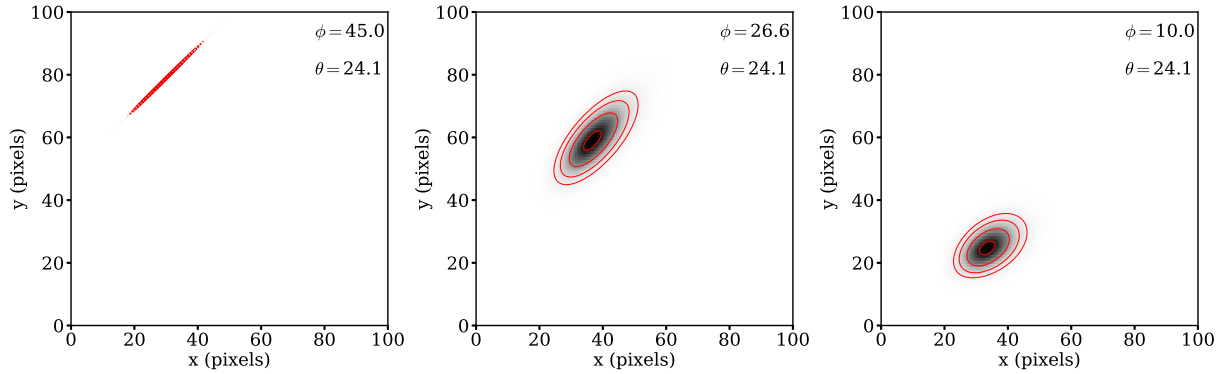

Figure A.3: PSFs derived from Equation A.6. (a) Interpolation on the z-1 axis due to $\phi = 45$, resulting in smearing only in the inclination direction. (b) Centered interpolation in the yz grid. Note that $\sigma_x = \sigma_y$ despite the principal axes of the distribution no longer being aligned with x and y as in Figure A.2. (c) Non-centered interpolation in the yz grid which causes an asymmetric distribution. Contours denote the reduction in peak amplitude of 10%, 50%, 75% and 87.5%.

of ray propagation) yields the following:

$$
\begin{aligned}
I_{101} &= I_{\rm source}\left(1 - \frac{dx}{dy}\frac{\sin\phi}{\cos\phi}\right)\left(\frac{dx}{dz}\frac{\tan\theta}{\cos\phi}\right), \\
I_{201} &= I_{101}\left(1 - \frac{dx}{dy}\frac{\sin\phi}{\cos\phi}\right)\left(1 - \frac{dx}{dz}\frac{\tan\theta}{\cos\phi}\right) = I_{\rm source}\left(1 - \frac{dx}{dy}\frac{\sin\phi}{\cos\phi}\right)^2\left(1 - \frac{dx}{dz}\frac{\tan\theta}{\cos\phi}\right)\left(\frac{dx}{dz}\frac{\tan\theta}{\cos\phi}\right), \\
I_{301} &= I_{201}\left(1 - \frac{dx}{dy}\frac{\sin\phi}{\cos\phi}\right)\left(1 - \frac{dx}{dz}\frac{\tan\theta}{\cos\phi}\right) = I_{\rm source}\left(1 - \frac{dx}{dy}\frac{\sin\phi}{\cos\phi}\right)^3\left(1 - \frac{dx}{dz}\frac{\tan\theta}{\cos\phi}\right)^2\left(\frac{dx}{dz}\frac{\tan\theta}{\cos\phi}\right), \\
I_{401} &= \ldots, \\
I_{110} &= 0, \\
I_{111} &= I_{\rm source}\left(\frac{dx}{dy}\frac{\sin\phi}{\cos\phi}\right)\left(\frac{dx}{dz}\frac{\tan\theta}{\cos\phi}\right), \\
I_{211} &= 2I_{\rm source}\left(1 - \frac{dx}{dy}\frac{\sin\phi}{\cos\phi}\right)\left(\frac{dx}{dy}\frac{\sin\phi}{\cos\phi}\right)\left(1 - \frac{dx}{dz}\frac{\tan\theta}{\cos\phi}\right)\left(\frac{dx}{dz}\frac{\tan\theta}{\cos\phi}\right),
\end{aligned}
$$

and

$$
I_{311} = \ldots . \tag{A.5}
$$

Continuing this procedure and recognizing the negative binomial distribution with $n_x > n_z$ yields:

$$
I_{\rm n_x n_y n_z} = I_{\rm source} \times I_{\rm n_x n_z} \times I_{\rm n_y n_x},
$$

with

$$I_{\mathrm{n_x n_z}} = \frac{n_x - 1!}{(n_x - n_z)!(n_z - 1)!}\left(1 - \frac{dx}{dz}\frac{\tan\theta}{\cos\phi}\right)^{n_x - n_z}\left(\frac{dx}{dz}\frac{\tan\theta}{\cos\phi}\right)^{n_z}$$

and

$$I_{\mathrm{n_y n_x}} = \frac{n_x!}{n_y!(n_x - n_y)!}\left(1 - \frac{dx}{dy}\frac{\sin\phi}{\cos\phi}\right)^{n_x - n_y}\left(\frac{dx}{dy}\frac{\sin\phi}{\cos\phi}\right)^{n_y}. \tag{A.6}$$

Note that $I_{\mathrm{n_x n_z}}$ in this solution is a negative binomial distribution, while the $I_{\mathrm{n_y n_x}}$ is a regular binomial distribution. $I_{\mathrm{n_x n_z}}$, as previously for interpolation on horizontal planes, describes diffusion in n_x and depends on the number of n_z levels through which the ray has passed. $I_{\mathrm{n_y n_x}}$, on the other hand, depends on n_x and n_y as diffusion in the two horizontal directions are no longer independent. The PSFs derived from Equation A.6 are shown in Figure A.3 for three inclination angles. They have been scaled to account for apparent foreshortening to show appearance of the PSF at inclined viewing angles. Note that the distributions are no longer aligned with the x and y axes. This is a consequence of the mixing introduced in by the $I_{\mathrm{n_y n_x}}$ term. Since the spread in $I_{\mathrm{n_y n_x}}$ depends on n_x, the distribution in Figure A.3c is asymmetric, with larger broadening for larger n_x values. The variances associated with these distributions are

$$\sigma_x = \sqrt{n_z \frac{dz}{dx}\frac{\cos\phi}{\tan\theta}\left(\frac{dz}{dx}\frac{\cos\phi}{\tan\theta} - 1\right)},$$

and

$$\sigma_y = \sqrt{n_x \frac{dx}{dy}\frac{\sin\phi}{\cos\phi}\left(1 - \frac{dx}{dy}\frac{\sin\phi}{\cos\phi}\right)}, \tag{A.7}$$

with the variance in the y direction reflecting the asymmetry.

The derivation above is valid for ray angles for which the interpolation occurs in the yz plane. For angles which the interpolation occurs in the xz plane, the solution is given by Equations A.6 and A.7 with x and y and $\sin\phi$ and $\cos\phi$ interchanged.

As in Sec. A1, the specific intensity is conserved. Explicitly, as before,

$$
\begin{aligned}
I_{\rm total} &= \sum_{n_x=N_z}^{\infty} \sum_{n_y=0}^{n_x} I_{\rm n_x n_y N_z} \\
&= I_{\rm source} \left(\frac{dx}{dz}\frac{\tan\theta}{\cos\phi}\right)^{N_z} \left[\sum_{n_x=N_z}^{\infty} \frac{n_x-1!}{(n_x-N_z)!(N_z-1)!}\left(1-\frac{dx}{dz}\frac{\tan\theta}{\cos\phi}\right)^{n_x-N_z}\left(1-\frac{dx}{dy}\frac{\sin\phi}{\cos\phi}\right)^{n_x}\right. \\
&\quad \times \left.\left[\sum_{n_y=0}^{n_x} \frac{n_x!}{n_y!(n_x-n_y)!}\left(\frac{\frac{dx}{dy}\frac{\sin\phi}{\cos\phi}}{1-\frac{dx}{dy}\frac{\sin\phi}{\cos\phi}}\right)^{n_y}\right]\right] \\
&= I_{\rm source} \left(\frac{dx}{dz}\frac{\tan\theta}{\cos\phi}\right)^{N_z} \left[\sum_{n_x=N_z}^{\infty} \frac{n_x-1!}{(n_x-N_z)!(N_z-1)!}\left(1-\frac{dx}{dz}\frac{\tan\theta}{\cos\phi}\right)^{n_x-N_z}\right] \\
&= I_{\rm source}\,, \qquad \text{(A.8)}
\end{aligned}
$$

where we have used the binomial and negative binomial series expansions $(1+x)^{\alpha} = \sum_{k=0}^{\alpha} \binom{\alpha}{k} x^k$ with $\alpha = n_y$ and $1/(1-x)^{\beta} = \sum_{n=0}^{\infty} \binom{n+\beta}{n} x^n$ with $\beta = N_z - 1$ and $n = n_x - N_z$.

Appendix B

Theory of Speckle Imaging

B.1 Image Formation Through a Turbulent Atmosphere

Propagation of a wavefront from an astronomical source to a ground-based telescope can be described through the interferometric view of imaging. This view utilizes the mutual coherence of two points on the source (i.e. the Sun) and computes the coherence at the image plane of the telescope. As the two wavefronts propagate from the source to the telescope aperture they undergo diffraction, described by the Huygens-Fresnel Principle, and interfere at the entrance of the telescope. All of the atmospheric perturbations due to Earth's turbulent atmosphere are assumed to be located in a thin screen at the telescope aperture; the contributions of which will be analyzed in later subsections. The intensity on the image screen is measured by following the mutual coherence of the two point sources from the source, through the pupil plane, and arriving at the image plane. The derivations in this appendix closely follow the notation and descriptions provided by Goodman (2005) for the Fourier treatment of imaging and Roggemann et al. (1996) for wavefront propagation through a turbulent atmosphere.

The following subsections present the background in the interferometric view of imaging in this regime. The first section demonstrates the derivation of the imaging equation and the assumptions implicit in there, including that of an incoherent source. The second section covers the Kolmogorov statistics of atmospheric turbulence and its relationship to interferometry. The third section derives the speckle transfer function from the preceding sections.

B.1.1 Wavefront Propagation

We begin with a monochromatic wave, $U(P_0)$, which undergoes diffraction as it propagates. We are interested in the resulting wavefront at point P_1 which is described by the Huygens-Fresnel principle:

$$U(P_1) = \frac{1}{i\lambda} \int \int_{\Sigma} U(P_0) \frac{\exp[ikr]}{r} \cos(\theta) dS \tag{B.1}$$

where λ is the wavelength, r is the distance between P_0 and P_1, and θ is the angle between $\vec{r}$ and the normal to the surface (see Figure B.1).

We aim to compute the intensity on the image plane, which is done through the mutual intensity, $J(\vec{x_1}, \vec{x_2})$ for $\vec{x_1} = \vec{x_2} = \vec{x}$, where

$$I(\vec{x}) = J(\vec{x}, \vec{x}) = \langle U(\vec{x}) U^*(\vec{x}) \rangle. \tag{B.2}$$

The expectation values can be applied over space or time for ergodic processes (such as those from the atmosphere), and for imaging are generally taken to be over the integration time of the detector. For narrowband light, the maximum path length difference is much smaller than the coherence length of the light and therefore there is no dependence on time differences due to the path lengths in the calculation of the image intensity.

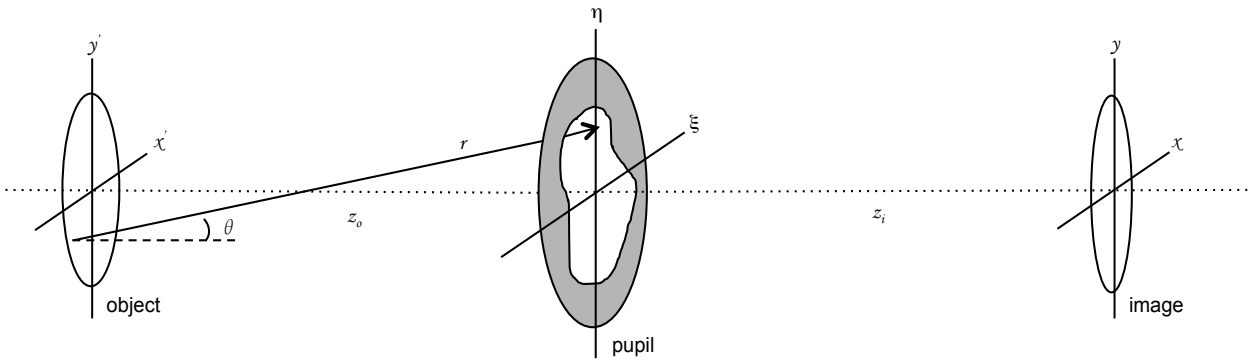

Figure B.1: Coordinate conventions for the source, aperture, and images planes.

Using the Huygens-Fresnel principle in Equation B.1, the intensity is

$$I(\vec{x}) = \langle \frac{1}{\lambda^2} \int \int_{-\infty}^{\infty} d\vec{\xi_1} d\vec{\xi_2} W(\vec{\xi_1}) W^*(\vec{\xi_2}) U(\vec{\xi_1}) U^*(\vec{\xi_2}) \frac{\exp[ik(r_1 - r_2)]}{r_1 r_2} \cos(\theta_1) \cos(\theta_2) \rangle. \tag{B.3}$$

where

$$W(\vec{\xi}) = \begin{cases} \frac{1}{\pi}, & \text{if } \left|\vec{\xi}\right| \leq D/2 \\ 0, & \text{if } \left|\vec{\xi}\right| > D/2 \end{cases}$$

is the pupil function defining the finite extent of the aperture. The expectation values operate only on the terms $W(\vec{\xi})$ — containing all the perturbations due to the atmosphere — and $U(\vec{\xi})$ since no other terms have any implicit dependence on time. Additionally, we separate the averaging between the two variables since they are statistically independent from each other (i.e. the atmosphere and solar time variations are independent from each other). We then rewrite Equation B.3 as

$$I(\vec{x}) = \frac{1}{\lambda^2} \int \int_{-\infty}^{\infty} d\vec{\xi_1} d\vec{\xi_2} \langle W(\vec{\xi_1}) W^*(\vec{\xi_2}) \rangle \langle U(\vec{\xi_1}) U^*(\vec{\xi_2}) \rangle \frac{\exp[ik(r_1 - r_2)]}{r_1 r_2} \cos(\theta_1) \cos(\theta_2) \, . \tag{B.4}$$

where we have also recognized $\langle U(\vec{\xi_1}) U^*(\vec{\xi_2}) \rangle = J(\vec{\xi_1}, \vec{\xi_2})$, which is the mutual intensity in the pupil plane.

We take a slight deviation from Equation B.4 to calculate $J(\vec{\xi_1}, \vec{\xi_2})$. Using Equation B.1 and the notation in Figure B.1, we write $J(\vec{\xi_1}, \vec{\xi_2})$ as

$$J(\vec{\xi_1}, \vec{\xi_2}) = \frac{1}{\lambda^2} \int \int_{-\infty}^{\infty} d\vec{x_1'} d\vec{x_2'} \langle U(\vec{x_1'}) U^*(\vec{x_2'}) \rangle \frac{\exp[ik(r_1' - r_2')]}{r_1' r_2'} \cos(\theta_1') \cos(\theta_2') \, . \tag{B.5}$$

where the finite extend of the source (i.e., the Sun) is implicit in the definitions of the wavefronts $U(\vec{x'})$. To form an image from the wavefronts in Equation B.3, a lens or curved mirror must be used. We implement the geometry of a parabolic mirror in conjunction with the Fresnel approximation, applicable for 'large' distances (more than a few wavelengths) between the pupil and the image screen. This is shown in Figure B.2. where

$$r' = \sqrt{z'^2 + x'^2 + y'^2 - 2\xi x' - 2\eta y'} \approx z \left[1 + \frac{\vec{x'}^2}{2x^2} - \frac{\vec{x'} \cdot \vec{\xi}}{z^2} \right] \tag{B.6}$$

Using the Fresnel approximation for $r' \approx z' >> \left|\vec{x'}\right|$ and applying the Taylor series expansion to Equation B.6, Equation B.5 becomes

$$J(\vec{\xi_1}, \vec{\xi_2}) = \frac{1}{\lambda^2 z^2} \int \int_{-\infty}^{\infty} d\vec{x_1}' d\vec{x_2}' \langle U(\vec{x_1}') U^*(\vec{x_2}') \rangle \exp \left[ik \left(\frac{\vec{x_1}'^2 - \vec{x_2}'^2}{2z'} - \frac{\vec{x_1}' \cdot \vec{\xi_1} - \vec{x_2}' \cdot \vec{\xi_2}}{z'} \right) \right] . \tag{B.7}$$

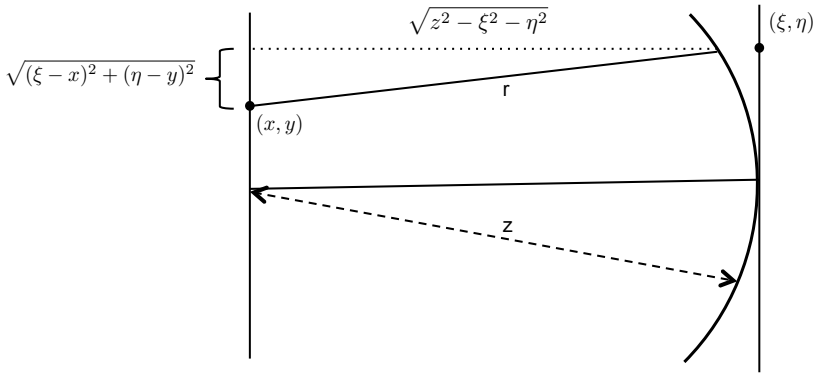

Figure B.2: Curved mirror geometry.

Since the Sun is structured at scales much smaller than the photon mean free path (see e.g., Judge et al. 2015), we can use the fact that the Sun is incoherent at the scales resolvable by DKIST (15 km). Therefore $\langle U(\vec{x_1}')U^*(\vec{x_2}')\rangle = \kappa I(\vec{x_1}')\delta(\vec{x_1}' - \vec{x_2}')$ where κ is a constant used to maintain equality, giving Equation B.7 as (with $\vec{x_1}' = \vec{x}$)

$$J(\vec{\xi_1},\vec{\xi_2}) = \frac{\kappa}{\lambda^2 z'^2}\int_{-\infty}^{\infty} d\vec{x}' I(\vec{x}') \exp\left[-ik\vec{x}'\cdot\frac{\vec{\xi_1}-\vec{\xi_2}}{z'}\right] = \frac{\kappa}{\lambda^2 z'^2}\mathcal{F}\left\{I(\vec{x}')\right\}_{\mathrm{f}=\frac{\vec{\xi_2}-\vec{\xi_1}}{\lambda z'}}. \tag{B.8}$$

Equation B.8 is the Van Cittert-Zernike theorem, which states that for an incoherent source, the mutual intensity is related to the Fourier transform of the source intensity.

With Equation B.8, we now return our attention to Equation B.4. Using the same geometry of Figure B.2 and the Fresnel approximation as done in Equation B.7, we find the image intensity as

$$I(\vec{x}) = \frac{\kappa}{\lambda^4 z^2 z'^2}\int\int_{-\infty}^{\infty} d\vec{\xi_1} d\vec{\xi_2}\langle W(\vec{\xi_1})W^*(\vec{\xi_2})\rangle \mathcal{F}\left\{I(\vec{x}')\right\}_{\mathrm{f}=\frac{\vec{\xi_2}-\vec{\xi_1}}{\lambda z'}} \exp\left[\frac{ik}{z}\vec{x}\cdot(\vec{\xi_1}-\vec{\xi_2})\right]. \tag{B.9}$$

Using $k = 2\pi/\lambda$ and taking the Fourier transform of Equation B.9, we obtain

$$\begin{aligned}
\tilde{I}(\vec{f}) &= \frac{\kappa}{\lambda^4 z^2 z'^2} \int \int_{-\infty}^{\infty} d\vec{\xi_1} d\vec{\xi_2} \langle W(\vec{\xi_1}) W^*(\vec{\xi_2}) \rangle \mathcal{F}\left\{ I(\vec{x}') \right\}_{\mathrm{f}=\frac{\tilde{\xi_2}-\tilde{\xi_1}}{\lambda z'}} \\
&\qquad \times \int_{-\infty}^{\infty} d\vec{x} \exp\left[\frac{2\pi i}{\lambda z} \vec{x} \cdot (\vec{\xi_1} - \vec{\xi_2}) \right] \exp\left[2\pi i \vec{x} \cdot \vec{f} \right] \\
&= \frac{\kappa}{\lambda^4 z^2 z'^2} \int \int_{-\infty}^{\infty} d\vec{\xi_1} d\vec{\xi_2} \langle W(\vec{\xi_1}) W^*(\vec{\xi_2}) \rangle \mathcal{F}\left\{ I(\vec{x}') \right\}_{\mathrm{f}=\frac{\tilde{\xi_2}-\tilde{\xi_1}}{\lambda z'}} \delta(\vec{f} - \frac{\vec{\xi_1} - \vec{\xi_2}}{\lambda z}) \\
&= \frac{\kappa}{\lambda^2 z'^2} \int_{-\infty}^{\infty} d\vec{\xi} \langle W(\vec{\xi}) W^*(\vec{\xi} - \lambda z \vec{f}) \rangle \mathcal{F}\left\{ I(\vec{x}') \right\}_{\mathrm{f}=-\frac{z}{z'}\tilde{\mathrm{f}}} \\
&= \frac{\kappa}{\lambda^2 z'^2} \tilde{I}_{\mathrm{o}}(\vec{f}) \int_{-\infty}^{\infty} d\vec{\xi} \langle W(\vec{\xi}) W^*(\vec{\xi} - \lambda z \vec{f}) \rangle
\end{aligned} \tag{B.10}$$

Normalizing Equation B.10 to $\int_{-\infty}^{\infty} d\vec{\xi} \langle W(0) W^*(0) \rangle$ then gives the well known result of up to a magnification factor which is generally assumed to be unity,

$$\tilde{I}_i(\vec{f}) = \tilde{I}_{\mathrm{o}}(\vec{f}) \times OTF(\vec{f}) \tag{B.11}$$

where

$$OTF(\vec{f}) = \int_{-\infty}^{\infty} d\vec{\xi} \langle W(\vec{\xi}) W^*(\vec{\xi} - \lambda z \vec{f}) \rangle. \tag{B.12}$$

Equation B.11 is the incoherent imaging equation and Equation B.12 is the generalized OTF for an arbitrary pupil.

B.1.2 Influence of Atmospheric Turbulence on Wavefront Propagation

We now turn our attention to the form of the pupil functions in Equation B.12. So far, no constraints have been put on the form of the function $W(\vec{\xi})$ other than its sole dependency on the pupil plane coordinates. It therefore represents the general pupil function and will contain all wavefront perturbations due to the atmospheric turbulence. We now write the pupil function in the form:

$$W(\vec{\xi}) = W_{\mathrm{p}}(\vec{\xi}) \exp[i\Phi(\vec{\xi}) + l(\vec{\xi})]. \tag{B.13}$$

$W_{\mathrm{p}}(\vec{\xi})$ defines the finite extent of the aperture, and $\Phi(\vec{\xi})$ and $l(\vec{\xi})$ define the phase and amplitude fluctuations due to the atmospheric turbulence, respectively. We now explore the forms of these phase and amplitude fluctuations.

The phase and log amplitude fluctuations in Equation B.13 can be described as turbulent induced index of refraction variations due to Earth's turbulent atmosphere. For a single layer of turbulence at a height h and thickness δh above the telescope aperture, the wavefront phase and amplitude variations are given as

$$\begin{aligned} \Phi(\vec{\xi}) &= \mathrm{Re}\left[\frac{2\pi}{\lambda}\int_h^{h+\delta h} n(\vec{\xi},\zeta)d\zeta\right] \\ l(\vec{\xi}) &= \mathrm{Im}\left[\frac{2\pi}{\lambda}\int_h^{h+\delta h} n(\vec{\xi},\zeta)d\zeta\right] \end{aligned} \tag{B.14}$$

where $n(\vec{\xi},\zeta)$ is the perturbation in the index of refraction from the mean value $n(\vec{\xi},\zeta) = N(\vec{\xi},\zeta) - \langle N(\vec{\xi},\zeta)\rangle_\zeta$. Combining Equation B.12 and B.13 gives

$$\begin{aligned} OTF(\vec{f}) = &\int_{-\infty}^{\infty} d\vec{\xi} W_\mathrm{p}(\vec{\xi}) W_\mathrm{p}^*(\vec{\xi} - \lambda z\vec{f}) \\ &\times \left\langle \exp\left[i\left(\Phi(\vec{\xi}) - \Phi(\vec{\xi} - \lambda z\vec{f})\right) + \left(l(\vec{\xi}) - l(\vec{\xi} - \lambda z\vec{f})\right)\right]\right\rangle. \end{aligned} \tag{B.15}$$

We take a moment to note the form of the exponential in Equation B.15. The difference terms for the phase and log amplitude fluctuations depend only on the spatial separation of two points. Because the pupil plane has a finite size which is small compared to atmospheric scales, these difference terms allows us to neglect large spatial scales. This makes the problem tractable as we can now ignore the problems of infinite variances that will ultimately arise later in the definition of the speckle transfer function (STF). For example, spatial scale variations on the size of the Earth exist in the atmosphere, such as that due to diurnal heat gradient. Because we are only interested in the difference in phase and amplitude fluctuations in the horizontal plane, we can ignore the largest scales which are not sampled by the telescope. The scales of interest then are those at the atmospheric turbulence scale.

The averaging in Equation B.15 is typically thought of as the detector integration time. For a long-exposure or speckle burst images in solar observations, this time scale is approximately 5 s. In that time, the atmosphere — which evolves on timescales of 10 ms — has seen on the order of 500 realizations. Since the averaging in Equation B.15 is over many atmospheric realizations,

we can apply the Central Limit Theorem which states that the mean values of many independent random variables (i.e. atmospheric phase and amplitude fluctuations) tends toward a Gaussian distribution.

For a Gaussian distributed variable, x,

$$\langle g(x)\rangle = \int_{-\infty}^{\infty} dx g(x) f(x) \tag{B.16}$$

where f(x) is the normal distribution. Applying this to the form of Equation B.15 and that the atmospheric phase and amplitude fluctuations are gaussian random variables, we obtain

$$\langle \exp[ix]\rangle = \frac{1}{\sqrt{2\pi\sigma^2}} \int_{-\infty}^{\infty} dx \exp[ix] \exp[-x^2/2\sigma^2]. \tag{B.17}$$

Through integration and the fact that $\langle x\rangle = 0$, since the mean value of the index of refraction fluctuations have already been removed, this reduces Equation B.17 to

$$\langle \exp[ix]\rangle = \exp[-\frac{1}{2}\sigma^2] = \exp[-\frac{1}{2}\langle x^2\rangle]. \tag{B.18}$$

Assuming that log amplitude and phase fluctuations are independent, we can now write Equation B.15 as

$$\begin{aligned} OTF(\vec{f}) = & \int_{-\infty}^{\infty} d\vec{\xi} W_{\mathrm{p}}(\vec{\xi}) W_{\mathrm{p}}^*(\vec{\xi} - \lambda z \vec{f}) \\ & \times \exp\left[i \left\langle \left(\Phi(\vec{\xi}) - \Phi(\vec{\xi} - \lambda z \vec{f}) \right)^2 \right\rangle + \left\langle \left(l(\vec{\xi}) - l(\vec{\xi} - \lambda z \vec{f}) \right)^2 \right\rangle \right]. \end{aligned} \tag{B.19}$$

Applying the definitions of the phase and log amplitude structure functions (see e.g., Fried 1966b) where

$$D_{\mathrm{F}}(\lambda z \vec{f}) = \langle (F(\vec{\xi}) - F(\vec{\xi} - \lambda z \vec{f}))^2 \rangle, \tag{B.20}$$

yeilds

$$OTF(\vec{f}) = \int_{-\infty}^{\infty} d\vec{\xi} W_{\mathrm{p}}(\vec{\xi}) W_{\mathrm{p}}^*(\vec{\xi} - \lambda z \vec{f}) \exp\left[i D_{\Phi}(\lambda z \vec{f}) + D_l(\lambda z \vec{f}) \right]. \tag{B.21}$$

The structure functions are related to the distribution of size and number of the turbulent eddies which result in the refraction variations. For the Earth's atmosphere, the structure functions are typically related to the structure constant, C_n^2, which characterizes the strength of the

turbulence as a function of height in the atmosphere. Typically, contributions from D_l are ignored due to the relatively small fluctuations in amplitude compared with the phase (Roddier 1981). The phase structure function is then given by Fried (1966a) as

$$D_\Phi(\lambda z \vec{f}) = 6.88\left(\frac{|\Delta\vec{x}|}{r_{o_i}}\right)^{5/3}$$
$$r_o = 0.185\left[\frac{4\pi^2}{\kappa^2 C_{n_i}^2 \Delta z_i}\right]^{5/3}, \tag{B.22}$$

where r_o is the Fried parameter.

B.2 Derivation of the Speckle Transfer Function

Using the derivation above, we now derive the speckle transfer function including partial compensation from an AO system. The amplitude transmission of a wavefront with variations in optical phase, $\Phi(\vec{r})$, through a circular unobstructed aperture, $W(\vec{r})$, is described by the generalized pupil function in Equation B.13 The instantaneous STF, $S(\vec{s})$, is the auto-correlation of the generalized pupil function, given by Equation B.15 where the log amplitude fluctuations have been ignored. This results in

$$S(\vec{s}) = \int d\vec{r} W\left(\vec{r}+\frac{1}{2}\vec{s}\right) W\left(\vec{r}-\frac{1}{2}\vec{s}\right)$$
$$\times \exp\left[i\left(\Phi\left(\vec{r}+\frac{1}{2}\vec{s}\right) - \Phi\left(\vec{r}-\frac{1}{2}\vec{s}\right)\right)\right], \tag{B.23}$$

where $\vec{s} = \frac{\vec{f}}{f_c}D$ represents the normalized position in the entrance pupil of the telescope with $f_c = D/\lambda$ is the spatial frequency cutoff of the telescope.

We assume that all static aberrations are removed by the AO system, therefore the term $\Phi(\vec{r})$ describes the combined phase variations of the atmosphere and the AO compensation. Following the calculations of Wang & Markey (1978) and Korff (1973), using the notation of Wöger & von der Lühe (2007), we separate the phase into the atmospheric component, $\varphi(\vec{r})$, and the AO compensation,

$\phi(\vec{r})$, so Equation B.23 becomes

$$\begin{aligned} S(\vec{s}) = \int d\vec{r} W\left(\vec{r}+\frac{1}{2}\vec{s}\right) W\left(\vec{r}-\frac{1}{2}\vec{s}\right) \\ \times \exp\left[i\left\{\left(\varphi\left(\vec{r}+\frac{1}{2}\vec{s}\right)-\phi\left(\vec{r}-\frac{1}{2}\vec{s}\right)\right)\right.\right. \\ \left.\left.-\left(\varphi\left(\vec{r}-\frac{1}{2}\vec{s}\right)-\phi\left(\vec{r}-\frac{1}{2}\vec{s}\right)\right)\right\}\right]. \end{aligned} \tag{B.24}$$

The phase terms can be represented in terms of mutually orthogonal Karhunen–Loève (KL) basis functions, $F_{\mathrm{i}}(\vec{r})$, where

$$\varphi(\vec{r}) = \sum_{i=2}^{\infty} a_i F_i(\vec{r}) \qquad \text{and} \qquad \phi(\vec{r}) = \sum_{i=2}^{N} \beta_i a_i F_i(\vec{r}). \tag{B.25}$$

The term a_{i} represents the expansion coefficient of the ith KL mode and β_i describes the degree of compensation by the AO system, with $-1 < \beta_i < 1$. For example, $\beta_i = 0$ represents a KL mode that is entirely uncorrected, while $\beta_i = 1$ represents a KL mode that is fully corrected by the AO system. A negative value for β_i is generally found for the case of anisoplanatism, where the phase screens of the atmosphere decorrelate off the on-axis viewing angle.

The Fourier amplitudes can be reconstructed using Labeyrie's method (Labeyrie 1970), with

$$\langle |I_j(\vec{s})|^2 \rangle = |O(\vec{s})|^2 \times \langle |S_j(\vec{s})|^2 \rangle. \tag{B.26}$$

the spatial power spectrum of the object, $|O(f)|$, can be determined if the speckle transfer function (STF), $\langle |S_j(\vec{s})|^2 \rangle$, is known. The ensemble average is taken over a series of burst images, or speckle burst, which have a time cadence at approximately the atmospheric evolution time ($\sim$10 ms).

To determine the STF from Equation 8.3, we introduce the abbreviation:

$$g'^{+} := g(\vec{r'} + \frac{1}{2}\vec{s}), \quad g'^{-} := g(\vec{r'} - \frac{1}{2}\vec{s}). \tag{B.27}$$

Using the expansion coefficients in equation 3, we obtain

$$\begin{aligned}\langle|S(\vec{s})|^2\rangle = &\int\int d\vec{r'}d\vec{r}W^+W^-W'^+W'^- \\ &\times\langle\exp\Bigg[-i\Bigg\{\Big(\varphi^+-\phi^+\Big)-\Big(\varphi^--\phi^-\Big) \\ &-\Big(\varphi'^+-\phi'^+\Big)-\Big(\varphi'^--\phi'^-\Big)\Bigg]\Bigg\}\rangle. \end{aligned} \tag{B.28}$$

Using the definition of the phase structure function in Equation B.22, the equality $\langle exp(ix)\rangle = exp(\frac{1}{2}\langle x^2\rangle)$ for a gaussian random variable x discussed previously, we recover Equation 12 from (Wöger & von der Lühe 2007):

$$\begin{aligned}\langle|S(\vec{s})|^2\rangle = &\int\int d\vec{r'}d\vec{r}W^+W^-W'^+W'^- \\ &\exp\Bigg[-\mathscr{D}(\vec{s})-\mathscr{D}(\Delta\vec{r})+\frac{1}{2}\{\mathscr{D}(\Delta\vec{r}+\vec{s})+\mathscr{D}(\Delta\vec{r}-\vec{s})\} \\ &+K(\vec{r},\vec{s})+L(\vec{r},\vec{s})+K(\vec{r'},\vec{s})+L(\vec{r'},\vec{s}) \\ &-\tilde{K}(\vec{r},\vec{r'},\vec{s})-\tilde{L}(\vec{r},\vec{r'},\vec{s})-\tilde{K}(\vec{r'},\vec{r},\vec{s})-\tilde{L}(\vec{r'},\vec{r},\vec{s})\Bigg] \end{aligned} \tag{B.29}$$

where

$$\begin{aligned}K(\vec{r},\vec{s}) &= \sum_{i=2}^{N}\sum_{j=2}^{N}\beta_{\mathrm{j}}\Big(1-\frac{1}{2}\beta_{\mathrm{i}}\Big)\langle a_{\mathrm{i}}a_{\mathrm{j}}\rangle(F_{\mathrm{i}}^+-F_{\mathrm{i}}^-)(F_{\mathrm{j}}^+-F_{\mathrm{j}}^-) \\ L(\vec{r},\vec{s}) &= \sum_{i=N+1}^{\infty}\sum_{j=2}^{N}\beta_{\mathrm{j}}\langle a_{\mathrm{i}}a_{\mathrm{j}}\rangle(F_{\mathrm{i}}^+-F_{\mathrm{i}}^-)(F_{\mathrm{j}}^+-F_{\mathrm{j}}^-) \end{aligned} \tag{B.30}$$

and

$$\begin{aligned}\tilde{K}(\vec{r},\vec{r'},\vec{s}) &= \sum_{i=2}^{N}\sum_{j=2}^{N}\beta_{\mathrm{j}}\Big(1-\frac{1}{2}\beta_{\mathrm{i}}\Big)\langle a_{\mathrm{i}}a_{\mathrm{j}}\rangle(F_{\mathrm{i}}^+-F_{\mathrm{i}}^-)(F_{\mathrm{j}}^{+'}-F_{\mathrm{j}}^{-'}) \\ \tilde{L}(\vec{r},\vec{r'},\vec{s}) &= \sum_{i=N+1}^{\infty}\sum_{j=2}^{N}\beta_{\mathrm{j}}\langle a_{\mathrm{i}}a_{\mathrm{j}}\rangle(F_{\mathrm{i}}^+-F_{\mathrm{i}}^-)(F_{\mathrm{j}}^{+'}-F_{\mathrm{j}}^{-'})\ . \end{aligned} \tag{B.31}$$

Applying the mutual orthogonality of the KL functions reduces the term $\langle a_{\mathrm{i}}a_{\mathrm{j}}\rangle$ to $\langle a_{\mathrm{i}}^2\rangle\delta_{\mathrm{ij}}$,

thereby reducing the terms in Equation B.29 to

$$
\begin{aligned}
K(\vec{r},\vec{s}) &= \sum_{i=2}^{N} \beta_{\mathrm{i}} \left(1 - \frac{1}{2}\beta_{\mathrm{i}}\right) \langle a_{\mathrm{i}}^2 \rangle (F_{\mathrm{i}}^{+} - F_{\mathrm{i}}^{-})(F_{\mathrm{i}}^{+} - F_{\mathrm{i}}^{-}) \\
\tilde{K}(\vec{r},\vec{r}',\vec{s}) &= \sum_{i=2}^{N} \beta_{\mathrm{i}} \left(1 - \frac{1}{2}\beta_{\mathrm{i}}\right) \langle a_{\mathrm{i}}^2 \rangle (F_{\mathrm{i}}^{+} - F_{\mathrm{i}}^{-})(F_{\mathrm{i}}^{+'} - F_{\mathrm{i}}^{-'}) \\
L(\vec{r},\vec{s}) &= 0 \\
\tilde{L}(\vec{r},\vec{r}',\vec{s}) &= 0 \ .
\end{aligned}
\tag{B.32}
$$

We then arrive at the form of the STF in Equation 8.5 as

$$
\begin{aligned}
\langle |S(\vec{s})|^2 \rangle = \int\int d\vec{r}' d\vec{r} W^{+} W^{-} W'^{+} W'^{-} \\
\exp\Bigg[- \mathscr{D}(\vec{s}) - \mathscr{D}(\Delta\vec{r}) + \frac{1}{2}\{\mathscr{D}(\Delta\vec{r} + \vec{s}) + \mathscr{D}(\Delta\vec{r} - \vec{s})\} \\
+ K(\vec{r},\vec{s}) + K(\vec{r}',\vec{s}) - \tilde{K}(\vec{r},\vec{r}',\vec{s}) - \tilde{K}(\vec{r}',\vec{r},\vec{s}) \Bigg]
\end{aligned}
\tag{B.33}
$$

defined in terms of the mutually orthogonal KL functions.